Computational Mechanical Characterisation of Schwarz P Unit Cell-Based Tissue Scaffolds Fabricated via Two-Photon Polymerisation (2PP)

By

Adi Zakwan Zabidi

(MEng)

Thesis submitted to the University of Nottingham

for the degree of Doctor of Philosophy

September 2018

Abstract

Schwarz P unit cell-based tissue scaffolds have been fabricated via two-photon polymerisation (2PP). In this thesis, a computational approach to characterising the mechanical properties of the scaffolds made of poly(D,L-lactide-co-ε-caprolactone)(PLCL) copolymer via micromechanical analysis is presented.

The stereolithography (.STL) model of the Schwarz P unit cell design used as input for 2PP was 'reverse engineered' to obtain a surface geometry model for implementation in computational analyses. In the experimental model of this study, the mechanical properties of bulk material PLCL and fabricated tissue scaffolds were experimentally characterised. Data obtained from fabricated tissue scaffolds were used as a basis of comparison to data obtained from mechanical characterisation of the scaffold via computational analyses.

Computational model of this study involved the implementation of micromechanical analysis together with the Schwarz P surface geometry model and bulk material data obtained previously in linear and non-linear analyses. Initial investigations in linear analyses showed significant discrepancy between the experimental and computational model due to geometrical transformations between the input Schwarz P unit cell design and unit cells comprising the fabricated tissue scaffolds. This was confirmed further through measurement analyses of scanning electron microscope (SEM) micrographs of the scaffolds. A methodology to mediate the geometrical transformations through CAD modeling techniques was investigated before re-implementation into revised linear analyses. Results showed excellent agreement between the computational and experimental results with only a small margin of error at 6.94%. Investigations in non-linear analyses demonstrated parallels between stress-strain response obtained from micromechanical analysis and those from *in vivo* loading conditions in confined compression of Schwarz P unit cell-based tissue scaffolds. Implementation of micromechanical analysis to oversee relationships between different dimensional parameters to the resulting effective modulus was also investigated through linear analyses. Mathematical expressions describing the relationships were then derived.

This thesis concludes with the implications of this study with suggestions for improvement. Suggestions for future work are also put forward.

Table of Contents

Chapter 1

Introduction

1.1 Tissue Engineering

Tissue engineering has attracted the interest of scientists from a wide range of disciplines such as medicine, engineering and biology [1–4]. It is a wide multidisciplinary field involving the application of principles and methods of engineering and life sciences to understand structure-function relationships in normal and pathological mammalian tissues as well as to develop biological substitutes able to restore, maintain or improve tissue function [5]. This field reaches far back as early as 1933 when Bisceglie used mouse tumor cells encased in a polymer membrane to be inserted in the abdominal cavity of a pig. It was found that the tumor cells were able to live long enough to not be killed by the immune system [6].

The bone plays a key role in human physiological functions such as protection, movement, support of other critical organs, blood productions, mineral storage and homeostasis and blood pH regulation. Bone related diseases such as osteogenesis imperfecta, osteoarthritis, osteomyelitis and osteoporosis results in loss or dysfunction of skeletal tissue [7,8]. In the treatment of bone defects, a substitutionary material is used as a filler. Autogenous bone grafting (also known as autografting) is considered the gold standard for the treatment of bone defects. In autografting, a patient's host bone is taken from another site such as the pelvis or iliac crest to fill a particular bone defect. This creates two different surgical sites; the site for host bone and the site of bone defect. It has been reported that this method has a complication rate as high as 30% with the

complications potentially resulting from donor site morbidity, pain, paresthesia, prolonged hospitalization and rehabilitation, risk of infection, hematoma, inflammation and restrictions in availability [7].

Another method of treatment is allografting, which uses bone tissue from a donor for implantation at the site of bone defect. Despite being FDA approved and implemented for years, this method of treatment is further complicated by the necessary healing period post-transplantation [9]. Allografting also carries risks in terms of infection due to the donor-recipient transplantation with a reported rate of incidence as high as 13% from complications resulting from disease transmission and host immune responses [7].

The field of tissue engineering and regenerative medicine has sought approaches to mediate the substantial limitations and disadvantages brought on by the conventional methods. These approaches involve bringing together the harnessing of stem cells and biological factors into scaffolds to for the purpose of enhancing bone formation [8].

1.2 Tissue Engineering Scaffolds

Tissue scaffolds act as temporary substrates for cell growth by providing a porous structure for cell growth and tissue formation in a three-dimensional manner [10]. Earlier scaffold constructs focused on providing mechanical support and stability at a particular site of bone defect while also stimulating the ingrowth of cells from surrounding healthy tissues as well as guide tissue formation processes. With developments in tissue engineering, cells can now be seeded within the constructs of a scaffold and subsequently enhance tissue regeneration functions [11]. These follow on from foundational concepts found in the relationship between cell growth with respect to biophysical stimuli and mechano-transduction. Resulting biomechanical forces between an implanted scaffold and surrounding bone tissue (due to net stiffness) modulates cell shapes and the associated mechano-transduction processes to subsequently give way to different cellular responses such as tissue differentiation, focal adhesions, cytoskeletal reorganisation, cytoskeletal tension and signaling cascades [12,13].

A particular tissue scaffold should encourage adherence between its architecture and seeded therapeutic cells to promote cell-biomaterial interactions and the deposition of extracellular matrix (ECM) [14]. The ECM acts as a platform through which biophysical and biochemical stimuli are transferred [12,15–18]. Cells adhere to the ECM through the release of adhesion molecules which subsequently initiate signaling events which enable the cells to respond to the biophysical and biochemical stimuli [19]. With the above, the ECM plays a functional role in the remodeling of tissues and organs while also providing structural support [20].

The biomaterials science aspect of tissue scaffold design has mainly taken a trial and error approach. Tissue scaffolds are first prepared in a laboratory environment before

undergoing experiments either *in vitro* or *in vivo*. Based on the results, modifications are made on the tissue scaffolds in order to make improvements and the scaffolds with undesirable results are disposed of or simply kept aside [21]. Advancements in terms of hardware and software have pushed computer aided design (CAD) beyond the conventional borders of their applications demonstrated in automotive, civil and aeronautical engineering. With developments in imaging technologies and reverse engineering techniques, CAD can now be practiced in the realms of biomedical engineering with applications in clinical medicine through to the manufacturing of customised implants in a new field known as computer aided tissue engineering (CATE) [22]. CAD offers the opportunity to reduce experimental testing stages and shorten the duration of tissue scaffolds design through the use of computer techniques based on mechanical design [21]. Pairing the above with additive manufacturing techniques, a particular scaffold can be easily fabricated and be reproducible.

1.3 Aims & Objectives

The main aim of the conducted work was to characterise the mechanical properties of Schwarz P unit cell-based tissue scaffolds via a computational approach. Schwarz P unit cell-based tissue scaffolds have been fabricated via two-photon polymerisation (2PP) as part of the European Union Research and Innovation 7th Framework Programme (FP7) under grant agreement no. 2633 63 (INNOVABONE) with TETRA – Society for Sensoric, Robotics and Automation GmbH (Ilmenau, Germany). An ideal computational approach should be able to;

(a) Have suitability in its implementation to the structure of the tissue scaffold in question
(b) Characterise the mechanical properties of the tissue scaffold
(c) Maintain efficiency in terms of time and computational resources in processing the computational approach in conjunction to the scaffold considered

The objectives that need to be achieved in conjunction to the aim are as follows;

(a) To investigate and determine a computational approach suitable to characterising the mechanical properties of Schwarz P unit-cell based tissue scaffolds
(b) Determine the required model input for computational analysis
(c) Determine the material data input to be assigned to the model for computational analysis
(d) Derive the necessary boundary conditions for implementation of the computational approach in conjunction to the model considered
(e) Characterise the mechanical properties of Schwarz P unit-cell based tissue scaffolds in an experimental context

(f) Compare the experimental and computational results obtained from the mechanical characterisation of the tissue scaffolds

(g) Validate the computational approach used based on the comparison made above

(h) Validate the implemented derived boundary conditions based on the computational approach against its own results

(i) Investigate the relationships between different dimensional parameters to the resulting mechanical characteristics of the tissue scaffold after successful validation in (g) and (h)

This study explores the mechanical characterisation of Schwarz P unit-cell based tissue scaffolds fabricated using copolymer materials based on methacrylated poly(D,L-lactide-co-ε-caprolactone) (PLCL) via the computational approach, micromechanical analysis. It is to the author's knowledge that no previous work has been done on performing micromechanical analysis to characterise the mechanical properties of the tissue scaffolds above in the context of bone tissue engineering. Implementation of scaffolds in the context of bone tissue engineering requires consideration of mechanical and biological aspect to their design. Thus, computational analysis for the purposes of mechanical characterisation would considerably be advantageous. It is also to the author's knowledge that the novelty of the work also lies in the copolymer material used in conjunction to computational analysis.

1.4 Thesis Layout

The structure of the study performed is graphically presented as a flowchart in Figure 1-1.

Chapter 2 provides a literature review in consideration of this study. Basic requirements for tissue scaffold design along with common materials used for scaffold fabrication are discussed. A general background on computer aided tissue modeling is discussed before bringing into focus a background on the Schwarz P architecture. Scaffold fabrication methods are then discussed according to traditional methods and fabrication techniques relevant through CATE respectively. The final part of this chapter discusses a general background in computational work involving mathematical modeling in regards to different aspects of tissue scaffold implementation. Some examples include their design, mechanical characterisation and fluid flow. Focus then turns to the computational approach considered for this study i.e. micromechanical analysis.

Chapter 3 presents the CAD modeling involved for computational analysis. A small background into the limitations of stereolithography (.STL) packaging format for CAD models is discussed before assessing the required methodology needed to mediate those limitations. This methodology will 'reverse engineer' a .STL file containing the Schwarz P unit cell model into a surface geometry model that is then usable in the context of computational analysis.

Chapter 4 presents the experimental model in regards to characterising the mechanical properties of the bulk material comprising the fabricated tissue scaffolds i.e. methacrylated poly(D,L-lactide-co-ε-caprolactone) (PLCL); and the fabricated tissue scaffolds themselves. PLCL of different lactide (L) to caprolactone (C) compositions have been investigated under INNOVABONE. Hence discussions in selecting a particular composition as a background before introducing the methodology to

characterise the mechanical properties of bulk PLCL with the selected composition. Based on the results obtained, different forms of material data are extracted to be used as input in computational models. The methodology to characterise the mechanical properties of Schwarz P unit cell-based tissue scaffolds fabricated via two-photon polymerisation (2PP) are then introduced before presentation of the results. The results obtained will be used as a basis of comparison to the results obtained from mechanical characterisation of the same scaffolds assigned with the same material performed via computational means.

Chapter 5 presents the computational model in this study. This chapter firstly introduces the computational approach considered i.e. micromechanical analysis. Background in regards to the approach is discussed before delving into derivations for boundary conditions and methodology for its application in conjunction to the Schwarz P unit cell architecture. Micromechanical analysis is compared to a different computational approach to justify its suitability in terms of the results obtained. Validation is also performed based on the results obtained to ensure correct implementation of the derived boundary conditions for micromechanical analysis. Chapter 5 is then divided into three sub-chapters which will consider linear analysis, non-linear analysis and predictive modeling of Schwarz P unit cell designs; all implementing micromechanical analysis.

The sub-chapter for linear analysis investigates comparisons between results of mechanical characterisation of Schwarz P unit cell-based tissue scaffolds obtained from experiments and micromechanical analysis. Initial investigations showed significant discrepancy between the computational and experimental results. This was found to be due to geometrical transformations between the input original Schwarz P unit cell design (defined in the .STL file) used during 2PP and the unit cells comprising the fabricated

tissue scaffold. A methodology was constructed and presented to mediate the transformations in terms of CAD modeling before subsequent reimplementation in revised linear analyses. Revised linear analyses required the derivations for micromechanical analysis to be re-examined. This has been discussed in the sub-chapter. Revised analyses shows excellent agreement with experimental models and thus validated micromechanical analysis as a suitable approach to computationally characterise the mechanical properties of the tissue scaffold structure in question. The following sub-chapter investigates the comparison of the mechanical characterisation of Schwarz P unit cell-based tissue scaffolds obtained from experiments and micromechanical analysis in a non-linear context. Here, non-linear analysis follows from the revised analyses performed previously with the only difference being in terms of the non-linear material model that is used.

The sub-chapter for predictive modeling investigates the relationships between different dimensional parameters making up the Schwarz P architecture to the resulting effective modulus. The relationships were assessed through 3-dimensional surface plots from which mathematical expressions are then defined. These mathematical expressions serve as predictive models to determine the suitability of a design defined in terms of the different dimensional parameters in accordance to the effective modulus. The implication of this is further discussed in the sub-chapter.

Finally, Chapter 6 concludes the study by overseeing different implications of this study. Suggestions for improvements for this study are also presented in the chapter along with future possible work.

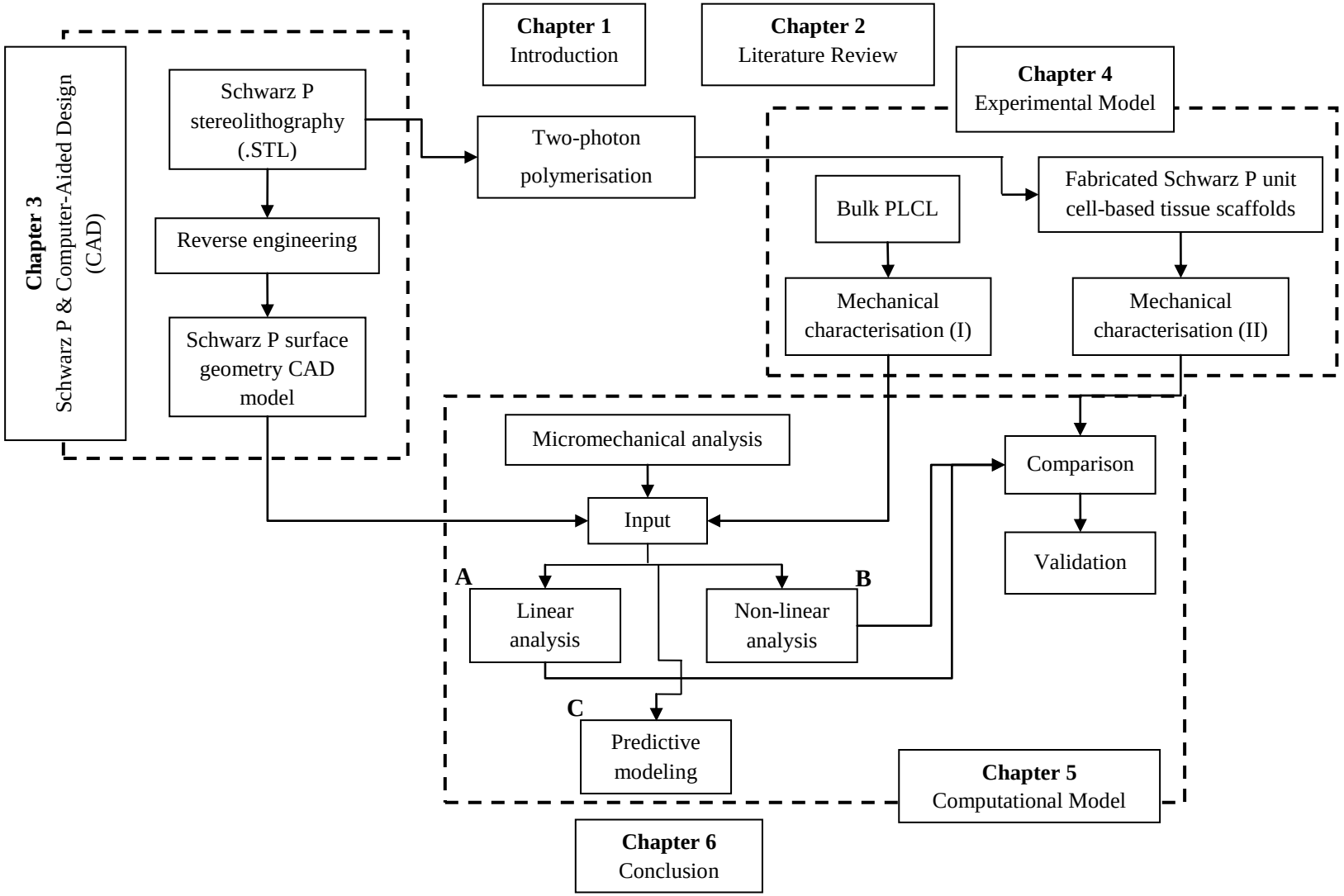

Figure 1-1 : Flowchart presenting the structure of the study and how different chapters connect. Chapter 5 makes up the main bulk of this study and is integrated into and with Chapters 3 and 4.

Chapter 2

Literature Review

2.1 Introduction

This chapter presents the relevant background knowledge for this study by taking into focus different aspects of bone tissue engineering scaffolds. The basic requirements essential to tissue scaffold design is first discussed before considering different common biomaterials used for their fabrication. A general background on computer aided tissue modeling is discussed before introducing the Schwarz P architecture considered in this study. Subsequently, scaffold fabrication methods are then discussed according to traditional methods. The emergence of computer aided tissue engineering (CATE) has brought additive manufacturing to the forefront of scaffold fabrication. Different techniques in regards to this will be explored before delving into the fabrication method that was used for the scaffolds considered in this study. A general background on previous work in terms of computational and mathematical modeling in regards to different aspects of tissue scaffold implementation is also discussed. The computational approach considered for this study is then brought into focus.

2.2 Bone Tissue Scaffold Design

2.2.1 Background

The implantation of a tissue scaffold in a bone defect initiates the first step in the healing process. In the case where no distraction methods such as external fixation devices are used in conjunction with scaffold implantation, the scaffold will bear the load of the defective region and is subjected to stress. Bone modeling will be initiated due to mechano-sensing of the bone and subsequent degradation of the tissue scaffold. Once the bone tissue has been repaired, the normal biomechanical functions of the bone tissue are then restored to its normal state [23]. With this, it can be deduced that the requirements for a functioning scaffold is attributed to its mechanical as well as biological properties.

The success of a bone tissue scaffold is dependent on its ability to stimulate and aid in the onset of the bone modeling process through to its completion with a healed bone defect [23]. This success on the other hand is dependent on several parameters that serve to be requirements that should be taken into consideration in scaffold fabrication. These parameters are discussed in the following sub-sections.

2.2.2 Mechanical Properties

The mechanical properties of scaffolds are one of the main factors that determine their success in terms of functionality once implanted. Experiencing various different types of stresses such as compression, tension, torsion and shearing, careful consideration of their mechanical properties is required especially if implemented in load-bearing applications [24–27]. Scaffolds with high mechanical properties in terms of stiffness may lead to stress shielding which would subsequently lead to weakening of bone around the region of implantation and loosening effects due to poor cell tissue integration [28]. However, scaffolds with low mechanical properties results in poor load bearing capacity which

potentially leads to structural failure. Careful consideration of the mechanical properties of scaffold is also crucial as they become a determinant factor in controlling cell behavior particularly in the context of mechanotransduction [11]. The mechanical properties of scaffolds should match the mechanical properties of the region of native tissue it is being implanted in [29].

In bone tissue engineering applications, scaffolds should generally have similar mechanical properties to that of bone. These mechanical properties should also be dependent on the anatomical location and type of bone tissue i.e. cortical or trabecular [30,31]. The modulus of cortical (compact) bone has been reported to range between 7GPa – 20GPa with values between 15GPa and 19GPa being more typical [32–34]. The modulus of cortical bone has also been reported to range between 7GPa – 30GPa [35]. On the other hand, trabecular (cancellous) bone has been found to have modulus values ranging between 1.5GPa – 11.2GPa with typical values being between 2GPa and 5GPa [36–39]. It has also been reported that the modulus of trabecular bone ranges between 0.02GPa – 0.5GPa [35]. The morphological and mechanical specifications in designing implants for bone regeneration being a dependent factor on the anatomical conditions and requirements at the site of defect has been previously studied [40]. Using finite element anaylsis (FEA), a numerical study was conducted to determine whether the above is true in regards to bone remodeling. It has been reported that bone remodeling is optimum when the scaffold elastic tensor either matches or is slightly higher than the elastic properties bone at the site of defect [41]. The scaffolds' elastic tensor is a measure of its stiffness in terms of mechanical properties.

Bone modeling is based on mechanotransduction, a process of converting mechanical stimuli into chemical signals that affect cellular responses through different mechanisms.

Considered responsible for maintaining the balance between bone formation and bone resorption, the mechanical properties of scaffolds in terms of elastic modulus (or Young's modulus) is required to simulate the dynamic and mechanical nature of physiological activities of native bone [7]. Cells receive mechanical feedback once they adhere to the surfaces of a scaffold with or without the presence of applied forces. These cells adjust their cytoskeletal system by generating forces through their actin-myosin system in response to differences in the stiffness of scaffolds. The changes in their cytoskeletal organization play a part in signaling pathways by transferring mechanical feedback into chemical responses. Furthermore, the changes also determines the cell shapes and hence their behavior in terms of cell growth, migration and differentiation [11].

With all the above, a scaffold should be able to withstand the physiological stresses that are applied while also exhibiting a suitable stiffness that would encourage cell interaction. This only stresses the necessary need for mechanical evaluations in regards to the scaffolds properties and performance.

2.2.3 Pore Structure

The pore structure of a particular scaffold can be parameterised in terms of porosity, pore size, interconnectivity, micro-architecture and the surface area to volume ratio; all dependent factors for tissue regeneration and integration with surrounding tissue at the site of implantation [42].

Porosity plays a critical role in determining the extent to which cell attachment, migration, proliferation and differentiation occurs. In addition, the porosity is a determining property for bone tissue ingrowth and vascularization by enabling the transport of nutrients as well as metabolic wastes [43]. Bone interstitial fluid flows through the porous regions of bone whereby the application of mechanical strain causes the volume of some pores to

decrease and others to increase. This imbalance creates a bone fluid pressure difference to give fluid flow that also streams electric potentials [44]. With bone tissue scaffold implanted in a defect, the inherent porosity allows the fluid flow from regions of healthy bone to flow through. This will further stimulate the cellular response seeded within the scaffold and subsequently enhance the bone regeneration process. A previous study has reported that porosity values between 50% and 90% are suitable for scaffolds in non-load bearing applications [45]. A minimum porosity of 55% has been investigated to give way to an interconnected porous structure which encourages cell ingrowth, vascularisation as well as transport of metabolic products [46]. A separate study has reported a minimum of 60% porosity to encourage the growth of new bone tissues within the pores [47]. A listing has been outlined charting pore size and porosity requirements according to various scaffold types to induce different cellular activities [48].

An increase in porosity leads to the increase in relative permeability and subsequently vascularization and mineral desposition of bone tissue. A study conducted to study the correlation between pore morphology and interconnectivity with respect to bone ingrowth has found that the minimum relative hydrodynamic permeability required for vascularization and mineralization is $3 \times 10^{-11} \mathrm{m}^2$ [49]. In regions of cancellous bone, the relative permeability is in the range of $1.2 \times 10^{-10}\ \mathrm{m}^2 - 8.05 \times 10^{-9}\ \mathrm{m}^2$ while the relative permeability in regions of cortical bone is in the range $1 \times 10^{-23}\ \mathrm{m}^2 - 1 \times 10^{-13}\ \mathrm{m}^2$. Overall, the relative permeability should be within or higher than the ranges stated with respect to the site of implantation [50].

The extent to which migration and proliferation of cells occur along with vascularisation is determined by the pore size. Currently, no optimal pore size has been determined and results of studies remain ambiguous. To add to the complexity, it has also been

hypothesised that the optimal pore size also varies with different cell types [51]. Scaffolds with pore sizes ranging between 20μm and 1,500μm have been used in bone tissue engineering applications. Studies have demonstrated that the minimum pore size for significant bone growth is between 75μm to 100μm while pore sizes ranging between 100μm to 135μm was found to be optimum. Pore sizes ranging between 50μm to 500μm were determined to be optimum for load bearing applications [52]. A study investigating scaffolds seeded with bone morphogenetic protein suspended in fibrin gel has reported that pore sizes ranging between 350μm and 800μm only played a limited role in bone regeneration when implanted subcutaneously in immune-compromised mice [53]. A study looking into the potential of implementing ceramic materials as permanently implantable skeletal prostheses have found that bone ingrowth occurs with pore sizes greater than 100μm. Further increase of pore size to 150μm and greater encourages osteon formation [54]. Titanium plates with pore sizes of 50, 75, 100 and 125μm implanted in rabbit femurs showed no difference in terms of bone in-growth. Another study looking into the relationship between the porosity of 3D scaffolds and osteogenesis has determined that large pore sizes favor direct osteogenesis due to high vascularization and oxygen flow while smaller pore sizes resulted in osteochondral ossification. Implants with pore sizes of more than 300μm demonstrated better osteogenic properties [55]. In another study, polycaprolactone (PCL) scaffolds with pore sizes ranging between 186μm and 200μm were found to promote fibroblast infiltrations while the same scaffolds with pore sizes ranging between 290μm and 310μm encouraged bone formation [56].

A scaffold with a randomly defined micro-architecture can bring about poor biomechanical properties despite being able to produce a significant amount of regenerated tissue. Uneven pore sizes can result in non-uniform cell density formation

while small pore sizes can result in occlusions that prevents cellular penetration and matrix formation [42]. A micro-architecture with a high surface area to volume ratio allows the accommodation for a large number of anchorage-dependent cells to adhere to. The cells will then be able to grow and form a cell mass or tissue. The extent to which this cell mass forms affects the mechanical strength of the grown tissue. Hence, it can be implied that the surface area to volume ratio becomes a dependent factor on the mechanical strength of the tissue grown [42].

2.2.4 Biocompatibility

Biocompatibility is referred to the ability of a material to perform with the appropriate host response in a specific situation [57]. Expanding the definition above into a concept, the definition of biocompatibility entails three tenets that a material has to perform rather than simply exist in tissues; (i) the response evoked has to be appropriate for the application; (ii) nature of the response to a specific material and; (iii) its appropriateness varies in the context of one situation to another [58]. In a practical sense, biocompatibility dictates whether cells are able to migrate and adhere to the surface of a scaffold material without eliciting any adverse inflammatory reactions that could result in its bodily rejection [59]. This requirement can be characterized by several components i.e. toxicity, cytotoxicity, genotoxicity, mutagenicity, carcinogenicity and immunogenicity.

Toxicity refers to the ability to bring about damage to a particular biological system through chemical means. Divided into two, systemic and local toxicity can be differentiated by the distance at which adverse reactions occur from the application site. Cytotoxicity refers to the ability to cause damage to cells which could subsequently lead to cell death via necrosis or programmed cell death, otherwise known as apoptosis [60].

Immunogenicity is characterized by the ability of the material to bring about an immune response or the degree to which it provokes a response. An allergic reaction to the substance can be illicited in cases where the cells in contact with the substance have been previously sensitised. Genotoxicity refers to alterations in the basepair sequencing of genome DNA. Even though cells are able to repair damage due to genotoxicity by various mechanisms, genetic damage can still potentially be passed on to subsequent generations resulting in an effect named mutagenicity [60].

2.2.5 Biodegradability

Biodegradability ensures the resorption of the tissue scaffold construct to allow for its replacement with bone extracellular matrix while also facilitating load transmission through the developing bone [7,59]. A particular material should be able to degrade in a controlled rate so as to match the rate of formation of bone tissue [61,62]. It has been reported that the tissue scaffold construct should be resorbed through metabolic pathways after between 12 to 18 months to allow for tissue ingrowth and regeneration. In addition, the material should also be able to degrade without producing any toxic by-products [7].

2.3 Biomaterials for Tissue Scaffold Fabrication

2.3.1 Background

There is a delicate balance in ensuring the mechanical integrity of a scaffold while also ensuring the porosity is ideal for bone tissue formation. Scaffolds with larger pore sizes give way to larger void spaces which in turn can encourage capillary formation and subsequently direct osteogenesis [63]. However, these larger pore sizes compromise the mechanical integrity of the scaffold structure. With this, a tissue scaffold must have pore sizes that are sufficient to fulfill nutrient and waste diffusion requirements of a tissue to encourage its growth but also ensure mechanical integrity [53]. However, the requirement for mechanical properties can also be fulfilled through the selection of an ideal material.

In terms of mechanical properties, the scaffold material should be able to withstand any physiological stresses during surgical handling and maintain mechanical integrity while functioning efficiently without significant failure once implanted [59]. This is essential as bones play a role in the transmission of load during physiological movements such as standing, walking and running. The following sub-sections present common biomaterial used for scaffold fabrication.

2.3.2 Bioceramics

Ceramic materials with specific biological or physiological functions can be referred to as bioceramics [64]. In terms of their properties, bioceramics exhibit biocompatibility, excellent surface compatibility, anti-thrombus effects, bactericidal effects, good physical and chemical stability [65]. Bioceramics also exhibit good mechanical compatibility as bone grows into the pores of ceramic to develop a highly convoluted interface [66,67]. Compared to polymers and metals, bioceramics demonstrate better tissue responses [68].

Bioceramics can be classified into three main groups with fundamental differences being in terms of their illicited tissue responses. These groups include bioactive, resorbable ceramics and nearly inert. Bioactive and resorbable ceramics have been extensive used in tissue engineering scaffolds compared to inert ceramics due to their capabilities in forming a stable bond with host tissue while also maintaining gradual degradation over a period of time to be replaced by the natural host tissue [69]. This has been demonstrated in previous studies [70–72]. Bioactive ceramics such as calcium phosphate (CaP) based biomaterials have a composition and structure similar to the mineral phase of bone; and are known to enhance osteoblast differentiation and growth [59,69]. CaP bioceramics have been used in various medical and dental applications such as the treatment for bone defects and fracture, total joint replacement, spinal surgery, dental implants, periodontal therapy and cranio-maxillofacial reconstruction [73–75]. It has been reported that the use of these ceramics only brought about minimal immunologic reactions, foreign body reactions and systemic toxicity contributed by their protein-free nature [76]. Despite the advantages above, CaP bioceramics are attributed to poor mechanical strength, lack of organic phase such as collagen, the presence of impurities, micro-scale grain size along with non-homogenous particle sizes and shapes [69].

One common CaP bioceramic is tricalcium phosphate (TCP) which has good biocompatibility and bonds with bone tissue without rejection hence making it suitable for the applications of bone repair. In addition, TCP supplies calcium (Ca) and phosphate (P) ions for bone formation after implantation [64]. Despite this, TCP materials have a rapid rate of degradation *in vivo* that could result in complications in terms of load transmission due to less support from the constructs of implanted tissue scaffold (due to high rate of resorption exceeding the rate of bone tissue formation) as new bone tissue develops its strength and stiffness [7]. Hydroxyapatite (HA) is a CaP based bioceramic

with an inorganic composition similar to natural bone tissue and is attributed to biocompatible, non-toxic and osteoconductive properties. In a study investigating the binding between HA and bone has found that HA forms a strong chemical bond with bone tissue in a process known as osseiointegration [77]. Synthetic forms of HA have a slow rate of degradation which is an undesirable property since constructs of the scaffold will not be resorbed enough in time for the replacement and integration of newly formed bone extracellular matrix [7].

Bioactive glass ceramics have been known to primarily form strong bonds with bone tissue by developing a stable interface while also triggering various biological responses such as tissue regeneration and angiogenesis in tandem to their degradation over time [78,79]. The properties of these ceramics are brought about by exposure to physiological environments which in turn forms a biologically active HA layer on the glass surface. This layer provides a bonding interface with host tissue while also releasing dissolution products such as silicon (Si), sodium (Na), calcium (Ca), phosphate ions to stimulate the cells into producing new tissue [80].

Despite all of the above, bioactive ceramics suffer from shaping difficulties and brittle formation thus limiting its applications. Studies have shown these ceramics have poor fidelity, poor reliability and limited capabilities to sustain the mechanical loading required for weight-bearing applications [81,82].

2.3.3 Natural Polymers

Natural polymers were among the first to be considered as biodegradable scaffold materials in a clinical context due to their overall interactions with various cell types and lack of immune response [83]. These naturally derived materials have the added advantage of biological recognition that may positively support cell adhesion and

function [84]. Natural polymers such as chitosan, collagen, elastin, gelatin, alginate and silk fibers have been implemented in bone tissue engineering due to similarities to extracellular matrix (ECM), biocompatibility and biodegradability [85]. The most common among the natural polymers is collagen.

Collagen is a fibrous protein and makes up the main component of the ECM of mammalian tissues such as bone, cartilage, tendon, ligaments and skin [86–89]. With twenty-nine known types, each possessing different characteristics, collagens' abundant nature together with its role in the growth and support of organs have allowed it be used as scaffolds in a wide variety of tissue engineering applications. These applications include hard tissue regeneration in bone; and soft tissue regeneration in cartilage, vasculature and nerves [90–95]. Among collagen types I, II, III, V and XI which have been tested for implementation in tissue engineering applications, type I has been described as the "gold standard" due to their association with lesser immune reactivity [83,96]. One study investigating the use of collagen type I as the matrix of bone marrow stromal cells have found that they could differentiate into osteoblasts *in vivo* while collagen type II, III and V did not [97]. This would imply the characteristics of collagen type I matrix to provide a suitable environment to induce osteoblastic differentiation *in vitro* and osteogenesis *in vivo* [84].

Despite the above scaffolds made from collagen can be relatively difficult to synthesise without undermining the integrity of their intended structure [96]. There are also concerns over its use such as the potential for pathogen transmission, immunogenicity, sourcing as well as poor handling [98].

The use of natural polymers comes with the disadvantage of possible immunogenicity, pathogenic impurities and less control over their mechanical properties, biodegradability

and batch-to-batch consistency. Their usage may also be costly in cases of limited supplies. Hence, synthetic polymers have been considered as an alternative [84].

2.3.4 Synthetic Polymers

Synthetic polymers were realised to be a cheaper alternative and allow for better functionality compared to natural polymers [83]. These polymers offer the advantage of the ability to tailor their mechanical properties and degradation characteristics by either varying the polymers itself or the composition of the individual polymer [99–101]. Due to this advantage, synthetic biodegradable polymers have been widely used as vehicles for cell transplantation as well as scaffolds for tissue engineering [84]. Linear aliphatic polyesters are considered to be the first biodegradable synthetic polymers to be approved by the Food and Drug Administration (FDA) for use in *in vivo* applications that include resorbable sutures and orthopaedic fixation devices [102].

Some common linear aliphatic polyesters include polylactic acid (PLA), polyglycolic acid (PGA) and their copolymers (PLGA). These polymers have been used in the manufacturing of cartilage tissue engineering scaffolds with advantages in terms of their biodegradation, biocompatibility, high toughness and absorbability [69]. The polymers above are also biodegradable through hydrolysis to release oligomers or monomers [103]. These by-products are metabolised *in vivo* through its conversion to water and carbon dioxide that are subsequently expelled from the body through respiration [104]. This however can also be seen as a disadvantage. In a different literature, concern is raised over the degradation of PLGA that produces carbon dioxide which lowers local pH and subsequently result in cell and tissue necrosis [105]. It has also been reported that a disadvantage to the synthetic polymers mentioned above is the hydrophobic nature of the

polymers which can limit tissue regeneration due to poor wetting and lack of cellular attachment and interaction [103].

Efforts have been in place to improve the functionality of these polymers [84]. Synthetic polymers have been used in conjunction to natural polymers to improve upon the disadvantages. In the context of scaffold structures, their surfaces are functionalised using specific ligands and protein molecules that enhance cellular responses [83]. The development of nano-bioceramic/polymer composites has the potential to improve interaction with host tissue or cells while also overcoming challenges brought on by biodegradable polymers in tissue engineering scaffolds. The development is an initiative to produce smart composite biomaterials with nanoscale interactions between organic phases and the bioactive inorganic phases. This would give a scaffold that degrades as a single material instead of variable rates of degradation from the glass and polymer phase [106].

2.4 Computer Aided Tissue Scaffold Design Modeling

2.4.1 Background

Tissue scaffolds fabricated via traditional methods are composed of irregular structure consisting of randomly arranged struts. The tissue scaffolds are prepared in a laboratory environment before undergoing experiments. Based on results obtained from the experiments, modifications are subsequently made to the scaffolds in order to make improvements. The modified scaffolds are kept for further analysis while the older scaffolds (the ones from which improvement are made) are either disposed or kept aside. Computer aided design (CAD) modeling seeks to reduce the experimental trial and error testing stages and also speed up the process of tissue scaffold design through the use of computer modeling techniques which has its foundation in mechanical design [21]. This section seeks to provide a background in regards to CAD in the context of tissue scaffolds before focusing on a specific model considered for this study. This model is based on Schwarz P (Primitive) triply periodic minimal surfaces (TPMS).

2.4.2 CAD & Tissue Scaffolds

Computer-aided design (CAD) software takes a more reproducible approach by allowing precise control over scaffold microstructural parameters such as the pore size, shape and interconnectivity [107]. Most CAD systems implement the use of solid or surface modeling systems such as the constructive solid geometry (CSG) and boundary representation (B-Rep) design methods.

Complex models can be designed and represented by combining standard solid primitives such as cubes, spheres and cylinders through Boolean operations through CSG-based software. B-Rep based software on the other hand represents solids in terms of boundaries comprising of vertices, edges and faces. With increase in the complexity of

the model in terms of requirements for size and fine architecture, the models produced by B-Rep significantly increases in size demanding more computational resources. In overcoming this, pore unit cell libraries consisting of unit cells with relatively simple geometry and predefined architecture have been created using commercial CAD systems [108]. This library is known as the 'computer-aided system for tissue scaffolds' or CASTS [22]. Examples of these unit cells are shown in Figure 2-1.

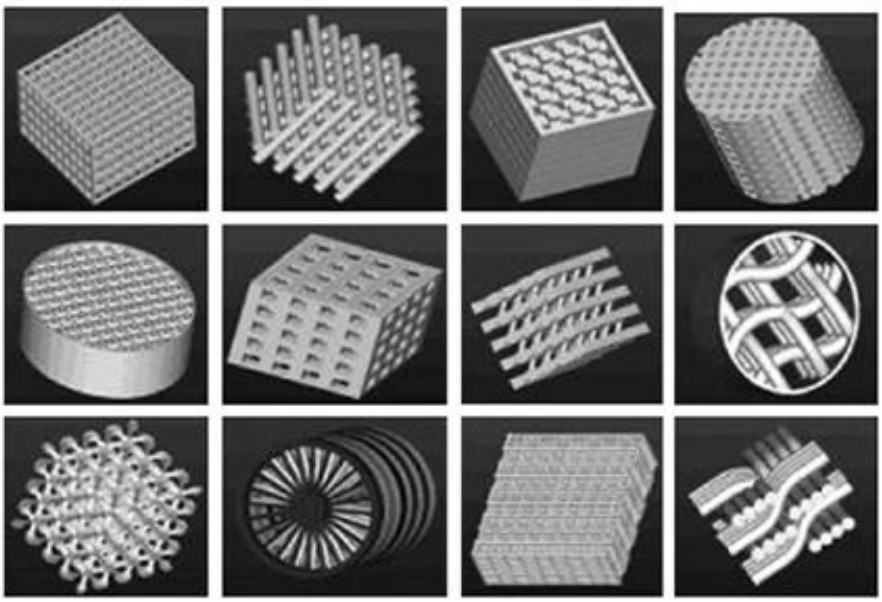

Figure 2-1 : Examples of unit cells designed based on different feature primitives from CASTS [22].

Based on a candidate unit cell from the library, it is 'patterned' or repeated in three different directions to produce an overall three dimensional geometry of a tissue scaffold. An algorithm has been devised in conjunction to the library to automate the entire process of matching desired anatomical shapes. With this, different scaffold architectural variables such as pore size, porosity level and surface area to volume ration can be calculated based on input design parameters [109].

Triply periodic minimal surfaces (TPMS) have gained attraction within different scientific and engineering disciplines including the field of tissue engineering. In the 19th century, Schwarz first made reference to TPMS through the introduction of Primitive and Diamond surfaces [110]. TPMS can also be found in natural biological systems such as weevils, beetle shells and butterflies [110–112]. With no self-intersecting or enfolded surfaces, each TPMS structure can be patterned into a 3-dimensional space. In addition, the surfaces are mathematically created such that the mean curvature at each point on the surface is equivalent to zero [110]. Examples of TPMS surfaces are graphically presented in Figure 2-2.

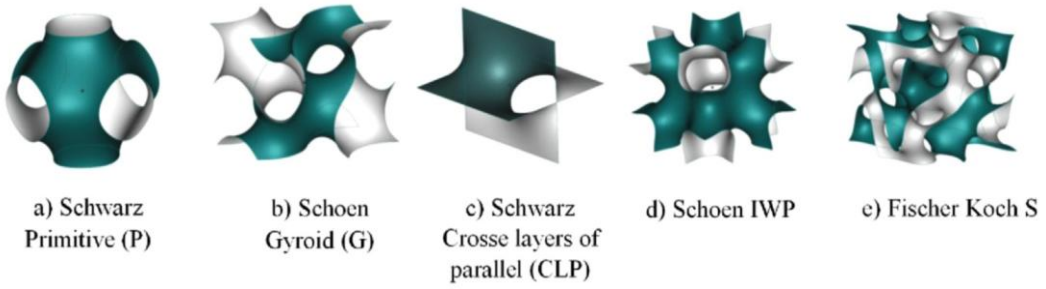

Figure 2-2 : Visual presentations of TPMS architecture [115].

TPMS topologies have been implemented in various applications which include heat transfer, fluid permeability and acoustic attenuation [111,113,114]. The architecture of TPMS surfaces exhibit properties which make them ideal in systems that can improved upon through the implementation of enhanced fluid dynamics [115]. In the field of tissue engineering, TPMS has particularly been implemented as biomorphic scaffold designs [116]. With smoothly curved surfaces, TPMS is able to provide a viable environment for the recuperation and regeneration of damaged tissue cells [117]. In previous literature, the use of gyroid and diamond TPMS architecture as building blocks for tissue scaffolds have been investigated [118]. In a separate investigation, the use of nine different TPMS

architecture as designs for tissue scaffolds have been studied [119]. This study considers the Schwarz P (Primitive) TPMS as the architecture for bone tissue scaffolds.

2.4.3 Schwarz P (Primitive) TPMS

Practical applications of porous composite structures with primitive architectures which include Schwarz P (Primitive) TPMS structures (shown in Figure 2-3) has found place in the field of bone tissue engineering and tissue engineering scaffolds [118,120].

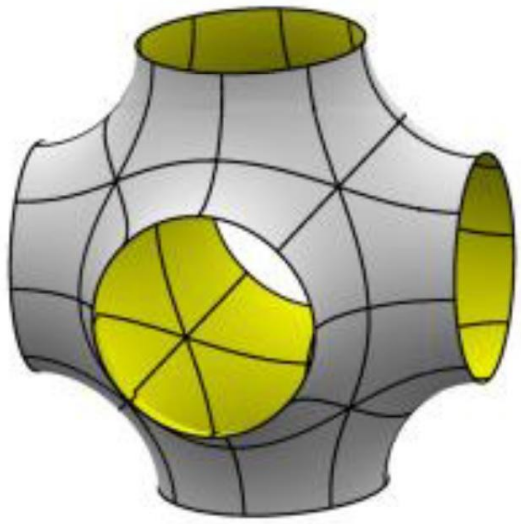

Figure 2-3 : Visual presentation of the Schwarz P (Primitive) architecture [123].

In practical applications where the Schwarz P surface is thickened, investigations characterising the mechanical properties of a Schwarz P structure through compressive loading has determined optimal stress distributions compared to other TPMS structure [121]. The Schwarz P structure can be characterised to exhibit a high load bearing capacity due to its inherent strain distributions [122]. With two different modeling constraints, the mechanical properties of the structure can be controlled. These two modeling constraints include thickness variations at constant surface radius and radius variations at constant thickness [123]. These are graphically presented in Figure 2-4.

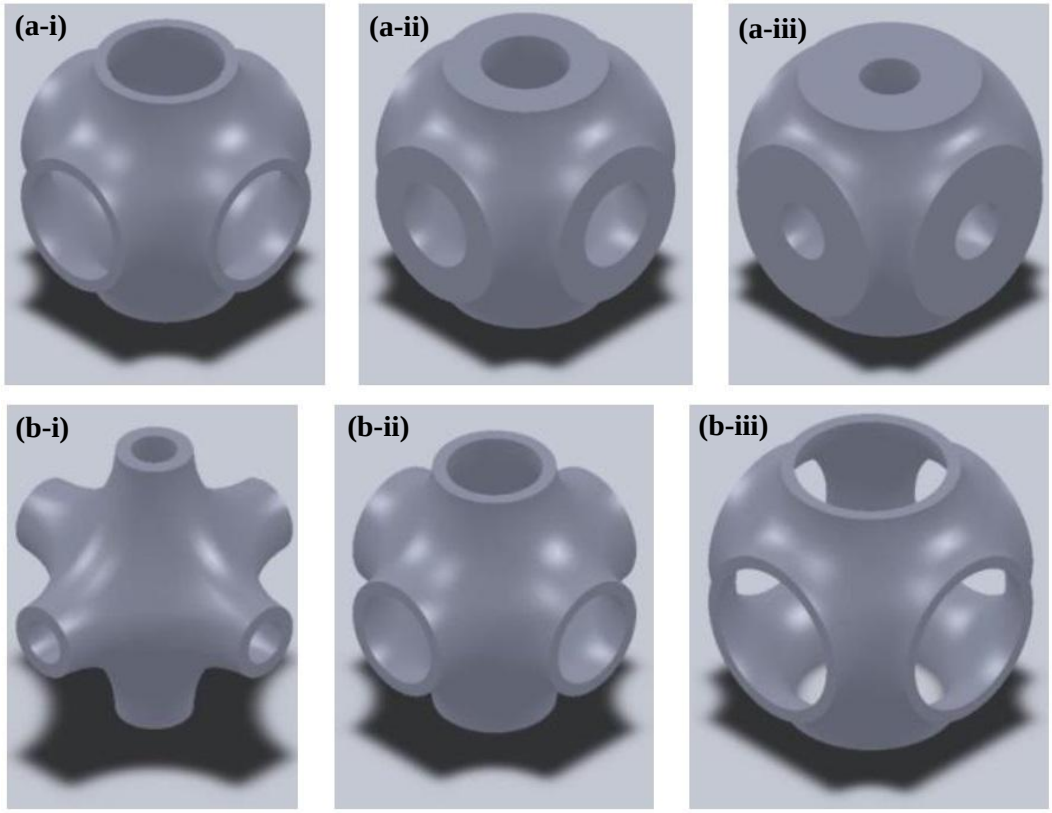

Figure 2-4 : Schwarz P minimal surfaces with two different modeling control constraints; (a-i) - (a-iii) : Schwarz P structures with thickness variations at constant surface radius; (b-i) - (b-iii) : Schwarz P structures with radius variations at constant thickness [123].

The Schwarz P structure has also been characterised to have the largest fluid permeability compared to all other TPMS architectures in a previous study [124]. In due regards to the fluid permeability properties attributed to the Schwarz P structure, tissue scaffolds implementing said structure has the potential to fulfill one of the biological design criteria in terms of transport properties.

2.5 Tissue Scaffold Fabrication

2.5.1 Background

In the body, tissues are organised into 3-dimensional structures as functional organs and organ systems. Each tissue or organ comes with various characteristic architectures and is dependent on its biological function. Hence, these architectures are deemed to provide appropriate channels for mass transport of signaling molecules, nutritional supplies and metabolic waste removal; and spatial organisation. These spatial cellular organisation are a determinant factor for cell-cell and cell-matrix interactions and is crucial for normal tissue and organ function [125]. A successful scaffold design should be able to provide a 3-dimensional environment that facilitates cell distribution and guide tissue regeneration [126].

Different methods have been developed to fabricate scaffolds for tissue engineering. This section discusses the traditional methods and additive manufacturing techniques that have been involved in the fabrication of scaffolds. Attention is then brought to the additive manufacturing technique that has been used in the study i.e. two-photon polymerisation.

2.5.2 Conventional Methods

Porous tissue scaffold structure have been able to be fabricated via conventional methods such as solvent casting, particulate leaching, gas foaming, phase separation and freeze drying.

Solvent casting followed by precipitation or particulate leaching is considered one of the most straight-forward methods in tissue scaffold fabrication [127,128]. Solvent casting has its method based on the evaporation of a solvent to form the scaffolds and can be performed in two different techniques. The first technique involves dipping the mold into

a polymeric solution and allow for sufficient time to draw off the solution. This would give a layer of polymeric membrane. The other technique is the reverse of the first technique and involves adding the polymeric solution into the mold. After allowing sufficient time for solvent evaporation, a layer of polymeric membrane which adheres to the mold is produced [129]. There is concern that scaffolds fabricated via this method retain some of the toxicity. The toxic solvents can be removed by a time-consuming procedure to fully dry the scaffolds using a vacuum [130]. To overcome this limitation, solvent casting is combined with particulate leaching. This involves the use of a water-soluble porogen such as the salt sodium chloride (NaCl) [131,132]. Polymers such as PLLA or PLGA are first dissolved in chloroform or methylene chloride and then cast onto a petri dish filled with the porogen. After allowing the solvent to evaporate, the composite is leached in water for two days to remove the porogen. Controlling the porosity of the scaffold structure fabricated through this method is dependent on the amount of salt added. The pore size of the scaffold structure on the other hand is dependent on the size of salt crystals used [129,132]. The pore size can also be controlled by considering the shape of the porogen [133]. The main disadvantage over the implementation of solvent casting and particulate leaching is the lack of control over the the pore shapes and pore interconnectivity [134]. The leaching step for water-soluble porogens is a time-consuming process. The use of organic solvents in regards to the fabrication method precludes the addition of pharmacological agents to the scaffold during fabrication. This would subsequently preclude it from being used in tissue regeneration applications [129]. Different methods have been developed to improve upon the limitations that come with the solvent casting and particulate leaching fabrication method.

The gas foaming fabrication method came out of the need to eliminate the use of organic solvents in the pore-making process. The use of organic solvents is replaced by the utlisation of gas as a porogen [135]. Solid polymer discs made of PGA, PLLA or PLGA are made using compression molding with a mold heated at a high temperature. These discs are subsequently placed in a chamber and exposed to carbon dioxide, CO_2 at high pressure at 800psi (equivalent to 5.5MPa) for three days to saturate the polymer with gas. The pressure is then rapidly reduced to atmospheric pressure [130,135]. The main advantage of this technique is the elimination of the use of harsh organic solvents which would potentially leave toxic residues. With this, no leaching step makes part for the overall fabrication time [136]. However, the gas foaming technique comes at the disadvantage of difficulty in ensuring pore connectivity and controlling pore sizes [137,138]. Improper pore connectivity in the scaffold structure would make cell seeding and cell migration difficult. Another disadvantage lies with the polymer discs which were made with the application of high temperatures. The high temperatures involved prohibit the use of bioactive molecules in the scaffolds [129].

Phase separation involves the use of temperature change to separate a polymeric solution into two different phases i.e. polymer lean phase (has low polymer concentration) and the polymer rich phase (has high polymer concentration) [139,140]. The polymer rich phase subsequently solidifies to form a matrix while the polymer lean phase turns into pores with the removal of solvents [141]. The two different processes of phase separation are solid-liquid phase separation and liquid-liquid phase separation. The solid-liquid phase separation induces solvent crystallization from a polymer solution by lowering the temperature. Pores are formed from the removal of solvent crystals. Through the liquid-liquid phase separation process, polymer solutions with an upper critical solution temperature form a biocontinuous structure between the polymer lean phase and the

polymer rich phase [126]. The advantage of the phase separation fabrication method lies in its ease to be combined with other fabrication methods such as particulate leaching to produce scaffolds with more control over pore morphology [130]. The phase separation method can also be combined with rapid prototyping to create nano fibrous scaffolds for purpose of tissue engineering applications [142]. Despite the above, the method involves the use of organic solvents such as ethanol or methanol and thus inhibiting the use of bioactive molecules or cells during scaffold fabrication [129]. This is a similar disadvantage found with the solvent casting and particulate leaching fabrication method. The diameters of pores formed using this method has been reported to be on the order of a few to tens of microns and are non-uniformly distributed which is unsuitable for tissue engineering applications [126]. This will become an obstacle to cell seeding procedures as well as cell migration throughout the confines of the scaffold.

The first use of the freeze drying fabrication method was done to fabricate PLGA scaffolds [143]. Working on the principle of sublimation, freeze drying can be divided into three different steps. A polymer is first dissolved in a solvent to obtain a solution with desired concentration before being frozen at a low temperature between -70℃ and -80℃. The frozen sample is then placed into a pressure chamber with pressure that is lowered to a few milibars through partial vacuum in a step known as the primary drying process. During this step, ice in the material is removed by direct sublimation. In the secondary drying process, most of the unfrozen water in the material is removed through desorption [141]. The ratio between water and polymer solution; and the viscosity of emulsion i.e. concentration of the polymer are dependent factors to the porosity and pore size of the scaffolds fabricated [129]. The pore size and pore structure of scaffolds produced can be controlled by varying the freezing rate, where a fast freezing rate can be applied to produce smaller sized pores [130,144]. The main advantage of freeze drying is

its non-utlisation of high temperatures (such as in phase separation) and separate leaching steps (such as in solvent casting and particulate leaching [130]. The use of water and ice crystals instead of organic solvents removes the potentiality for toxic residues which thus makes the fabrication method suitable for biomedical applications. However, hierarchical structures such as vascularised systems are still a challenge to be fabricated through this approach [141].

Generalising the above, tissue scaffolds fabricated via the traditional methods are not easily reproducible in a consistent manner [42,129]. In addition, producing tissue scaffolds with complex micro- and nano- architectural features are difficult to achieve via the conventional methods [122]. More importantly, the methods only enable a modest amount of control over pore size, pore geometry, pore interconnectivity, distribution of pores within the constructs of the scaffold as well as the construction of the inner channels [145] .

2.5.3 Additive Manufacturing

The emergence of additive manufacturing techniques have allowed tissue scaffold designs made through computer aided design (CAD) modeling to transition from a digital environment to a physical form. Through additive manufacturing techniques, the fabrication of tissue scaffolds generally involve the process of joining materials to make physical models based on 3-dimensional model data i.e. CAD model in a layer by layer manner and hence the term ‘additive’ [109]. The implementation of additive manufacturing can be pushed further through its integration with imaging techniques to produce scaffolds that are customised in size and shape and subsequently allow the scaffolds to be application-specific or patient-specific [130]. Some common additive manufacturing techniques implemented in the fabrication of tissue scaffolds are 3D

printing (3DP), fused deposition modeling, selected laser sintering (SLS) and stereolithography.

3D printing was considered to be the first additive manufacturing technique proposed for implementation in biomedical and tissue engineering applications [146,147]. This method generally involves creating 3D structure by inkjet printing liquid binder to join loose powder [148]. Material in the forms of powder made of metal, ceramics or composites are first spread onto a platform with a roller, followed by the printing of two-dimensional patterns by the inkjet print head onto the powder layer. The inkjet print head bases its movements based on the cross-sectional CAD model data of the structure it contains. The next powder layer is then spread and the process is repeated until the structure has been completely fabricated [149]. Since the fabrication technique of 3DP is done under room temperature, scaffolds fabricated through this technique potentially allow the incorporation of growth factors [150,151]. One disadvantage of this fabrication technique is the dependency of the pore size of fabricated scaffolds on the powder size of the stock material and closure of the pores by the stock material [147]. Pore sizes available have been found to be limited to smaller pore values lesser than 50μm. Larger pore sizes can be obtained by mixing porogens with the powders before scaffold fabrication [152]. However, leaching processes must be performed which subsequently adds extra overall fabrication time. In addition, organic solvents are used as binders to dissolve the polymer powder in the printed regions [151,153]. There is also concern over the weak mechanical properties of the resulting structure [154].

Fused deposition modeling (FDM) is the first technique that builds a foundation on the extrusion of molten polymer. This technique involves feeding of filaments made of thermoplastic materials into a pinch roller or screw feed mechanism which is

subsequently pushed into a liquefier. The liquefied filaments are then deposited through a computer controlled nozzle i.e. extruded onto a translational platform. Due to relatively low temperature, solidification of the fused filaments occurs and the extruded filaments are deposited in a layer by layer manner to complete the 3D model [145,155]. The accuracy of the structure produced through this technique is dependent on temperature control. The architecture on the other hand is determined by fabrication parameters such as the nozzle diameter, deposition speed, the space between filaments in the same layer, layer thickness and deposition angle [155]. The use of FDM is limited due to its use of heat to melt the filaments. The process temperature is dependent on the melting temperature of the material being used. With these high temperatures, cells can hardly be printed together with the material to form a cell-containing scaffold as the temperature would generally be too high for cells to survive or for bioactive molecules to retain their activity. This would also cause difficulty in the incorporation of biomolecules such as growth factors into the scaffold [156]. FDM also comes at a disadvantage over the need to use thermoplastics, long fabrication times and difficulty to establish microporosity that promotes neovascularisation and cell ingrowth within scaffolds [155].

Selective laser sintering (SLS) is a laser-based fabrication system which uses a carbon dioxide beam, CO_2 beam to fabricate constructs based on 3D digital data uploaded to a computer in the form of a computer aided design (CAD) model containing the structure to be fabricated. A layer of powder is first spread on a surface before the laser beam scans the surface of a powder bed to selectively sinter-bond polymer or composite powder particles by heating them to a temperature above the glass transition temperature. The sinter-bonds created forms a single layer of the structure to be fabricated [149,151,157]. A layer of powder is then spread again before undergoing the laser scanning. As each layer is fused to the layer immediately underneath it, the processes above are repeated

until the structure of the scaffold has been completely fabricated [157]. With the additive layer by layer nature of fabrication, SLS allows the fabrication of scaffolds with complex internal and external geometries. In addition, the use of organic solvents is also unnecessary due to the layer by layer fabrication [158]. Since the sintering process inherent with SLS does not result in complete melting of powder particles, the porosity between the original particles can be preserved. The porosity of fabricated structures can be controlled through the adjustment of process parameters which include laser power and scan speed [159]. The resolution of features on the other hand is factored by the particle size of powder used, the diameter of the focused laser beam and heat transfer in the powder bed. A wide range of pure and mixture of materials can be processed through SLS under the condition that they do not decompose under exposure to laser beam. The selection of material is also limited to their respective particle size of 10μm due to poor spreading and rapid sintering which would diminish the edge features [151]. Another disadvantage is the heat conduction that arises as a result of the focusing of the laser beam. This heat conduction causes accidental sintering of peripheral powder particles in a phenomenon called the "growth effect" which would subsequently lead to diminished resolution of the fabricated construct [155].

Developed in the late 1980s, stereolithography (SLA) is considered to be the first developed additive manufacturing technique [151]. SLA generally involves the focusing of an ultraviolet laser beam to irradiate predetermined sites on the surface of an aqueous photocurable polymer material. This subsequently results in photopolymerisation which solidifies the predetermined areas to be attached to a platform while the peripheral areas remain liquid in a single layer. Depending on the configuration of the SLA i.e. bottom-up or top-down, the platform moves accordingly after which successive layers are subsequently cured through the same process until the whole scaffold structure has been

fully fabricated. The excess resin is then drained and washed off [149,155,160]. One of the main advantages of SLA is its ability to construct scaffolds at a high resolution, closely mimicking that of the input CAD design as has been investigated in a previous study [161]. SLA also comes with the advantage of the ability to create complex shapes with internal architecture and the ease of removal of unpolymerised resin [151]. In terms of disadvantages, SLA is limited by the range of biocompatible resins with proper processing properties which require that the materials be photopolymers which can utilise photoinitiators [160]. The limited materials mainly used were based on poly(propylene fumarate) or PPF, trimethylene carbonate or gelatin [162].

It has been reported that two-photon polymerisation (2PP) has the capabilities to fabricate arbitrary 3-dimensional microstructures with feature sizes smaller than the diffraction limit of an applied laser wavelength [163,164]. Femtosecond lasers used during 2PP has been reported to be powerful for advanced materials processing at a micro- and nano-scale level compared to traditional laser processing techniques with its attribution of ultrashort pulse widths and extremely high peak intensity [165]. In addition, the repeatability and reproducibility of 2PP has also been reported. CAD model files can be directly transferred to the structure in its physical form out of photopolymer in tens of minutes. The whole process of producing the structure which consists of a few steps can be performed under one hour. Both processes mentioned can be repeated immediately as required and/or if parameters of the structure require modifications before undergoing the fabrication process again [166]. Implementation of 2PP is widespread with applications found in photonic crystals, microfluidic devices, biomedical science, microoptics, dielectrics and metamaterials [167].

This study considers the implementation of two-photon polymerisation as the fabrication method for Schwarz P unit cell based tissue scaffolds obtained from manufacturers.

2.5.4 Two-Photon Polymerisation (2PP)

Unlike other traditional 3D prototyping techniques which include ultra-violet (UV) laser stereolithography, inkjet printing and laser sintering, two-photon polymerisation (2PP) is able to fabricate 3D structures at a submicron resolution. Through 2PP, nearly simultaneous absorption of two photons within a small volume in a photosensitive resin results in chemical reactions between photoinitiator molecules and monomers [168]. Lasers capable of emitting femtosecond pulses are exposed to photoresists (materials that are photosensitive) in its liquid state resulting in its conversion to a solid phase. Through two photon absorption (TPA) cross-linking of polymer chains occurs and the exposed volume becomes insoluble to the solvent used in order to develop the structures. With this, the micron-sized focal volume will be able to translate the CAD model data in a physical form through the laser beam using computer-controlled motion stages [169]. Complex interdependent key parameters involved during the fabrication process come into play during the fabrication of a particular model or structure. These include the focusing optics, processing parameters i.e. laser power, writing speed, pulse rate; and the photoresists [163]. General principle errors of 2PP and geometry errors during the scanning stages are also liable to the resulting structure [167].

2PP works as a lay-by-lay method in which every layer is stacked up by fundamental element-voxels [167]. A voxel, otherwise known as a volumetric pixel is defined to be the unit volume of material cured by 2PP [168]. Hence, the accuracy of a fabricated structure is highly dependent on the voxels and their respective feature size. The structuring process of a particular model is realised between the relative motion of a

stationary emission of femtosecond lasers and the positioning stage. Typical positioning stages used are the 3-dimensional piezoelectric stage, the linear motor-driven stage and the step motor stages. Piezo stages are considered to be the most accurate positioning stages. However, this comes at the cost of scanning speeds and working fields that are limited to hundreds of μm. Step motor stages offer increased scanning speed at the detriment of precision [166]. Linear motor-driven stages offer positioning accuracy better than 400nm. Errors in terms of offset from the ideal position and posture of the voxels during the staging process can result in geometrical errors in the fabricated structure. Principle errors of 2PP follow from the technology of the fabrication process itself where the stacking of voxels lead to step effects. Stereolithography (.STL) model file format is considered a standard for input when it comes to 3D printing. STL models decompose a particular model into a series of flat triangles and hence do not entirely capture the surface curvatures of a particular model [167]. A visual representation of the step effect errors and the errors in terms of STL models is shown in Figure 2-5.

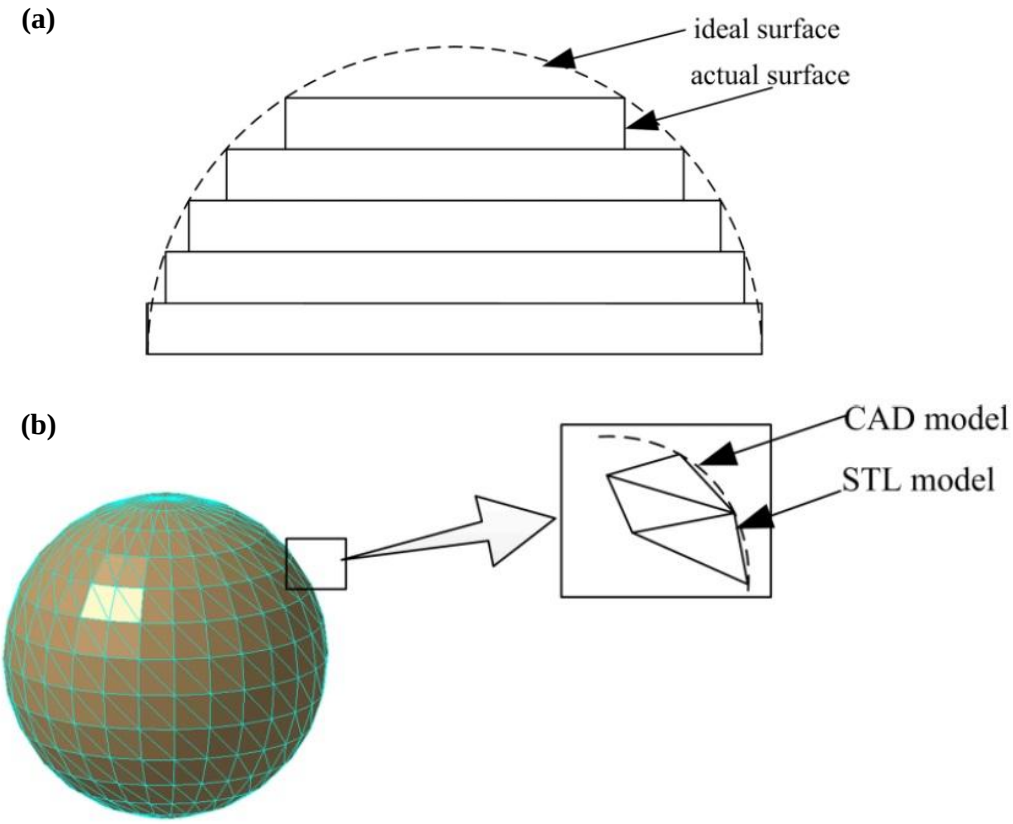

Figure 2-5 : Principle errors found in two-photon polymerisation and 3D printing in general; (a) Step effect; (b) Errors from triangulations in stereolithography (STL) models where surface curvatures of models are not completely captured [155].

In forming polymerised voxels, the activation energy otherwise known as the polymerised threshold fluence must exceed the threshold dose of a photoresist. The threshold dose (in energy per unit area) is mathematically related to the product of two-photon absorption (TPA) coefficient, the square of the peak intensity of the laser, the number of pulses, the pulsewidth and the thickness of the photoresist. The threshold dose can be mathematically expressed in Equation (1) [164].

$$F(L) \leq \beta {I_P}^2 NL\tau \quad (1)\ [164]$$

for which,

$F(L)$: Threshold dose

β : Two- photon absorption (TPA) coefficient

I_P : Peak intensity of the laser

N : Number of pulses

L : Thickness of photoresist

τ : Pulsewidth

The TPA coefficient mentioned above is also consequently related to the photoinitiator concentration [164].

Consider the configuration for laser power defined by its peak intensity. As previously stated, femtosecond lasers used during 2PP are associated with ultrashort pulse widths and extremely high peak intensities [170]. It is essential that the incident laser power is selected appropriately so that 2PP occurs without laser damage of photoresists. This would occur at incident intensities higher than required for polymerisation of the photoresist i.e. damage threshold. Based on a mathematical model, the damage threshold is related to the activation energy required for polymerisation to occur i.e. polymerised threshold fluence [171]. With this, careful selection must be made to all consecutive parameters making up the variable for polymerised threshold fluence in conjunction to the peak intensity of the incident laser power such that polymerisation occurs without laser damage of photoresists. Laser damage would result in formation of bubbles that become an obstacle towards further printing. The resulting structure would also be weaker as the bubbles become the site for early onset fracture under compression. The

damage threshold is also dependent on the writing speed and the proximity of features of the structure being fabricated i.e. proximity effects [171].

The polymerised threshold fluence is a material dependent property and is related to the degree of polymer conversion. It has been reported that polymer conversion increases with increasing laser power up to a saturation point at comparatively higher laser powers. Above the saturation point, the laser power does not have any effect to the degree of crosslinking [163]. Dependency between laser power and the degree of polymer conversion can be assessed from polymerised width lines by taking the assumption that the laser beam profile has a Gaussian intensity distribution in the focal plane [172]. The dependency can be mathematically expressed as shown in Equation (2).

$$W = \quad w_o\sqrt{\ln\left({}^{P}/_{P_{th}}\right)} \qquad (2)\ [172]$$

for which,

W : Width of polymerised line

ω_o : Focal spot size

P : Applied laser power

P_{th} : Laser power threshold for polymerisation

The influence of writing speed to polymerisation during 2PP is implied through exposure time i.e. time between pulse of femtosecond lasers. Here, increased writing speeds would correspond to diminished exposure time [173]. After a threshold exposure time, a voxel of a certain size is formed around the light intensity maximum of the focal spot [174]. The voxel expands in an anisotropic direction where it grows faster along the axial direction rather than along the focal plane [164]. At longer exposure times, the growth of

the voxel size gradually grows through radical expansion to the outside of the initially formed voxel. The relationship between laser power, P and exposure time, t to the diameter, d and height, h of the polymerised voxel is given in Equation (3) and Equation (4) [175].

$$d(P,t) \propto \sqrt{\ln(P^2 t)} \quad \text{(3) [175]}$$

$$h(P,t) \propto \sqrt{(P^2 t)^{1/2} - 1} \quad \text{(4) [175]}$$

The expansion of voxels with respect to the exposure time in terms of writing speed has been demonstrated in line writing experiments [173,176–178]. General findings show that high writing speeds give way to thinner polymerised line widths. The relationship between the widths of polymerised lines and the writing speed can be mathematically expressed through the threshold effect as shown in Equation (5).

$$W = \omega_o \sqrt{2\left[\ln\left(\sqrt{\frac{2}{\pi}} \times \frac{P}{\omega_o v F}\right)\right]} \quad \text{(5) [173]}$$

for which,

W : Width of polymerised line

ω_o : Beam radius

P : Average laser power

v : Writing speed

F : Threshold dose (in per unit area)

In conjunction to the threshold effect, the mechanism by which the increased polymerised line width occurs can also be explained through heat accumulation. Effects of localized temperature increase due to the repetitive bursts of femtosecond laser pulse can be characterised by material cooling time and the specific heat capacity of the material. The width of polymerised lines increases with time between bursts being smaller than the material cooling time. Here, the heat does not have enough time to disperse from the polymerised volume and accumulates. The opposite happens when the time between bursts is larger than the material cooling time [173].

The photoinitiator plays a role in the 2PP fabrication process while also having possible consequences from a biological aspect particularly for structures intended for use in the field of tissue engineering. Increase in photoinitiator concentration gives way to increased polymerisation rate [179]. This would accelerate the writing process of 2PP. However, this can give way to unknown changes in material characteristics as a result of the increase in photoinitiator concentration. Biocompatibility issues may also arise as a result from the increase in photoinitiator concentration [178]. Previous literature has stressed the requirements for efficient post-polymerisation purification procedures for the removal of photoinitiator residues, free radicals and macromonomers from the scaffold to be able to provide an environment which cultivates cell viability and cellular activities [180].

2.6 Computer Aided Tissue Scaffold Informatics and Biomimetics

2.6.1 Background

The common strategy in optimising tissue scaffold fabrications in a laboratory environment is mainly based on a trial and error approach from which modifications are then made based on the results obtained [21,181]. Mathematical models have been developed in order to characterise tissue scaffolds in terms of their mechanical and biomimetic properties [41].

This section gives a background of mathematical models that have been previously developed to characterise different aspects of scaffold design. The computational approach used for this study is micromechanical analysis. Hence, a sub-section will be devoted to provide a background in regards to the mathematical model surrounding the approach.

2.6.2 Previous Mathematical Models

Mathematical models have been developed in order to characterize tissue scaffolds in terms of their mechanical and biomimetic properties [41]. These mathematical models have been incorporated into simulations based on the finite element method enabling studies in regards to the mechanical properties, mechanical performance and biomimetic properties of tissue scaffolds to be evaluated [109]. These simulations can be conducted in conjunction with models obtained through the CAD-based or image-based approach. The flowchart in Figure 2-6 shows the steps in the design of a scaffold with the introduction of finite element analysis (FEA) as a predictive tool.

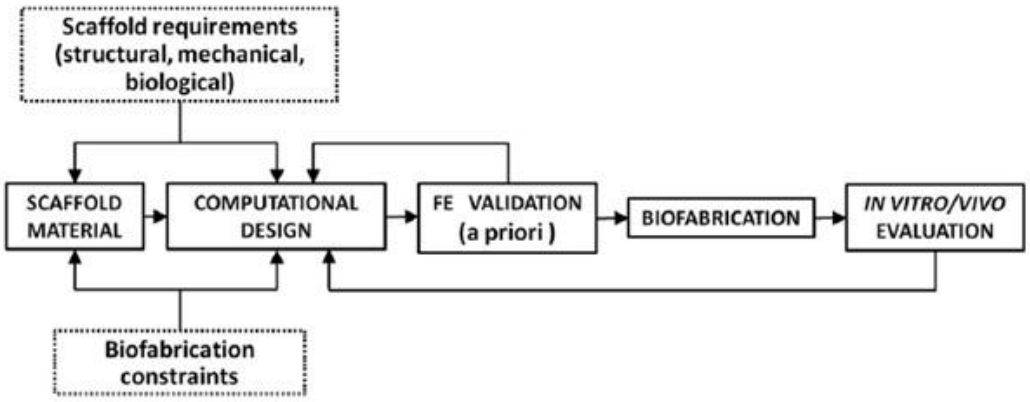

Figure 2-6 : Key steps in designing tissue scaffolds implementing finite element analysis (FEA) to predict results and make further improvements [109].

Homogenisation is a technical term used to describe materials composed of different several constituents which are mixed together. The homogenisation theory has been founded to determine the averaged properties of the material by considering their respective constituents and periodic structure. This is done by obtaining a homogenous model consisting of homogenised coefficients that are also dependent on the coefficients of the constituents as the periodicity tends to zero [182]. This thus has allowed the quantification of the structural heterogeneity and the mechanical properties of a tissue scaffold. Different homogenisation methods to characterise the effective properties porous scaffolds or heterogenous tissue include standard mechanics modeling, homogenisation theory and finite element methods. The aforementioned approaches particularly the standard mechanics modeling and finite element methods which both use a representative volume element (RVE) come with inherent limitations in obtaining effective mechanical properties. It was found that the results obtained are dependent on the size of the RVE and the boundary conditions imposed [183].

The asymptotic expansion homogenisation theory developed from studies of partial differential equations with rapidly varying coefficients overcomes the limitations

mentioned. However, its implementation requires a series of computational algorithms for its numerical implementation. This has been implemented in a previous study in conjunction to finite element methods to predict the effective mechanical properties of a tissue scaffold and to understand the effects of the deformation of a scaffold in regards to applied loading. This study has also implemented computer-aided modeling from the image-based approach through the selection of unit cells and its integration with the shape of a particular tissue to form the final tissue scaffold [183,184].

Another study proposed a numerical framework to determine the optimum design of a porous scaffold by using computational simulations in regards to bone tissue regeneration initiated by scaffold implantation that encompass new bone formation and the degradation of scaffold constructs. The degradation was modeled based on the dependence on water content that diffuses from the scaffold surface to the bulk material while the bone formation was modeled based on the rate equation for trabecular surface remodeling [185].

Studies involving simulations focused on remodeling in terms of tissue differentiation has also been done. Here, mechano-regulation algorithms have been used to make predictions as to how mechanical forces modulate tissue differentiation and bone remodeling. With advancements in the algorithm as well as its implementation, the extent to which bone regeneration can be maximized within a scaffold was investigated in regards to several selected parameters such as porosity, Young's modulus and the dissolution rate that are dependent on the magnitude of local loading [186].

Pore morphology heavily influences mass transport properties of nutrients and wastes. This in turn affects the viability, proliferation of cells as well as the extent of tissue regeneration. Therefore, knowledge needs to be gained in regards to the fluid flow within

and around the confines of a scaffold in order to control culture conditions and cell behavior. Development of large shear stresses within the scaffold as a result of high flow rate can influence cellular metabolism or even damage seeded cells especially *in vitro*. Optimal fluid shear stress has been demonstrated to promote cell proliferation, differentiation and matrix deposition [109]. This provides a rationale for the need of computational fluid dynamics (CFD) to quantify fluid flow within or around tissue scaffolds.

One study implemented the use of 2 different geometrical inputs i.e. CAD-based modeling and image-based modeling via micro-CT to determine the accuracy of CFD models for the prediction of scaffold permeability and compare the results based on empirical formulation. The study demonstrated the capabilities in using image-based modeling data as a CFD analysis input to determine the permeability of scanned scaffolds [187].

The mechanical and biological aspects of simulations can potentially be combined to enable the study of both of these aspects in regards to related scaffold design parameters. It has been reported that only a few studies have been conducted to correlate CFD results together with scaffold microarchitectural parameters [109]. However, this can be done through the capabilities inherent in finite element processing software to perform fluid-solid interaction (FSI) modeling.

The study presented here concerns the mechanical aspect of tissue scaffold design where the characterisation of the mechanical properties of Schwarz P unit cell based tissue scaffolds is determined in the context of a computational approach. The computational approach considered in this study is micromechanical analysis.

2.6.3 Micromechanical Analysis

Micromechanical analysis has its origins found in the need to account and understand the behaviour of materials with sophisticated microstructures. These include fibres, particle reinforced concretes and textile composites [188]. The approach involves reducing a periodic arrangement of microscopic unit cells from a macroscopic structure i.e. tissue scaffold to a single unit cell. That unit cell is hence deemed to be the representative unit cell. In the case of particle reinforced composites, the particle arrangement in the matrix of composites is idealised to be regularly packed and thus give way to a wide variety of unit cells. These particle arrangements can be classified based on the study of crystals from which a unit cell can be selected. Despite the idealisations, one main advantage to the establishment of the unit cells is the ability to accommodate irregular shaped particles. It also allows the representation of microcracks around the particles and debonding between particle surfaces [189]. For a particular packing system (idealised based on crystals), geometric translational symmetries that persist can be analysed for a representative unit cell after which boundary conditions to implement micromechanical analysis can then be derived.

Several typical packing systems such as the simple cubic, body centered cubic, face centered cubic and close packed hexagonal packing have been examined in previous literature [189]. These packing systems can be described into 3-dimensional Voronoi tessellations of unit cells that are described as domains enclosed by planes that bisect the segments connecting the center of a particle to that of neighboring particles. These unit cells are then considered to be the representative unit cell, also known as Voronoi cell. A visual presentation of two different packing systems and their respective Voronoi cells are shown in Figure 2-7.

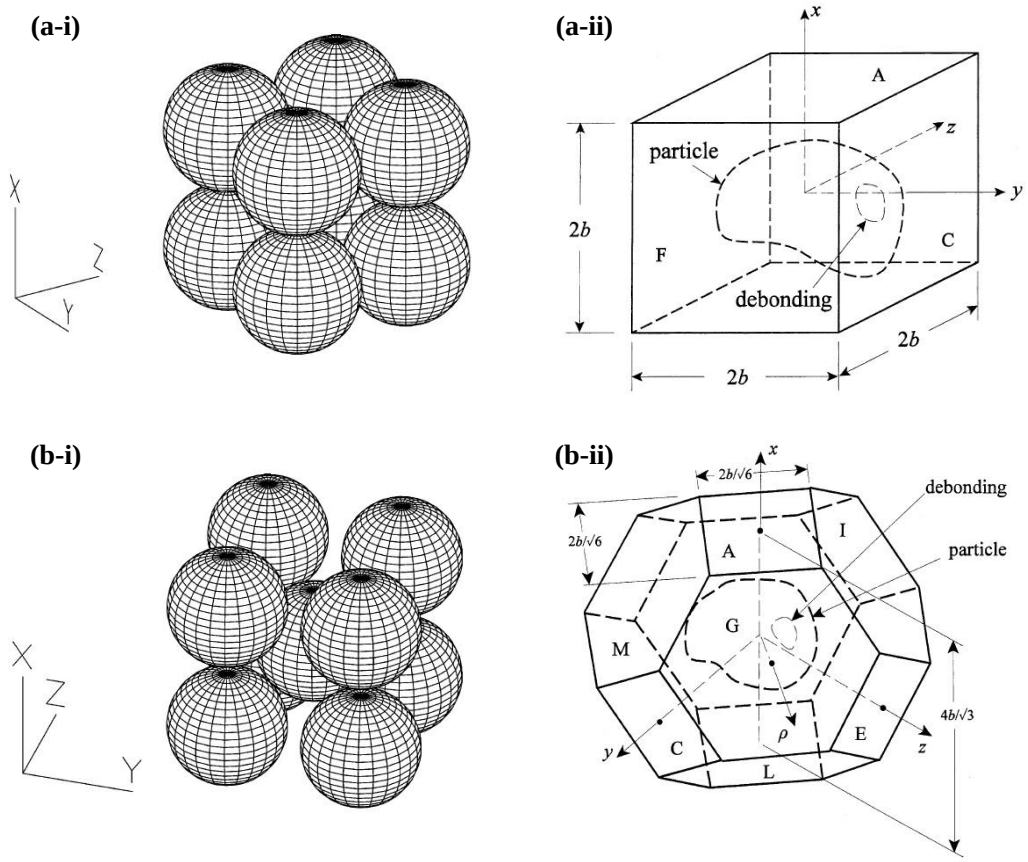

Figure 2-7 : Visual presentations of two different packing systems; (a-i) Simple cubic packing system; (a-ii) Voronoi cell for a simple cubic packing system; (b-i) Body centered cubic packing system; (b-ii) Voronoi cell for a body centered cubic packing system [188].

Through translational symmetries, the application of macroscopic stresses or strains on a single unit cell is applied identically to other unit cells as representative images of the unit cell being considered. With this, the macroscopic strains and the relative displacements at a particular point in a unit cell is mathematically related to the image of that point in another unit cell in accordance to Equation (6).

$$u' - u = (x' - x)\varepsilon_x^0 + (y' - y)\gamma_{xy}^0 + (z' - z)\gamma_{xz}^0$$

$$v' - v = (y' - y)\varepsilon_y^0 + (z' - z)\gamma_{yz}^0$$

$$w' - w = (z' - z)\varepsilon_z^0 \quad (6)$$

for which,

x, y and z : Coordinates of point P

u, v and w : Displacements associated with point P

x', y' and z' : Coordinates of the point P'

u', v' and w' : Displacements associated with point P'

$\varepsilon_x^0, \varepsilon_y^0, \varepsilon_z^0$: Macroscopic strains

$\gamma_{yz}^0, \gamma_{xz}^0, \gamma_{xy}^0$: Macroscopic shear strains

Constraining the displacements where $u = v = w = 0$ at any arbitrary point in a unit cell eliminates rigid body translations in a 3-dimensional direction and thus allow Equation (6) to be obtained. Rotations of the x-axis about the y-axis and the z-axis and the rotations of the y-axis about the x-axis are constrained such that ${\partial w}/{\partial x} = {\partial v}/{\partial x} = {\partial w}/{\partial y} = 0$ at $x = y = z = 0$. With the above, Equation (6) can then be implemented further to derive the necessary displacement boundary conditions in conjunction to a selected packing system.

The macroscopic strains involved in the derivations for boundary conditions can be treated as the independent degrees of freedom through which load can be imposed. Concentrated forces can also be applied to the different independent degrees of freedom as an alternative [190,191]. Macroscopic stresses are thus effectively imposed on the

representative unit cell in consideration. The relationship between the macroscopic stress and concentrated load can be overseen through the principle of virtual work which is applicable for linear and non-linear structures [192–194]. According to the principal of virtual work, the external virtual work is equivalent to the internal virtual work [193]. The internal virtual work for elastic structures carrying static loads with the absence of energy dissipation is in the form of strain energy [195].

As micromechanical analysis reduces a macroscopic structure with periodic arrangement of microscopic unit cells to a single representative unit cell through geometric translational symmetries, the work done on the macrostructure i.e. external virtual work is thus equivalent to the internal strain energy of the representative unit cells i.e. internal virtual work in the form of internal strain energy. Consider the application of a macroscopic load, F_i to an elastic structure. The load-displacement curve is shown in the following.

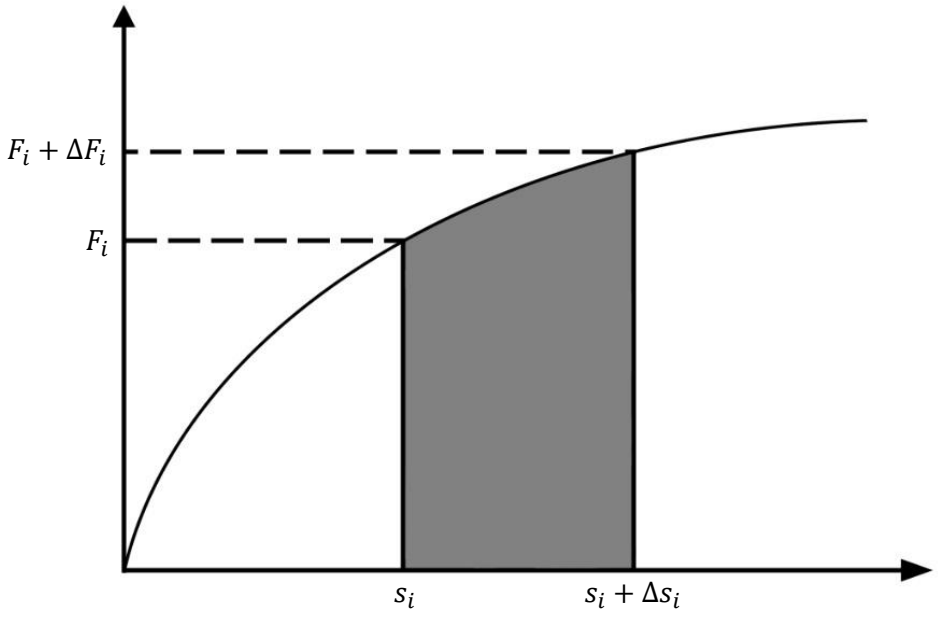

An increase in F_i results in a respective increase in displacement by Δs_i. As ΔF_i tends to zero, the incremental work done, ΔW as F_i results in the change in displacement, Δs_i is approximately $F_i \Delta s_i$. More accurately,

$$\Delta W = \int_{s_i}^{s_i+\Delta s_i} F_i(s_i)\, ds_i$$

For an elastic and linear structure, the function for the force in terms of displacement, $F_i(s_i) = ks_i$. As the force applied increases from zero to F_i with the resulting respective displacements from zero to s_i, the work done, W is equivalent to the following,

$$W = \int_0^{s_i} F_i\, ds_i = \int_0^{s_i} ks_i\, ds_i$$

$$= \frac{1}{2}[k(s_i)^2]$$

$$W = \frac{1}{2} F_i s_i$$

Hence, the work done for a system of forces, F over corresponding displacements, s is equivalent to the following,

$$W = \frac{1}{2}\{F\}^T\{s\}$$

Considering a small cubic element with a volume of dV in the same elastic structure, the incremental strain energy, dU is equivalent to the following,

$$dU = \frac{1}{2}\left(\sigma_{xx}\varepsilon_{xx} + \sigma_{yy}\varepsilon_{yy} + \sigma_{zz}\varepsilon_{zz} + \tau_{xy}\gamma_{xy} + \tau_{xz}\gamma_{xz} + \tau_{yz}\gamma_{yz}\right) dV$$

The total strain energy,

$$U = \frac{1}{2}\int_V \left(\sigma_{xx}\varepsilon_{xx} + \sigma_{yy}\varepsilon_{yy} + \sigma_{zz}\varepsilon_{zz} + \tau_{xy}\gamma_{xy} + \tau_{xz}\gamma_{xz} + \tau_{yz}\gamma_{yz}\right) dV$$

$$= \frac{1}{2}\int_V \{\sigma\}^T\{\varepsilon\}\ dV$$

With the external virtual work being equivalent to the internal virtual work,

$$\frac{1}{2}\{F\}^T\{s\} = \frac{1}{2}\int_V \{\sigma\}^T\{\varepsilon\}\ dV$$

The equivalency between external and internal virtual work can be implemented further to determine the effective properties.

With the above, the necessary literature review in regards to different aspects of this study has been presented. Schwarz P (Primitive) architectures have been implemented in two-photon polymerisation (2PP) to fabricate Schwarz P unit cell-based tissue scaffolds. A computational approach i.e. micromechanical analysis was used to characterise the mechanical properties of aforementioned scaffolds. This is investigated in the forthcoming chapters.

Chapter 3

Schwarz P & Computer-Aided Design (CAD)

3.1 Introduction

Computer-aided design (CAD) models of Schwarz P unit cells have been used extensively throughout the course of this study. As part of the INNOVABONE project, a Schwarz P unit cell packaged into a stereolithography (.STL) file was used as an input to fabricate Schwarz P unit cell-based tissue scaffolds via two-photon polymerisation (2PP). These fabricated tissue scaffolds formed the basis for experimental models for the purpose of mechanical characterisation.

In general, stereolithography files store information about a particular model as a collection of triangles without any information pertaining to the connectivity between the vertices of the triangles. In the context of computational models in this study, this renders the design model of the Schwarz P unit cell only purposeful as a visual representation rather than be implemented for any CAD modeling and computational analysis. Therefore, a methodology in converting i.e. ‘reverse engineering’ the .STL file into a useable CAD model will be discussed here. Justification will also be made in regards to the relevance of the conversion for the purpose of computational models.

3.2 Schwarz P Unit Cell Surface Geometry

The Schwarz P unit cell .STL model is graphically presented in Figure 3-1. With the .STL model being only purposeful as a visual representation without any information pertaining to the connectivity of the triangles, re-establishing the connectivity is necessary.

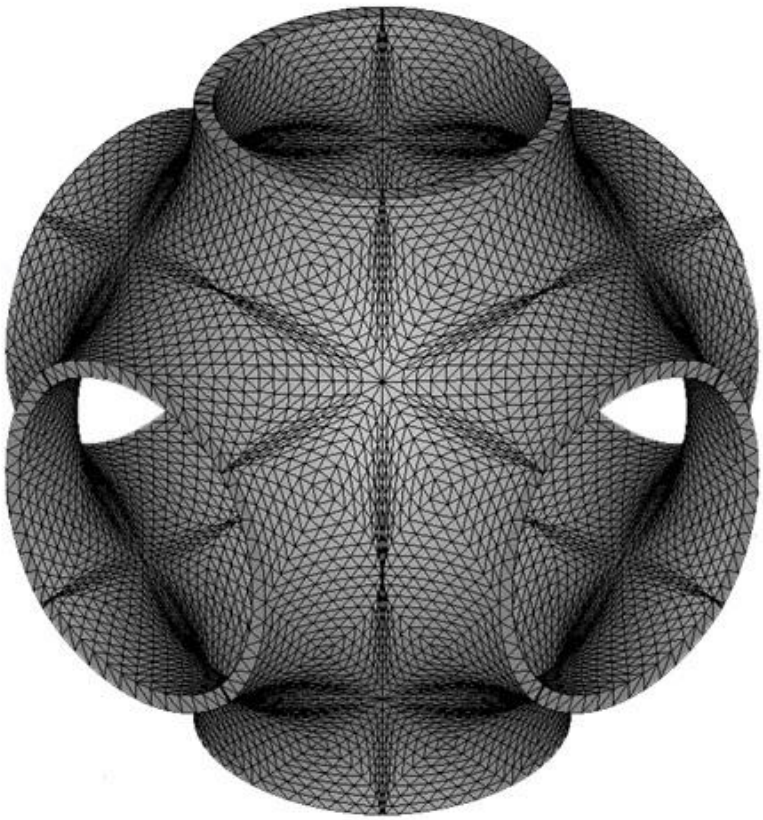

Figure 3-1 : Stereolithography (.STL) model of a Schwarz P unit cell.

The creation of a surface geometry model by 'reverse engineering' the .STL file would achieve this objective and subsequently enable common CAD modeling techniques to be implemented as required throughout this study. Based on the creation of the surface geometry, a 3-dimensional volumetric model of a Schwarz P unit cell can be obtained.

This would allow the discretisation of the model to be implemented further into computational approaches involving finite elements.

Two different pathways are available to ‘reverse engineer’ the .STL file and obtain the surface geometry; both involving the software Altair Hyperworks (Altair Engineering Inc., Michigan, US). These are discussed in the following sections.

3.3 Automated Surface Creation

This approach allows surface partitions to be automatically created from the .STL model of the Schwarz P unit cell. Here, the ‘From FE’ option was used from the ‘Surfaces’ tool. A trial was performed to oversee the quality of the surface model formed from the approach. The sub-options used and subsequent surface model obtained from the approach is presented in Figure 3-2.

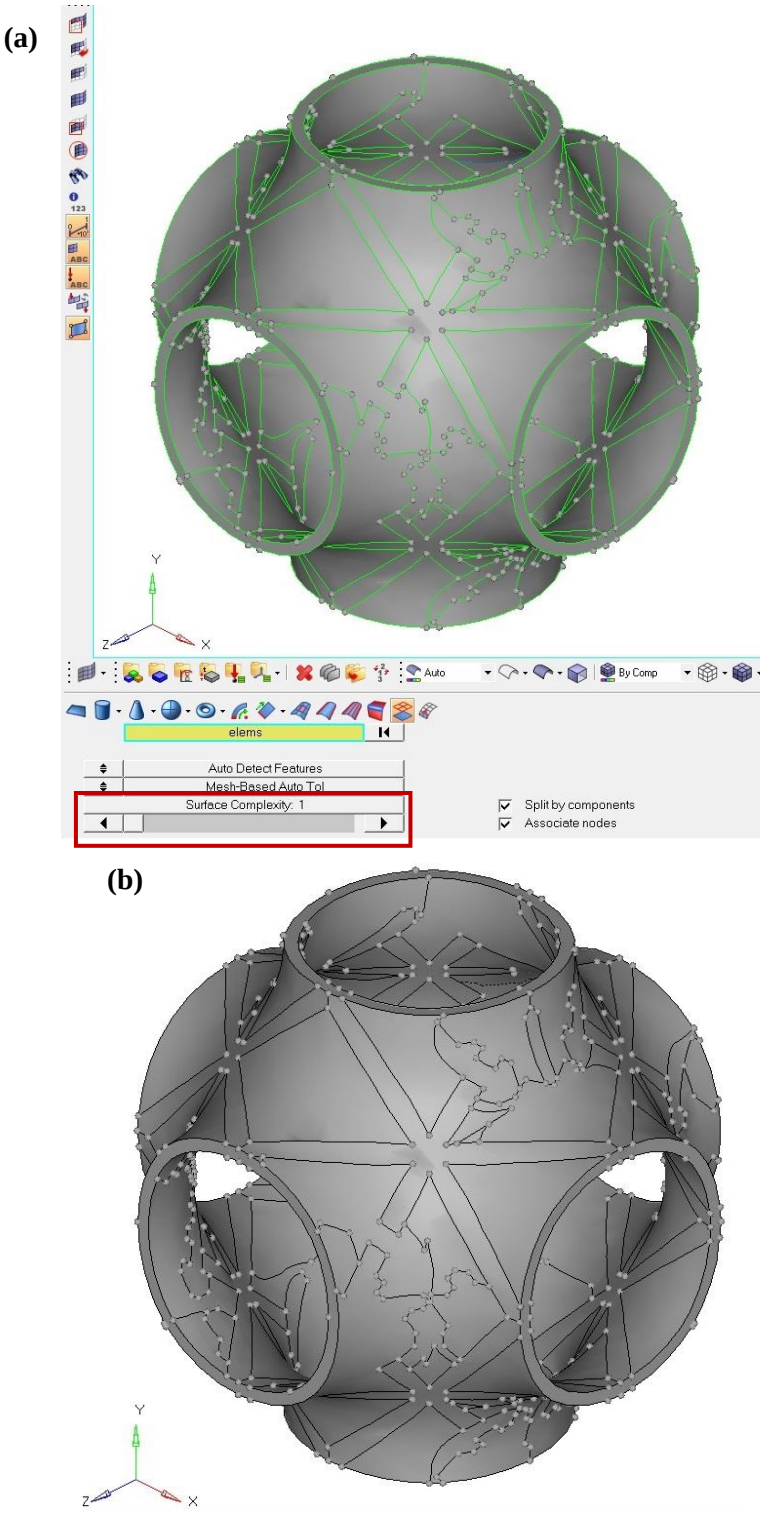

Figure 3-2 : Automatic surface creation options used and subsequent surface model obtained at a surface complexity level 1 (shown in the red box). (a) Surface options used and surface partitions obtained; (b) Surface model at surface complexity of 1.

The resulting surface model gives very irregular surface partitions. This would highly likely lead to severe difficulties in using the surface model for future implementation of CAD modeling techniques as well as meshing issues for computational studies. To oversee mediation of this problem, the ‘Surface complexity’ was increased and the resulting surface models were obtained as presented in Figure 3-3 through Figure 3-6.

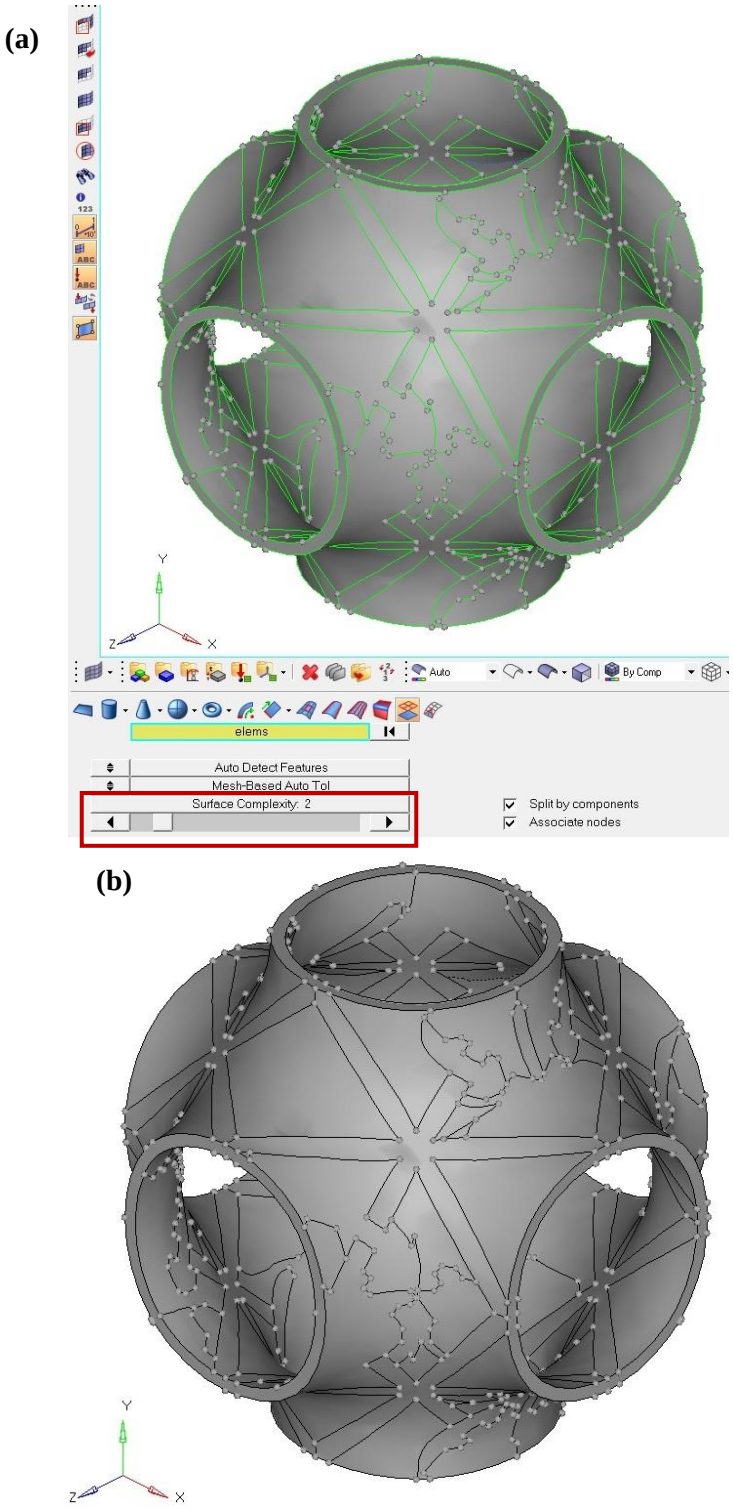

Figure 3-3 : Automatic surface creation options used and subsequent surface model obtained at a surface complexity level 2. (a) Surface options used and surface partitions obtained; (b) Surface model at surface complexity of 2.

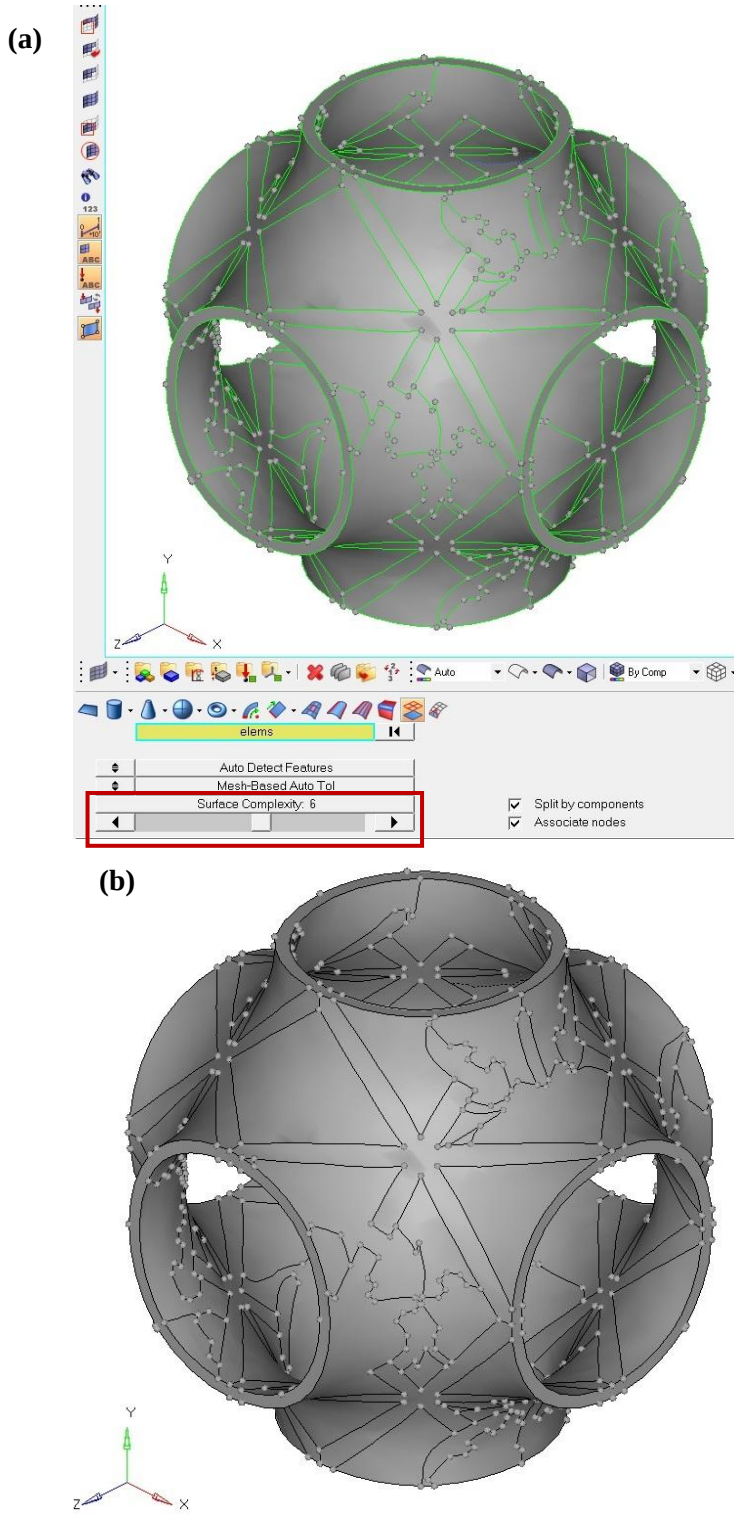

Figure 3-4 : Automatic surface creation options used and subsequent surface model obtained at a surface complexity level 6. (a) Surface options used and surface partitions obtained; (b) Surface model at surface complexity of 6.

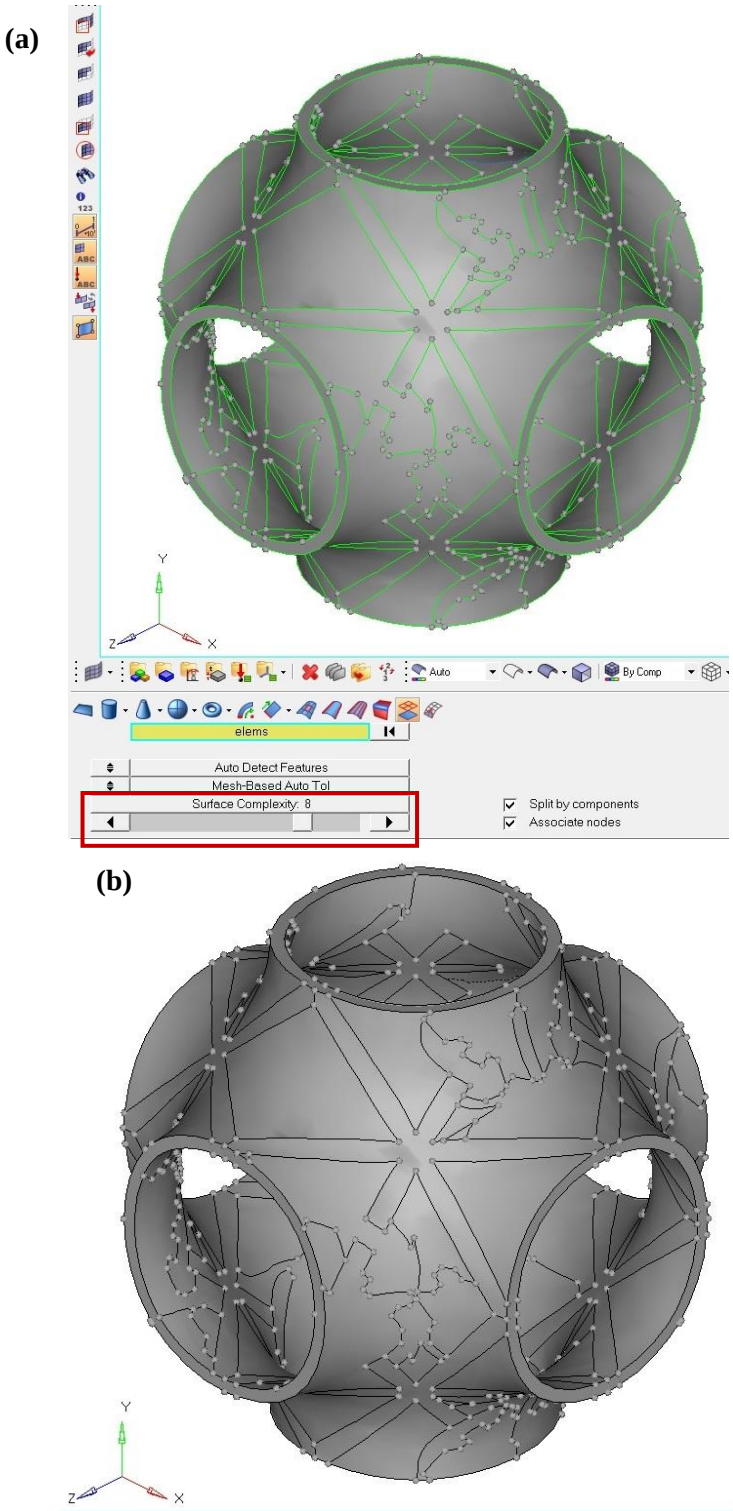

Figure 3-5 : Automatic surface creation options used and subsequent surface model obtained at a surface complexity level 8. (a) Surface options used and surface partitions obtained; (b) Surface model at surface complexity of 8.

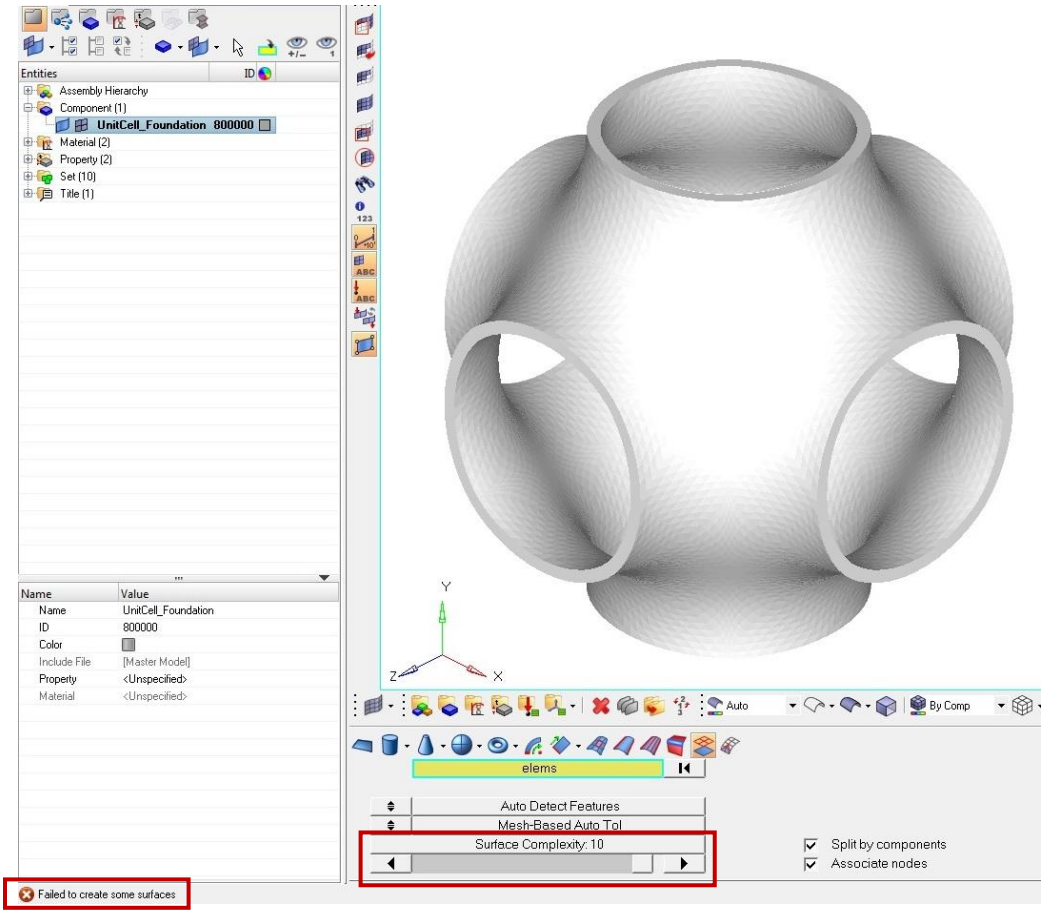

Figure 3-6 : Automatic surface creation option used with a surface complexity of 10. The option failed to construct any surface model as indicated in the red box on the lower left.

Increasing the surface complexity had no effect in creating proper surface partitions. At the maximum surface complexity level of 10, no surface partitions were able to be produced. With the above, the automated surface creation approach generally only gave undesirable results and hence required the use of a manual surface creation approach.

3.4 Manual Surface Creation

The manual surface creation approach generally involves the construction of line segments as a foundation from which surface patches can then be subsequently created. Despite the absence of connectivity information between the vertices of triangles in the .STL model, nodes can be constructed at points formed by the vertices. These nodes would subsequently lay the foundation from which the lines can be constructed. A flow chart in regards to the above is shown in Figure 3-7.

Figure 3-7 : Flowchart for the construction of surface patches.

Consider the area of the .STL model circled in red as shown in Figure 3-8.

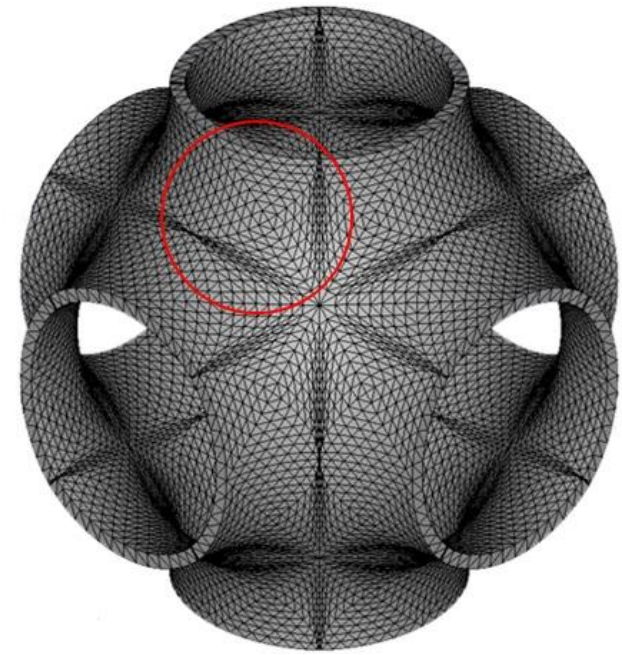

Figure 3-8 : Area of the .STL model circled in red for consideration.

Nodes were constructed at vertices lining the pore throat and along vertices that would split the surface geometry evenly as shown in Figure 3-9.

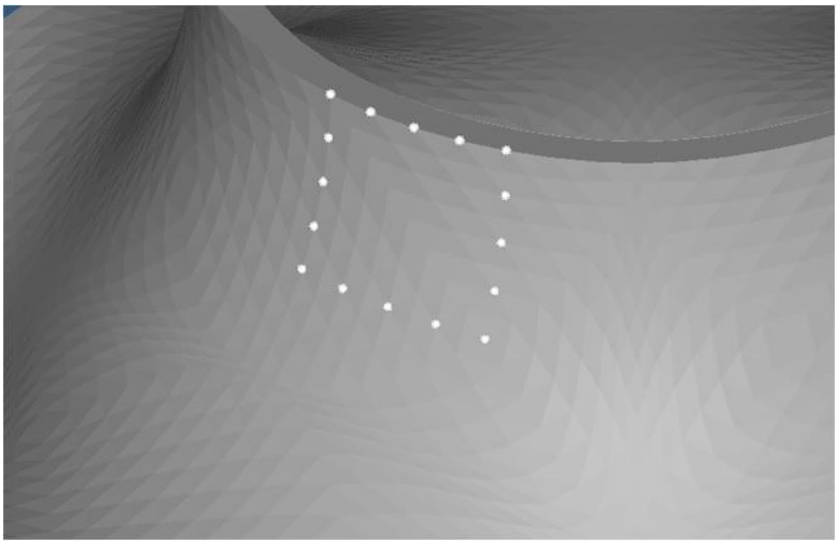

Figure 3-9 : Creation of nodes at vertices.

Line segments can then be constructed joining one node to another to form an enclosed boundary as shown in Figure 3-10.

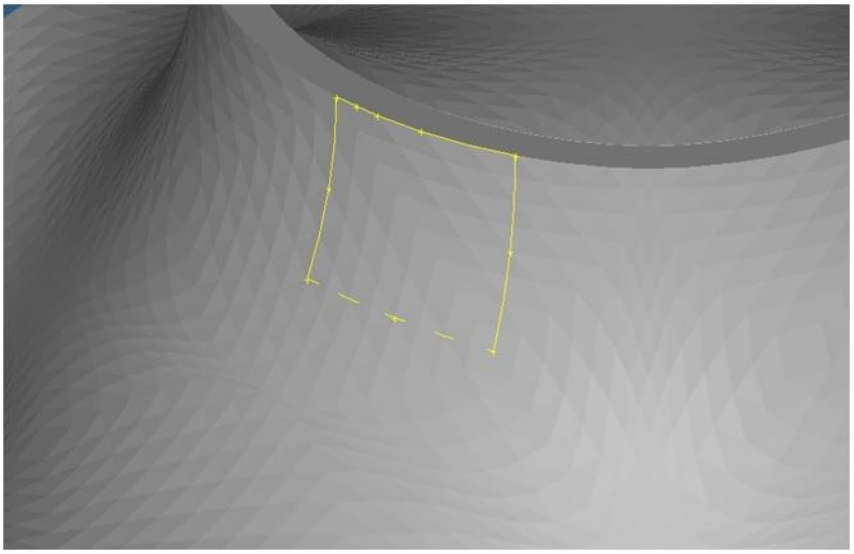

Figure 3-10 : Enclosed boundary formed by line segments constructed to connect one node to another.

A surface patch can subsequently be created by using the ‘Spline/Filler’ option under the ‘Surfaces’ tool and selecting the enclosed boundary formed by the lines. The result at this stage is presented in Figure 3-11.

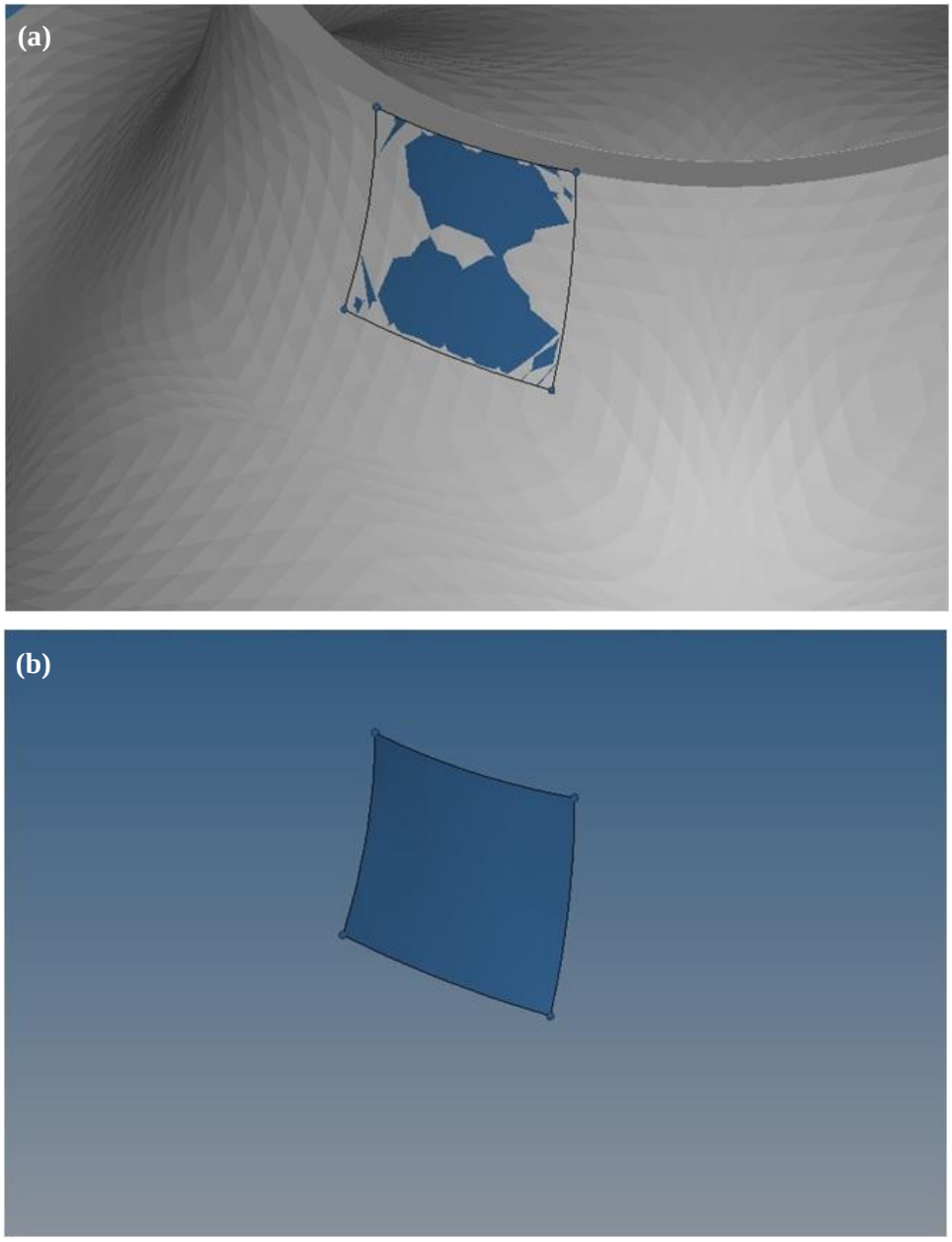

Figure 3-11 : Creation of a surface patch from the constructed enclosed boundary. (a) Surface patch overlaying the .STL model; (b) Surface patch in isolation.

Repeating the same above procedures for other areas of the .STL model, the surface geometry CAD model of the Schwarz P unit cell can be obtained as shown in Figure 3-12.

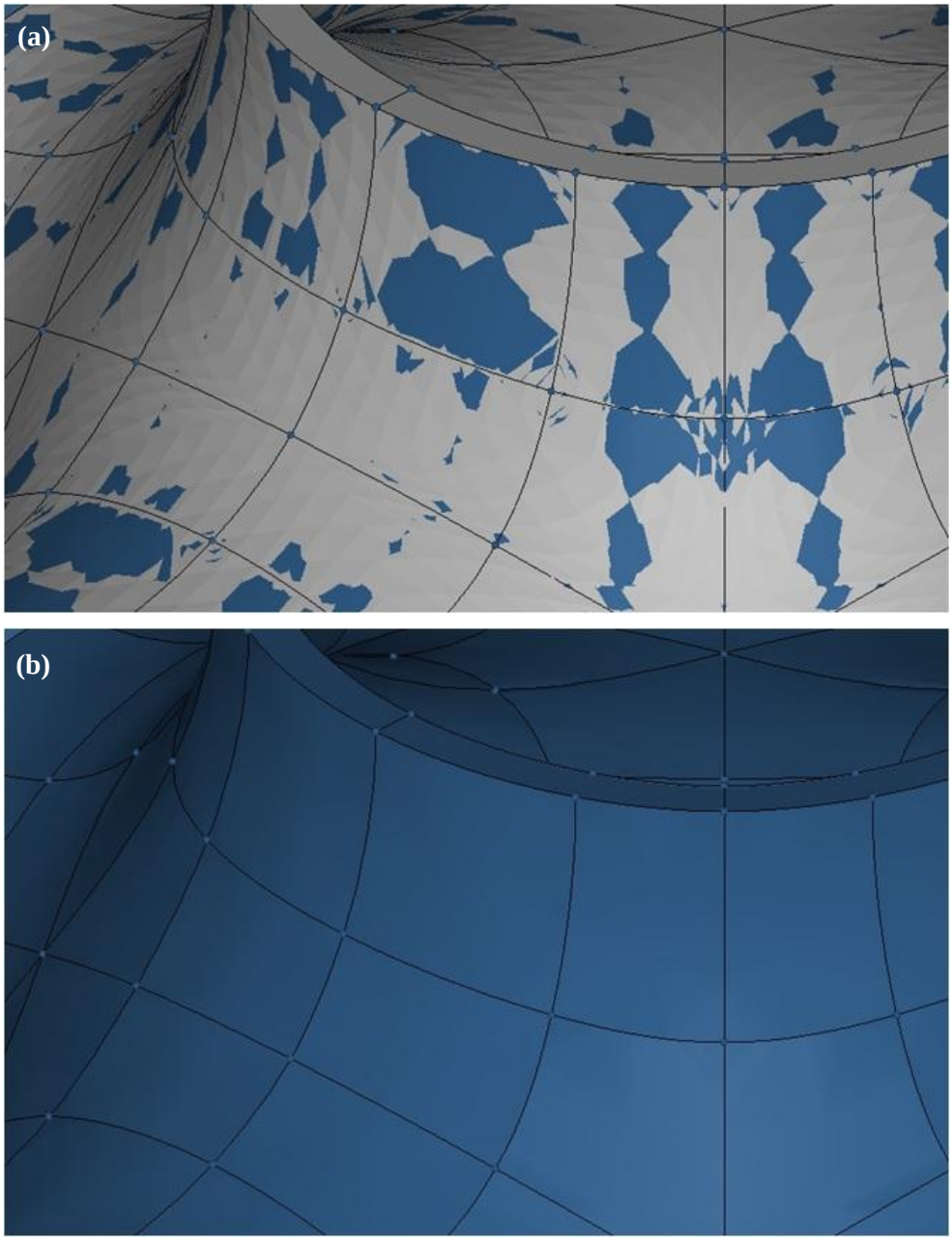

Figure 3-12 : Collection of surface patches from repeating the discussed procedures. (a) Surface patches overlaying the .STL model; (b) Collection of surface patches in isolation from the .STL model.

To ensure proper connectivity between the surfaces, the 'Equivalence' option within the 'Edge Edit' tool was used. A cleanup tolerance of 1×10^{-4} was used as a basis for equivalence. In the case where disconnections between surface patches are still prevalent, the cleanup tolerance was increased in minute amounts. Increasing the cleanup tolerance significantly more than it should be can result in distortions of the surface geometry. A comparison of the surface geometry of the Schwarz P unit cell obtained from the manual and automatic approach are presented in Figure 3-13.

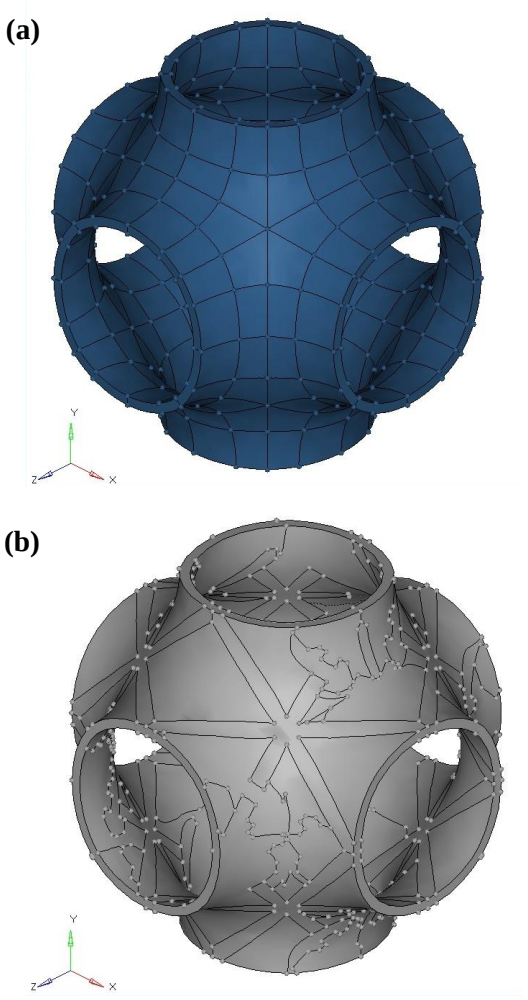

Figure 3-13 : Comparison of the surface geometry model obtained from the automatic and manual surface creation procedures. (a) Surface geometry model obtained from manual surface creation; (b) Surface geometry model obtained from automatic surface creation.

Due to the cleaner and more organized surface patching comprising the surface geometry model obtained from the manual surface creation, the said model is used extensively throughout for the rest of the study. This includes its usage in the implementation for CAD modeling techniques as well as finite element meshing procedures for computational models.

3.5 Schwarz P Unit Cell Configuration

With the surface geometry now established, the configuration of the Schwarz P unit cell can be defined in terms of its dimensional parameters. These include the height, width, length, wall thickness, pore throat size and the pore size. Measurements for these parameters can be obtained in Altair Hyperworks with respect to the references in Figure 3-14. The pore wall thickness and pore throat size is measured on faces parallel to the plane view being considered. With each plane view being composed of two directional axes i.e. vertical and horizontal directional axis, two measurements for wall thickness and pore throat for each face are made. Representation for the above is shown in Figure 3-15 using the YZ plane view of the unit cell as a representative example.

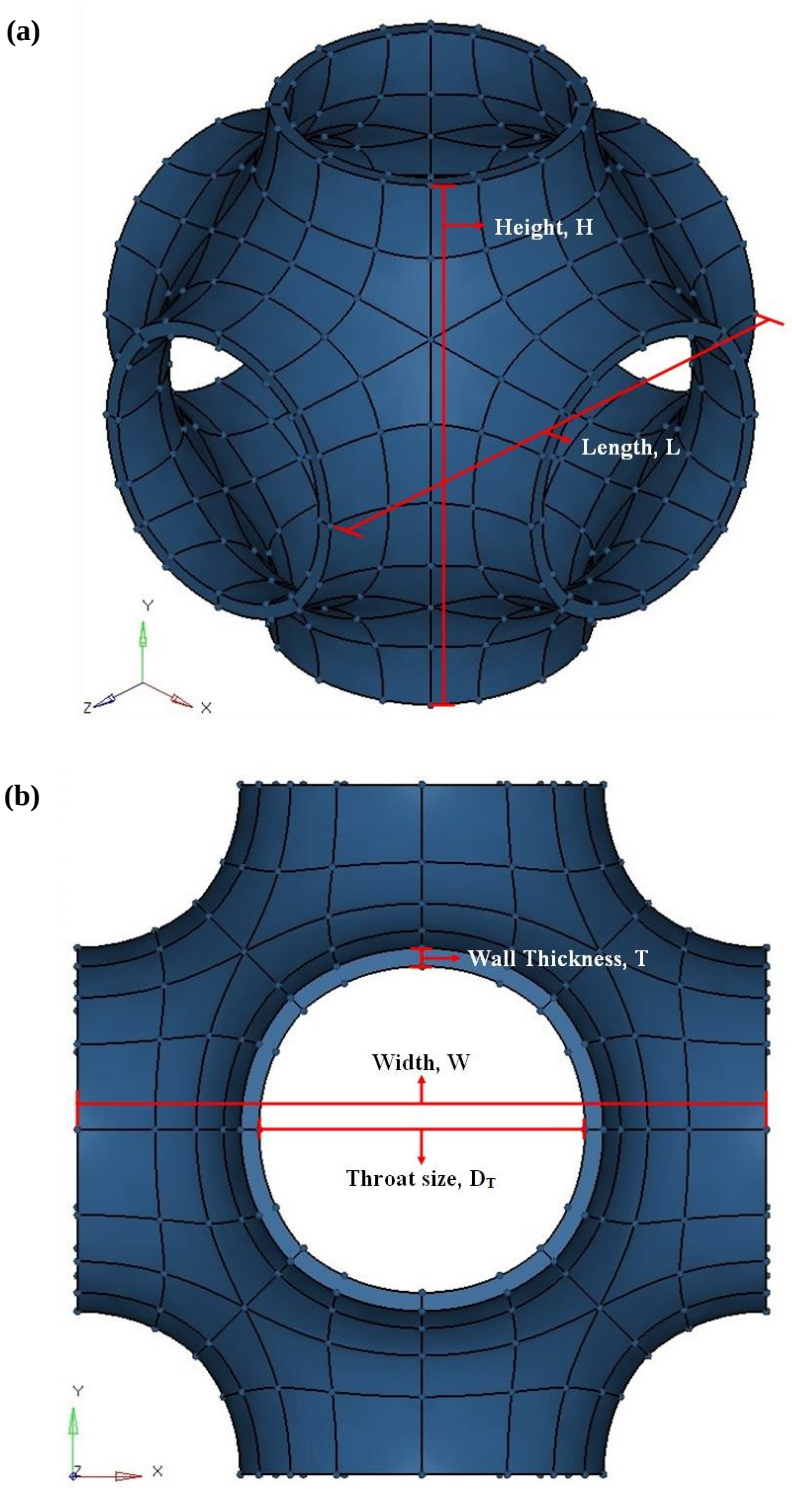

Figure 3-14 : References for dimensional parameters on a Schwarz P unit cell. (a) References for height and length; (b) References for wall thickness, width and throat size.

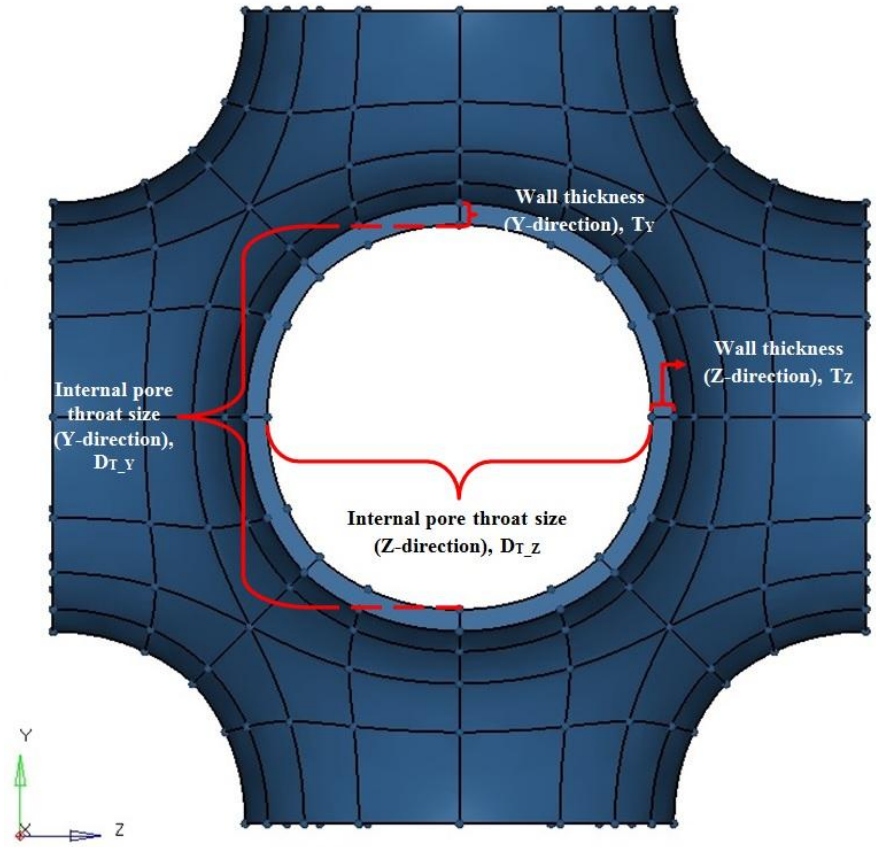

Figure 3-15 : Representative example for the measurements of wall thickness and internal pore throat size on the YZ plane view. The parameters for wall thickness and internal pore throat size both consist of two measurements depending on the directional axis from which the measurement is made.

The pore size is measured between two opposite intersection points formed by lines connecting 3 adjacent pores on the 'split plane' as shown in Figure 3-16.

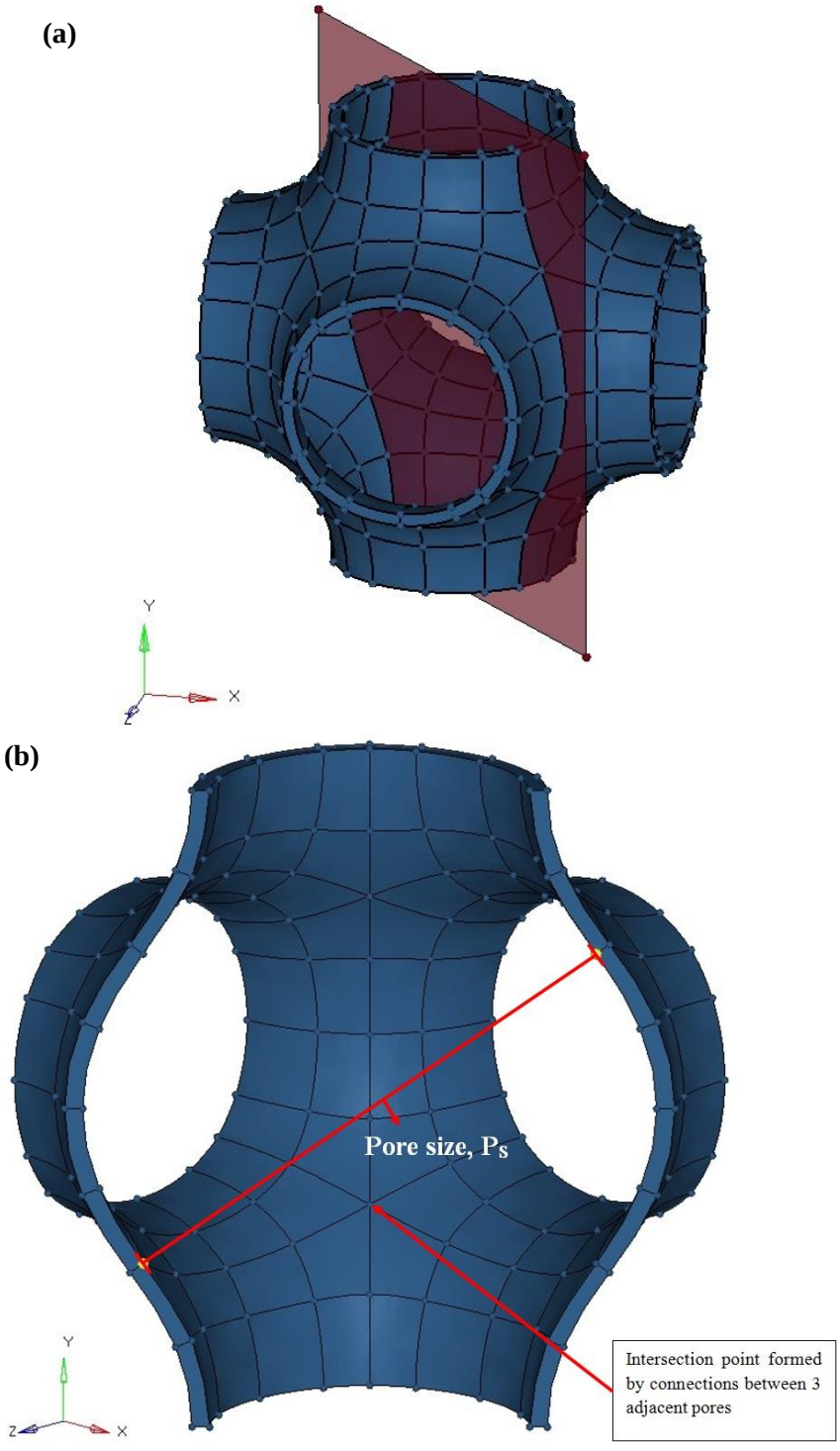

Figure 3-16 : Measurement reference for the pore size of Schwarz P unit cells. (a) Reference for plane YZ/YX i.e Split plane; (b) Reference for pore size and indication of an intersection point formed by line originating from 3 adjacent pores.

To determine the porosity, the Schwarz P unit cell is compared to itself as the porous space is filled. The unit cell can be made to be filled by creating surfaces to ensure the pore throat is closed. By generally discretising the Schwarz P unit cell and the Schwarz P unit cell without the pore space into finite elements, a query of the total volume of elements can be made through ABAQUS (Dassault Systemes) for each model. The porosity can then be determined through Equation (7). The unit cell models and their respective general discretisation into finite elements for the purpose above are represented in Figure 3-17.

$$Porosity = \frac{V_T - V_S}{V_T} \qquad (7)$$

for which,

V_T : Volume of the unit cell with enclosed pore space

V_S : Volume of the unit cell

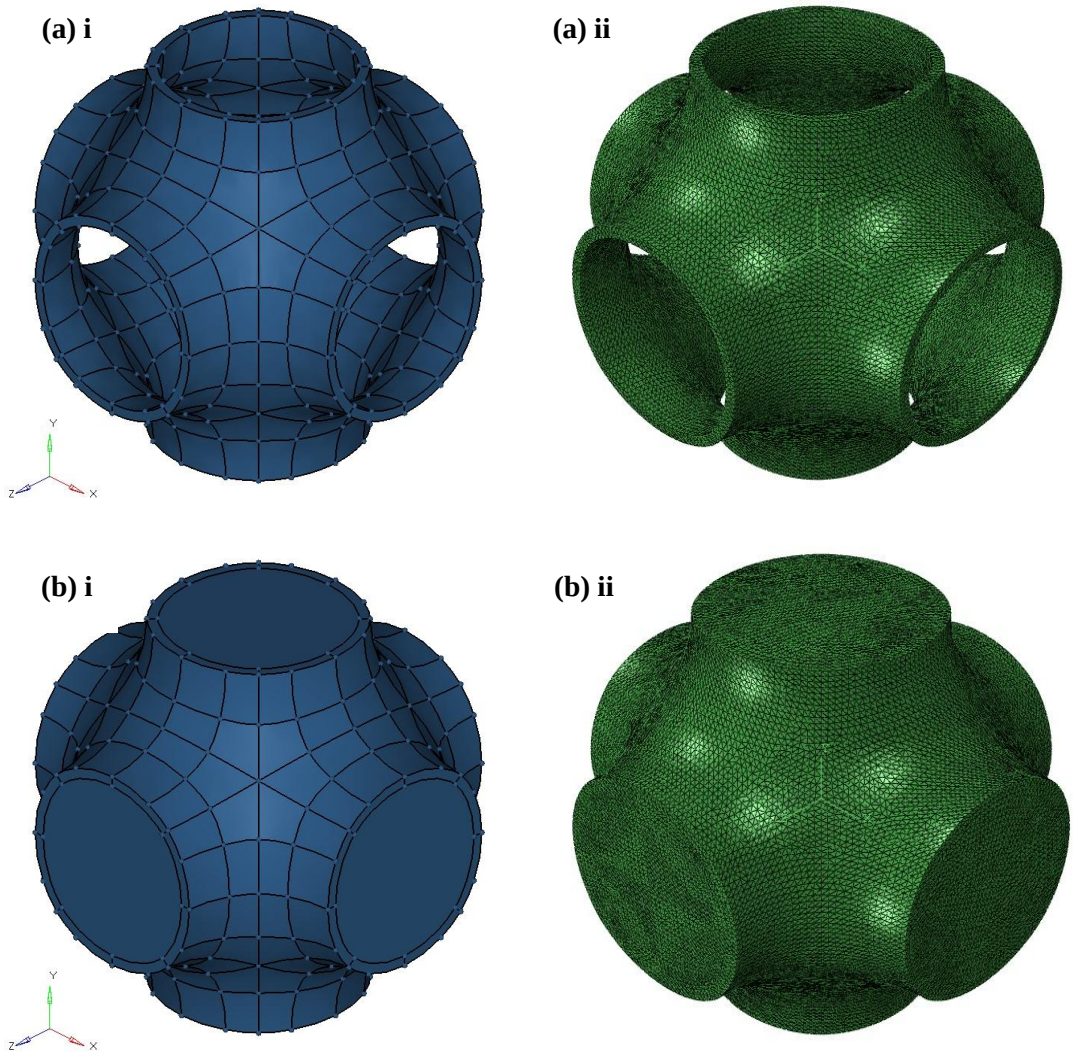

Figure 3-17 : Schwarz P unit cells and their respective mesh discretisations. (a)i Schwarz P unit cell model; (a)ii Discretised Schwarz P unit cell model into finite elements; (b)i Schwarz P unit cell model with an enclosed pore space; (b)ii Discretised model of the Schwarz P unit cell with an enclosed pore space in (b)i.

With the measurement references established, the height, width, length and wall thickness are tabulated in Table 3-1. The measurements for pore properties which include the pore size, the pore throat size and the porosity of the Schwarz P unit cell are tabulated in Table 3-2. For brevity, the averaged wall thickness and averaged pore throat size are tabulated. The measurements for the parameters were averaged between those made at the two different directional axes for each plane view in consideration.

Table 3-1 : Measurements for dimensional parameters of height, width, length and wall thickness for the Schwarz P unit cell design. The wall thickness is averaged between measurements made in the horizontal and vertical direction according to the plane view considered. The height, width and length are of equal measurements. The average wall thickness measured along the planes YZ, YX and XZ are also of equal measurements.

Height (mm)	Width (mm)	Length (mm)	Average wall thickness (mm)		
			Plane YZ	Plane YX	Plane XZ
0.52			0.01385		

Table 3-2 : Measurements for pore properties i.e. pore size, pore throat size (internal) and porosity for the Schwarz P unit cell design. The pore throat size shown is averaged between measurements made in the horizontal and vertical direction according to the plane view considered.

Pore size (mm)	Internal pore throat size (mm)			Porosity (%)
	Plane YZ	Plane YX	Plane XZ	
0.4365	0.2462			88.23

Chapter 4

Experimental Model

4.1 Introduction

Under the INNOVABONE project, Schwarz P unit cell-based tissue scaffolds have been fabricated using copolymer materials based on methacrylated poly(D,L-lactide-co-ε-caprolactone) (PLCL). PLCL of differing compositions have been used for fabrication with ratios of lactide (L) to caprolactone (C); 16:4 (LCM3), 18:2 (LCM4) and 9:1 (LCM6). With the scaffolds being intended for use in bone regeneration, cellular response studies performed under the project have determined that scaffolds with LCM3 exhibited a quick recovery rate after compression and a better cellular response compared to other compositions despite having low Young's modulus. This provides the potential to simultaneously fulfill essential requirements from a mechanical and biological aspect in regards to the implementation of scaffolds. Therefore, PLCL with a composition of LC16:4 (LCM3) and Schwarz P unit cell-based tissue scaffolds with said composition will be the focus throughout the course of this study.

The computational model considered in this study comprises of two different types of analysis i.e. linear and non-linear analysis; both requiring material input data obtainable from the experimental model. The computational model also involves comparisons between results of mechanical characterisation of Schwarz P unit cell-based tissue scaffolds obtained computationally and experimentally. This chapter is divided into two respective sections for 'Bulk LCM3 Material' and 'Schwarz P Tissue Scaffold

Mechanical Characterisation'. The section for 'Bulk LCM3 Material Data' details the methodology in obtaining material data from bulk LCM3 material. Results obtained are used as input for computational studies. The section for 'Schwarz P Tissue Scaffold Mechanical Characterisation' as the name suggests, details the methodology in characterising the mechanical properties of Schwarz P tissue scaffolds fabricated with LCM3. The results obtained will be used as a basis of comparison to the results obtained from the mechanical characterisation of the scaffolds performed through a computational approach.

4.2 Bulk LCM3 Material Data

4.2.1 Background

Material data from bulk LCM3 are used as input for computational studies. Different forms of data are also required depending on the type of analysis to be performed i.e. non-linear analysis and linear analysis. Despite this, the stress-strain curves of the bulk material forms the foundational basis for input in computational studies. A flowchart is presented in Figure 4-1 to outline the processes and involvement of different data forms to computational models based on the stress-strain curve.

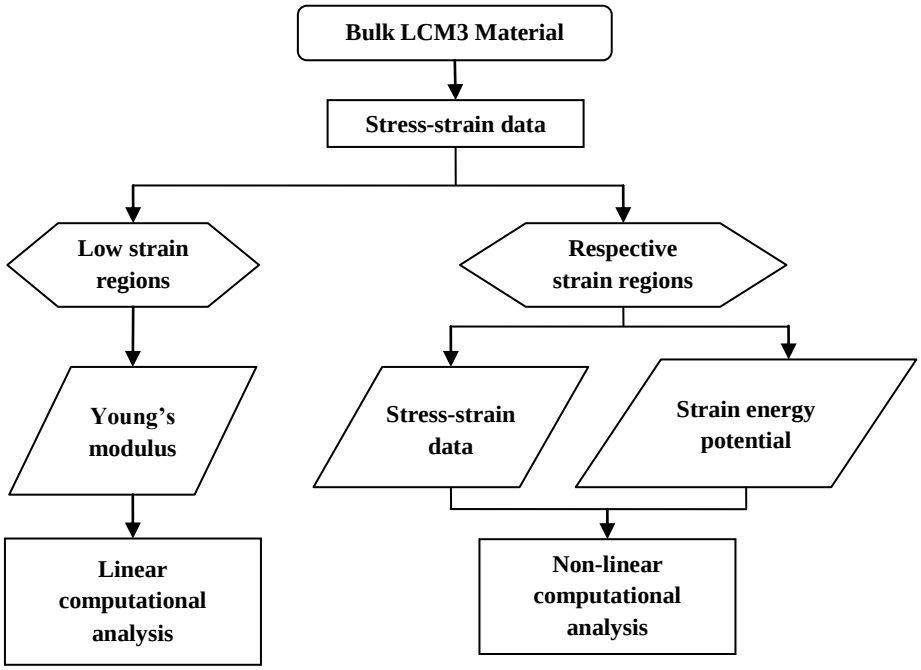

Figure 4-1 : Flowchart showing the required material data inputs for different types of computational analysis. Based on the stress-strain data obtained, attention is given to low strain regions to determine the Young's modulus for bulk LCM3 specimens. The Young's modulus and Poisson's ratio are used as input for linear computational analyses. Attention is also given to respective strain regions of stress-strain data obtained from bulk LCM3 specimens. A form of strain energy potential is determined based on the data. Stress-strain data together with the selected strain energy potential are then used as inputs for non-linear computational analyses.

With the flowchart in Figure 4-1, a sub-section for experimental methodology is divided into three different subsub-sections. The first subsub-section is devoted to discussing the methodology for the fabrication of bulk LCM3 cylinders. The following subsub-section discusses the methodology involved in obtaining stress-strain curve data and subsequently the Young's modulus through the implementation of the fabricated cylinders. A methodology in selecting a strain energy potential based on the data obtained is also discussed in the respective subsub-section that follows.

Subsequently, a sub-section is devoted to the presentation of results which will first highlight stress-strain data obtained for different bulk LCM3 specimens before being further sub-divided according to the strain regions in focus i.e. low strain regions and respective strain regions to establish material data input for the linear and non-linear computational analysis.

4.2.2 Methodology

4.2.2.1 Bulk LCM3 Cylinder Fabrication

Cylindrical samples of LCM3 measuring in 6mm in diameter and 10mm in height were produced by mixing the liquid precursor with 0.1wt% of Irgacure 369 (Ciba Chemical, Switzerland) photoinitiator. The pre-determined amount of Irgacure 369 was dissolved in acetone to give a concentration of 40mg/mL before mixing with the LC16:4-liquid precursor mixture. This mixture was subsequently stirred overnight at 60℃ until excess solvent was evaporated to give a homogenous solution. The LCM3-Irgacure mixture solution was cast into cylindrical plastic moulds measuring 6mm in diameter and 10mm in height before being crosslinked using a UV irradiation source (Proma UV Exposure unit with vacuum 260W, Germany) for 9 minutes. The resulting copolymer cylindrical

specimens were immersed in acetone for 7 days with a change of solvent for each day to remove residuals of unreacted monomers and initiators before vacuum drying.

4.2.2.2 Stress-Strain Data

An Instron 5969 testing machine was used to mechanically compress bulk LCM3 cylinder samples to failure at a crosshead speed of 1.3mm min^{-1} as detailed in ASTM D695 with a 5kN load cell. Compressing the samples height-wise, the strain rate is approximately 0.13min^{-1}. During compression experiments, the machine was set to trip when the measured compressive load exceeded 4.5kN. In the case of specimen fracture before exceeding said limit, the machine was stopped manually.

The compression tests were repeated across 5 different specimens with each load-displacement data being recorded. The load-displacement data was then interpreted for stress-strain data using the equations that follows.

Stress, $\sigma = {}^{F}/_{A}$ for,

F : Compressive load

A : Surface area of specimen $= \pi \left({}^{diameter, d}/_{2}\right)^2$

$= \pi (radius, r)^2$

Strain, $\varepsilon = {}^{L_E}/_{L_i}$ for,

L_E : Extension

L_i : Original height of the specimen

The Young's modulus for each stress-strain curve data was determined as outlined in British Standard BS EN ISO 604:1997. Through the standard, the Young's modulus (compressive) is defined as in Equation (8).

$$E_c = \frac{\sigma_2 - \sigma_1}{\varepsilon_2 - \varepsilon_1} \qquad (8)$$

for which,

σ_1 Compressive stress at strain ε_1

σ_2 Compressive stress at strain ε_2

ε_1 Compressive strain = 0.0025 (0.25%)

ε_2 Compressive strain = 0.0005 (0.05%)

This is easily obtained through the use of a linear 'Trendline' constructed at stress values with strains ranging between 0.0005 and 0.0025 on the stress-strain curve.

4.2.2.3 Strain Energy Potential

Implementing PLCL as a material for Schwarz P unit cells in non-linear computational analyses will take a hyperelastic material model. Hyperelastic material models require specification of one of the seven forms of strain energy potential alongside nominal stress-strain data (obtained from compression experiments) for material definition. These forms include the polynomial forms i.e. reduced polynomial, neo-Hookean, Mooney-Rivlin and Yeoh; the Ogden form, Arruda-Boyce form and the Van der Waals form. ABAQUS provides an 'Evaluate' option to determine material response based on input experimental stress-strain curves. The 'Evaluate' option would produce a 'Stability Limit Information' report showing the stability of material response results in accordance to different tests (uniaxial tension/compression, biaxial tension/compression, planar tension/compression and volumetric tension/compression) along with the coefficients for

the strain energy potential. The coefficients obtained are evaluated to give stress-strain data for each respective strain energy potential. Comparisons are made between the experimental stress-strain data of a specimen and the stress-strain data for strain energy potential by determining the error between the two before subsequent selection of strain energy potential.

For a considered specimen, all different forms of strain energy potential are filtered based on the stability of material response results whereby only forms that are labeled stable throughout all tests are taken into account. It shall be noted here that for most stress-strain curves, evaluating the Van der Waals form of strain energy potential gave non-convergent results and was therefore excluded from analyses and selection. A custom MATLAB algorithm cycles through curve data for each strain energy potential to determine the root-mean square error (RMSE) to the experimental stress-strain curve. The algorithm then determines the strain energy potential that gives the least RMSE value. The strain energy potential with the least RMSE value is used for specification alongside the stress-strain curve of the specimen considered.

4.2.3 Results

Five bulk LCM3 cylinders underwent compression to failure to obtain stress-strain data. Stress-strain data obtained showed variations between different samples. It was not feasible to utilise all five stress-strain data to extract further material data for computational models. Instead a lower, averaged and upper limit material data can be implemented to obtain results that are bounded within a range. Since the lower and upper limit material data can be obtained from the lowest and highest stress-strain curve exhibited by a specimen respectively, only the averaged data needs to be determined.

Obtaining the averaged data required post-processing of stress-strain curves due to each specimen having load values recorded at different displacements i.e. stress values recorded at different strains. This was done using a combination of custom algorithms in MATLAB and a proprietary package, SLM. The algorithm evaluates the stress values at strains ranging from 0 to 0.60 for 3,000 data points for each curve. The stresses were then averaged at each particular value of strain within the range to give the averaged stress-strain data. The evaluation of stress was restricted to a maximum strain value of 0.60 to prevent unnecessary need to extrapolate data for any specimens. The algorithm is appended in Appendix A.

The stress-strain curves for all 5 specimens including the averaged curve are graphically presented in Figure 4-2.

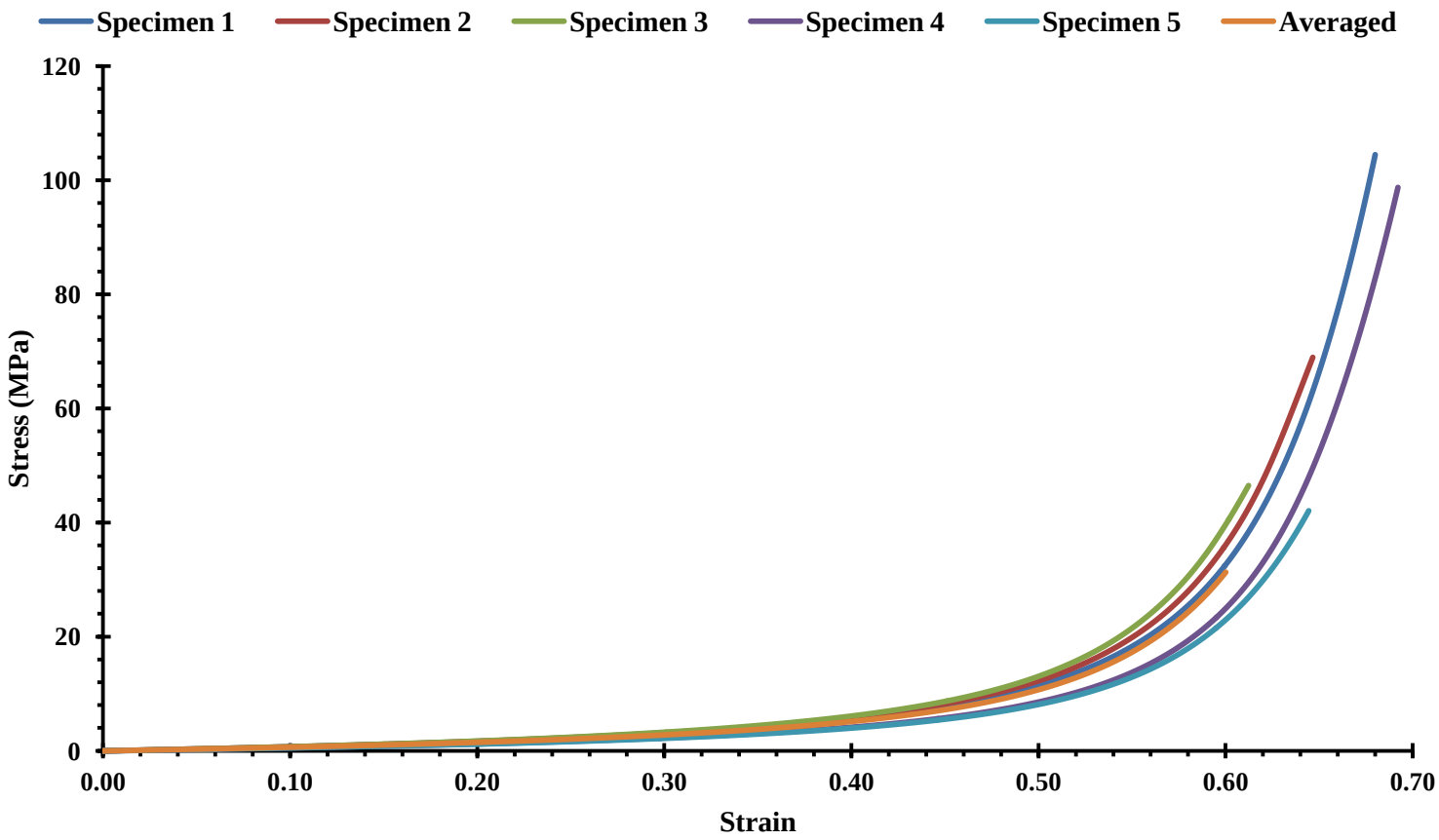

Figure 4-2 : Graphical plot consisting of stress-strain curves for all specimens including the averaged data. The stress-strain curves are only shown for stresses at strain values between 0 and the strain at which each respective specimen starts to fail. The averaged data was obtained using a custom algorithm which evaluates the stress at particular values of strains between 0 and 0.60 for 3,000 data points. The maximum strain is restricted to 0.60 in the evaluation to prevent unnecessary need for data extrapolation which would imply stress-strain above failure.

With the stress-strain curves shown, it will be confirmed here that alongside the averaged data obtained, the stress-strain curve for specimen 5 and 3 will be used as lower and upper bounding data respectively. These three stress-strain curves will be focused further to analyse and extract material data required for computational studies in the following subsub-sections.

4.2.3.1 Low Strain Regions

Computational studies involving linear analyses require material definition in terms of Young's modulus and Poisson's ratio. Based on investigations performed under INNOVABONE, the Poisson's ratio for LCM3 is taken to be 0.3. Therefore only the Young's modulus needs to be determined. Consider stresses at strains between 0.0005 and 0.0025 (shown in bounding box) for specimen 3 as a representative example for the calculation of Young's modulus in Figure 4-3. The stress-strain curve is only shown between 0 and 0.01 rather than the whole strain region for specimen 3 so that the bounding box appears larger in scale. As discussed in Subsub-section 4.2.2.2, a linear trendline was formed to complement the equation of the line in the linear region. The gradient in the equation of the respective trendline is then taken to be the Young's modulus of the specimen.

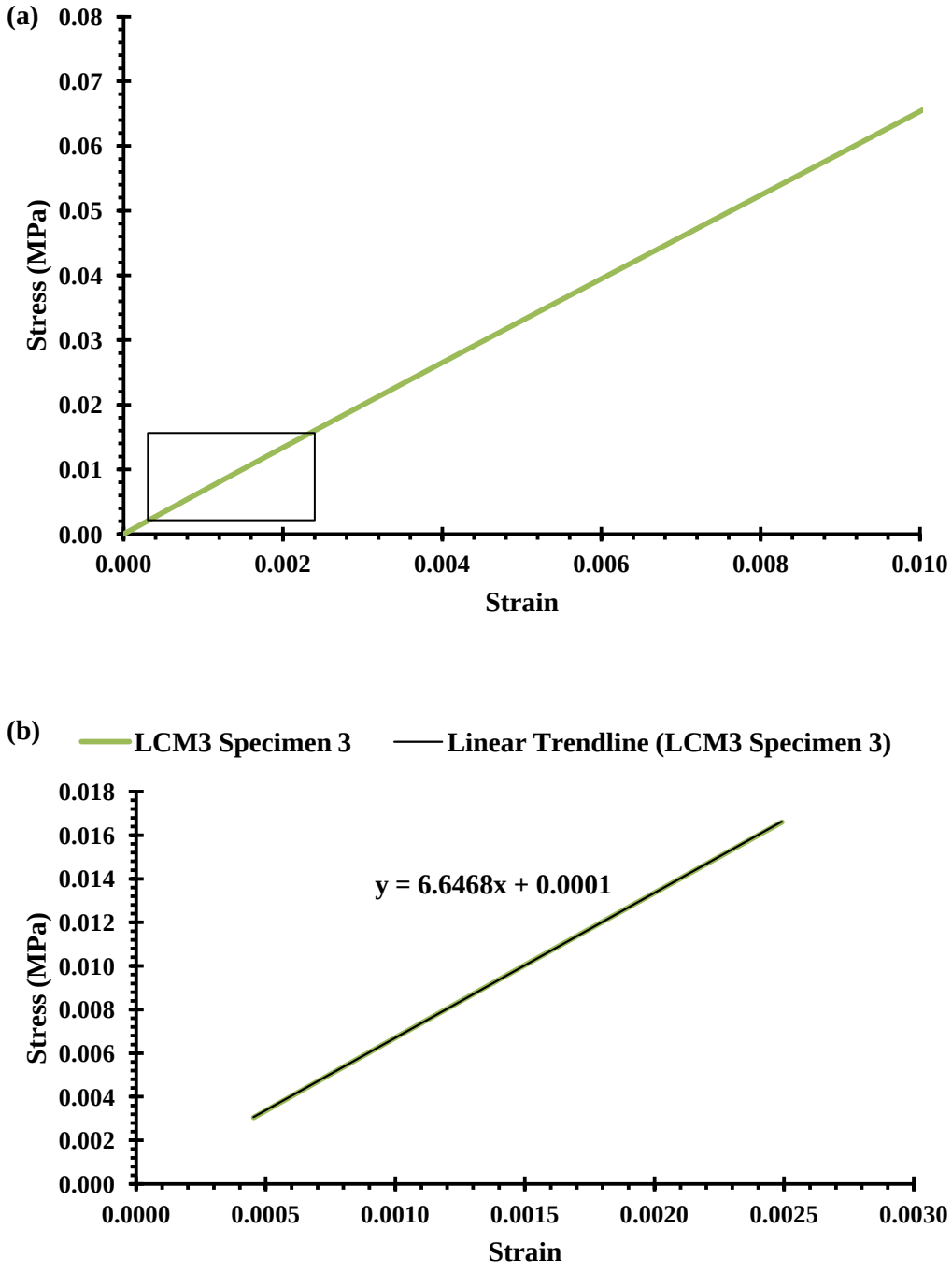

Figure 4-3 : (a) Stresses for strains ranging between 0 and 0.01 with a bounding box for consideration in the calculation for Young's modulus for LCM3 specimen 3. Strains are only shown between 0 and 0.10 only to allow the location of the bounding box to be observed with more clarity; (b) Linear trendline formed within the bounding box. The upper and lower limit strain values for the bounding

region are chosen in accordance to standards set in British Standard BS EN INO 604:1997 which takes into account the occurrence of a toe region which explains the value of y-intercept not being equivalent to 0.

With the equation of the trendline established, the gradient and hence the Young's modulus of specimen 3 LCM3 is determined to be 6.65 MPa. Performing the above processes for the averaged data and specimen 5, the Young's modulus for respective specimens are tabulated in Table 4-1.

Table 4-1 : LCM3 material data definition for linear analyses in computational models.

Specimen	Young's modulus (MPa)	Poisson's ratio
Upper limit : 3	6.65	0.3
Average	5.74	
Lower limit : 5	4.39	

The material data for linear computational analyses in regards to LCM3 have then been established and can then be used for input.

4.2.3.2 Respective Strain Regions

Computational studies involving non-linear analyses with hyperelastic material models require the specification of nominal stress-strain data and a selection of one strain energy potential. The methodology in obtaining these has been described previously in Sub-section 4.2.2. Considering specimen 5 as a representative example in determining the RMSE values for different forms of strain energy potential, using the respective experimental stress-strain data in the built-in 'Evaluate' option in ABAQUS gave several stable results in regards to different forms of strain energy potential as shown in Figure

4-4. After subsequent utilisation of the custom algorithm, RMSE values between the experimental data and the stress-strain data for each stable form of strain energy potential is obtained. Performing the above for specimen 3 and the averaged data, the stable forms of energy potential and their respective RMSE values for specimens considered are tabulated in Table 4-2.

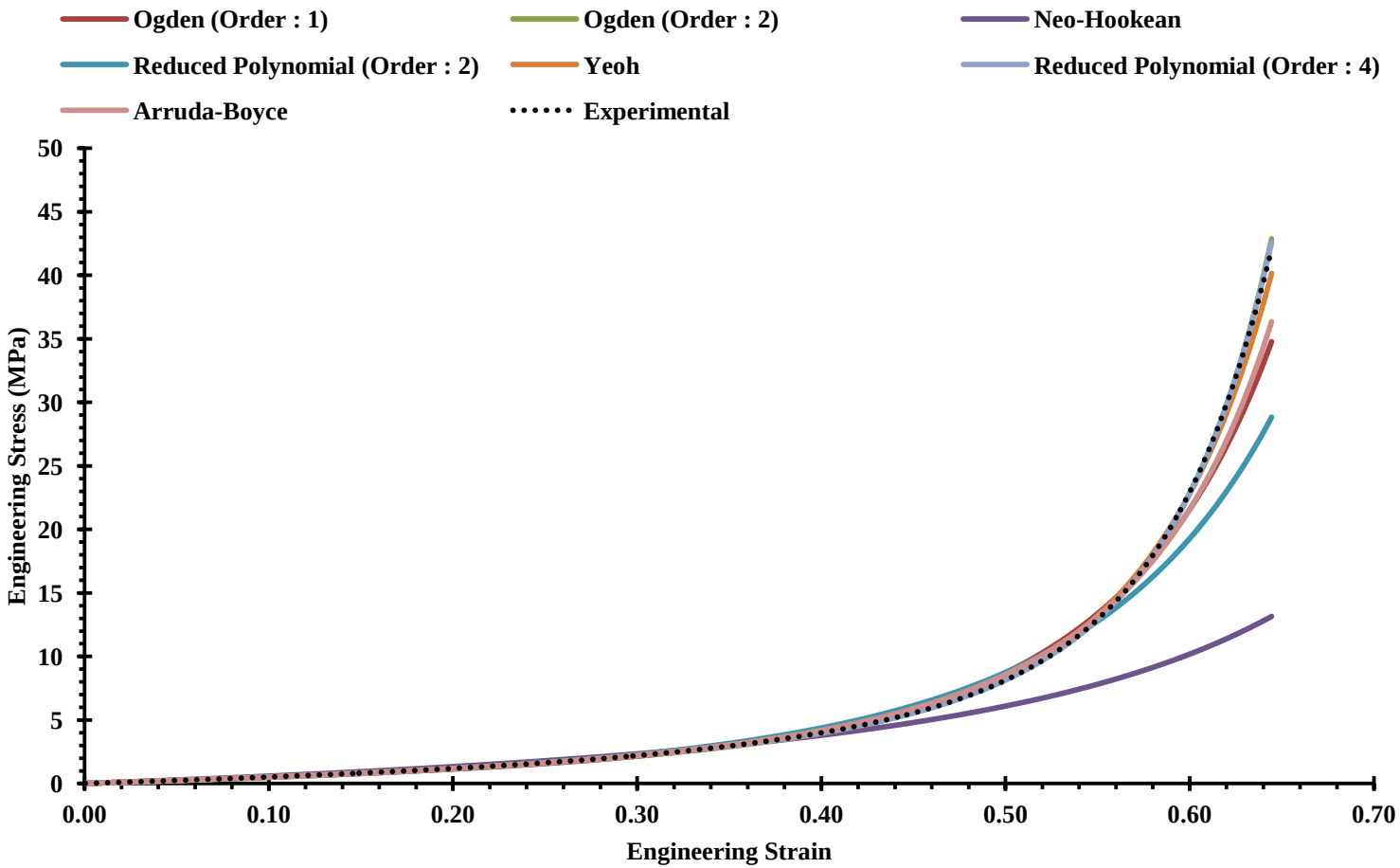

Figure 4-4 : Experimental stress-strain curve for specimen 5 of LCM3 and corresponding strain energy potential curves for different forms obtained from the 'Evaluate' option in ABAQUS.

Table 4-2 : RMSE values for stable forms of strain energy potential and corresponding order when compared to the experimental stress-strain data for different LCM3 specimens.

Specimen	Strain energy potential	Order	RMSE
Upper limit : 3	**Ogden**	1	0.963
		2	0.037
		3	0.036
		4	0.032
		5	0.036
		6	6.607
	Reduced polynomial	1 (Neo-Hookean)	2.161
		2	0.330
		3 (Yeoh)	0.043
		4	0.917
	Arruda-Boyce		0.963
Average	**Ogden**	1	1.794
		2	0.159
		3	0.115
		4	0.096
		5	9.363
	Reduced polynomial	1 (Neo-Hookean)	3.648
		2	0.438
		3 (Yeoh)	0.116
		4	1.794
Lower limit : 5	**Ogden**	1	1.145
		2	0.074
	Reduced polynomial	1 (Neo-Hookean)	5.959
		2	2.228
		3 (Yeoh)	0.289
		4	0.047
	Arruda-Boyce		0.948

A form of strain energy potential is selected based on the lowest RMSE values. For the averaged stress-strain data and the stress-strain data for specimen 3, Ogden with a strain energy potential order of 5 has the lowest RMSE. However, specimen 5 has an Ogden with a strain energy potential order of 2 as the lowest RMSE. A similar form of strain energy potential between all 3 data needs to be specified as it pertains to LCM3 as a whole. Therefore, reduced polynomial with a strain energy potential order of 4 is selected for material specification.

With the above, the material data for non-linear computational analyses in regards to a hyperelastic material model for LCM3 has been established. Nominal stress-strain data and the selected strain energy potential can then be used as input for analyses.

4.3 Schwarz P Tissue Scaffold Mechanical Characterisation

4.3.1 Background

The mechanical characterisation of physical fabricated tissue scaffolds serves as a basis of comparison to non-linear computational analyses performed in this study. The following sections describe the fabrication of Schwarz P unit cell-based tissue scaffolds along with experimental methodology in characterising its mechanical properties. The subsequent section outlines the results obtained from mechanical characterisation of the tissue scaffolds comprised of PLCL with LC16:4 (LCM3).

4.3.2 Tissue Scaffold Fabrication

Schwarz P unit cell-based tissue scaffolds were fabricated using the additive manufacturing technique, two-photon polymerisation (2PP). Through 2PP, femtosecond laser pulses are initiated on photosensitive or photoresistive materials resulting in two-photon absorption and subsequent material polymerisation. Syntheses of the liquid precursor making up the photoresist for scaffolds considered in this study have been detailed in previous literature [122]. Generally, methacrylated lactic acid/ε-caprolactone (mLC) comonomer with lactide (L) to caprolactone (C) ratio of 16:4 was synthesised through a ring opening polymerisation process. BA740 photoinitiator was dissolved in 0.2mg/μL before being added to the copolymer precursors to give a resulting 0.2% concentration mixture. The mixture was then continuously stirred overnight at a temperature of 60℃ in order to remove residual solvents and thus form a uniform solution. A M3DL 2PP scanner setup (LZH Hannover, Germany) consisting of a femtosecond laser source was implemented for scaffold fabrication. During laser pulses, a tri-axial positioning stage dynamically moves in tolerance of nanometers in accordance to the computer model of a Schwarz P unit cell with the support of a galvano-scanner

(Aerotech, USA). This computer model of the Schwarz P unit cell is packaged into a stereolithography file as described in Chapter 3. The result is an $4 \times 9 \times 4$ array of Schwarz P unit cells in the x, y and z directions; measuring approximately $2 \times 4 \times 2$mm. An SEM micrograph of the fabricated scaffold is presented in Figure 4-5.

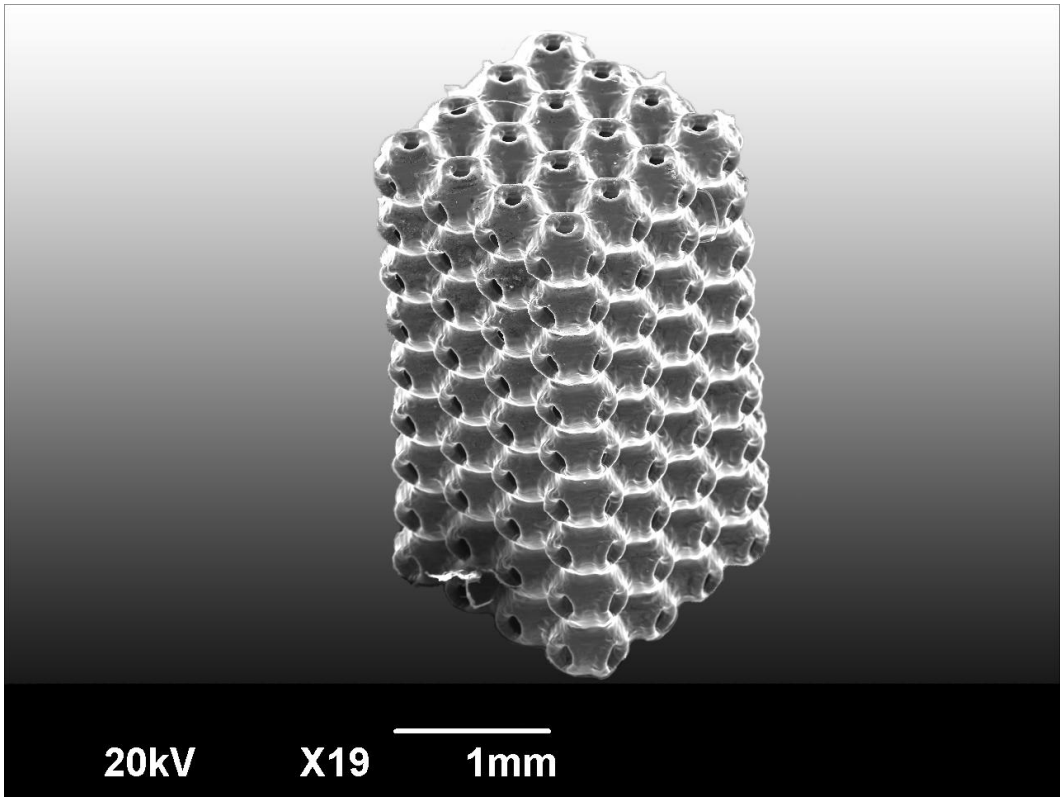

Figure 4-5 : SEM micrograph of a fabricated physical Schwarz P unit cell-based tissue scaffold comprising of $4 \times 9 \times 4$ unit cells and approximately measures $2 \times 4 \times 2$ mm in the x, y and z directions respectively.

4.3.3 Methodology

Physical tissue scaffolds were compressed to 20% strain from its original height at a crosshead speed of 0.5mm min^{-1} with a 5N load cell using a Hounsfield testing machine. Compressing the scaffold samples height-wise, the strain rate is approximately 0.125 min^{-1} (0.13min^{-1} at 2 s.f.). The compression was restricted to 20% strain to prevent permanent deformation of the scaffolds. Results were recorded in terms of load-displacement data which was subsequently calculated for stress-strain data. Forming a graphical presentation of the data would give the stress-strain curve for a particular tissue scaffold sample. During compression, stresses were recorded at the same strain values among all different samples. Simple averaging of stresses at each one of these strain values for all the samples were evaluated to determine an averaged stress-strain curve. The stiffness i.e. compressive modulus of a sample was determined based on the equation of a linear region formed at low strain values. The above was repeated for 5 different tissue scaffold samples in total.

4.3.4 Results

Graphical presentation of the obtained stress-strain data obtained for all five specimens are shown in Figure 4-6.

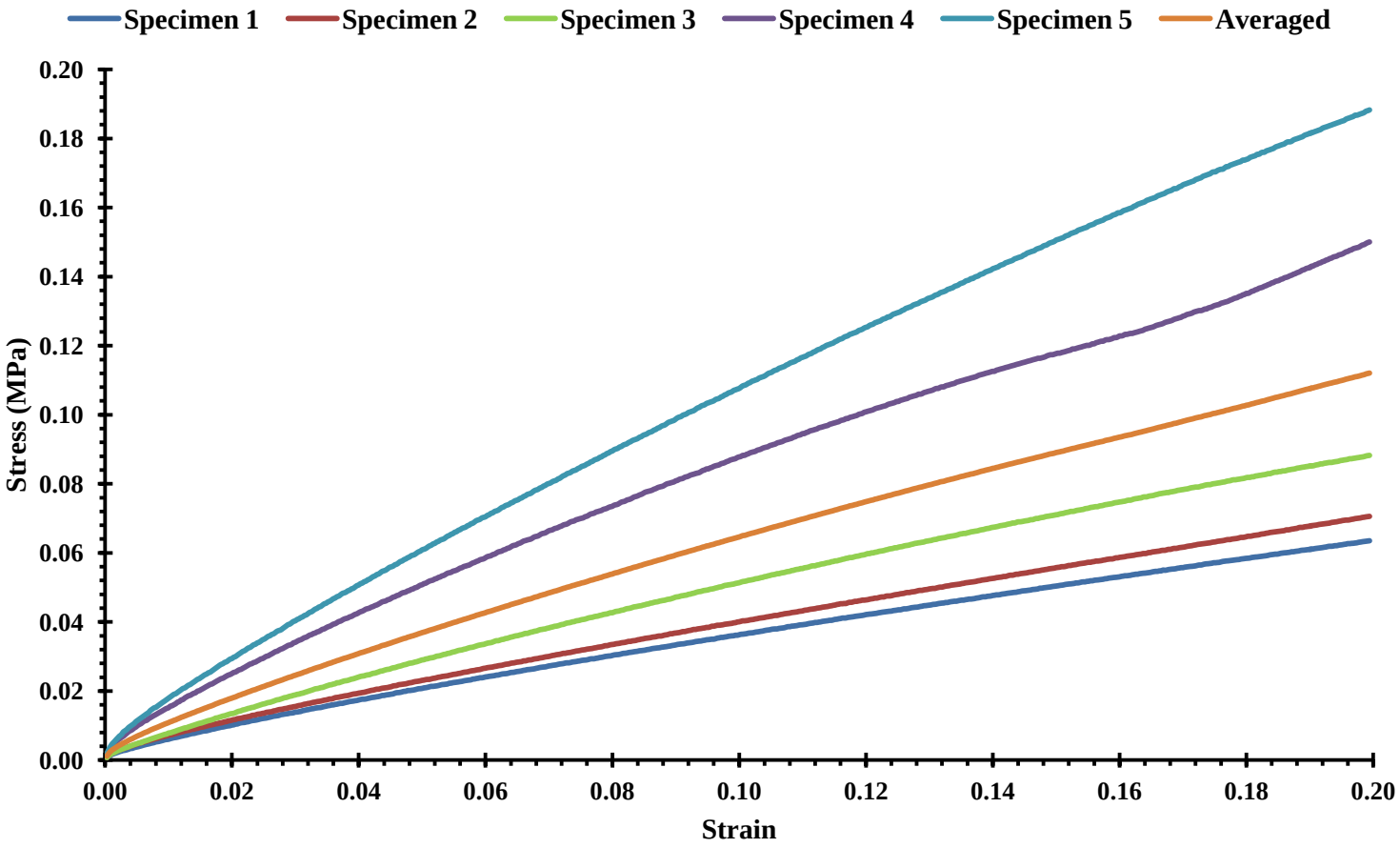

Figure 4-6 : Stress-strain curves for the averaged and all 5 specimens of fabricated Schwarz P unit cell-based tissue scaffolds obtained from compression experiments. The compression was only performed at a maximum 20% strain from its original height to prevent permanent deformation of scaffolds. The averaged stress was evaluated at each strain value among all samples.

The determination of the stiffness is performed in a similar manner to determine the Young's modulus of bulk LCM3 samples discussed in Subsub-section 4.2.2.2 of Section 4.2. However, the strain region between 0.0005 and 0.0025 set out previously (set according to standard) cannot be considered due to linear regions falling outside of that region for each respective stress-strain data obtained. A data point which approximately lies immediately after the 'toe region' in terms of the stress-strain curve was selected as the lower limit for consideration of a linear region. Subsequently 50 stress-strain data after the lower limit data was selected as the upper limit. This gives a linear region between the two limits determined.

Consider specimen 3 as a representative example in determining the stiffness of a scaffold sample as shown in Figure 4-7. The stress-strain curve is only shown between 0 and 0.10 to show the bounding box for consideration of the linear region with more clarity.

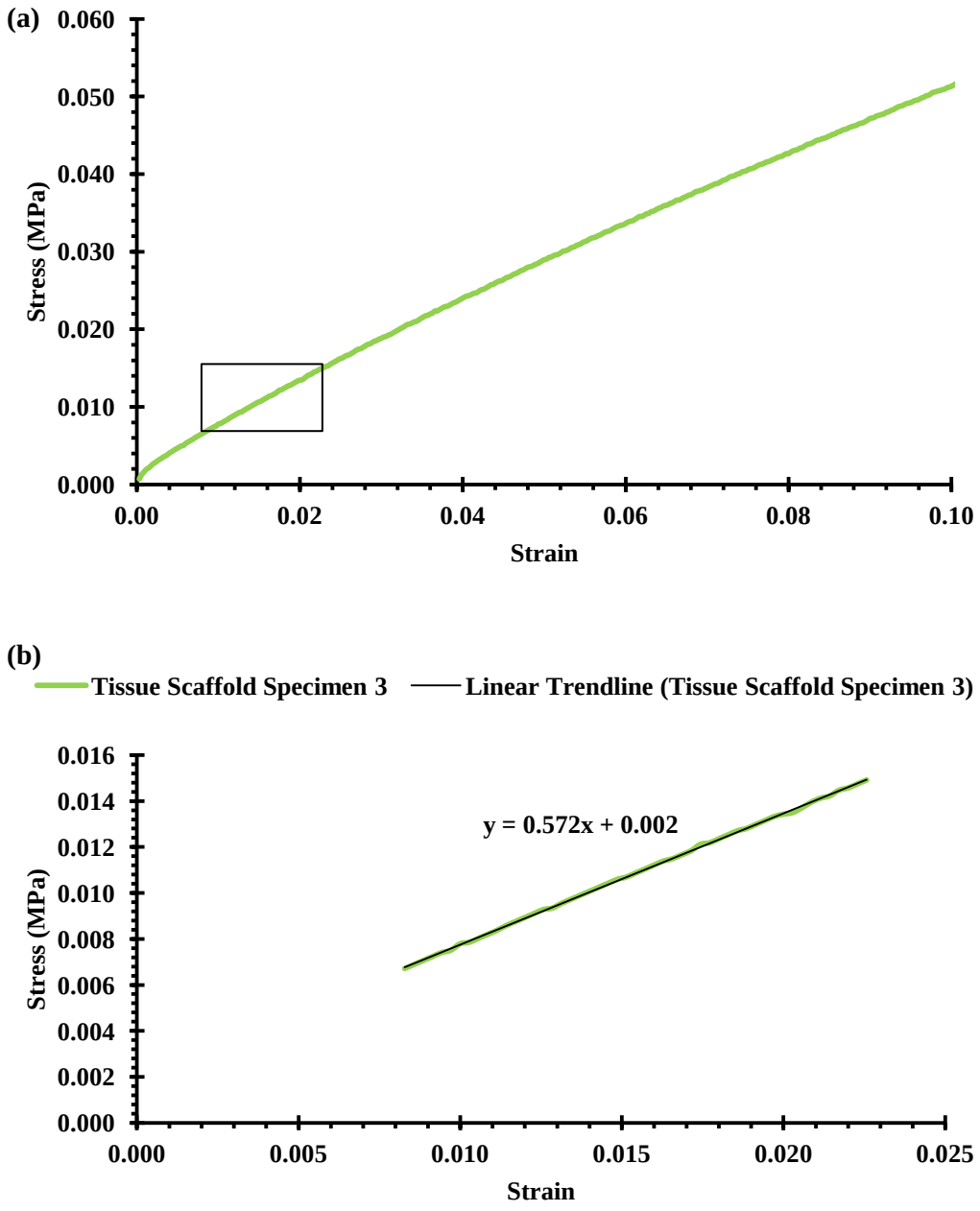

Figure 4-7 : Stresses for strains ranging between 0 and 0.10 with a bounding box for consideration of the linear region to determine the stiffness of LCM3 tissue scaffold specimen 3. The stress-strain data was only shown between 0 and 0.10 to allow the bounding box to be observed with clarity; (b) Linear trendline formed within the bounding box between strain values of 0.0083 and 0.023. The value of the y-intercept in the equation of the trendline signifies the occurrence of the toe region similar to stress-strain data for bulk LCM3 samples.

With the equation of the trendline in Figure 4-7(b), the gradient and hence the stiffness of LCM3 tissue scaffolds specimen 3 is determined to be 0.57 MPa. Performing the above all other specimens, the stiffness of fabricated Schwarz P unit cell-based tissue scaffolds are averaged at 0.69 ± 0.29 MPa with an obtainable maximum of 1.14 MPa and minimum of 0.40 MPa.

With the above, the experimental stiffness values for fabricated Schwarz P unit cell-based tissue scaffolds have been established. The range of stiffness values can then be used as a basis of comparison to results obtained through computational approaches in mechanical characterisation of the scaffolds.

4.4 Discussion

Obtained stress-strain data from compression experiments of bulk LCM3 cylinders gave variances between different specimens. Two different consistencies in terms of stress-strain data can be observed among the different specimens; one formed by specimens 1, 2 and 3 while the other is formed by specimens 4 and 5. The different specimens also failed at different strains. One possible source resulting in the variances between the stress-strain data between different specimens is the presence of air bubbles within the matrix of the cylinder. The presence of air bubbles was apparent in bulk cylinders of PLCL with a lactide (L) to caprolactone (C) ratio of 18:2 i.e. LCM4 as shown in Figure 4-8.

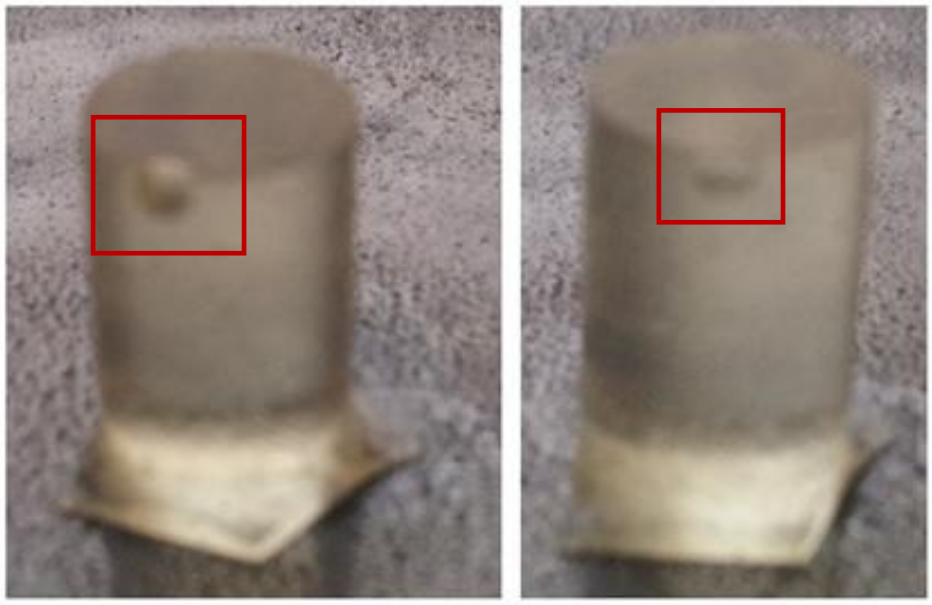

Figure 4-8 : Presence of air bubbles on the external surface of bulk LCM4 cylinders (indicated within the red box).

Despite not being observably significant as in LCM4, the presence of tiny air bubbles (unobservable with the naked eye) within the matrix of LCM3 cylinder would definitely effect its' respective mechanical properties. The presence of these air bubbles form

mechanically fragile regions in the form of voids which pose as potential locations of failure which degrade mechanical performance [196,197].

A previous investigation performed to characterise the mechanical properties of carbon fibre/epoxy laminates have found that the tensile, compressive, bending and inter-laminar strength generally decreased as porosity made up by void content increased from 0.33% to 1.5% [198]. Another previous literature investigating the effect of void content on the compressive strength of carbon fibre/epoxy resin composites found a roughly linear correlation between void content and compressive strength. Findings within the investigation found a reduction of 40% in terms of compressive strength at a volume fraction consisting of 4% voids [199]. In a separate study, it has been reported that porosity levels below 2% gives way to noticeable reduction in compressive strength with higher reductions at higher void content [200]. A study investigating the influence of void content on the structural flexural performance of unidirectional glass fibre reinforced polypropelene composites have found that the flexural modulus and strength decreases by about 1.5% as the void content increased from 1% to 14% [201]. The findings from the study generally complemented the findings in a recent study investigating the flexural strength and flexural modulus of carbon fibre reinforced polycarbonate composite laminates where both aforementioned properties exhibited a decreasing trend with the increase in void content [202]. Taking into account the aforementioned consistencies between stress-strain data of specimens mentioned earlier, it can be implied that specimens 1, 2 and 3 comprised of consistent void content averaging around one value while specimens 4 and 5 comprised of consistent void content averaging around a different value.

The presence of voids in the form of air bubbles influence the distribution of stress which induces stress concentration and subsequently become potential sites for local failure [197,203]. The initiation of micro-cracks from different voids enjoins to form macro-cracks which further propagate throughout a matrix. Further stress concentration leads to failure of the matrix [203]. This would explain how different specimens failed at different strains.

Compression experiments of fabricated Schwarz P unit cell-based tissue scaffolds also gave variances between different specimens. Considering that a Schwarz P unit cell consists of equivalent internal/external pore diameters measured in the horizontal and vertical directions, the aspect ratio for the parameter mentioned is equivalent to 1. However, previous investigations in the INNOVABONE project found that the aspect ratio of unit cells comprising the fabricated scaffolds were not equivalent to 1 [122]. This would thus imply differences in terms of pore size between the intended Schwarz P unit cell and unit cells comprising the scaffolds. The mechanical properties of a scaffold are dependent on the respective mechanical properties of the material used for their fabrication and the inherent pore structure [204]. The relationship between pore size and resulting mechanical properties of scaffolds have been investigated in previous literature. Porous structures fabricated from titanium with smaller pore sizes exhibited higher strength compared to that with larger pore sizes [205]. This complemented a study considering porous structure fabricated from nickel-titanium (NiTi) alloy consisting of different pore sizes. Results show that the compressive strength gradually decreased as the mean pore size increases [206]. Poly-ε-caprolactone-hydroxyapatite (PCL-HA) scaffolds have been fabricated via the conventional method of particulate leaching in which the porosity was varied in correlation to the porogen size and concentration used. Findings from the study showed that the mechanical property of the scaffold defined by

the Young's modulus was influenced by both porosity and pore sizes. The use of larger porogen sizes to subsequently give larger pore sizes in the fabricated scaffold resulted in reduction of Young's modulus [207]. Poly(lactic-co-glycolic-acid) (PLGA) scaffolds fabricated at different pore sizes via solvent casting/salt leaching showed that the compressive strength of scaffolds decreased with the increase in pore size [204]. Relating the findings relating pore size and mechanical properties to obtained stress-strain data of fabricated Schwarz P unit cell-based tissue scaffolds, it can be implied that each respective scaffold specimen consisted of different mean pore sizes which thus resulted in variances between different stress-strain data. It is observable that two specimens i.e. specimens 1 and 2 exhibited approximately consistent stress-strain data compared to the other specimens. Here it can be implied that the mean pore size for these two specimens are within a small range from each other.

Chapter 5

Computational Model

5.1 Introduction

The computer-aided design (CAD) surface geometry model of the Schwarz P unit cell has been established in Chapter 3. The material data required for computational analyses have been obtained and established in the previous chapter. The material data are used for two different types of analysis i.e. linear computational analyses and non-linear computational analysis; both involving the same computational approach of micromechanical analyses to characterise the mechanical properties of Schwarz P unit cell-based tissue scaffolds. This study firstly focuses on linear and non-linear computational analysis for mechanical characterisation in context of comparisons with results obtained through experimental mechanical characterisation of physical fabricated tissue scaffolds. In other words, mechanical characterisation of Schwarz P unit cell-based tissue scaffolds will be compared between the computational and experimental models. With this, the computational model will be validated against the experimental model before proceeding further into predictive modeling of Schwarz P unit cell designs in conjunction to their mechanical properties through linear analyses. The flowchart for the above is graphically presented in Figure 5-1.

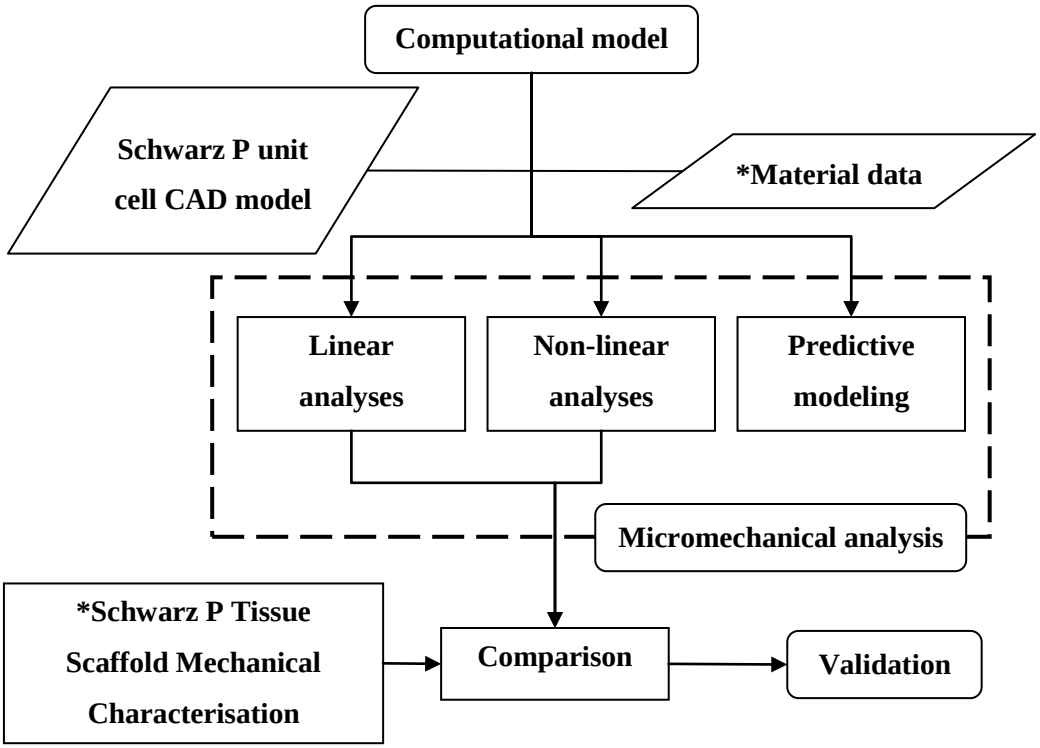

Figure 5-1 : Flowchart showing the involvement of different input into computational analyses. Micromechanical analysis is the computational approach considered to characterise the mechanical properties of Schwarz P unit cell-based tissue scaffolds. Results obtained from linear and non-linear analyses are compared and validated against results obtained from compression experiments of fabricated Schwarz P tissue scaffolds. Following validation, linear analyses can be further committed into predictive modeling with confidence. CAD models of the Schwarz P unit cell surface geometry and the material data are integrated as input for computational analyses. The required form of material data have been discussed in the previous chapter with respect to the type of analysis i.e. linear or non-linear.

The chapter is divided into three different sub-chapters. The first two sub-chapters investigates the implementation of micromechanical analysis to the Schwarz P unit cell design used as input for fabrication of physical tissue scaffold models in linear and non-linear analyses. Here, comparisons between results obtained from the implementation of the approach and the experimental results obtained in Chapter 4 are discussed. A section

in regards to a methodology to mediate discrepancies between the computational and experimental model will be also discussed. This methodology generally involves reconstructing the Schwarz P unit cell CAD model to take measurements of unit cells comprising the fabricated tissue scaffolds. A discussion in regards to revision on the derivations for micromechanical analysis to accommodate changes to the unit cell will subsequently be presented.

The third sub-chapter will be devoted to the implementation of micromechanical analysis in a predictive modeling of Schwarz P unit cell designs through linear analyses. The relationship between different dimensional parameters making up the Schwarz P unit cell architecture to the resulting mechanical properties will be discussed. With two different modeling control constraints i.e. Schwarz P structures with thickness variations at constant surface radius and Schwarz P structures with radius variations at constant thickness, only Schwarz P structures with thickness variations at constant surface radius will be considered.

5.2 Micromechanical Analysis

5.2.1 Background

Micromechanical analysis has its origins found in accounting the material behaviour of particle-reinforced composites. With advancements in the development of computing power, finite element methods have been adopted with micromechanical analysis to determine accurate distributions of stresses and strains in said composites. Considering the packing of particles within the matrix composite, its arrangement can be idealised as crystal packing systems. Based on these packing systems, its geometric symmetries can be exploited to determine a representative unit cell i.e. Voronoi cell. This allows the mechanical characterisation of a tissue scaffold with a periodic unit cell microstructure to be reduced to the analysis of a single representative unit cell through derivations of boundary conditions. Macroscopic loads can be applied along with the boundary conditions before evaluation of the effective properties of the structure in question. It shall be noted here that the term ‘effective modulus’ will be used to denote modulus values obtained through computational means. The effective modulus is therefore comparable to the stiffness i.e. compressive modulus values obtained in the experimental model.

This section will discuss the idealisation of the Schwarz P unit cell-based tissue scaffolds considered in this study as a crystal packing system. Derivations of boundary conditions for the selected crystal packing system will subsequently be made before discussing the methodology in its implementation to CAD models of Schwarz P unit cells. Validation methods to ensure correct implementation of boundary conditions will also be discussed. Two different computational approaches i.e. micromechanical analysis and homogenisation via finite element will be applied to a CAD model of the Schwarz P unit

cell for mechanical characterisation. Comparisons will be made between results obtained from both approaches to justify the integrity and validity of micromechanical analysis as an effective approach to characterising the mechanical properties of Schwarz P unit cell-based tissue scaffolds.

5.2.2 Selection for Crystal Packing System & Representative Unit Cell

During the fabrication process of Schwarz P unit cell-based tissue scaffolds via 2PP, a positioning stage moves in a 3-dimensional direction to produce an array of Schwarz P unit cells. Detailed discussion of the process has been described previously in Chapter 4. Scanning electron microscope (SEM) micrographs of the tissue scaffold are presented in Figure 5-2.

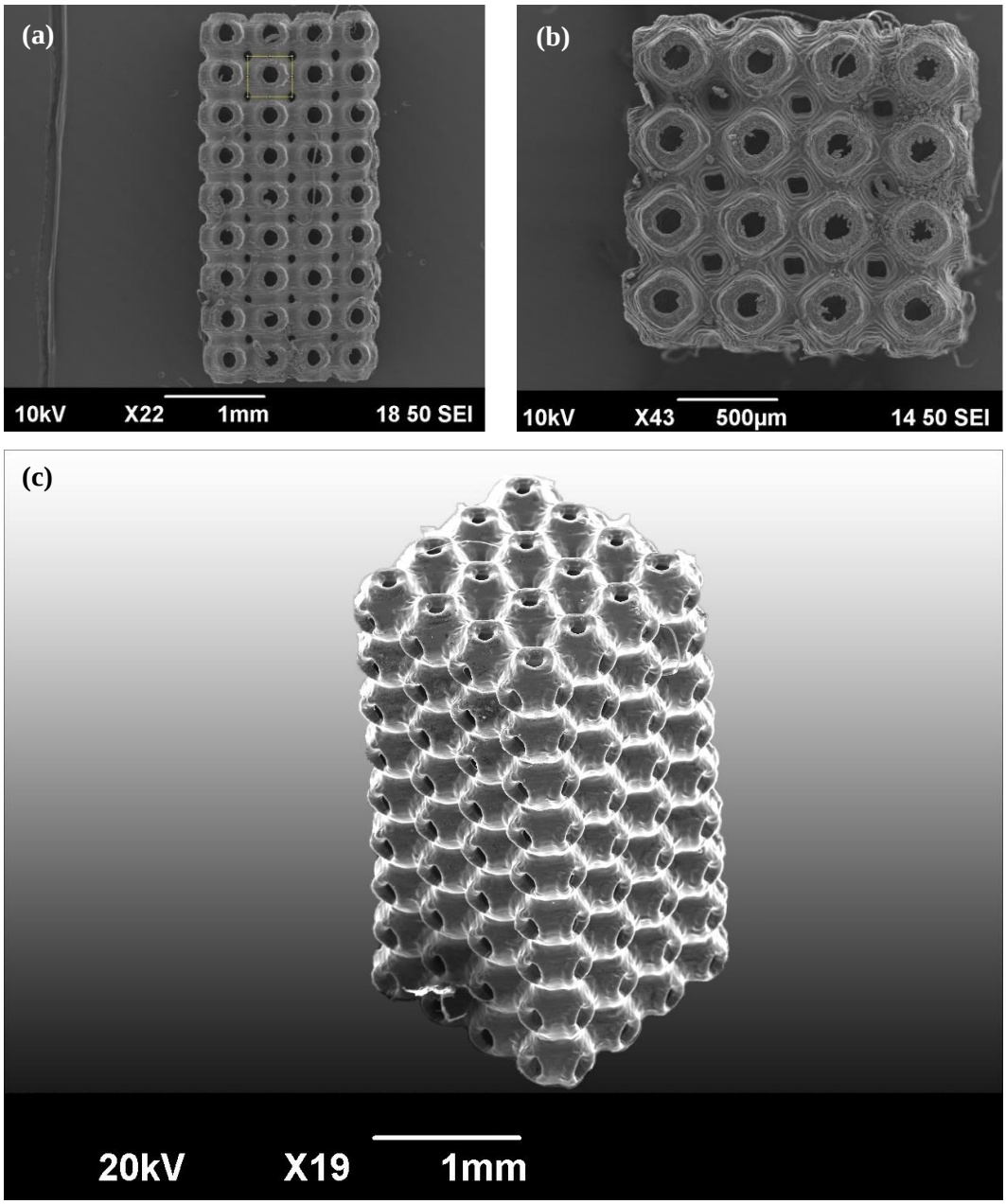

Figure 5-2 : SEM micrographs of fabricated physical tissue scaffolds. (a) Side view; (b) Top view; (c) General view.

A suitable packing system should reflect the arrangement of a representative unit cell to make up the periodic microstructure of the scaffold as a whole. Through Figure 5-2, it can be observed that a simple translation of a single Schwarz P unit cell in the x, y and z directions would give the scaffold structure. With the translational symmetries and taking

into account that a Schwarz P unit cell consists of equivalent height, width and length, the tissue scaffold can be represented as a simple cubic packing system with the Schwarz P unit cell itself as the representative unit cell.

5.2.3 Derivations for Simple Cubic Packing System

The translational symmetries exhibited in the structure of Schwarz P unit cell-based tissue scaffolds considered in this study can be represented by a simple cubic packing system with the Schwarz P unit cell itself as the representative unit cell. For brevity in presenting graphical representations in deriving the boundary conditions, the unit cell can and is represented by a simple cube as shown in Figure 5-3. Forming the packing system, the cube/unit cell is translated into a 3-dimensional array as shown in Figure 5-4. For clarity, Figure 5-4 can be compared to Figure 5-2(c).

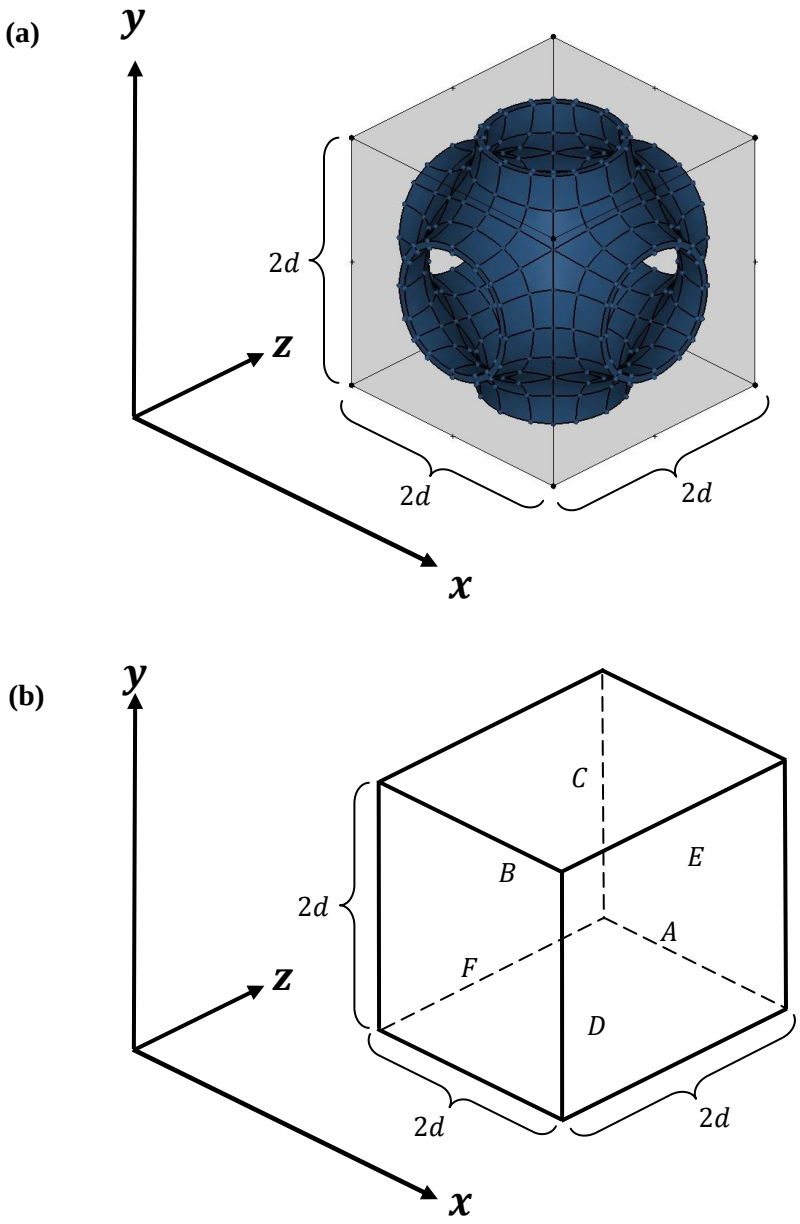

Figure 5-3 : Representation of the Schwarz P unit cell as a cube. (a) Schwarz P unit cell in an enclosed cube with the dimensions of 2d x 2d x 2d; (b) Cubic representation of the unit cell for the purpose of deriving boundary conditions.

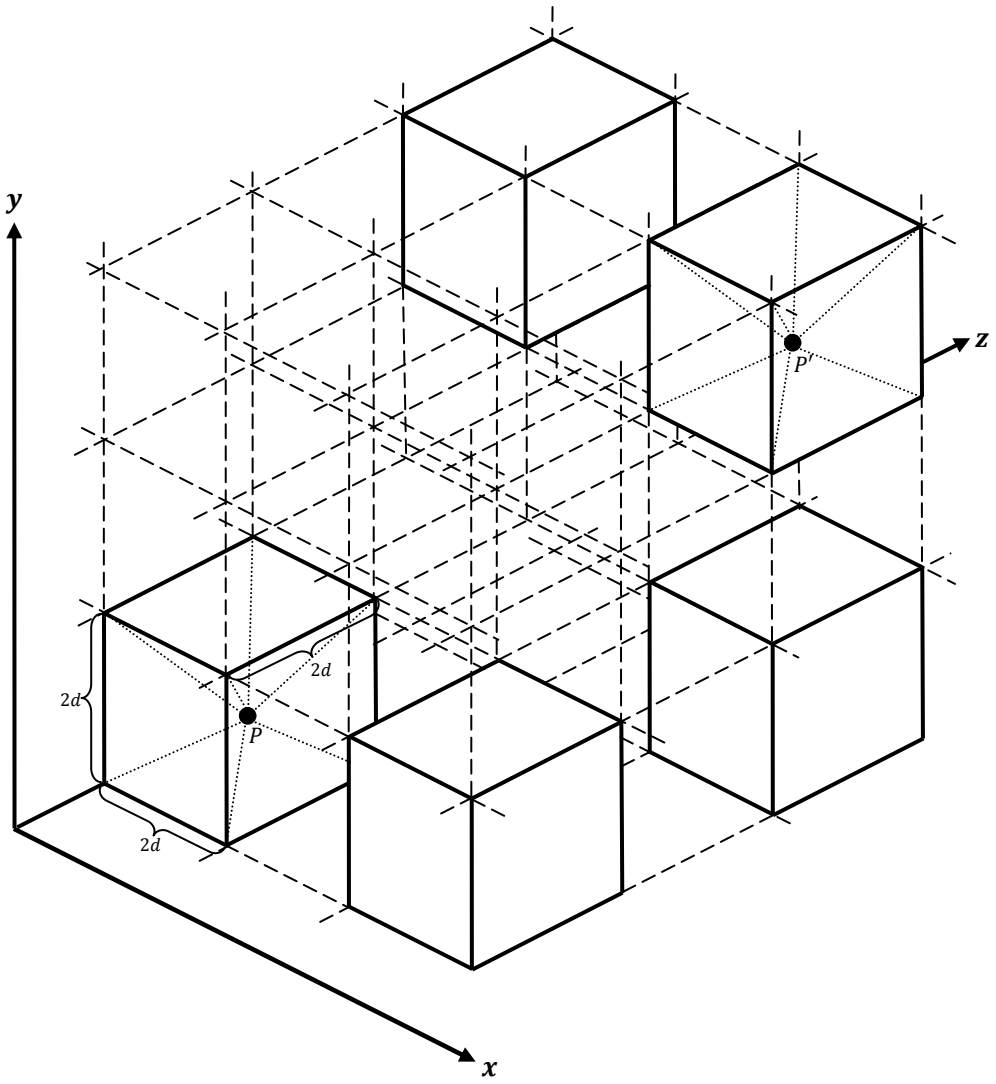

Figure 5-4 : Translation of the unit cell/cube represented in Figure 5-3 into a 3-dimensional array to form the tissue scaffold. The formation of the array would complement the array of unit cells comprising physical fabricated tissue scaffolds. This figure can be compared to the SEM micrograph of the fabricated tissue scaffold in Figure 5-2(c) for clarity.

Consider point P in a representative unit cell and its image, P' in another representative unit cell translated in a 3-dimensional direction as represented in Figure 5-4. The relationship between macroscopic strains and relative displacements can be expressed as shown in Equation (9).

$$u' - u = (x' - x)\varepsilon_x^0 + (y' - y)\gamma_{xy}^0 + (z' - z)\gamma_{xz}^0$$

$$v' - v = (y' - y)\varepsilon_y^0 + (z' - z)\gamma_{yz}^0$$

$$w' - w = (z' - z)\varepsilon_z^0 \quad (9)$$

for which,

x, y and z : Coordinates of point P

u, v and w : Displacements associated with point P

x', y' and z' : Coordinates of the point P'

u', v' and w' : Displacements associated with point P'

$\varepsilon_x^0, \varepsilon_y^0, \varepsilon_z^0$: Macroscopic strains

$\gamma_{yz}^0, \gamma_{xz}^0, \gamma_{xy}^0$: Macroscopic shear strains

The displacements of three rigid body translations are constrained to zero i.e. $u = v = w = 0$ at any arbitrary point away from faces and edges of a representative unit cell. To obtain the displacement fields in Equation (9), rotations of the x-axis about the y- and z-axes; and the y-axis about the x-axis are constrained as shown in Equation (10).

$$\frac{\partial w}{\partial x} = \frac{\partial v}{\partial x} = \frac{\partial w}{\partial y} = 0 \; at \; x = y = z = 0 \quad (10)$$

Equation (9) can then be implemented to derive the necessary boundary conditions. Considering Figure 5-4, point P' can be determined by translational symmetry transformations in a 3-dimensional direction as in Equation (11).

$$(x', y', z') = (x + 2id, y + 2jd, z + 2kd) \quad (11)$$

for which i, j and k are the number of representative unit cells in which P' is translated from P in the x, y and z directions respectively. Faces of the representative unit cells are paired by transformations tabulated as shown below in Table 5-1.

Table 5-1 : Equations defining the pairing between opposite faces of a representative unit cell.

Faces A and B	$x = d$ for face A	$x = -d$ for face B	$i = 1; j = k = 0$
Faces C and D	$y = d$ for face C	$y = -d$ for face D	$j = 1; i = k = 0$
Faces E and F	$z = d$ for face E	$z = -d$ for face F	$k = 1; i = j = 0$

Substituting the equations established in Table 5-1 into Equation (9), the displacement boundary conditions for each pair of faces as shown in Table 5-2 can be obtained.

Table 5-2 : Displacement boundary conditions for simple cubic packing system. With 6 different faces in a cubic representative unit cell, 3 different pairs of faces are obtained.

Pair faces	Displacement boundary conditions
A and B	$\lvert u_A - u_B \rvert_{y,z} = 2d\varepsilon_x^0$ $\lvert v_A - v_B \rvert_{y,z} = 0$ $\lvert w_A - w_B \rvert_{y,z} = 0$
C and D	$\lvert u_C - u_D \rvert_{x,z} = 2d\gamma_{xy}^0$ $\lvert v_C - v_D \rvert_{x,z} = 2d\varepsilon_y^0$ $\lvert w_C - w_D \rvert_{x,z} = 0$
E and F	$\lvert u_C - u_D \rvert_{x,z} = 2d\gamma_{xz}^0$ $\lvert v_C - v_D \rvert_{x,z} = 2d\gamma_{yz}^0$ $\lvert w_C - w_D \rvert_{x,z} = 2d\varepsilon_z^0$

The displacement boundary conditions tabulated in Table 5-2 are applied to nodes of the faces of the discretised Schwarz P unit cell model wherein the notations $|_{y,z}$, $|_{x,z}$ and $|_{x,y}$ indicate common directional axes of tessellated faces between each pair. The equations are independent for common tessellated nodes on the pairs of faces except for points along the edges shared by two faces. Therefore applying the boundary conditions on these edges will result in redundancy. An advantage to Schwarz P unit cells is that no two faces share a common edge. Hence, no further boundary conditions need to be established in regards to the edges and only the displacement boundary conditions for the faces are required for implementation of micromechanical analysis.

The macroscopic strains (ε_x^0, ε_y^0 and ε_z^0) and macroscopic shear strains (γ_{yz}^0, γ_{xz}^0 and γ_{xy}^0) contained in the displacement boundary conditions tabulated in Table 5-2 can each be treated as an independent degree of freedom [190,191]. These independent degrees of freedom can be prescribed to impose macroscopic strain. Macroscopic stresses can also be applied as an alternative through the application of concencentrated forces which are generalised as the product of force and length [189]. These forces are considered generalised as their energy conjugates are strains rather than displacements [191]. The relationship between the macroscopic stresses and the concentrated forces has been discussed in the literature review according to the principle of virtual work. Consider a generalised force, Q_x applied in the degree of freedom, ε_x^0 in the equivalency between the external and internal virtual work as a representative example. To prevent any confusion, the notations referring to the independent degree of freedom and macroscopic strain are used interchangeably. This follows in respect to the treatment of macroscopic strains and macroscopic shear strains as independent degrees of freedom [190,191].

$$\frac{1}{2}Q_x\varepsilon_x^0 = \frac{1}{2}\int_V \sigma_x^0\varepsilon_x^0\, dV$$

$$Q_x\varepsilon_x^0 = V\sigma_x^0\varepsilon_x^0$$

$$\sigma_x^0 = \frac{Q_x}{V}$$

Applying the above to the other independent degrees of freedom, the macroscopic stress and macroscopic shear stress can be determined as tabulated below. It shall be noted here that the generalised force are applied in accordance to its' denoted subscript which also corresponds to the independent degree of freedom in question.

Independent degree of freedom	**Macroscopic stress**
$\boldsymbol{\varepsilon_y^0}$	$\sigma_y^0 = \frac{Q_y}{V}$
$\boldsymbol{\varepsilon_z^0}$	$\sigma_z^0 = \frac{Q_z}{V}$

Independent degree of freedom	**Macroscopic shear stress**
$\boldsymbol{\gamma_{yz}^0}$	$\tau_{yz}^0 = \frac{Q_{yz}}{V}$
$\boldsymbol{\gamma_{xz}^0}$	$\tau_{zx}^0 = \frac{Q_{zx}}{V}$
$\boldsymbol{\gamma_{xy}^0}$	$\tau_{xy}^0 = \frac{Q_{xy}}{V}$

Through the expressions established, the relationships to obtain the effective properties can be determined as tabulated in the following.

Independent degree of freedom	**Effective properties**			
$\boldsymbol{\varepsilon_x^0}$	$E_x^0 = \frac{\sigma_x^0}{\varepsilon_x^0} = \frac{Q_x}{V\varepsilon_x^0}$	$v_{xy}^0 = -\frac{\varepsilon_y^0}{\varepsilon_x^0}$	$v_{xz}^0 = -\frac{\varepsilon_z^0}{\varepsilon_x^0}$	For $Q_y = Q_z = Q_{yz} = Q_{zx} = Q_{xy} = 0$

$\boldsymbol{\varepsilon_y^0}$	$E_y^0 = \frac{\sigma_y^0}{\varepsilon_y^0} = \frac{Q_y}{V\varepsilon_y^0}$	$v_{yx}^0 = -\frac{\varepsilon_x^0}{\varepsilon_y^0}$	$v_{yz}^0 = -\frac{\varepsilon_z^0}{\varepsilon_y^0}$	For $Q_x = Q_z = Q_{yz} = Q_{zx} = Q_{xy} = 0$
$\boldsymbol{\varepsilon_z^0}$	$E_z^0 = \frac{\sigma_z^0}{\varepsilon_z^0} = \frac{Q_z}{V\varepsilon_z^0}$	$v_{zx}^0 = -\frac{\varepsilon_x^0}{\varepsilon_z^0}$	$v_{zy}^0 = -\frac{\varepsilon_y^0}{\varepsilon_z^0}$	For $Q_x = Q_y = Q_{yz} = Q_{zx} = Q_{xy} = 0$
$\boldsymbol{\gamma_{yz}^0}$	$G_{yz}^0 = \frac{\tau_{yz}^0}{\gamma_{yz}^0} = \frac{Q_{yz}}{V\gamma_{yz}^0}$	For $Q_x = Q_y = Q_z = Q_{zx} = Q_{xy} = 0$		
$\boldsymbol{\gamma_{zx}^0}$	$G_{zx}^0 = \frac{\tau_{zx}^0}{\gamma_{zx}^0} = \frac{Q_{zx}}{V\gamma_{zx}^0}$	For $Q_x = Q_y = Q_z = Q_{yz} = Q_{xy} = 0$		
$\boldsymbol{\gamma_{xy}^0}$	$G_{xy}^0 = \frac{\tau_{xy}^0}{\gamma_{xy}^0} = \frac{Q_{xy}}{V\gamma_{xy}^0}$	For $Q_x = Q_y = Q_z = Q_{yz} = Q_{zx} = 0$		

5.2.4 Schwarz P Unit Cell Discretisation Methodology

As described in Sub-section 5.2.3, the displacement boundary conditions are applied to nodes of faces of the discretised Schwarz P unit cell model. In addition they are also applied in accordance to common directional axes for a particular pair tessellated faces. Therefore each node of one tessellated face needs to identify with a node on its opposite face through a common directional axes i.e. either $x = (f, 0,0)$, $y = (0, f, 0)$ or $z = (0,0, f)$ for f is the distance between two opposite faces. In the case of this study, the tessellated nodes on Face A should correspond with Face B along the x axis; the tessellated nodes on Face C should correspond with Face D along the y axis; and the tessellated nodes on Face E should correspond with Face F along the z axis.

A particular meshing procedure allowed the above to be achieved and is discussed in the following. It shall be noted here that in this study, the meshing of all unit cell models in regards to this procedure were performed through Altair Hyperworks 14.0 (Altair Engineering, Inc. Michigan, USA). The procedure generally involves meshing the faces first before meshing the remaining surfaces of the unit cell. A graphical presentation of the faces of a unit cell is indicated in white while the ‘remaining surfaces’ is indicated in blue as shown in Figure 5-5.

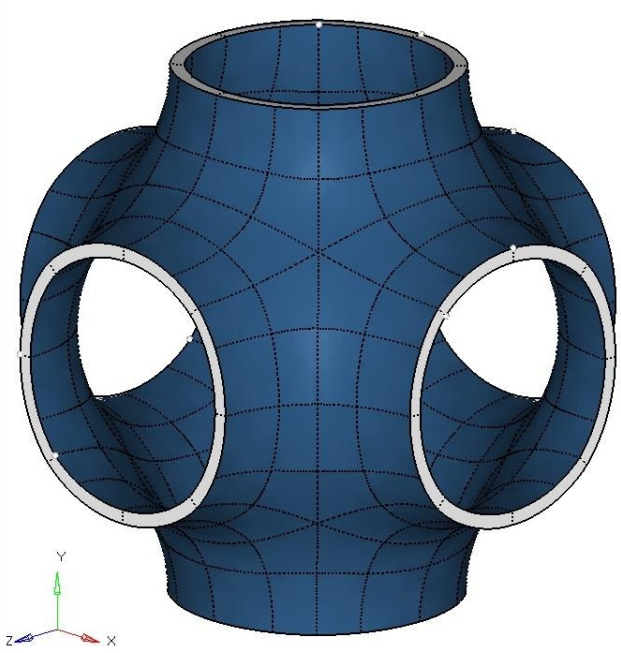

Figure 5-5 : Graphical presentation of the surfaces on a Schwarz P unit cell. The faces are indicated in white while the 'remaining surfaces' is indicated in blue. In all meshing procedures involved in this study, the faces (indicated in white) are discretised first before the remaining surfaces.

All the unit cell models involved in this study were discretised into second-order tetrahedral elements. Use of first-order tetrahedral elements would require discretisation with extremely fine meshes to obtain accurate results as they are usually overly stiff [208]. Using tetrahedral shaped elements simplifies the meshing procedure while also allowing surface curvatures to be captured more effectively in comparison to hexahedral elements.

In the procedure, a single face from a pair of faces is first meshed into ‘R-trias’ 2D elements. The ‘Translate’ utility under ‘Tools’ is then used by selecting the elements on the tessellated face to translate the elements to the un-tessellated opposite face at a distance equivalent to the distance between a pair of faces. With the height, width and length of the Schwarz P unit cell design being equivalent (as tabulated in Section 3.5 of

Chapter 3), the distance between a pair of faces is 0.52mm. A graphical presentation of the above is presented in Figure 5-6.

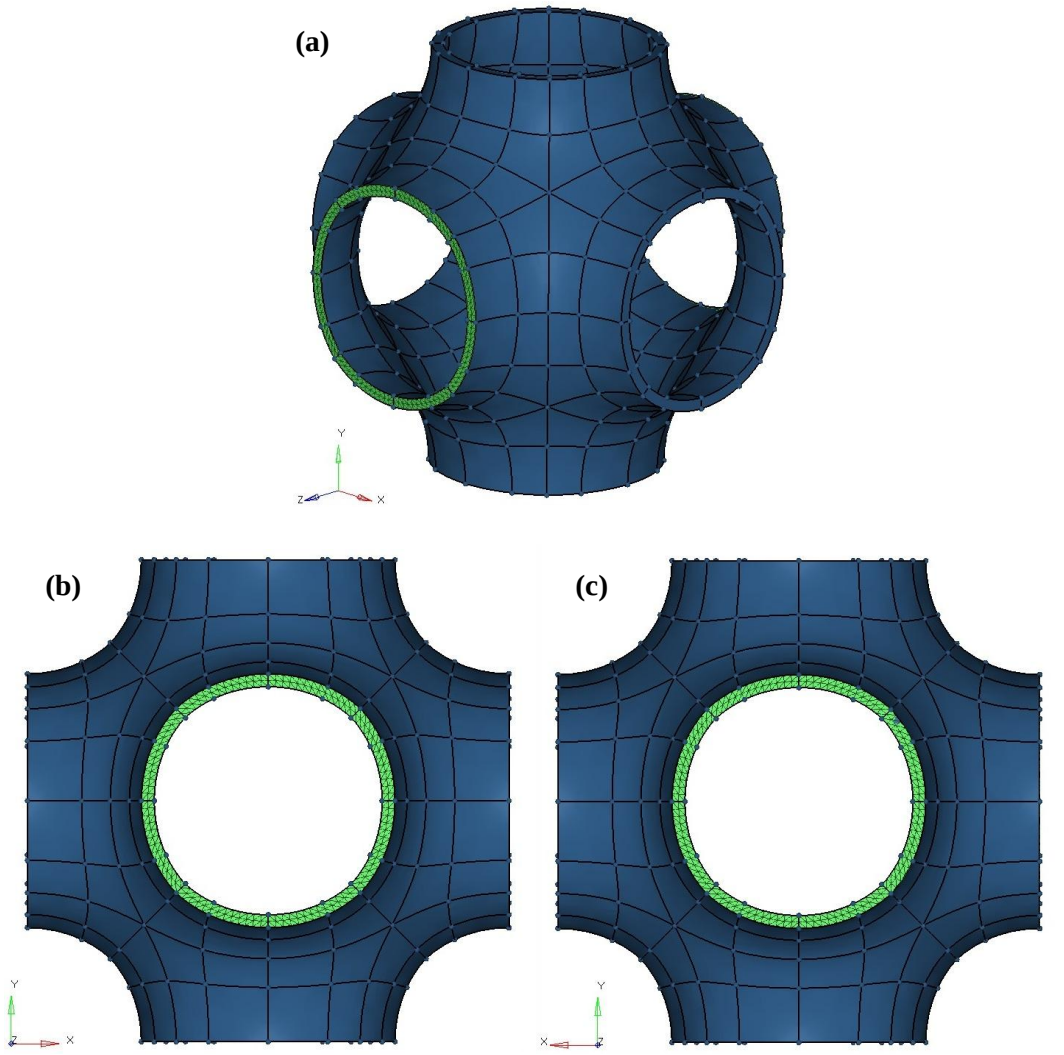

Figure 5-6 : 2D 'R-trias' meshing of a face lying along a common z-directional axis. (a) 2D mesh on a face to be translated to its opposite face; (b) Plane view of mesh to be translated; (c) Translated mesh on opposite face. Refer to reference axes on the bottom.

The same is done for the other 2 pairs of faces before subsequent 2D meshing of the remaining surfaces. The result of the meshing at this stage is graphically presented in Figure 5-7.

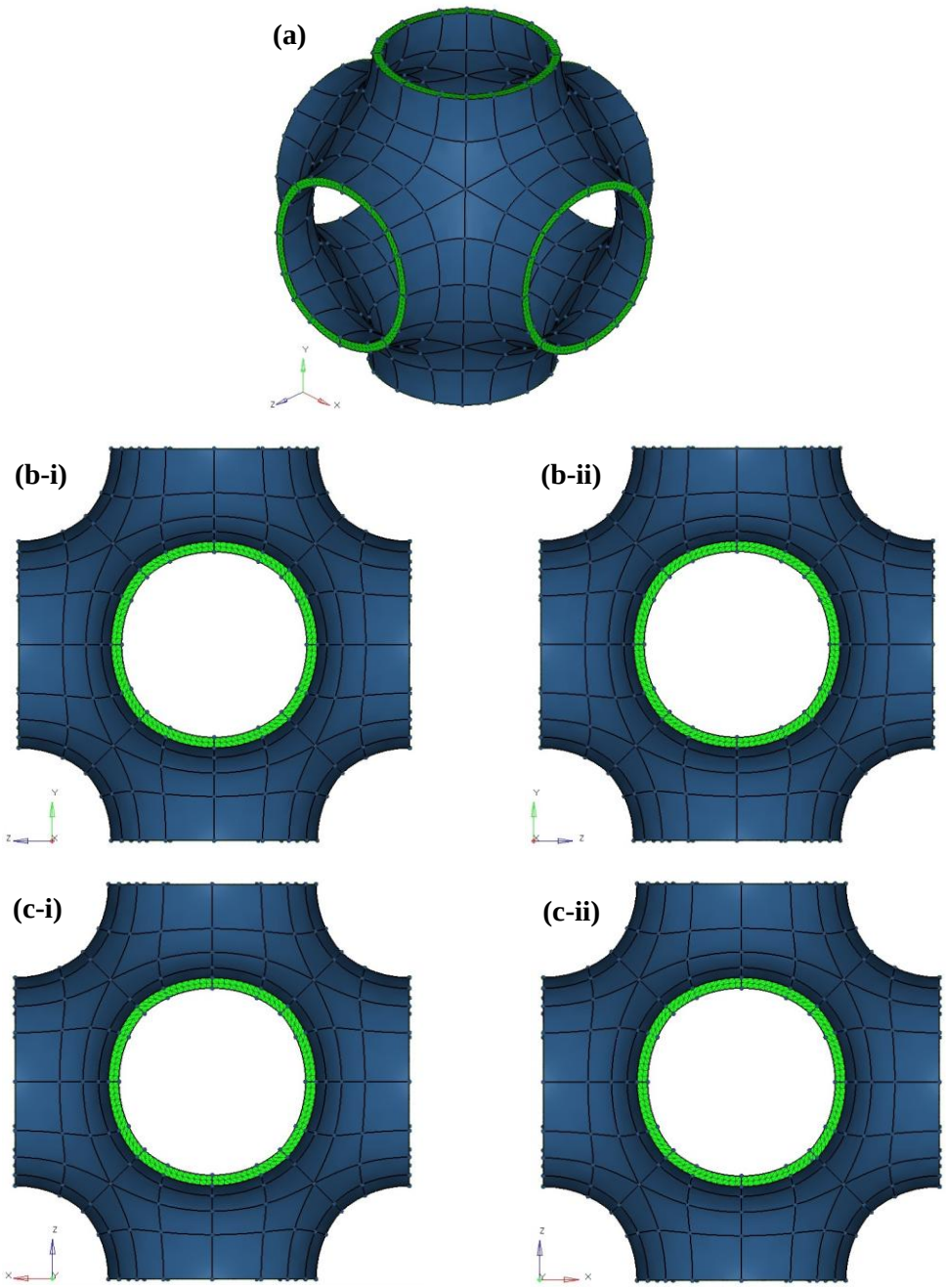

Figure 5-7 : 2D 'R-trias' meshing of a face lying along the remaining common directional axes i.e. x-axis and y-axis; (a) General view of meshed +x, +y and +z faces; (b-i) YZ plane view of a tessellated face on the +x axis; (b-ii) Plane view of tessellated face after translation of the tessellations in (b-i); (c-i) ZX plane view of a tessellated face on the +y axis; (c-ii) Plane view of tessellated face after translation of the tessellations in (c-i).

All of the 2D elements of the unit cell should and must be connected to each other at their vertices as these vertices form the nodes. To determine any disconnected elements, the meshed unit cell is checked for edges through the 'Edges' utility under 'Tool'. Presence of edges between the 2D meshed elements would indicate incorrect connections between elements and will be highlighted by the software. An example of this is presented in Figure 5-8.

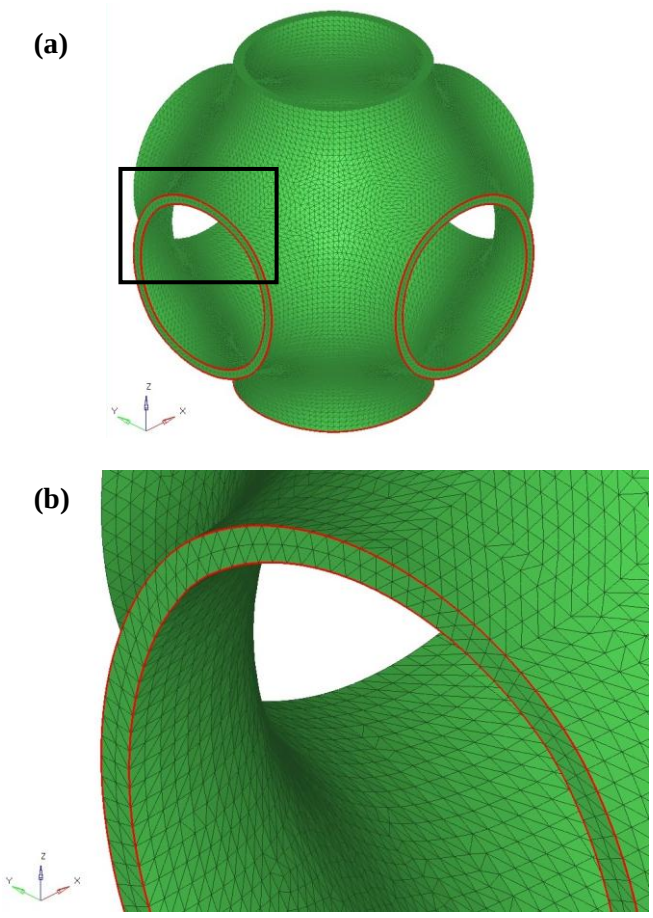

Figure 5-8 : Edges highlighted in red indicating disconnections between vertices of elements. It may be observed at user-level that the 2D elements are connected perfectly. However, the software detects inaccurate connections between elements in minute tolerances. (a) General view of edges present; (b) Close up view of edges within the confined black box.

Eliminating edges and subsequently correcting the connections between vertices of elements would require the use of the 'Equivalence' sub-utility located within the same utility. A tolerance value is chosen based on the length of an element before checking the presence of edges. If edges are still present, the tolerance value is continually increased until no edges are present. In extreme cases of incorrect connections between elements, an entire re-work of the mesh would be required. With the unit cell being fully enclosed with the meshes, a volumetric tetrahedral mesh can then be performed. This would give a unit cell that is discretised into 3-dimensional tetrahedral elements.

To determine whether the condition of each node on a particular face identifies exactly to its opposite face along a common directional axes, a custom algorithm was constructed in MATLAB. This custom algorithm pairs the nodes for each pair of faces and reports them in a comma-separated value (CSV) text file in accordance to the assigned face name i.e. A, B, C, D, E and F separately. This is a necessary crucial step as the node numbers are arranged in terms of their pairings for valid implementation of the displacement boundary conditions. For example, consider Face A and it's opposite Face B. If node numbers 120, 132, 158 and 142 on Face A identifies along the directional x-axis with node numbers 240, 221, 250 and 232 respectively on Face B, the outcome of the report should be as follows.

In the report for Face A:

120, 132, 158, 142, …

In the separate report for Face B:

240, 221, 250, 232, …

The discretised unit cell is then ready for material assignment as well as the implementation of necessary displacement boundary conditions for micromechanical analyses.

5.2.5 Input File

The derived displacement boundary conditions along with application of macroscopic load, descriptions of the model which include information in regards to model discretisation and assigned material model data needs to be compiled into a single file i.e. the input file for processing. In this study, constructing the input file consists of several generalised steps as shown in Figure 5-9.

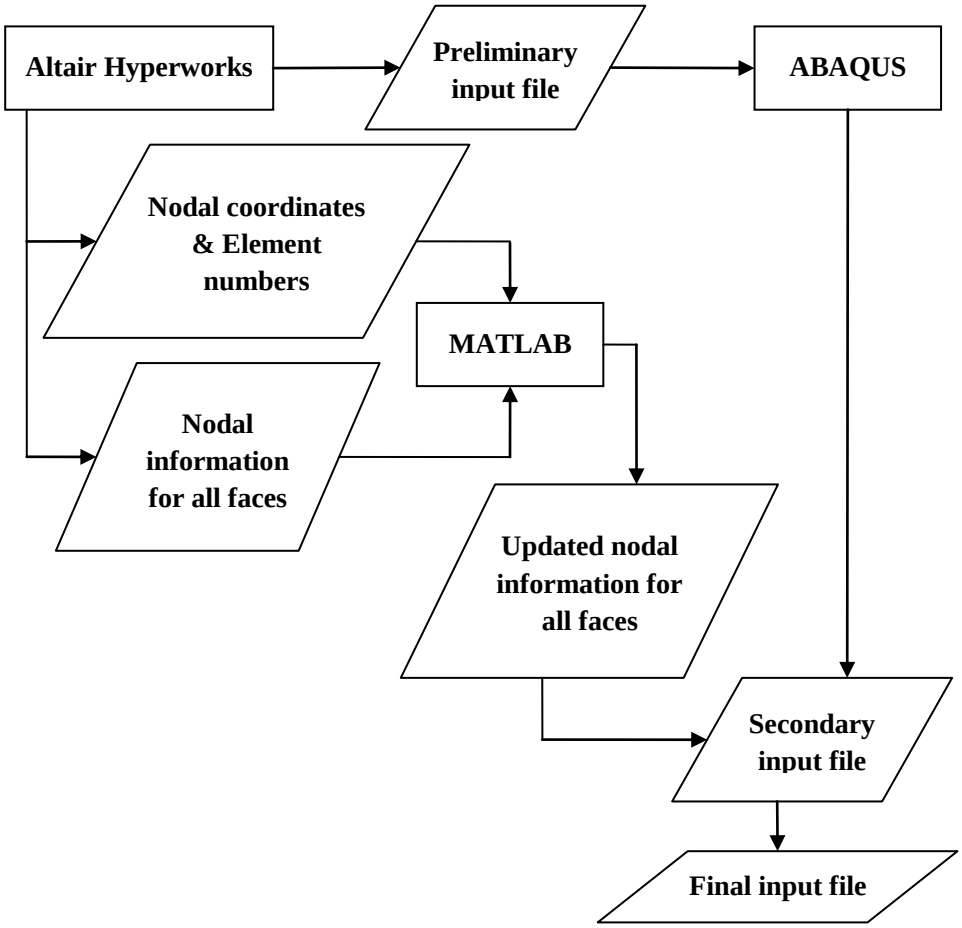

Figure 5-9 : Flowchart showing the processes in creating a final input file.

Eight different files are initially exported from Altair Hyperworks; 6 text files containing nodal set information in regards to each of the 6 discretised faces of the model, a text file containing information in regards to all the nodal coordinates and element numbers of the discretised model and a preliminary input file. The preliminary input file is imported into the software ABAQUS/CAE to allow the input file to be reformatted in a script that is standardised according to the software. The material data required for a particular analysis is input into the software before exporting a new input file i.e. secondary input file.

The text files containing information in regards to all the nodal coordinates and element numbers; and the nodal information for each discretised faces are implemented into a custom algorithm in MATLAB. As discussed in Sub-section 5.2.4, the custom algorithm pairs the nodes for each pair of opposite faces (A with B, C with D and E with F) to give updated nodal set information for each pair of faces.

Nodal set information in the secondary input file is then updated based on the nodal set information obtained from the custom algorithm. The displacement boundary conditions for micromechanical analysis and macroscopic load are manually edited into the secondary input file to be finalised and hence give the final input file. The final input file is then processed in ABAQUS/Standard before committing to post-processing to extract the results.

5.2.6 Validation Method for Correct Implementation of Displacement Boundary Conditions

Running the input ABAQUS file for micromechanical analysis, correct implementation of displacement boundary conditions to a representative unit cell should give periodic stress and strain distributions. A graphical presentation of this has been presented in Li et

al (2008) [189]. Extracting and compiling the results for average strain values obtained from micromechanical analysis at degree of freedoms ε_x^0, ε_y^0 and ε_z^0 should give symmetric values along the diagonal with approximately similar values within the diagonal as tabulated in Table 5-3. The same also applies for average shear strain values obtained from micromechanical analysis at degree of freedoms γ_{yz}^0, γ_{xz}^0 and γ_{xy}^0. However, values lying outside the diagonal can be approximated to zero due to their small values. A tabulated representation of this is presented in Table 5-4.

Table 5-3 : Tabulated representation of average strain values from micromechanical analyses to validate displacement boundary conditions established for a simple cubic packing system.

Degree of freedom of load/displacement application	**Average strain**		
	x	***y***	***z***
$\boldsymbol{\varepsilon_x^0}$	ε_1	ε_2	$\varepsilon_3(\approx \varepsilon_2)$
$\boldsymbol{\varepsilon_y^0}$	$\varepsilon_4(\approx \varepsilon_2 \approx \varepsilon_3)$	$\varepsilon_5(\approx \varepsilon_1)$	$\varepsilon_6(\approx \varepsilon_2 \approx \varepsilon_3)$
$\boldsymbol{\varepsilon_z^0}$	$\varepsilon_7(\approx \varepsilon_2 \approx \varepsilon_3)$	$\varepsilon_8(\approx \varepsilon_2 \approx \varepsilon_3)$	$\varepsilon_9(\approx \varepsilon_1)$

Table 5-4 : Tabulated representation of average shear strain values from micromechanical analyses to validate displacement boundary conditions established for a simple cubic packing system.

Degree of freedom of load/displacement application	**Average shear strain**		
	x	***y***	***z***
$\boldsymbol{\gamma_{yz}^0}$	γ_1	0	0
$\boldsymbol{\gamma_{xz}^0}$	0	$\gamma_2(\approx \gamma_1)$	0
$\boldsymbol{\gamma_{xy}^0}$	0	0	$\gamma_3(\approx \gamma_1)$

5.2.7 Justification for Approach

5.2.7.1 Micromechanical Analysis Vs. Homogenisation via Finite Elements

In justifying a computational approach to characterise the mechanical properties of Schwarz P unit cell-based tissue scaffolds, two different approaches which both implement the use of a representative volume element (interchangeable with the representative unit cell) will be used as a basis for comparison. These approaches are micromechanical analysis and homogenisation via the finite element method. The effect of mesh discretisation to the results obtained will be used as a point of reference for justification of a computational approach as they indicate the involvement of boundary effects. The methodology in implementing micromechanical analysis has been discussed in previous sub-sections. The approach for homogenisation via finite element including the required boundary conditions for implementation have been fully presented in depth in previous literature [183]. This approach involves applying strain to the top surface of a unit cell with the opposite bottom end constrained to a zero displacement boundary condition. The application for the homogenisation via finite element is described in Table 5-5 in conjunction to the aforementioned literature.

Table 5-5 : Tabulated parameters for the implementation of homogenisation via finite element to determine the effective modulus of the representative unit cell i.e. Schwarz P unit cell

Approach	Homogenisation via finite element
Geometry	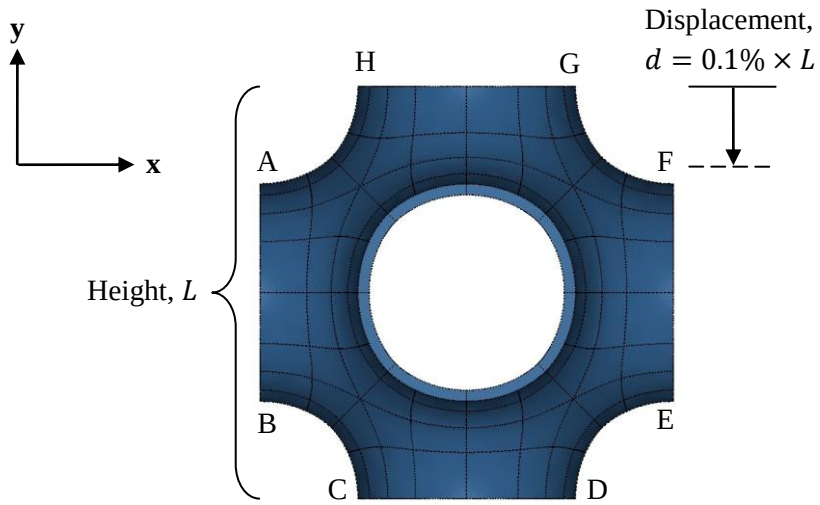
Material model	Young's modulus, E (taken from the range of those obtained from compression tests of bulk LCM3 Poisson's ratio, $v = 0.3$ Density, $\rho = 1.2$ g/cm^3 (1.2×10^{-9} tonnes/mm^3)
Analysis type	Elastic; 3D analysis
Displacement boundary conditions	Encastre ($U_x = U_y = U_z = U_{Rx} = U_{Ry} = U_{Rz} = 0$) specified on surfaces through planes CD Displacement of $0.1\% \times L$ in the negative Y-direction ($U_x = U_z = U_{Rx} = U_{Ry} = U_{Rz} = 0; U_y = -0.1\% \times L$) specified on surfaces through planes HG.
Applied loads	*Note : Loads are applied in the form of a displacement (as dictated in 'Dispalcement boundary conditions)

Simulation objective	To determine the reaction force obtained at the top surface area along the plane of HG of the unit cell. To determine the effective Young's modulus based on the values obtained.

To reduce complexity of the problem in justifying an approach, Schwarz P unit cells were implemented in linear analyses. Schwarz P unit cells were discretised with C3D10 elements at increasing levels of mesh refinement and assigned an isotropic, linearly elastic material model based on bulk material data for LCM3. This required material input data in the form of Young's modulus and Poisson's ratio. The Young's modulus was taken to take a value within the minimum to maximum range of modulus values obtained from compressions experiments of bulk LCM3 cylinders. This is to prevent confusion with the subsequent section which will consider comparisons between the experimental and computational model. The Poisson's ratio was taken to be 0.3. Justifying an approach is the main concern for this section. For each approach of micromechanical analyses and homogenisation via finite element, the same discretised unit cell model at a particular level of mesh refinement is used. The graphical representation in Figure 5-10 presents a discretised unit cell at one level of mesh refinement.

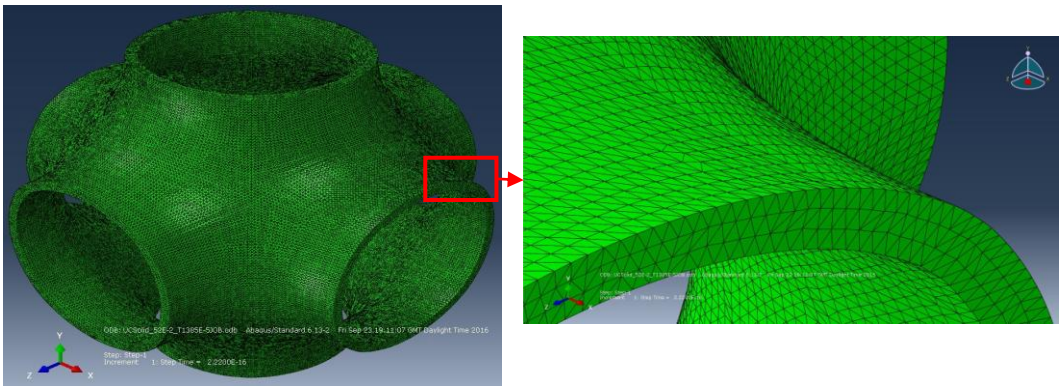

Figure 5-10 : Discretised Schwarz P unit cell model at one level of mesh refinement.

Results of the effective modulus at different levels of mesh refinement have been obtained from micromechanical analysis and homogenisation via finite element. This is graphically presented in Figure 5-11. A tabulated form of the results with specifications of the number of elements used for discretisation and the respective effective modulus results obtained in accordance to the two approaches are tabulated in Appendix B.1. The number of elements used for discretisation is indicative of the level of mesh refinement i.e. the higher the number of elements, the more fine the mesh.

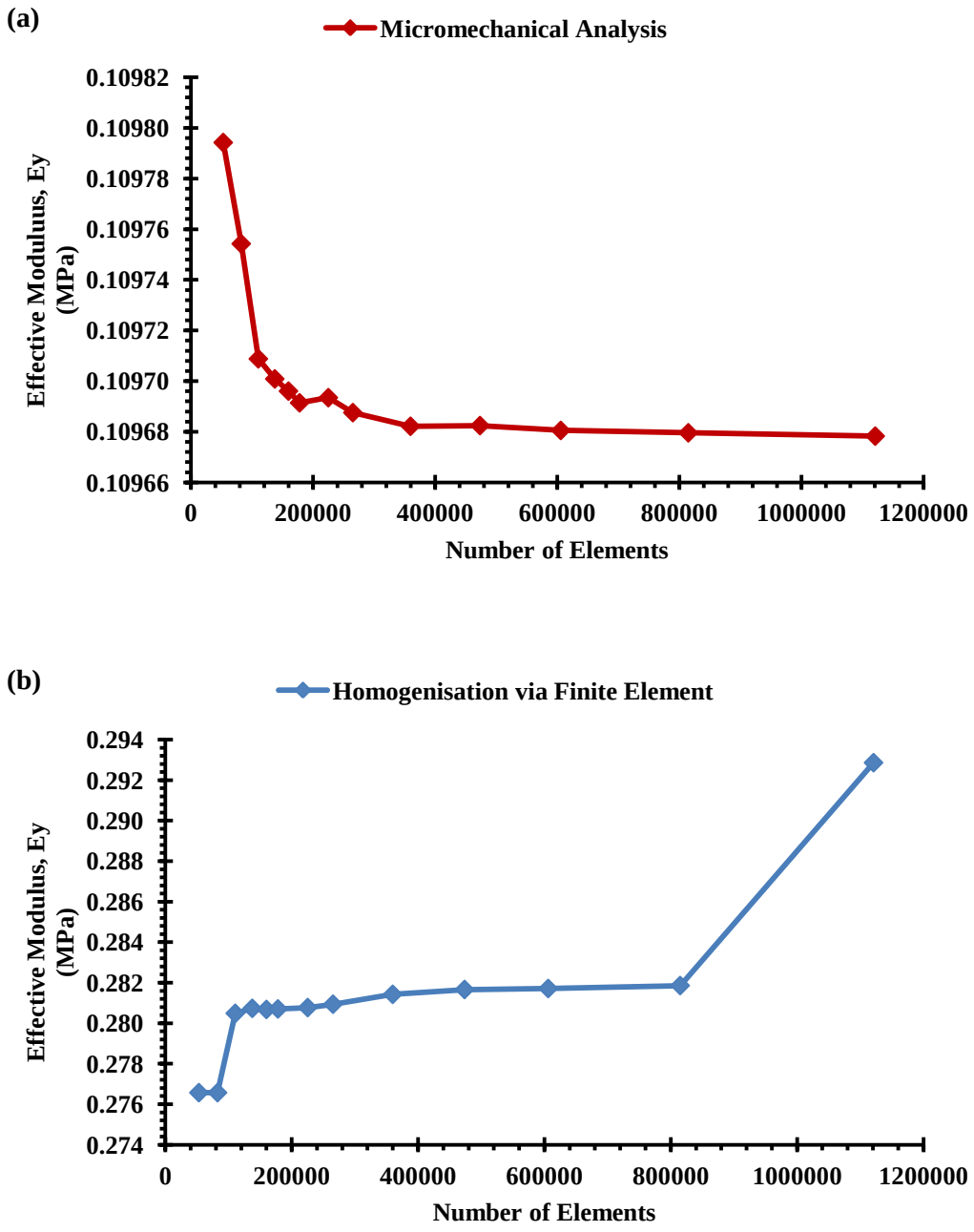

Figure 5-11 : Mesh analysis between effective modulus results obtained from (a) micromechanical analysis and (b) homogenisation via finite element; with increasing levels of mesh refinement. The level of mesh refinement is implied through the number of elements used for discretisation of Schwarz P unit cell. Effective modulus results obtained from micromechanical analysis became more stable with increasing number of elements used for discretisation. Effective modulus results obtained from

homogenisation via finite elements however gave step increases across the same range of number of elements.

Considering the results for micromechanical analysis, the effective modulus values became increasingly stable with increasing number of elements used to discretise the Schwarz P unit cell model. However when considering the modulus values to two significant figures throughout the range of number of elements, it can be observed that the effective modulus stabilises at 0.1097 ± 0.0001MPa.

Homogenisation via finite element gave step increases in terms of effective modulus values with no occurrence of stabilisation to any one particular value. Successive increase in the level of mesh refinement subsequently increases the number of discretised layers throughout cross-sectional thickness of the unit cell as shown in Figure 5-12. The number of layers throughout cross-sectional thickness with respect to the number of discretised elements is tabulated in Table 5-6. This subsequently results in increasing stiffness and therefore an increase in the effective modulus. This would also justify the need to implement a higher number of repeating unit of the representative unit cell and subsequently determine a converged stiffness as discussed in previous literature [183]. On the contrary, increasing the number of layers throughout cross-sectional thickness poses no problem for the alternative micromechanical analysis approach of characterising the mechanical properties of Schwarz P unit cells.

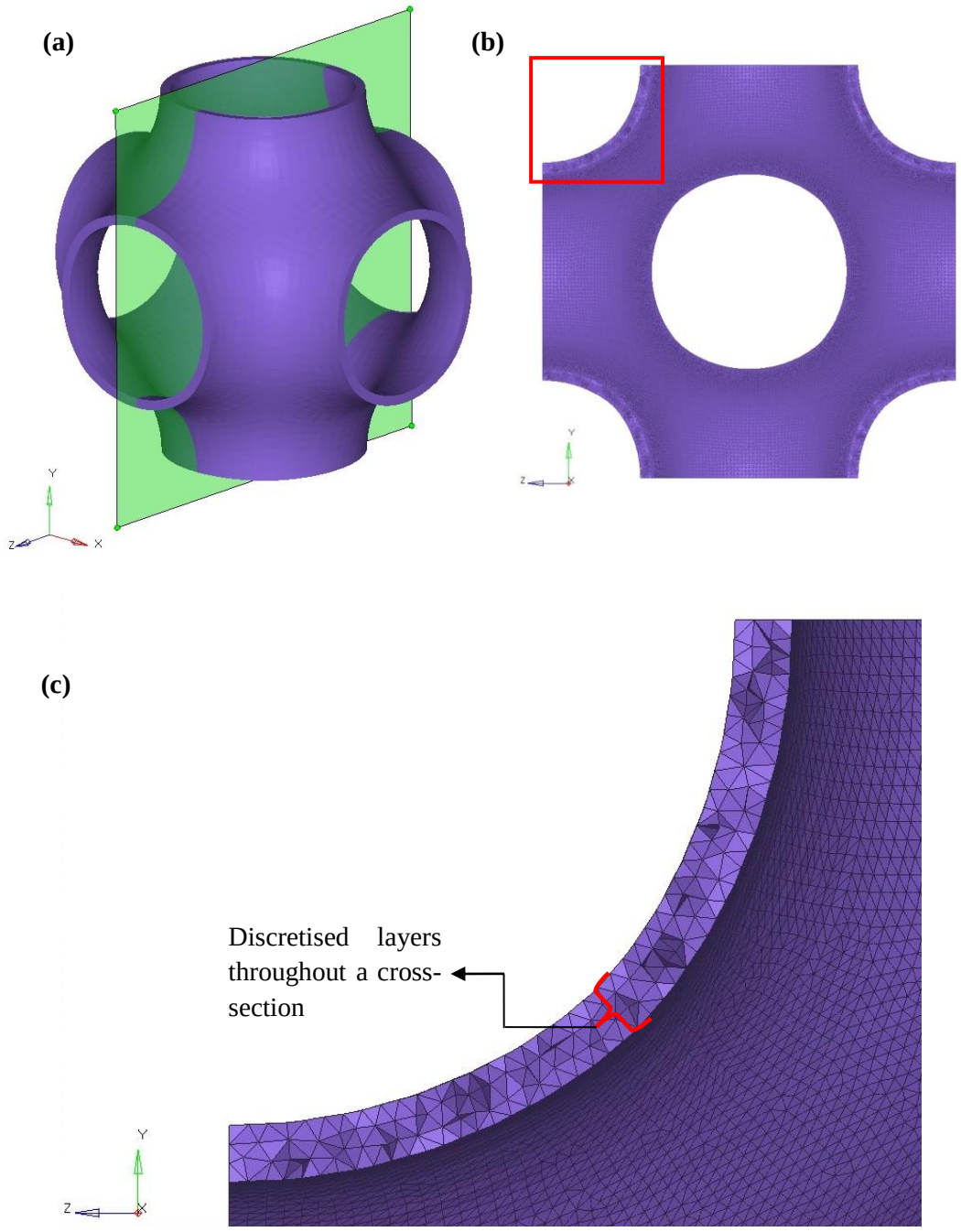

Figure 5-12 : Graphical presentation of the discretised layers throughout cross-sectional thickness. (a) Plane on the unit cell where a cross-scetion is made; (b) Cross-sectional slice at the plane shown previously in (a); (c) Discretised layers throughout cross-sectional thickness in the region bounded by the red box in (b).

Table 5-6 : Number of layers throughout cross-sectional thickness of discretised unit cell model with respect to the number of discretised elements.

Number of discretised elements, n_e	Number of layers
$n_e < 83{,}000$	1
$83{,}000 < n_e < 110{,}000$	Mixture of 1 and 2
$n_e > 110{,}000$	Mixture of 2 and 3

5.2.7.2 Validation for Displacement Boundary Conditions in Micromechanical Analysis

In the micromechanical analysis approach with displacement boundary conditions derived based around a simple cubic packing system, the obtained average strain and average shear strain values in the respective x, y and z directions should be the same. This would also give equivalent effective modulus values (corresponding to the average strain) and shear modulus (corresponding to the average shear strain) with respect to the 3 directions. The average strains and average shear strains obtained from micromechanical analyses of Schwarz P unit cells discretised with a total of 814,883 elements tabulated in Table 5-7 and Table 5-8 respectively as a representative example. The effective modulus and effective shear modulus with respect to the x, y and z directions are tabulated in Table 5-9. Periodic stress distributions should also be apparent in terms of stress contours on the unit cell. A graphical representation of this as load is applied in the x-direction is shown in Figure 5-13.

.

Table 5-7 : Average strain obtained from micromechanical analysis of a Schwarz P unit cell discretised with a total of 814,883 elements.

Degree of freedom of load application	Average strain (4 s.f.)		
	x	y	z
ε_x^0	0.03372	0.01410	0.01410
ε_y^0	0.01410	0.03372	0.01410
ε_z^0	0.01410	0.01410	0.03372

Table 5-8 : Average shear strain obtained from micromechanical analysis of a Schwarz P unit cell discretised with a total of 814,883 elements.

Degree of freedom of load application	Average shear strain (4 s.f.)		
	x	y	z
γ_{yz}^0	0.03166	1.215E-07 (≈ 0)	1.542E-07 (≈ 0)
γ_{xz}^0	1.215E-07 (≈ 0)	0.03166	3.815E-07 (≈ 0)
γ_{xy}^0	1.542E-07 (≈ 0)	3.815E-07 (≈ 0)	0.03166

Table 5-9 : Calculated effective modulus and effective shear modulus of a Schwarz P unit cell in the x, y and z directions. The effective modulus and effective shear modulus were determined using average strain and average shear strain results respectively in conjunction to the formulations discussed in 5.2.3.

Direction	Effective modulus (MPa)	Effective shear modulus (MPa)
x	0.1097	0.1168
y	0.1097	0.1168
z	0.1097	0.1168

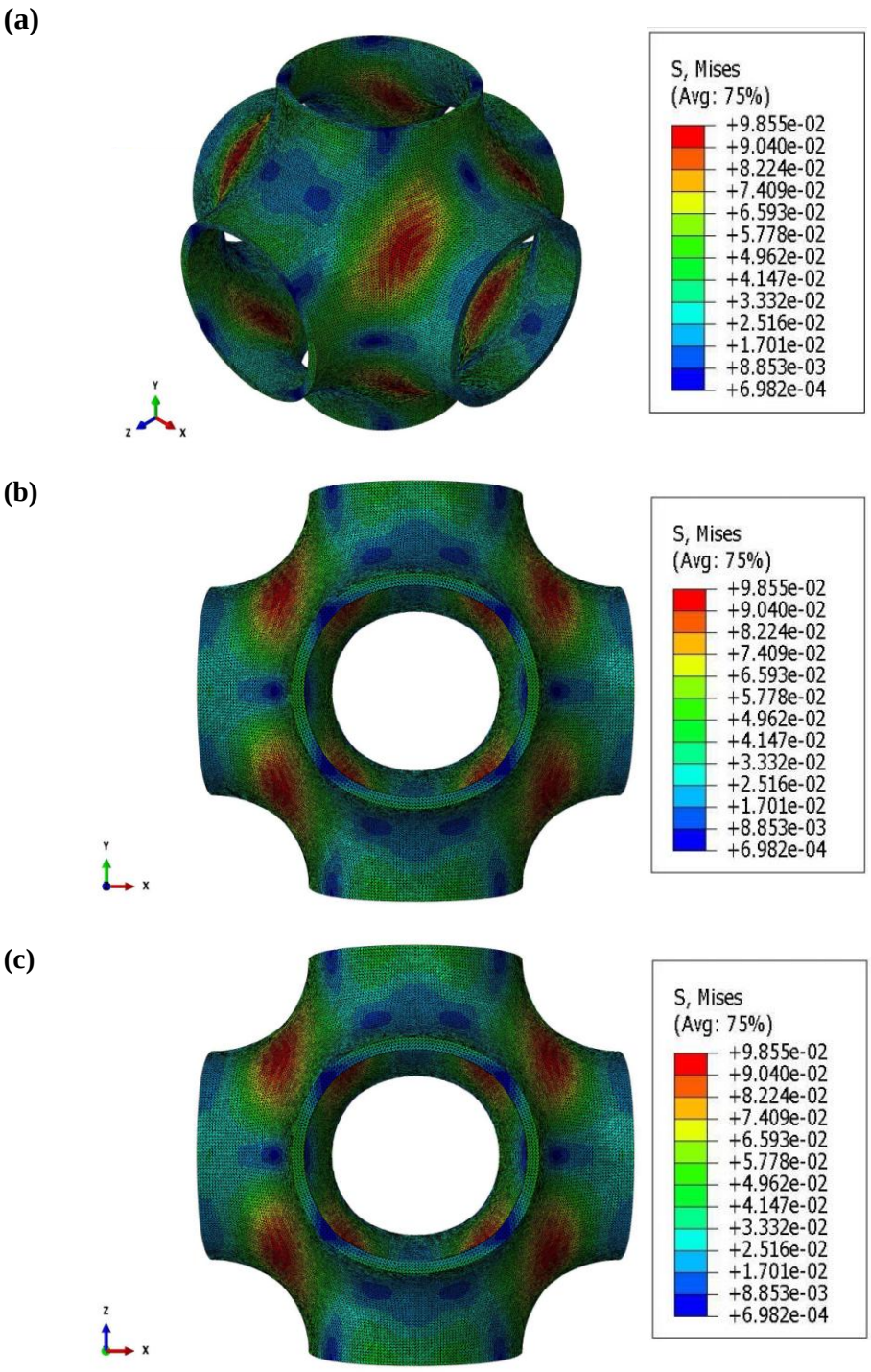

Figure 5-13 : Deformation of a Schwarz P unit cell showing periodic stress distributions after subsequent micromechanical analysis as load is applied in the x-direction; (a) General view; (b) YX plane view; (c) ZX plane view.

Based on validation methods discussed in Sub-section 5.2.6, the tabulated results for the average strain, average shear strain, the effective modulus and effective shear modulus along with the graphical presentations of periodic stress distributions under deformation after subsequent micromechanical analysis proves that the implemented displacement boundary conditions have been applied correctly. With the nature of approach that is able to reduce computational analysis of a periodic microstructure to the analysis of a single representative unit cell coupled with the capability to obtain stable effective modulus results across a wide range of mesh refinements, it stands to prove that micromechanical analysis is an efficient and justifiable approach to characterise the mechanical properties of Schwarz P unit cell-based tissue scaffolds.

Sub-Chapter 5A : Linear Analysis

5.3 Case I

5.3.1 Background

The implementation of micromechanical analysis as a suitable and efficient approach to characterise the mechanical properties of Schwarz P unit cell-based tissue scaffolds have been previously justified through comparisons made with the homogenisation via finite element approach. This sub-chapter discusses the implementation of micromechanical analysis to Schwarz P unit cells in a linear analysis in context of comparisons with experimental mechanical characterisation of physical fabricated tissue scaffolds discussed in Chapter 4. The discretisation of the unit cell and linear material model assigned to the unit cell will be discussed in regards to the analysis. With subsequent micromechanical analysis, the obtained results are compared to results obtained from experimental mechanical characterisation.

5.3.2 Schwarz P Unit Cell Discretisation

The Schwarz P unit cell CAD model was assumed to take a homogenous, isotropic and linearly elastic material model based on bulk material data for LCM3. Linear analyses require material input data in the form of Young's modulus and Poisson's ratio, both discussed in Chapter 4. Since compression experiments of bulk LCM3 cylinders gave discrepancies in terms of stress-strain curve among different samples, a lower, average and upper limit material data was used. Here, the Young's modulus for the lower limit (based on specimen 5), the average and the upper limit (based on specimen 3) were assigned to each discretised unit cell model for 3 separate analyses. The value of Poisson's ratio is taken to be 0.3. The unit cell model was discretised into second-order

tetrahedral C3D10 elements using the mesh discretisation methodology discussed in Sub-section 5.2.4 of Section 5.2. Information in regards to the discretised Schwarz P unit cell, the material model, the displacement boundary conditions for micromechanical analysis and the application of macroscopic load was compiled according to the methodology discussed in Sub-section 5.2.5 in the same section. The input file was process in a static, linear perturbation analysis through ABAQUS/Standard. The results obtained after subsequent processing is presented in the following sub-section.

5.3.3 Results

Micromechanical analysis of the Schwarz P unit cell model assigned with the 3 different material models of LCM3 gave results in terms of average strains and average shear strains. Based on the results, the effective modulus and effective shear modulus with respect to the x, y and z directions were determined and are tabulated in Table 5-10 respectively. The results for the average strains and average shear strains are tabulated in Appendix B.2.1.

Table 5-10 : Effective modulus and effective shear modulus values with respect to directional axes obtained from micromechanical analyses of discretised Schwarz P unit cell models assigned with 3 different LCM3 material models. Micromechanical analyses were performed in the context of linear analyses with the discretised unit cells being assigned linear material models of LCM3.

Material model	Direction	Effective modulus (MPa)	Effective shear modulus (MPa)
Specimen 5 (Lower limit)	***x***	0.0741	0.0789
	y	0.0741	0.0789
	z	0.0741	0.0789
Average	***x***	0.0968	0.1031
	y	0.0968	0.1031
	z	0.0968	0.1031
Specimen 3 (Upper limit)	***x***	0.1121	0.1194
	y	0.1121	0.1194
	z	0.1121	0.1194

As described in Section 5.2, micromechanical analysis allows the mechanical characterisation of a tissue scaffold macrostructure with a periodic unit cell microstructure to be reduced to the analysis of a single representative unit cell through derivations of boundary conditions. Therefore, results obtained from micromechanical analysis of that representative unit cell would effectively describe the mechanical characterisation of the tissue scaffold as a whole. A comparison of the effective modulus obtained from micromechanical analysis and the experimental modulus values obtained from compression experiments of Schwarz P unit cell-based tissue scaffolds are tabulated in Table 5-11.

Table 5-11 : Comparison of experimental modulus obtained from compression experiments of Schwarz P unit cell-based tissue scaffolds and the effective modulus obtained from micromechanical analyses. The standard deviation of the experimental modulus value represents the discrepancies between stiffness values among different fabricated tissue scaffold samples obtained from compression experiments. The standard deviation of the effective modulus is representative of different material models of LCM3 i.e. lower, averaged and upper limit assigned in linear analyses.

Model	**Modulus value (Mean ± Standard deviation) (MPa)**
Experimental	0.694 ± 0.293
Computational	0.0968 ± 0.0156

With the above, there is significant discrepancy between the experimental and computational modulus values obtained. The modulus value obtained through experimental compression experiments is significantly larger compared to that obtained from computational studies. The modulus value obtained from micromechanical analysis under-estimates the experimental modulus by 86.05%. Initial investigations under INNOVABONE have determined geometrical transformations in terms of different dimensional parameters for the fabricated Schwarz P unit cell-based tissue scaffolds [122]. This may explain the discrepancy found. A further investigation is thus required to mediate these geometrical transformations in order to establish the validity of the computational approach against experimental studies. The investigation will involve the implementation of scanning electron microscope (SEM) micrographs for measurement analyses of unit cells comprising the fabricated tissue scaffolds. A methodology to mediate the discrepancies by taking into account the geometrical transformations in terms of CAD modeling will also be discussed before proceeding with a revised linear analysis.

5.4 Schwarz P Unit Cell CAD Model Reconstruction

5.4.1 Background

Comparisons made between the experimental and computational modulus values showed significant discrepancy due to geometrical transformations from the input Schwarz P unit cell design to the output unit cells comprising the fabricated tissue scaffolds as implied by previous literature in regards to INNOVABONE [122]. This section investigates the geometrical transformations that occurred between the intended input Schwarz P unit cell design and the resulting unit cells comprising the physical tissue scaffolds fabricated via two-photon polymerisation (2PP). The methodology in performing the scans for SEM micrographs followed by methodology in making measurements pertaining to unit cells comprising the scaffolds will be discussed. It shall be noted here that due to the nanoscale size and soft nature of the samples, it was not possible to make cross-sectional cuts without any accidental perturbations to the original structure. Therefore, measurements were restricted to observable unit cells on the external sides of the sample.

A sub-section will also be dedicated to present the methodology in mediating the geometrical transformations in terms of CAD modeling to obtain a surface geometry CAD model that approximately represents the unit cells comprising the physical fabricated tissue scaffolds. Re-implementation of the CAD model with micromechanical analysis would therefore give a more accurate representation in comparison to the mechanical characterisation of Schwarz P unit cell-based tissue scaffolds performed experimentally.

5.4.2 Scanning Electron Microscope (SEM) Microscopy

In preparing the physical tissue scaffold for SEM, the scaffold sample was coated with platinum using a Polaron SC7640 coater (Quorum Technologies, UK) at 2.2kV for 90s. The platinum coating gives the surface of the scaffold sample an extra 10μm of thickness. A JEOL JSM-6490LV SEM microscope was then used to image the top and side surfaces of the samples.

In performing the scans, scaffold samples were laid flat on a plate before being placed in the machine. The perspective view of the scaffold as it is laid flat was indicated as the XY-axis. After subsequent scanning, the sample was taken out and carefully rotated to its side. The view perspective of the scaffold after this rotation was indicated as the YZ-axis. Differentiating the observable surface structure of the scaffold before and after rotation can be misconstrued as being similar. Therefore, care was taken into rotating the samples. After subsequent scanning for view of the YZ-axis, the sample was taken out and rotated height-wise for view of the top surface. This view perspective was then indicated as the XZ-axis. Each axis was nominated a dimensional parameter (i.e. height, width or length) to be referenced for a particular measurement. The directional axes and their respective dimensional parameter they represent based on view perspective of the SEM micrographs described above are tabulated in Table 5-12.

Table 5-12 : Reference for plane axes and representative dimensional parameter based on view perspectives during the scanning procedure for SEM.

Plane axes	SEM micrograph	Dimensional parameter
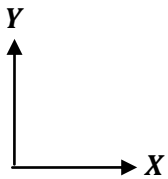	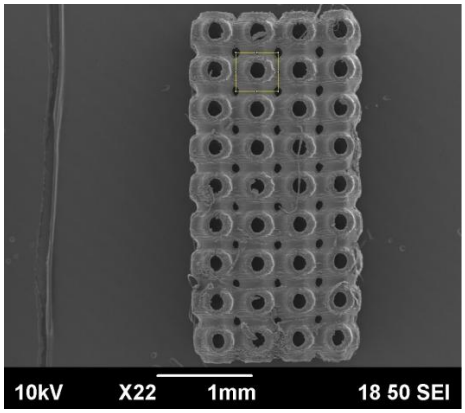	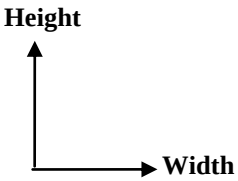
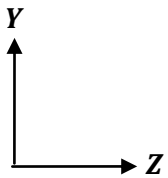	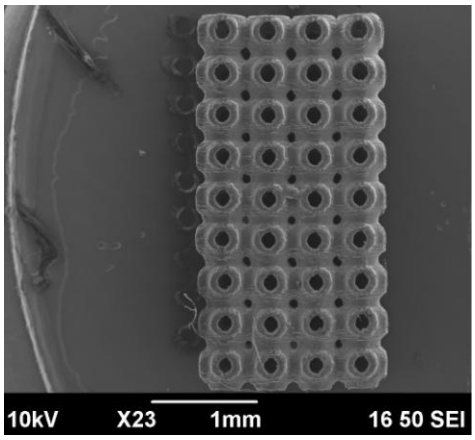	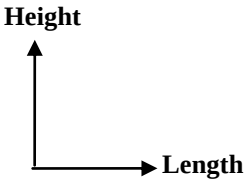
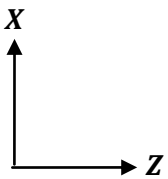	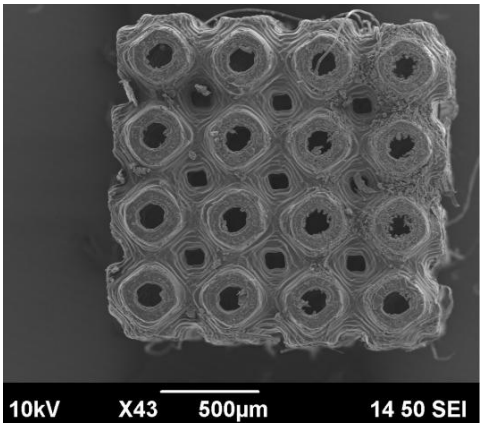	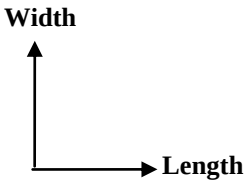

5.4.3 Schwarz P Unit Cell SEM Measurement Analysis Methodology

The SEM micrographs were implemented for use in an averaging technique to obtain a micrograph (respective of different view perspectives) containing an average of all observable unit cells. This mainly involves utilising tools within the software ImageJ (National Institute of Health, USA). Since measurements made from the software are given in terms of 'width' and 'height', it shall be noted here that any mention pertaining to results obtained from the measurements in terms of 'width' would imply a horizontal axial direction; and 'height' would imply a vertical axial direction in accordance to the plane view being considered. As such, these axial directions would imply the dimensional parameters charted in Table 5-12 with respect to the plane axes being considered.

Through ImageJ, a particular SEM micrograph is 'cut' into different observable unit cells. Rectangular selections are constructed to define boundaries of a particular unit cell. In defining the boundaries between two adjacent unit cells, a 'dip' should be observed to be marked as a point in forming a boundary. Consider two observable unit cells on an SEM micrograph of the tissue scaffolds viewed in the XY-plane perspective as a representative example as shown in Figure 5-14.

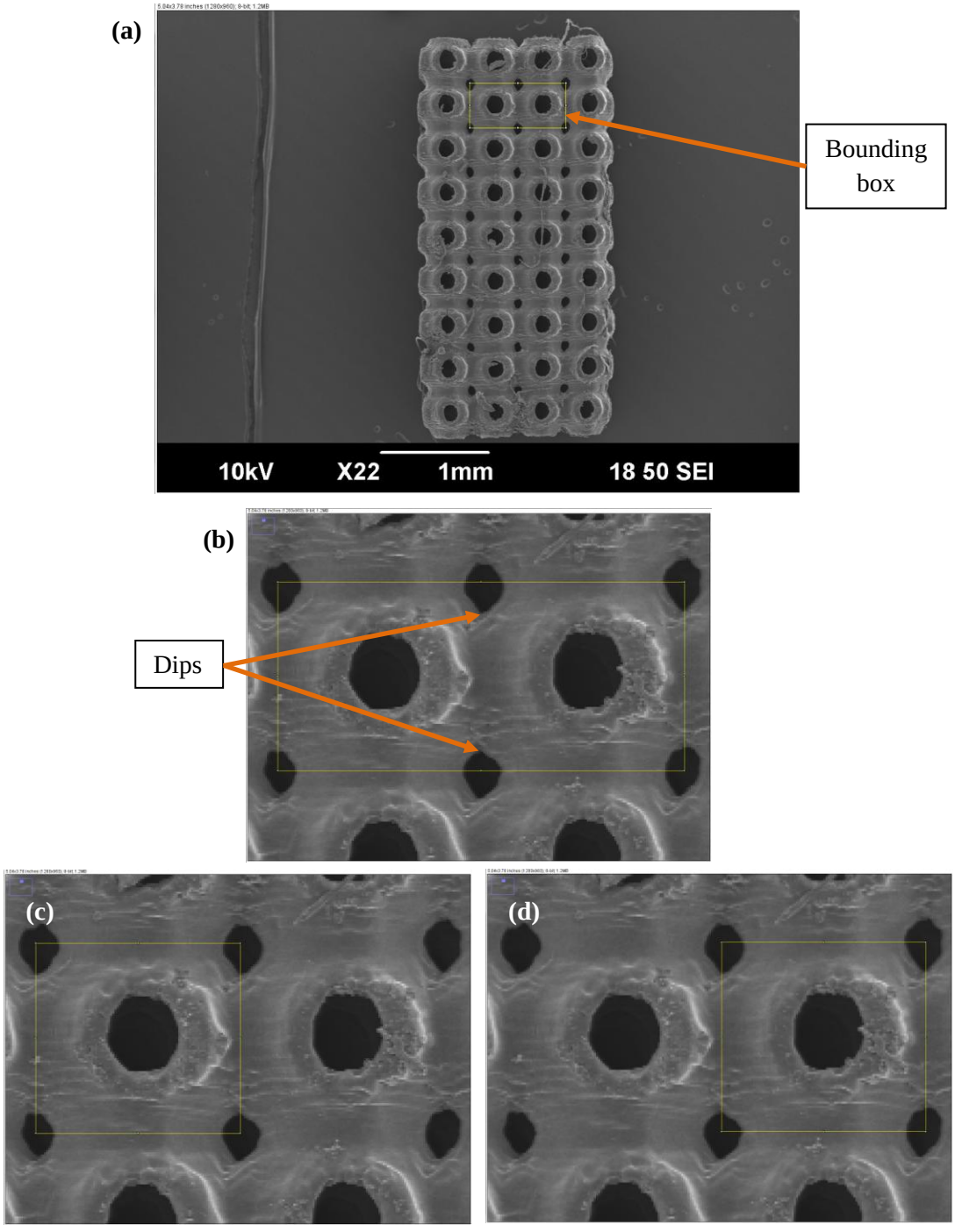

Figure 5-14 : Boundary construction between two adjacent unit cells. (a) Consideration of two unit cells in a SEM micrograph of the tissue scaffold viewed in the XY-plane perspective; (b) Magnified view of the unit cells and observation for 'dips' as marker points for boundaries; (c) & (d) Rectangular selection for unit cells considered in (a).

The selection made can then be copied into a separate graphic file i.e. JPEG without any changes in scale of resolution. The scale displayed with the SEM micrograph was also cropped into a separate graphic file to be used later. This process would give a collection of graphic files of unit cell micrographs making up the tissue scaffold in a particular view perspective. An example of 4 unit cells cropped into separate graphic files from an SEM micrograph of the tissue scaffold sample viewed in the XY-plane is shown in Figure 5-15.

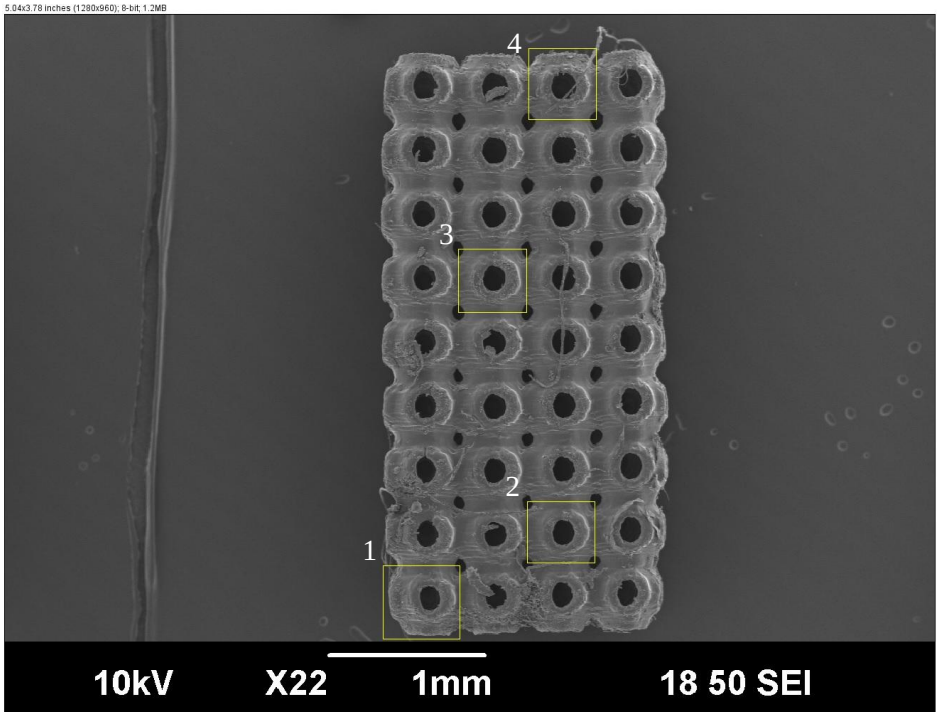

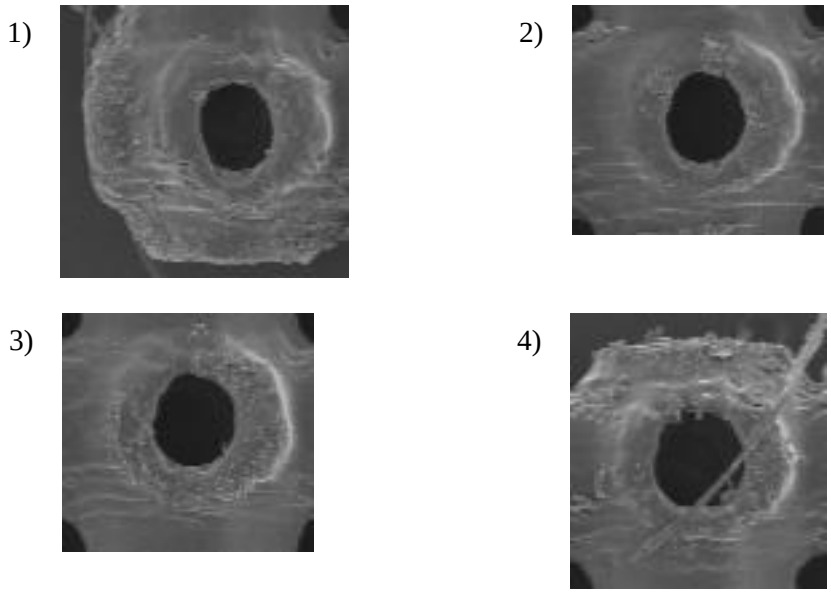

Figure 5-15 : Unit cell micrographs cropped into separate graphic files from the SEM of a whole tissue scaffold viewed in the XY-plane. The label numberings of the unit cell micrographs identify with its respective numbering in the SEM for the whole tissue scaffold.

Averaging the collection of SEM micrographs require a common point from which the micrographs can be ‘stacked’. This is taken to be the center point of the pore of each unit cell. Each unit cell micrograph underwent threshold to obtain a ‘mask’ that would enable the internal diameter of the pore throat to be observed. This was done by adjusting the value cutoff on the produced histogram given by ImageJ. The boundary of the internal diameter can subsequently be automatically traced using the ‘Wand Tool’ by making a selection within the bounded area. The center point of the pore formed by the boundary is then determined and recorded. This process is performed for every unit cell micrograph. An example of thresholding to obtain a ‘mask’ and subsequent tracing of the boundary of the internal pore diameter for unit cell number 3 (in Figure 5-15) is shown in Figure 5-16. The determination of the center point based on said boundary is also shown in the same figure.

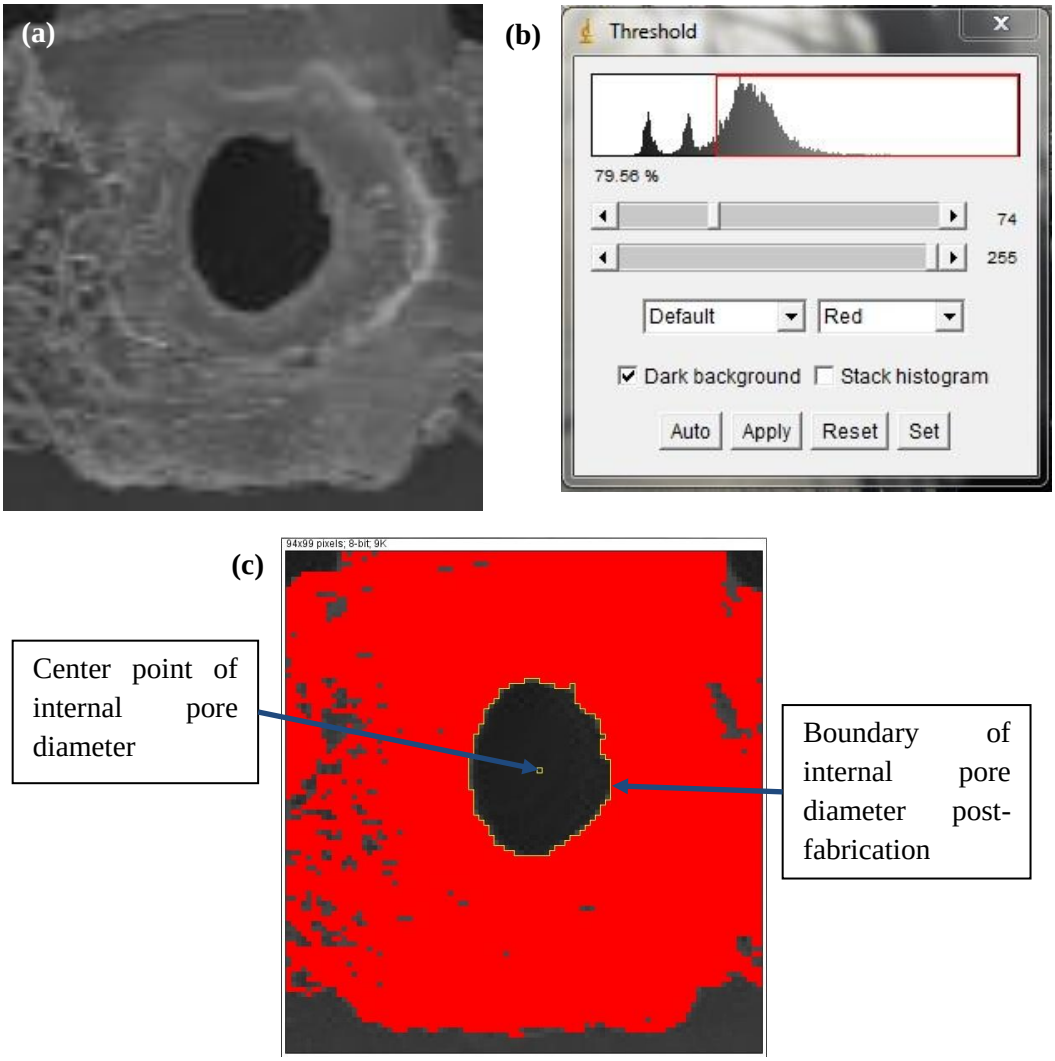

Figure 5-16 : Thresholding of unit cell number 3 (in Figure 5-15); (a) SEM micrograph of unit cell number 3; (b) Histogram produced by ImageJ with the selection of cutoff point; (c) 'Mask' of unit cell 3 after thresholding. The yellow line around the boundary of the internal diameter indicates the tracing done by ImageJ. The center point is plotted after its determination by the software.

With variances in the image dimensions of each unit cell micrograph, a custom Python algorithm was implemented to transpose the micrographs on a blank black canvas. The black canvas was created with a dimension large enough to cover the dimension of every unit cell micrograph. The custom algorithm transposes the center point within the internal

pore diameter obtained previously to the center of the blank canvas before subsequently being saved as a new and separate graphic file. An example for the above is shown using unit cell number 3 in Figure 5-17. The algorithm is appended in Appendix B.3.1.

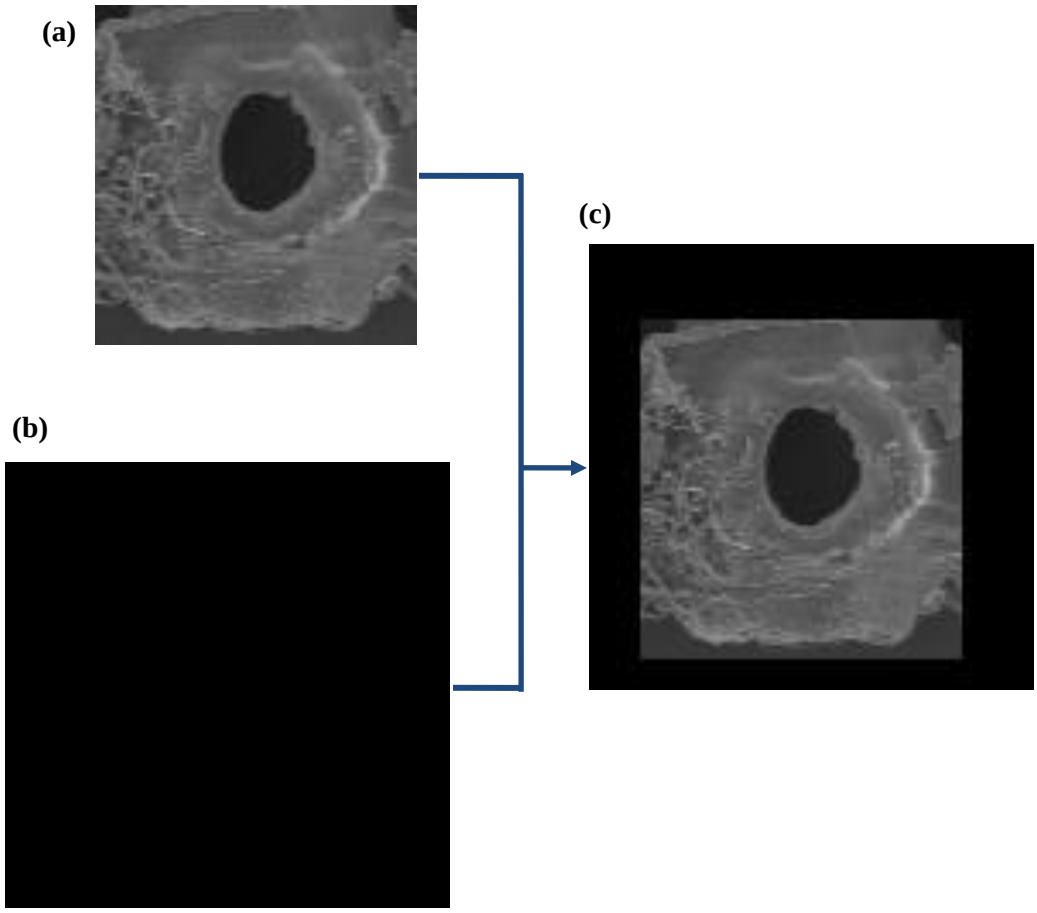

Figure 5-17 : Obtained micrograph after transposition of the center point of unit cell 3 on to the center of a blank black canvas; (a) Micrograph of unit cell 3; (b) Blank black canvas; (c) Micrograph after implementation of custom algorithm.

A different custom Python algorithm was then used to average the collection of unit cell micrographs with black backgrounds. The output of the algorithm is an averaged unit cell

micrograph attached with the scale of the original SEM micrograph of the tissue scaffold cropped initially as shown in Figure 5-18. This algorithm is appended in Appendix B.3.2.

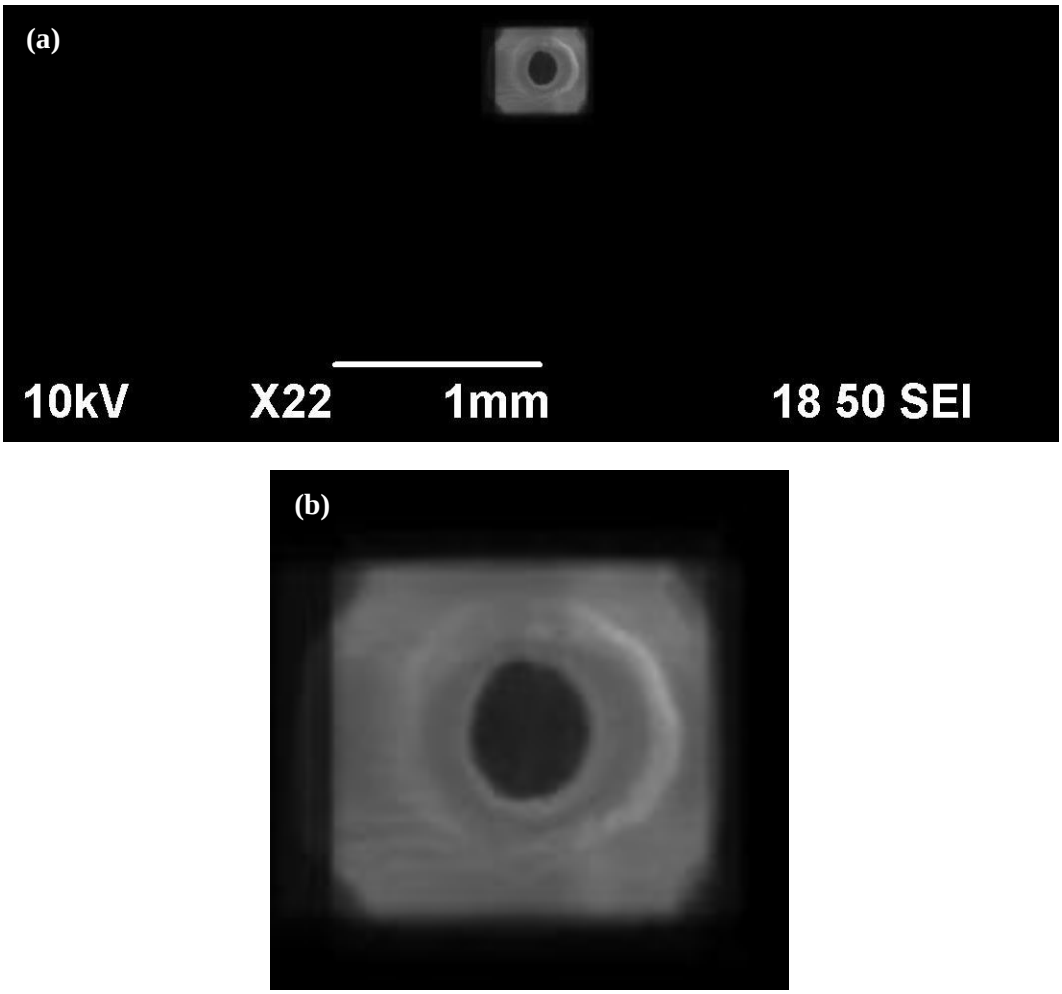

Figure 5-18 : Averaged unit cell micrograph obtained after implementation of custom Python algorithm. The algorithm averages the collection of unit cell micrographs that have been transposed on to a blank canvas obtained through the previous discussed algorithm. (a) Averaged unit cell micrograph with scale; (b) Magnified view of the averaged unit cell micrograph.

The average unit cell micrograph underwent thresholding to obtain a 'mask' that would define the boundaries of the unit cell as well as the internal pore diameter. This is shown in Figure 5-19.

(a)

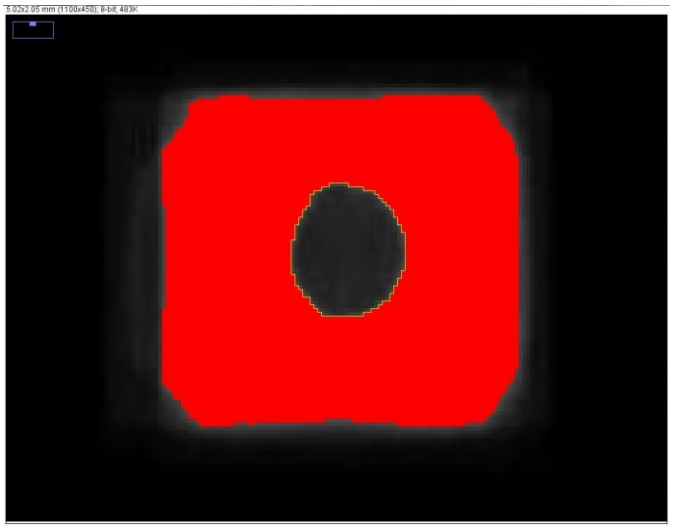

(b)

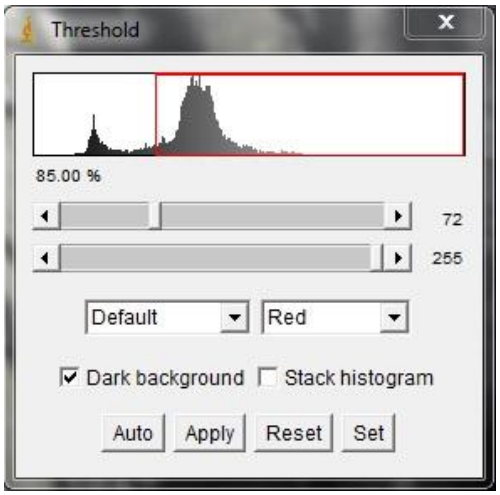

Figure 5-19 : Thresholding of the average unit cell micrograph with selection of the boundaries of the internal pore diameter lined in yellow. The view of the averaged unit cell micrograph is magnified to provide clarity. (a) 'Mask' of averaged unit cell; (b) Histogram produced by ImageJ with selection of cutoff value to obtain the mask in (a).

From there, a rectangular selection can be constructed based on boundaries of the mask to determine its size while an oval selection can be constructed to determine the internal pore diameter measured in terms of width and height as shown in Figure 5-20.

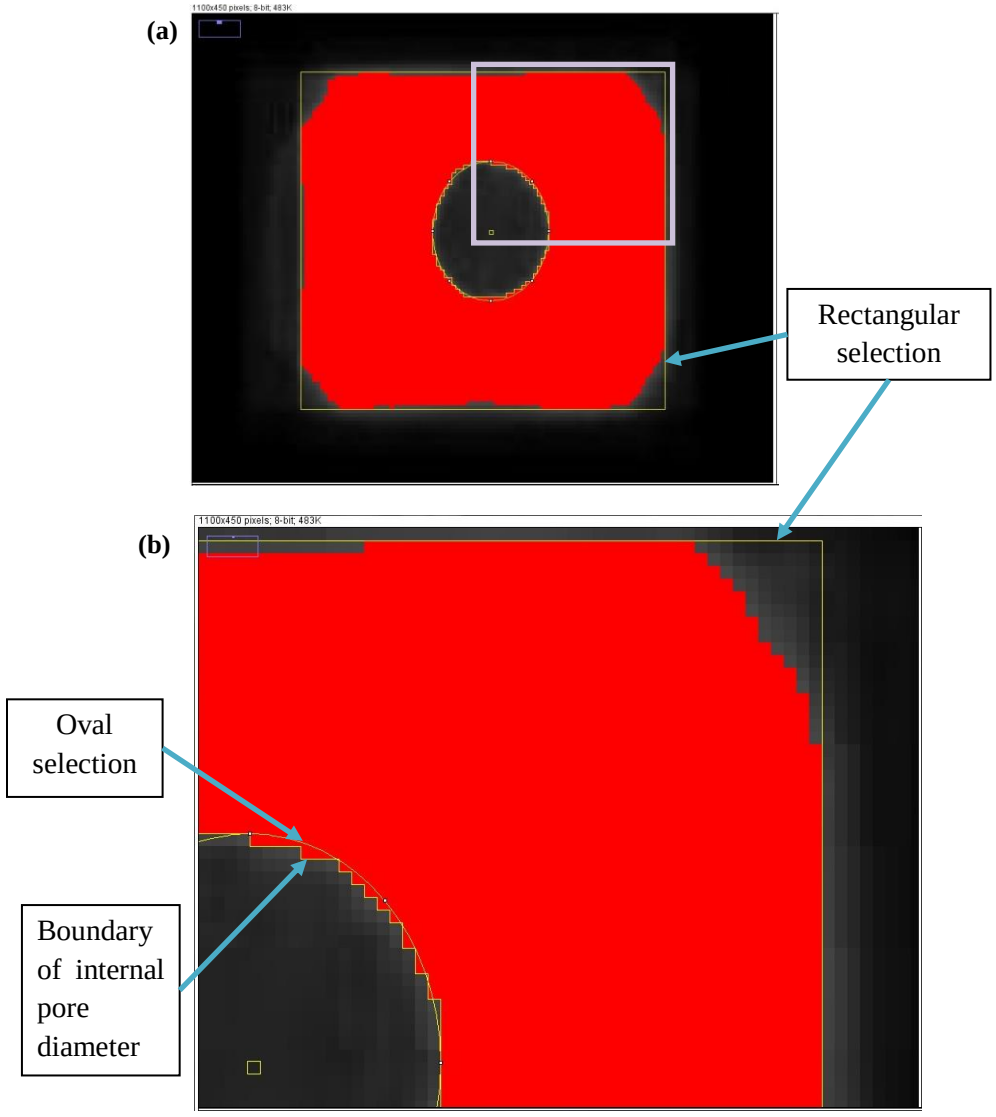

Figure 5-20 : ImageJ constructions made to the 'mask' obtained after subsequent thresholding on the average unit cell micrograph. The width and height obtained from respective rectangular and oval selections should be referred to the nominated dimensional parameters in regards to the two different axial directions (horizontal for width and vertical for height) with respect to the plane view being considered. (a) The rectangular selection was used to measure the width and height of the unit cell. The blue box is considered for presentation of the oval selection and boundary of the internal pore diameter; (b) Region within the blue box in (a). The boundary of the internal pore diameter traced using the 'Wand Tool' and construction of the oval selection to measure the internal pore diameter in terms of width and height.

By readjusting the cutoff values for the threshold, the external diameter of the pore throat can be made observable to a certain extent as shown in Figure 5-21. The oval selection can then be used to determine the external diameter measured in terms of width and height.

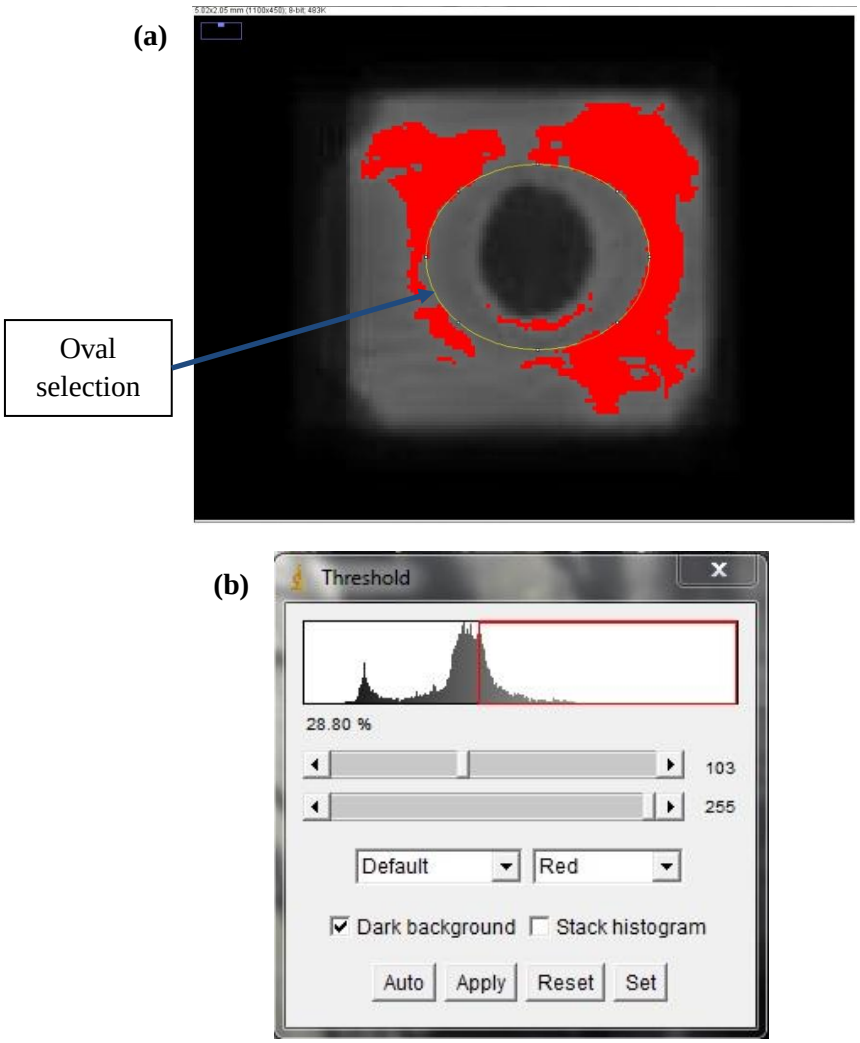

Figure 5-21 : Thresholding of the average unit cell micrograph to obtain an observable external pore diameter. (a) The boundary of the external pore diameter is measured via the oval selection; (b) Histogram produced by ImageJ with selection of cutoff value to obtain the mask in (a)

5.4.4 Geometrical Transformations

With measurement analyses having been performed according to the methodology discussed in the previous sub-section, it can be confirmed that geometrical transformations in terms of respective unit cells comprising fabricated tissue scaffolds from the intended Schwarz P unit cell design has occurred. The unit cells comprising the fabricated tissue scaffolds generally had unequal height, width and length with an increase in wall thickness than originally intended. A comparison of the height, width and length measurements obtained and that of the original Schwarz P unit cell design is tabulated in Table 5-13. A comparison of the wall thickness on the other hand is tabulated in Table 5-14. For brevity, the averaged values of wall thickness are tabulated.

Table 5-13 : Comparison of height, width and length measurements of observable unit cells comprising the physical fabricated tissue scaffolds obtained from measurement analysis of the averaged SEM micrograph and the intended Schwarz P unit cell design. Averaging of the SEM micrographs produces a single micrograph with respect to the plane view in consideration. However, one dimensional parameter can be represented in two different plane views i.e. two micrographs. For example, the dimensional parameter for height can be measured on tissue scaffold micrographs viewed from the YX and YZ plane view. Calculating the mean average for that particular dimensional parameter would also give the standard deviation.

Parameter	**Measurement (Mean $\pm$ Standard deviation) (mm)**	
	Unit cells comprising fabricated scaffolds	**Intended Schwarz P unit cell design**
Height	0.389 ± 0.008	0.520
Width	0.403 ± 0.018	
Length	0.413 ± 0.008	

Table 5-14 : Comparison of wall thickness measurements of observable unit cells comprising the physical fabricated tissue scaffolds obtained from measurement analyses of the averaged SEM micrograph and the intended Schwarz P unit cell design.

Plane	Wall Thickness Measurement (Mean ± Standard deviation) (mm)	
	Unit cells comprising fabricated scaffolds	**Intended Schwarz P unit cell design**
YX	0.0280 ± 0.018	0.0139
YZ	0.0288 ± 0.016	
XZ	0.0450 ± 0.000	

Discrepancies in height, width, length and wall thickness between unit cells comprising the fabricated tissue scaffolds and the intended Schwarz P unit cell design would definitely influence resulting modulus of the unit cell and subsequently the modulus of the scaffold as a whole. To mediate the discrepancies, the geometrical transformations that have occurred need to be taken into account in a revised linear computational analysis before subsequently ensuring validity of the computational approach used. The mean values for height, width, length and wall thickness measurements tabulated previously were used to reconstruct the Schwarz P unit cell CAD model for a new unit cell. This would give a reconstructed unit cell that would then approximately represent the average of unit cells comprising the fabricated tissue scaffold. It shall be noted here that based on the measurements, the reconstructed unit cell model is idealised to be of quarter symmetry in 3-dimensional space to allow proper implementation for a revised micromechanical analysis.

5.4.5 CAD Model Reconstruction

Different CAD model reconstruction techniques were implemented to remodel the Schwarz P unit cell to the dimensions obtained in the previous sub-section. The techniques implemented were performed through the software Altair Hyperworks and are discussed in the following subsubsections.

5.4.5.1 Scaling

The ‘Scale’ sub-utility under ‘Tools’ within Altair Hyperworks allows scaling to be performed in the x, y and z directions based on a selected point of origin. The scaling can be done uniformly throughout all 3 directions or non-uniformly for any combination of the 3 directions. In the case of Schwarz P unit cell models used throughout this study, the centre of the unit cell is the selected point of origin as indicated by the yellow dot in Figure 5-22.

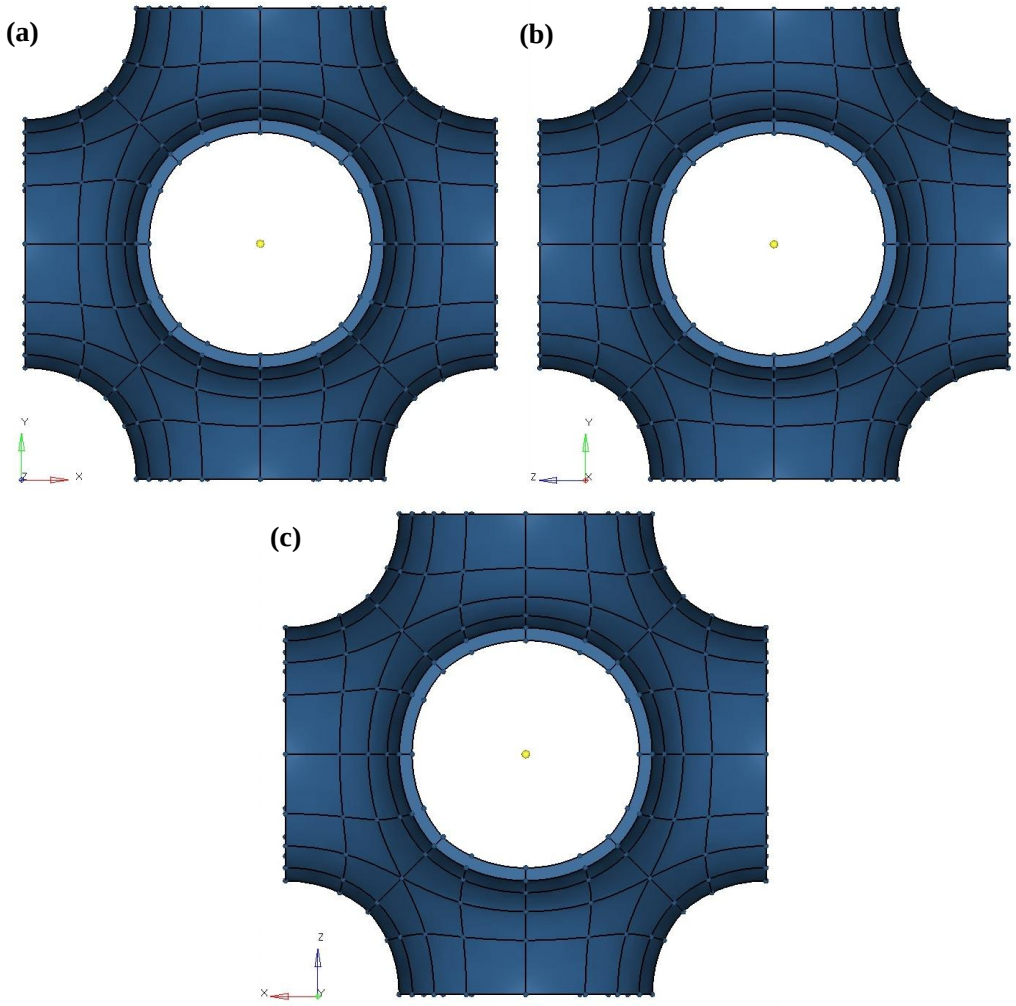

Figure 5-22 : Different view perspectives of the point of origin (indicated as the yellow dot) defined at (0,0,0). (a) Point of origin viewed on the YX plane; (b) Point of origin viewed on the YZ plane; (c) Point of origin viewed on the XZ plane.

Scaling was used to reconstruct the height, width and length of the Schwarz P unit cell model to accommodate respective measurements made from averaged SEM micrographs. In scaling, the x-axis, y-axis and z-axis were taken as the width, height and length measurements respectively. This complementary to indications made for plane views

made during the measurement analyses from SEM micrographs charted in Sub-section 5.4.2.

5.4.5.2 Offset

The ‘Offset’ option within the ‘Surface Edit’ sub-utility under ‘Geom’ was used to reconstruct the wall thickness and accommodate respective measurements from SEM micrographs. The measurement to which ‘Offset’ is performed is calculated based on the external and internal pore throat size. This will be discussed in the following section. The ‘Offset’ option was set to be a ‘Continuous Offset’ to ensure connectivity between different surface patches as they are subsequently processed. Increasing or decreasing the wall thickness via the ‘Offset’ option is dependent on the vector normal of selected surface geometry and is determined entirely by the software. Its direction can be indicated by selecting ‘Vector normal’ and can also be reversed if required. The wall thickness can be adjusted uniformly or non-uniformly throughout the pore throats. This is dependent on the surface patches selected during the ‘Offset’ process. An example of a unit cell model with equal height, width and length and uniform increase in wall thickness through all pores is graphically represented in Figure 5-23. The example can be compared to the wall thickness of the intended Schwarz P unit cell design presented in Figure 5-22.

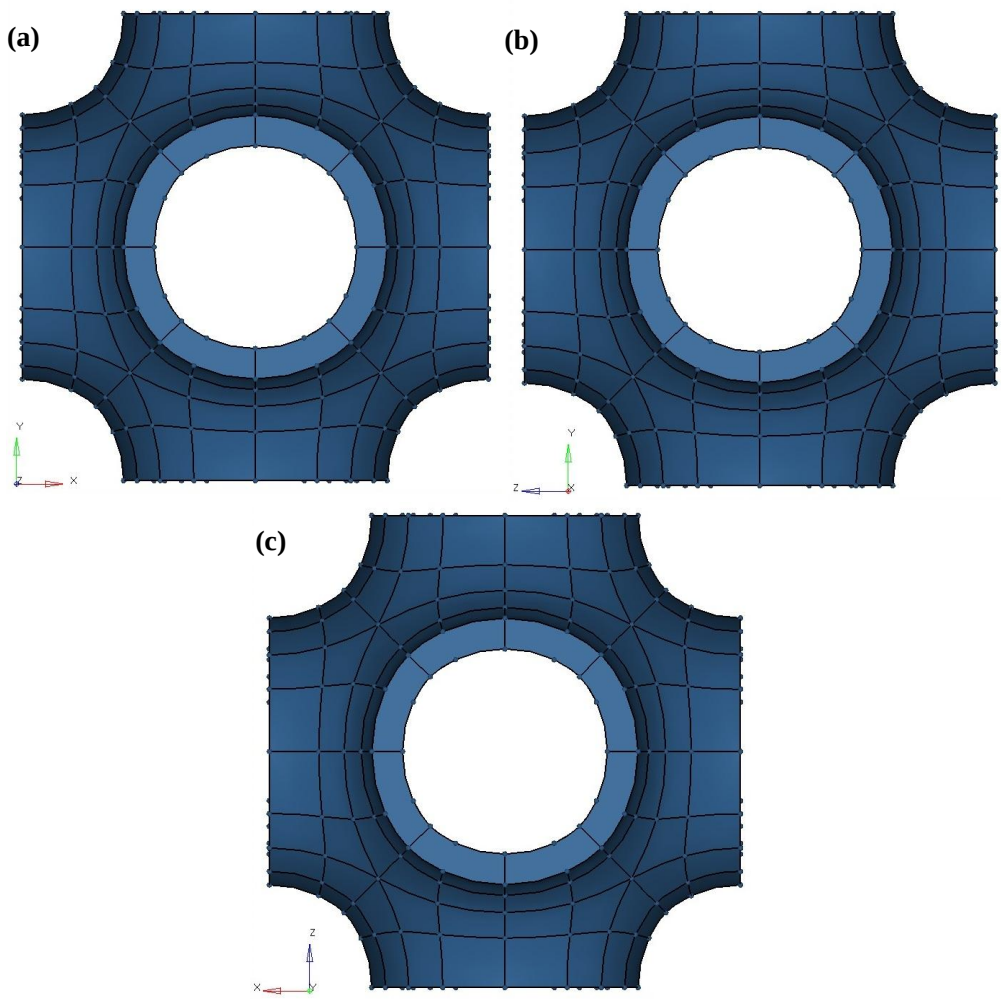

Figure 5-23 : Example of a unit cell model with the wall thickness increased via the 'Offset' technique viewed at different perspectives. (a) View of unit cell on YX plane; (b) View of unit cell on YZ plane; (c) View of unit cell on XZ plane.

5.4.5.3 Reconstruction Process

The reconstruction process generally builds upon the original Schwarz P unit cell surface geometry CAD model as a foundation. Based on measurements of height, width and length obtained from averaged unit cell SEM micrographs presented in Sub-Section 5.4.4, 'Scaling' was implemented first by taking the ratio between the measurements and that of

the height, width and length of the original Schwarz P unit cell. This is represented in Equations (12), (13) and (14).

$$R_H = \frac{H_F}{H_O} \quad (12)$$

$$R_W = \frac{W_F}{W_O} \quad (13)$$

$$R_L = \frac{L_F}{L_O} \quad (14)$$

for which,

$R_H =$ Ratio between the measured height of unit cell comprising the fabricated tissue scaffold, H_F and the height of the original Schwarz P unit cell, H_O (= 0.52mm)

$R_W =$ Ratio between the measured width of unit cell comprising the fabricated tissue scaffold, W_F and the width of the original Schwarz P unit cell, W_O (= 0.52mm)

$R_L =$ Ratio between the measured length of unit cell comprising the fabricated tissue scaffold, L_F and the length of the original Schwarz P unit cell, L_O (= 0.52mm)

Based on references for plane axes and the respective dimensional parameters they represent as tabulated in Table 5-12 in Sub-section 5.4.2, the values for R_H, R_W and R_L are used as input values for ‘Scaling’ in the y, x and z directions respectively. From this, the height, width and length can be reconstructed uniformly or non-uniformly based on the scaling ratio values.

With the scaling of the original Schwarz P unit cell model (either uniformly or non-uniformly), the wall thickness is also subsequently scaled to a particular measurement as a result. This implies changes in the internal and external pore throat diameter of the scaled model. To determine offset values to reconstruct wall thickness, the initial internal and external pore throat diameters of the scaled model is recorded according to the plane view and directional axes being considered. Adding in this consideration, the 'Offset' value is determined to be the difference between the diameters measured through Sub-section 5.4.3 and those measured above. The coating thickness (as discussed in Sub-section 5.4.2) is also taken into account. The calculation for 'Offset' value is represented in the following using the XY-plane axes as a representative example.

Plane view:

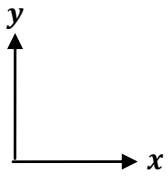

Internal pore throat size :

$$O_Y^{Int} = \frac{O_{Y\_F}^{Int} - O_{Y\_I}^{Int}}{2} \qquad O_X^{Int} = \frac{O_{X\_F}^{Int} - O_{X\_I}^{Int}}{2}$$

External pore throat size :

$$O_Y^{Ext} = \frac{O_{Y\_F}^{Ext} - O_{Y\_I}^{Ext}}{2} \qquad O_X^{Ext} = \frac{O_{X\_F}^{Ext} - O_{X\_I}^{Ext}}{2}$$

for which,

O_Y^{Int} = 'Offset' value in the y-direction in terms of internal pore throat (in the x-y plane)

$O_{Y\_F}^{Int}$ = Measured 'height' of the internal pore throat diameter of unit cell comprising the fabricated tissue scaffold

$O_{Y\_I}^{Int}$ = Initial measured 'height' of internal pore throat (measured from the Schwarz P unit cell after scaling)

O_X^{Int} = 'Offset' value in the x-direction (in the x-y plane)

$O_{X\_F}^{Int}$ = Measured 'width' of the internal pore throat diameter of unit cell comprising the fabricated tissue scaffold

$O_{X\_I}^{Int}$ = Initial measured 'width' of internal pore throat (measured from the Schwarz P unit cell after scaling)

O_{Y}^{Ext} = 'Offset' value in the y-direction in terms of external pore throat (in the x-y plane)

$O_{Y\_F}^{Ext}$ = Measured 'height' of the external pore throat diameter of unit cell comprising the fabricated tissue scaffold

$O_{Y\_I}^{Ext}$ = Initial measured 'height' of external pore throat (measured from the Schwarz P unit cell after scaling)

O_{X}^{Ext} = 'Offset' value in the x-direction (in the x-y plane)

$O_{X\_F}^{Ext}$ = Measured 'width' of the external pore throat diameter of unit cell comprising the fabricated tissue scaffold

$O_{X\_I}^{Ext}$ = Initial measured 'width' of external pore throat (measured from the Schwarz P unit cell after scaling)

With both 'Scaling' and 'Offset' applied, a custom pore shape can eventually be produced. This is obtained by making surface repairs to ensure smooth transitions and surface connectivity between different 'Offset' surfaces. An example of this is graphically presented in Figure 5-24.

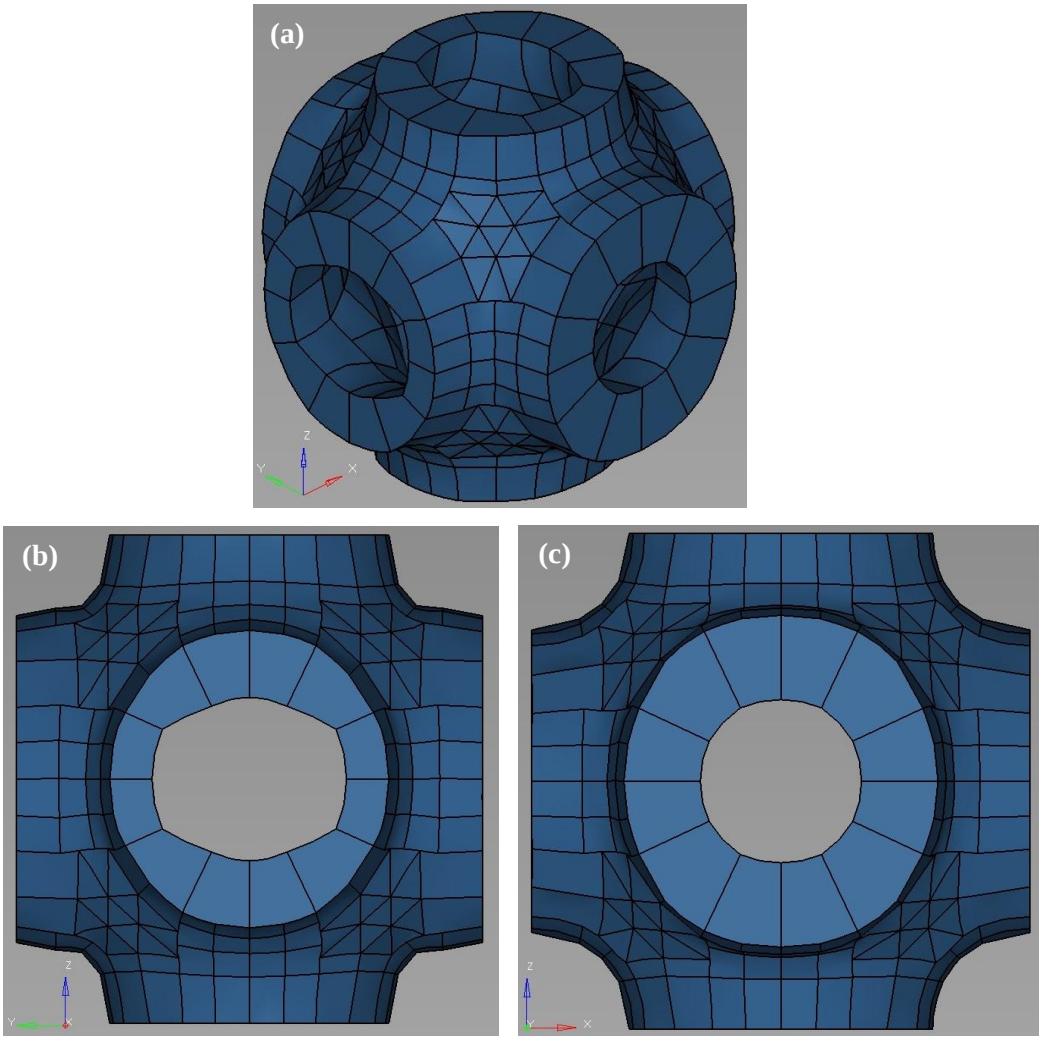

Figure 5-24 : Example of a unit cell model with wall thickness consisting of a combination uniform and non-uniform thickening at different pore throats. (a) General view of unit cell model; (b) Non-uniform wall thickening viewed at plane YZ; (c) Uniform thickening of pore throat wall viewed at plane XZ.

Performing the reconstruction process with respect to the application of different techniques, the unit cell model reconstructed based on measurements made from the averaged unit cell SEM micrographs in Sub-section 5.4.4 can be obtained. The graphical presentation of the reconstructed unit cell model is shown in Figure 5-25.

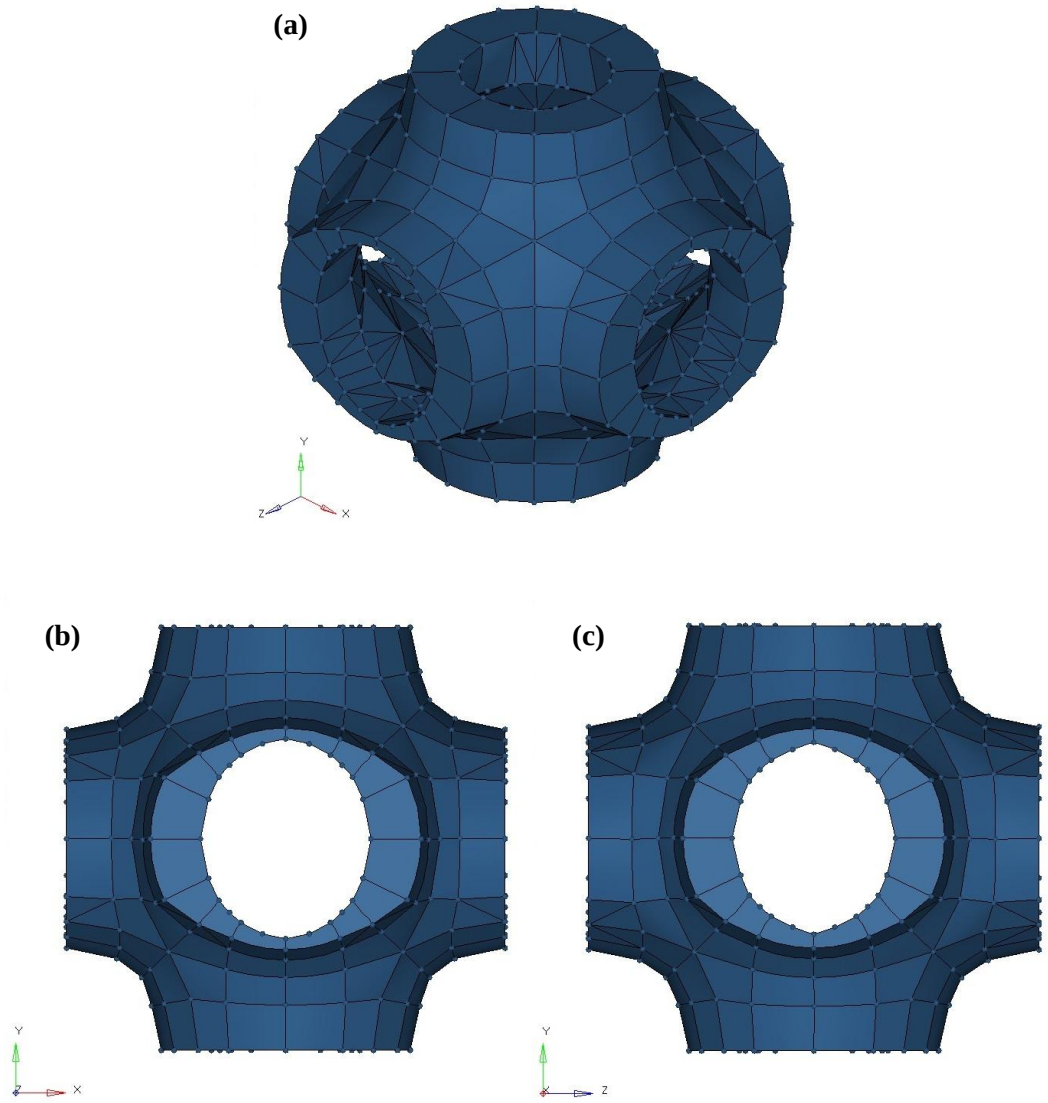

Figure 5-25 : Graphical presentation of the reconstructed unit cell model. The Schwarz P unit cell was reconstructed based on mean measurements established in Sub-section 5.4.4 with the discussed CAD modeling techniques. (a) General view of reconstructed unit cell; (b) YX plane view of the reconstructed unit cell; (c) YZ plane view of the reconstructed unit cell.

With the above, a CAD model of a unit cell approximately representing an average of unit cells comprising the fabricated Schwarz P unit cell-based tissue scaffolds has been reconstructed. The model is then prepared to be implemented in an updated

computational study involving revised derivations of micromechanical analysis to accommodate changes to the representative unit cell. This is discussed in the following section.

5.5 Revised Micromechanical Analysis

5.5.1 Background

The non-uniformity between height, width and length as determined from measurements made from averaged unit cell micrographs requires necessary alterations to be made on the derivations for boundary conditions in regards to micromechanical analysis. Since the arrangement of unit cells into a 3-dimensional array to form the tissue scaffold as a whole remains the same, the derivations can be made in a similar manner to a simple cubic packing system. However, the main difference is the representation for the reconstructed unit cell model in terms of a representative unit cell in regards to the crystal packing system.

The original intended Schwarz P unit cell design consisted of equal height, width and length and was therefore able to be represented as a cube in a simple cubic packing system while also being the ‘representative unit cell’. The reconstructed unit cell model consisted of non-uniform height, width and length and should then be represented as a cuboid in a simple cuboidal packing system with the reconstructed unit cell themselves being the ‘representative unit cell’. This section discusses the alterations made to the simple cubic packing system to determine new boundary conditions for a simple cuboidal packing system. References will be made to equations discussed in Sub-section 5.2.3 of Section 5.2 in performing the alterations. Validation methods to validate correct implementation of the derived boundary conditions for a simple cuboidal packing system will also be discussed.

5.5.2 Derivations for Simple Cuboidal Packing System

A unit cell with non-uniform height, width and length undergoing translational symmetries to obtain the same structure of fabricated tissue scaffolds in this study can be represented by a cuboidal packing system with the reconstructed unit cell model as the 'representative unit cell'. A reconstructed unit cell can then be represented by a simple cuboid as shown in Figure 5-26. A graphical representation of the cuboid/unit cell translated into a 3-dimensional array to give the packing system is shown in Figure 5-27.

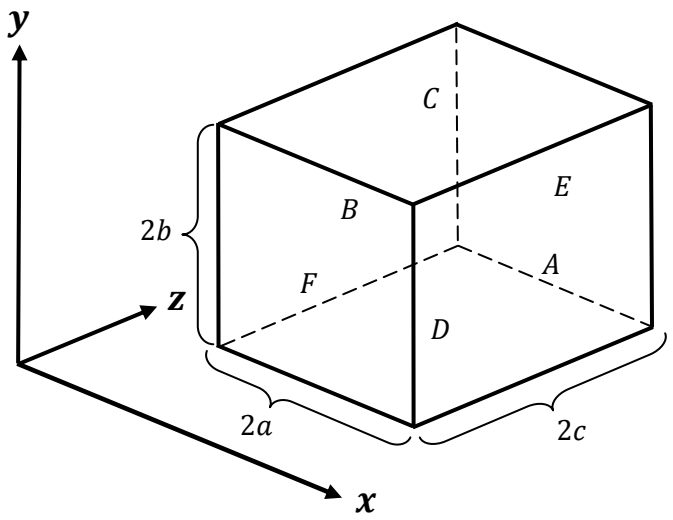

Figure 5-26 : Simple cuboid representing the reconstructed unit cell model taking height, width and length measurements from the measurement analyses made from averaged unit cell SEM micrographs. Translating these cuboids/unit cells into a 3-dimensional array gives a more realistic representation of the fabricated tissue scaffolds. This would subsequently allow results obtained from computational and experimental methods of mechanical characterisation to be more comparable.

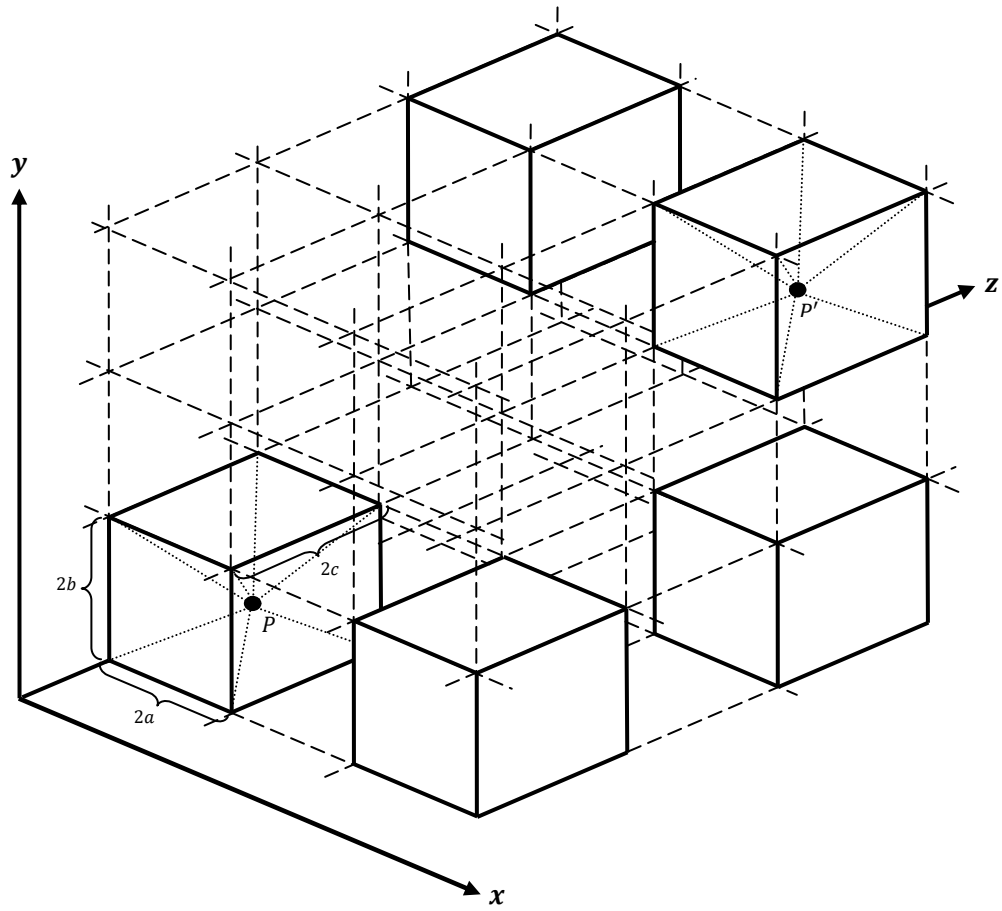

Figure 5-27 : Simple cuboidal packing system consisting of an array of cuboids/reconstructed unit cells translated in a 3-dimensional direction.

The relationship between macroscopic strains and relative displacements can be expressed in a similar manner as Equation (9) in Sub-section 5.2.3. In addition, obtaining the displacement fields in said equation can also be done in a similar manner to Equation (10) in the same sub-section.

Consider point P in a 'representative unit cell' and its image, P' in another representative unit cell translated in a 3-dimensional direction as represented in Figure 5-27. Point P'

can be determined by translational symmetry transformations in a 3-dimensional direction as shown in Equation (15).

$$(x', y', z') = (x + 2ia, y + 2jb, z + 2kc) \quad (15)$$

for which i, j and k are the number of 'representative cuboid unit cells' in which P' is translated from P in the x, y and z directions respectively. The faces of the representative unit cell can then be paired by transformations tabulated as shown in Table 5-15.

Table 5-15 : Equations defining the pairing between opposite faces of a cuboidal representative unit cell.

Faces A and B	$x = a$ for face A	$x = -a$ for face B	$i = 1; j = k = 0$
Faces C and D	$y = b$ for face C	$y = -b$ for face D	$j = 1; i = k = 0$
Faces E and F	$z = c$ for face E	$z = -c$ for face F	$k = 1; i = j = 0$

Substituting the equations established in Table 5-15 into Equation (15), the displacement boundary conditions for each pair of faces can be obtained as shown in Table 5-16.

Table 5-16 : Displacement boundary conditions for simple cuboidal packing system. Similar to a simple cubic packing system with a cubic representative unit cell, 3 different pairs of faces are obtained from 6 different faces.

Pair faces	Displacement boundary conditions
A and B	$\lvert u_A - u_B \rvert_{y,z} = 2a\varepsilon_x^0$ $\lvert v_A - v_B \rvert_{y,z} = 0$ $\lvert w_A - w_B \rvert_{y,z} = 0$

C and D	$\lvert u_C - u_D \rvert_{x,z} = 2b\gamma_{xy}^0$ $\lvert v_C - v_D \rvert_{x,z} = 2b\varepsilon_y^0$ $\lvert w_C - w_D \rvert_{x,z} = 0$
E and F	$\lvert u_C - u_D \rvert_{x,z} = 2c\gamma_{xz}^0$ $\lvert v_C - v_D \rvert_{x,z} = 2c\gamma_{yz}^0$ $\lvert w_C - w_D \rvert_{x,z} = 2c\varepsilon_z^0$

Similar to displacement boundary conditions in Section 5.2, the displacement boundary conditions tabulated in Table 5-16 are applied to nodes on the faces of the discretised reconstructed unit cell model for which the notations $\lvert_{y,z}$, $\lvert_{x,z}$ and $\lvert_{x,y}$ indicated common directional axes of tessellated faces between each pair. Again, no further boundary conditions need to be established in regards to the edges since no two faces in any of the reconstructed unit cell models share a common edge. Therefore, only the displacement boundary conditions are required for implementation of micromechanical analysis.

The effective properties of the reconstructed unit cell and subsequently the tissue scaffolds can be obtained by applying macroscopic load to different degrees of freedom along with the derived displacement boundary conditions. This has been discussed in Sub-section 5.2.3 of Section 5.2.

5.5.3 Validation for Correct Implementation of Revised Displacement Boundary Conditions

Correct implementation of displacement boundary conditions to a ‘representative unit cell’ in a cuboidal packing system can be assessed through the results for average strain and average shear strain. Compiling the results for average strain values should give

symmetric results along the diagonal with differing values within the diagonal as tabulated in Table 5-17. Tabulating the average shear strain values should also give symmetric results along the diagonal with differing values within the diagonal. Values lying outside the diagonal can be approximated to zero due to their small values. This is represented in Table 5-18.

Table 5-17 : Tabulated representation of average strain values obtained from micromechanical analysis to validate displacement boundary conditions established for a simple cuboidal packing system

Degree of freedom of load/displacement application	**Average strain**		
	$\boldsymbol{x}$	$\boldsymbol{y}$	$\boldsymbol{z}$
$\boldsymbol{\varepsilon_x^0}$	ε_1	ε_2	ε_3
$\boldsymbol{\varepsilon_y^0}$	$\varepsilon_4 (\approx \varepsilon_2)$	ε_5	ε_6
$\boldsymbol{\varepsilon_z^0}$	$\varepsilon_7 (\approx \varepsilon_3)$	$\varepsilon_8 (\approx \varepsilon_6)$	ε_9

Table 5-18 : Tabulated representation of average shear strain values obtained from micromechanical analysis to validate displacement boundary conditions established for a simple cuboidal packing system

Degree of freedom of load/displacement application	**Average shear strain**		
	$\boldsymbol{x}$	$\boldsymbol{y}$	$\boldsymbol{z}$
$\boldsymbol{\gamma_{yz}^0}$	γ_1	0	0
$\boldsymbol{\gamma_{xz}^0}$	0	γ_2	0
$\boldsymbol{\gamma_{xy}^0}$	0	0	γ_3

5.6 Case II (Revision of Case I)

5.6.1 Background

After initial investigations in Case I, it has been determined through SEM micrographs that geometrical transformations between the intended Schwarz P unit cell design and the resulting unit cells comprising the fabricated tissue scaffolds have occurred. Measurement analyses were done on averaged unit cell micrographs to obtain measurements of different dimensional parameters. The Schwarz P unit cell CAD model was reconstructed based on the measurements to approximately represent an average of unit cells comprising the scaffold.

This section discusses a revised linear analysis of the initial investigation that implements the reconstructed unit cell model to mediate the geometrical transformations. Revised derivations for displacement boundary conditions in regards to micromechanical analysis taking a simple cuboidal packing system is implemented to the reconstructed unit cell to determine the effective modulus. The modulus value obtained will then be compared to the experimental modulus value obtained from compression experiments of fabricated Schwarz P unit cell-based tissue scaffolds.

5.6.2 Configurations for Reconstructed Unit Cell

A single unit cell was reconstructed based on measurements of height, width, length and wall thickness made from the averaged SEM micrographs. Reconstruction was performed from the Schwarz P unit cell CAD model through the reconstruction techniques and process presented in Sub-section 5.4.5 of Section 5.4. For purposes of in-depth discussion, these parameters were not enough to describe differences between the reconstructed unit cell model and the original Schwarz P unit cell model in terms of the resulting effective

modulus obtained from subsequent micromechanical analysis without a solid foundation in their mechanics. Hence, several dimensional parameters are added into consideration alongside those mentioned above.

After subsequent reconstruction of the unit cell, the radius of curvature was measured. This was done using a combination of Altair Hyperworks and ImageJ at cross-sectional plane segments presented in Figure 5-28.

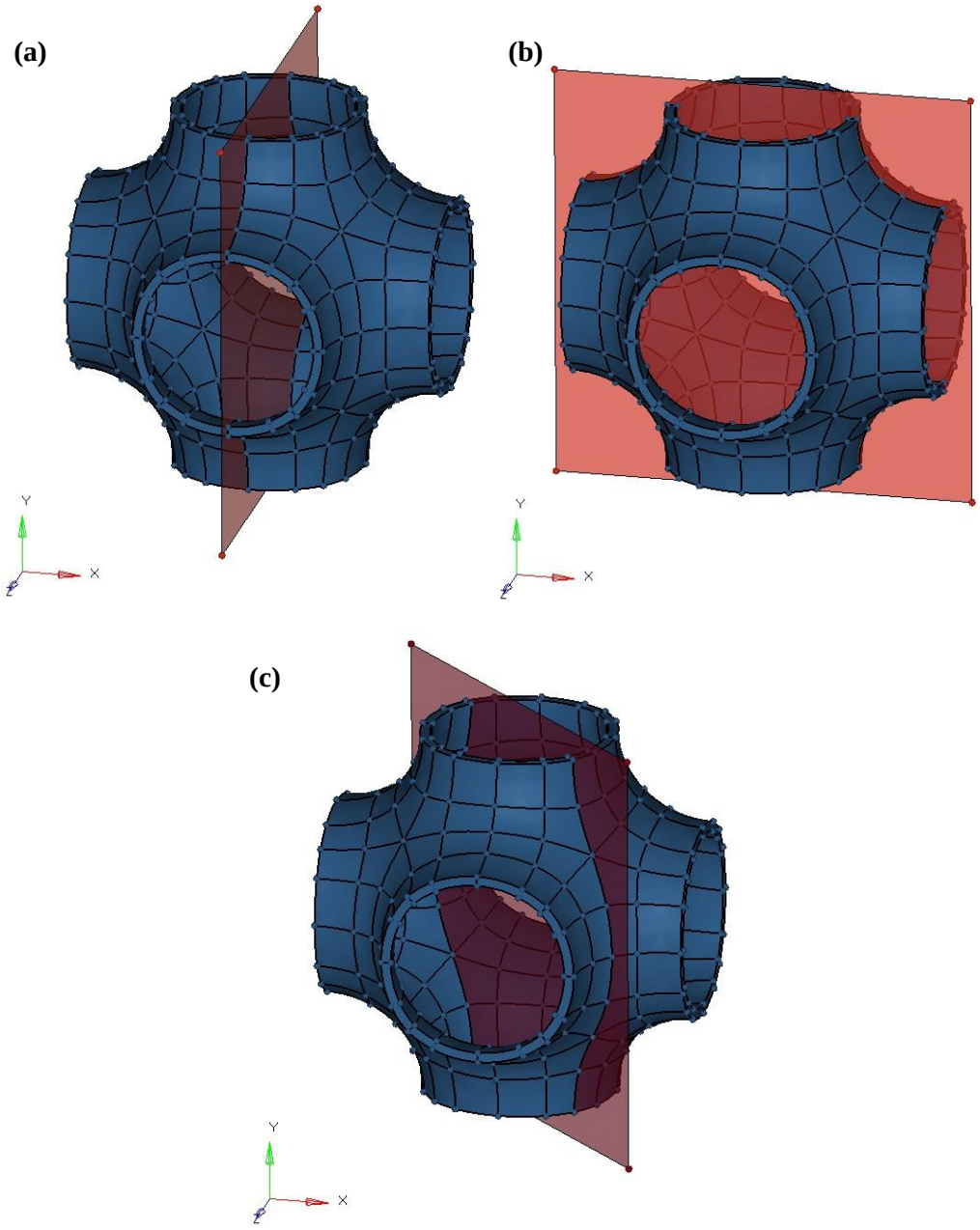

Figure 5-28 : Cross-sectional planes used as reference to measure the radius of curvature of unit cells; (a) Plane YZ; (b) Plane YX; (c) Plane YX/YZ i.e. Split plane.

For each plane view, line segments can be constructed based on cross-sections of the surface geometry that also lie on the cross-sectional planes presented in Figure 5-28 to

make measurements for the radius of curvature. An overlay of these line segments on a Schwarz P unit cell is presented in Figure 5-29. In creating line segments along the split plane, intersection points formed between lines segments originating from 3 adjacent pores are selected. An example of this is represented as yellow dots within the same figure.

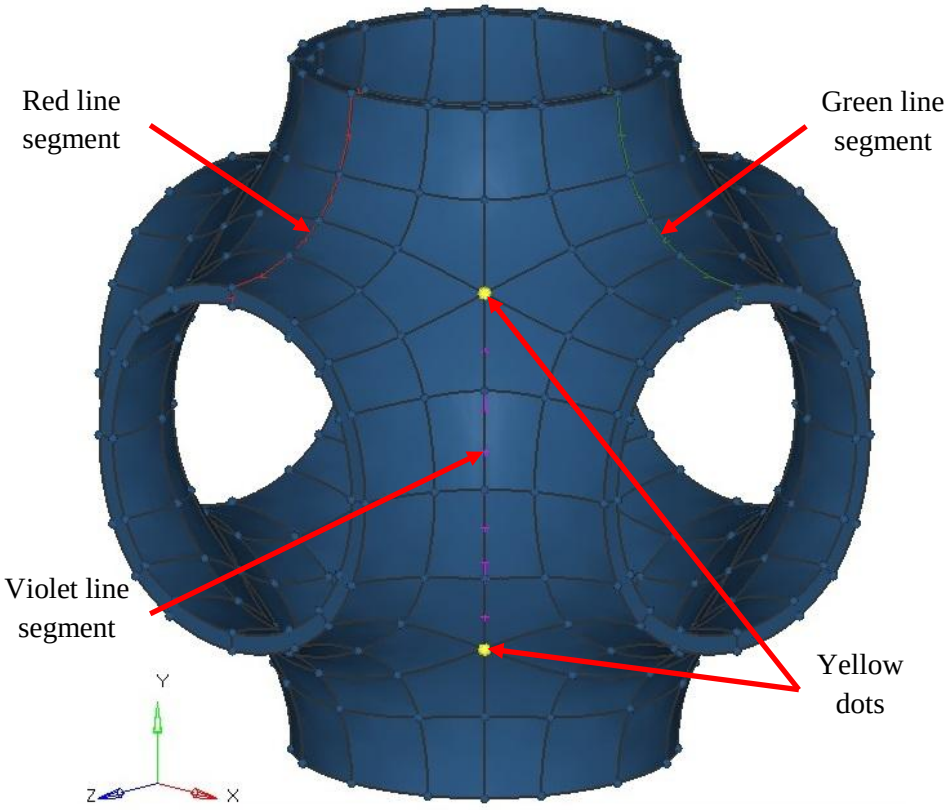

Figure 5-29 : Line segments on a Schwarz P unit cell. (Red) Line segment on the YZ plane; (Green) Line segment on the YX plane; (Violet) Line segment on the split plane; The line segment on the split plane is created between intersections points formed by line segments originating from 3 different adjacent pores. These intersections points are represented as yellow dots in the figure.

A midline within the enclosed line segments can be constructed before subsequently determining its length using Altair Hyperworks as shown in Figure 5-30.

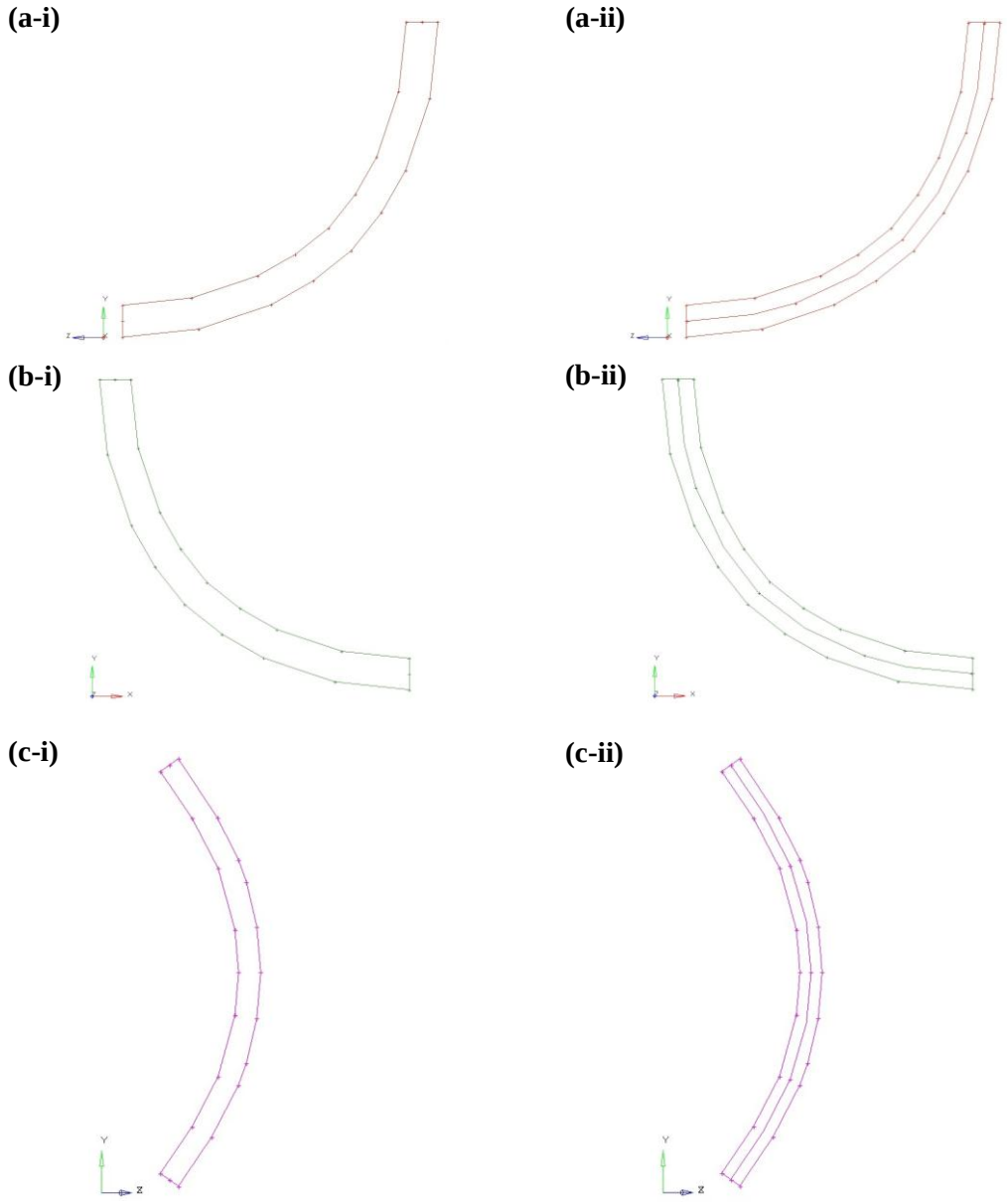

Figure 5-30 : Plane view of constructed line segments. (a-i) Line segment of cross-section at plane YZ; (a-ii) Construction of midline for line segment in a-i; (b-i) Line segment of cross-section at plane YX; (b-ii) Construction of midline for line segment in b-i; (c-i) Line segment of cross-section at the split plane; (c-ii) Construction of midline for line segment in c-i.

By approximating the midline to take a circular arc, the arc angle, θ can be determined via ImageJ. Subsequently, the radius of curvature can be determined using the equation, $s = r\theta$, for s is the length of the midline/curvature (measurable in Altair Hyperworks).

The configuration for the height, width, length and wall thickness for the reconstructed unit cell and the original intended Schwarz P unit cell design are tabulated in Table 5-19. The dimensional volume (product of height, width and length) and the measured radius of curvature are also tabulated in the same table. In regards to the wall thickness, the average length of the two ends of the enclosed line segments for each cross-sectional plane is tabulated. This should not be confused with the average wall thickness measured from unit cell micrographs at each plane view as tabulated in Sub-section 5.4.4. The reconstructed unit cell is given the nomenclature ‘A’ while the original Schwarz P unit cell design is indicated with the nomenclature ‘O’ as the model name.

Table 5-19 : Configurations for the reconstructed unit cell model based on dimensional parameters obtained through the averaging of SEM micrographs (indicated with the nomenclature 'A'); the determined dimensional volume and radius of curvature. The dimensional parameters, the dimensional volume and radius of curvature for the original Schwarz P unit cell is also tabulated and indicated with the nomenclature 'O' as the model name.

Model	Height (mm)	Width (mm)	Length (mm)	Dimensional volume (mm^3)	Average wall thickness (mm)			Radius of curvature (mm)		
					Plane YZ	Plane YX	Split Plane	Plane YZ	Plane YX	Split Plane
A	0.389	0.403	0.413	0.0648	0.0281	0.0294	0.0383	0.1122	0.1094	0.1233
O	0.520	0.520	0.520	0.1406	0.0139	0.0139	0.0139	0.1209	0.1209	0.1933

5.6.3 Discretisation of Reconstructed Unit Cell

The reconstructed unit cell CAD model was discretised using second-order tetrahedral C3D10 elements using the methodology described in Sub-section 5.2.4 of Section 5.2. Similar to Case I, a homogenous, isotropic and linearly elastic material model was assigned to the discretised reconstructed unit cell model and thus requires material input data in the form of Young's modulus and Poisson's ratio. The lower limit (based on specimen 5), the average and the upper limit (based on specimen 3) Young's modulus of LCM3 and a Poisson's ratio of 0.3 are assigned to the discretised unit cell model in 3 main separate analysis. The revised derivations of displacement boundary conditions for micromechanical analysis as discussed in Sub-section 5.5.2 of Section 5.5 were implemented on the reconstructed unit cell model. Information in regards to the discretised reconstructed unit cell model, the material model and the revised derivations of displacement boundary conditions along with the application of macroscopic load were compiled into an input file and subsequently processed in ABAQUS/Standard. The input file was processed in a static, linear perturbation analysis similar to Case I. The results obtained are discussed in the following sub-section.

5.6.4 Results

Revised micromechanical analysis was performed on the reconstructed unit cell model. It shall be confirmed here that the revised displacement boundary conditions for a simple cuboidal packing system have been implemented correctly. Tabulation of the obtained average strains and average shear strain results comply with the validation methods discussed in Sub-section 5.5.3. The values of average strain and average shear strain are symmetric along the diagonal with differing values within the diagonal with respect to each material model considered. This is presented in Table 5-20 and Table 5-21.

Table 5-20 : Average strain values obtained from micromechanical analysis of discretised reconstructed unit cell model assigned with 3 different LCM3 material models i.e. lower limit (specimen 5), the average and upper limit (specimen 3). The unit cell was reconstructed to approximately represent an average of unit cells comprising the fabricated tissue scaffold. The average strains for each material model are symmetric along the diagonal with differing values within the diagonal. This thus complies with the validation methods for correct implementation of displacement boundary conditions derived for the simple cuboidal packing system in revised micromechanical analysis.

Material model	Degree of freedom of load application	Average strain		
		x	y	z
Specimen 5 (Lower limit)	ε_x^0	0.102	0.0591	0.0123
	ε_y^0	0.0591	0.135	0.0527
	ε_z^0	0.0123	0.0527	0.0897
Average	ε_x^0	0.0787	0.0454	0.00945
	ε_y^0	0.0454	0.104	0.0405
	ε_z^0	0.00945	0.0405	0.0689
Specimen 3 (Upper limit)	ε_x^0	0.0677	0.0391	0.00813
	ε_y^0	0.0391	0.0894	0.0348
	ε_z^0	0.00813	0.0348	0.0593

Table 5-21 : Average shear strain values obtained from micromechanical analysis of discretised reconstructed unit cell model assigned with 3 different LCM3 models i.e. specimen 5 (for the lower limit), the calculated average and specimen 3 (for an upper limit). The average shear strains for each material model are symmetric along the diagonal with differing values within the diagonal. Values outside the diagonal can be approximated to zero. This thus complies with the validation methods for correct implementation of displacement boundary conditions derived for the simple cuboidal packing system in revised micromechanical analysis.

Material model	Degree of freedom of load application	Average shear strain		
		x	y	z
Specimen 5 (Lower limit)	γ_{yz}^{0}	0.122	4.754E-8 (≈ 0)	2.088E-7 (≈ 0)
	γ_{xz}^{0}	4.754E-8 (≈ 0)	0.176	3.782E-7 (≈ 0)
	γ_{xy}^{0}	2.088E-7 (≈ 0)	3.782E-7 (≈ 0)	0.125
Average	γ_{yz}^{0}	0.0939	3.653E-8 (≈ 0)	1.605E-7 (≈ 0)
	γ_{xz}^{0}	3.653E-8 (≈ 0)	0.135	2.906E-7 (≈ 0)
	γ_{xy}^{0}	1.605E-7 (≈ 0)	2.906E-7 (≈ 0)	0.0957
Specimen 3 (Upper limit)	γ_{yz}^{0}	0.0807	3.141E-8 (≈ 0)	1.380E-7 (≈ 0)
	γ_{xz}^{0}	3.141E-8 (≈ 0)	0.116	2.499E-7 (≈ 0)
	γ_{xy}^{0}	1.380E-7 (≈ 0)	2.499E-7 (≈ 0)	0.0823

Based on the average strain and average shear strain results obtained, the effective modulus and effective shear modulus with respect to the x, y and direction for the reconstructed unit cell model were determined. The results are tabulated in Table 5-22.

Table 5-22 : Effective modulus and effective shear modulus in accordance to directional axes obtained from micromechanical analyses of the discretised reconstructed unit cell model (model 'A'). The discretised reconstructed unit cell model was assigned with the lower, averaged and upper limit material data of LCM3 required for linear analyses.

Material model	Direction	Effective modulus (MPa)	Effective shear modulus (MPa)
Specimen 5 (Lower limit)	***x***	0.75	0.63
	y	0.57	0.44
	z	0.86	0.62
Average	***x***	0.98	0.82
	y	0.74	0.57
	z	1.12	0.81
Specimen 3 (Upper limit)	***x***	1.14	0.96
	y	0.86	0.66
	z	1.30	0.94

With the above, the effective modulus of the reconstructed unit cell is compared to experimental modulus results (obtained from compression experiments as discussed in Chapter 4) in Figure 5-31. The effective modulus results of the original Schwarz P unit cell design determined in Case I is also graphically presented in the same figure. Since physical tissue scaffolds were compressed height-wise (along the y-axis) before determining the experimental stress-strain curve and subsequent stiffness, only the effective modulus with respect to the y-axis (2^{nd} degree of freedom) is considered.

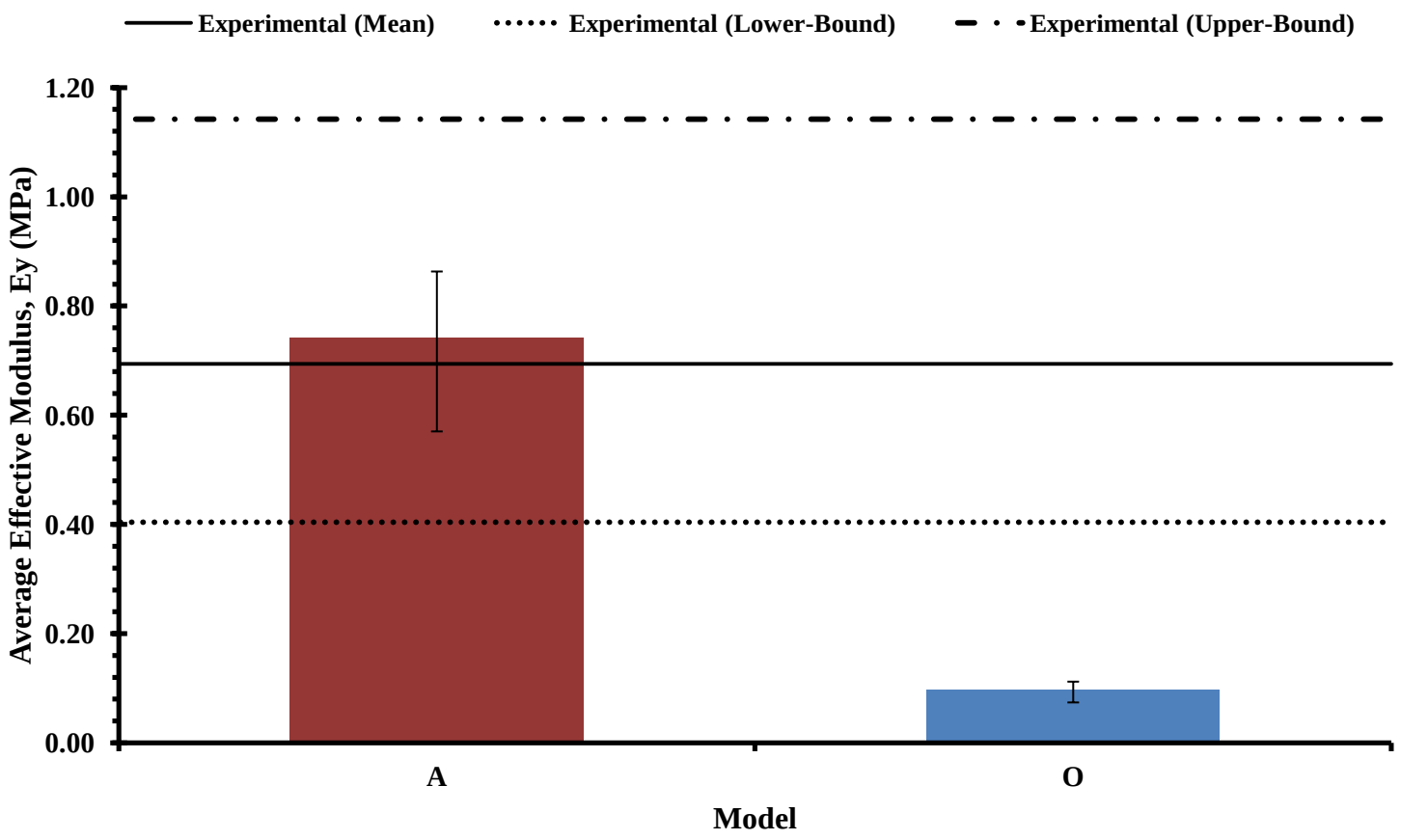

Figure 5-31 : Graphical comparison of the average effective modulus (in the 2nd degree of freedom) of the reconstructed unit cell model ('A') and the original Schwarz P unit cell model ('O') in comparison with experimental modulus values. The effective modulus was determined from respective average strain results (in the 2nd degree of freedom). The experimental results are represented as horizontal lines according to the lower limit, average and upper limit of stiffness values obtained from compression experiments of fabricated tissue scaffolds. The average effective modulus of the reconstructed unit cell model falls within the range of the experimental modulus.

The derivations for micromechanical analysis approximate a large array of the representative unit cell in a 3-dimensional direction. The sizes of the scaffolds are thus considered infinitesimal compared to the approximation. Despite this, awareness is required in consideration of the number of unit cells comprising the fabricated tissue scaffold sample lying along the same parallel direction as load application during experimental compression. The scaffolds were compressed height-wise (along the y-axis) where there are a large number of the Schwarz P unit cells parallel to the direction of load application. Considering the effective modulus results obtained from micromechanical analyses of the reconstructed unit cell (model 'A') and the original Schwarz P unit cell model (model 'O'). It can be observed that the effective modulus of the unit model reconstructed to approximately represent an average of unit cells comprising the fabricated tissue scaffold falls within range of the experimental modulus. Emphasising this further, model A only over-estimates the experimental mean by 6.94%. It can therefore be implied here that the margin of error is only 6.94% from the experimental mean. In addition, it can also be implied that the number of unit cells were sufficient for accurate approximation explained previously.

To further understand the relationships between different dimensional parameters and the resulting effective modulus, several parameters were derived and thus allow comparisons between model A and the original intended Schwarz P unit cell model i.e. model O. The dimensional volume is normalised to the volume of model O. The dimensional volume (simple product of height, width and length) is normalised to that of model O. The same applies for the wall thickness and radius of curvature with respect to different cross-sectional planes from which the measurements are made. These planes have been graphically presented in Figure 5-28. Graphical presentations of these results are shown

in Figure 5-32 through Figure 5-36. A tabulated version of the results is appended in Appendix B.4.1.

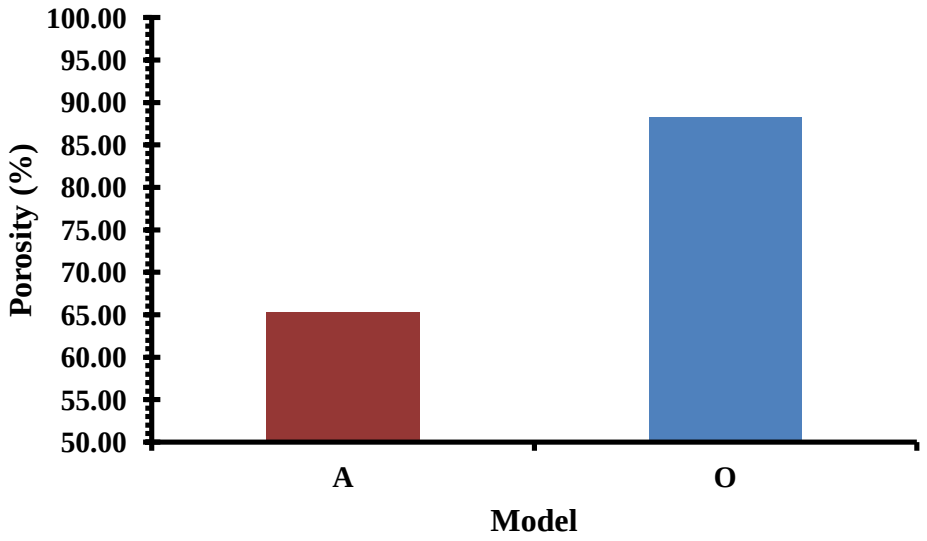

Figure 5-32 : Graphical comparison of porosity between the reconstructed unit cell model i.e. model A; and the original Schwarz P unit cell model i.e. model O.

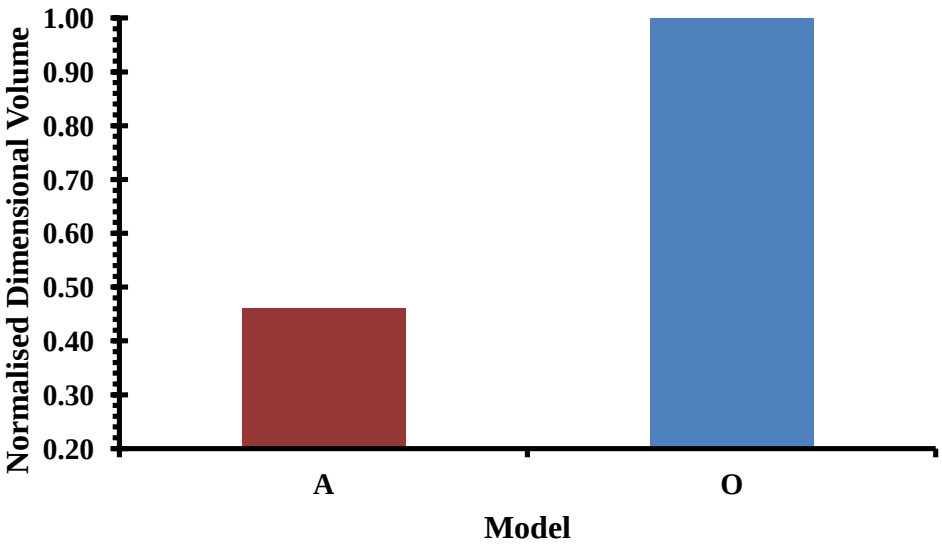

Figure 5-33 : Graphical comparisons of the normalised dimensional volume between the model A and model O.

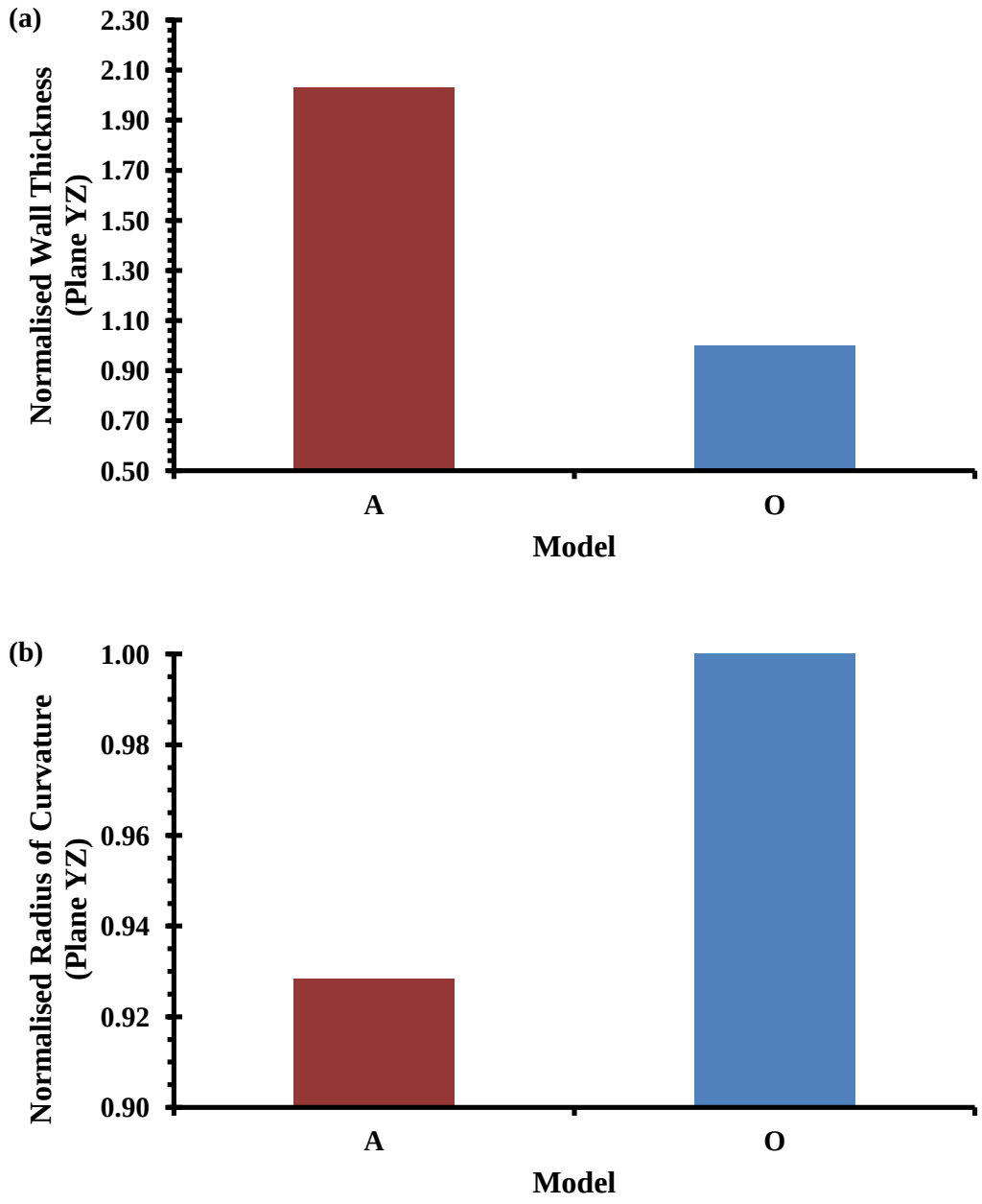

Figure 5-34 : Graphical comparison of normalised (a) wall thickness; (b) radius of curvaturel measured along the cross-section of plane YZ for model A and model O.

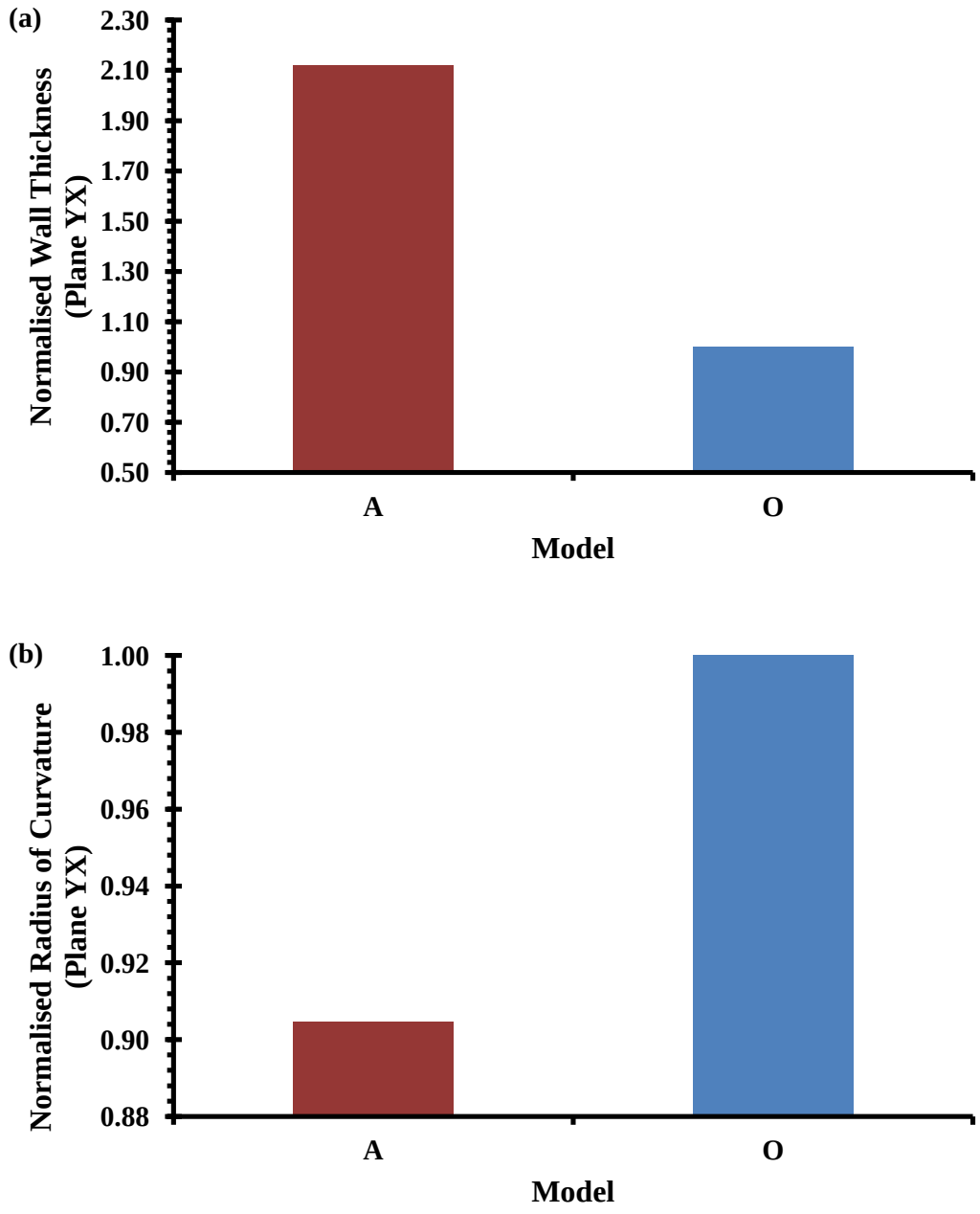

Figure 5-35 : Graphical comparison of normalised (a) wall thickness; (b) radius of curvature; measured along the cross-section of plane YX for model A and model O.

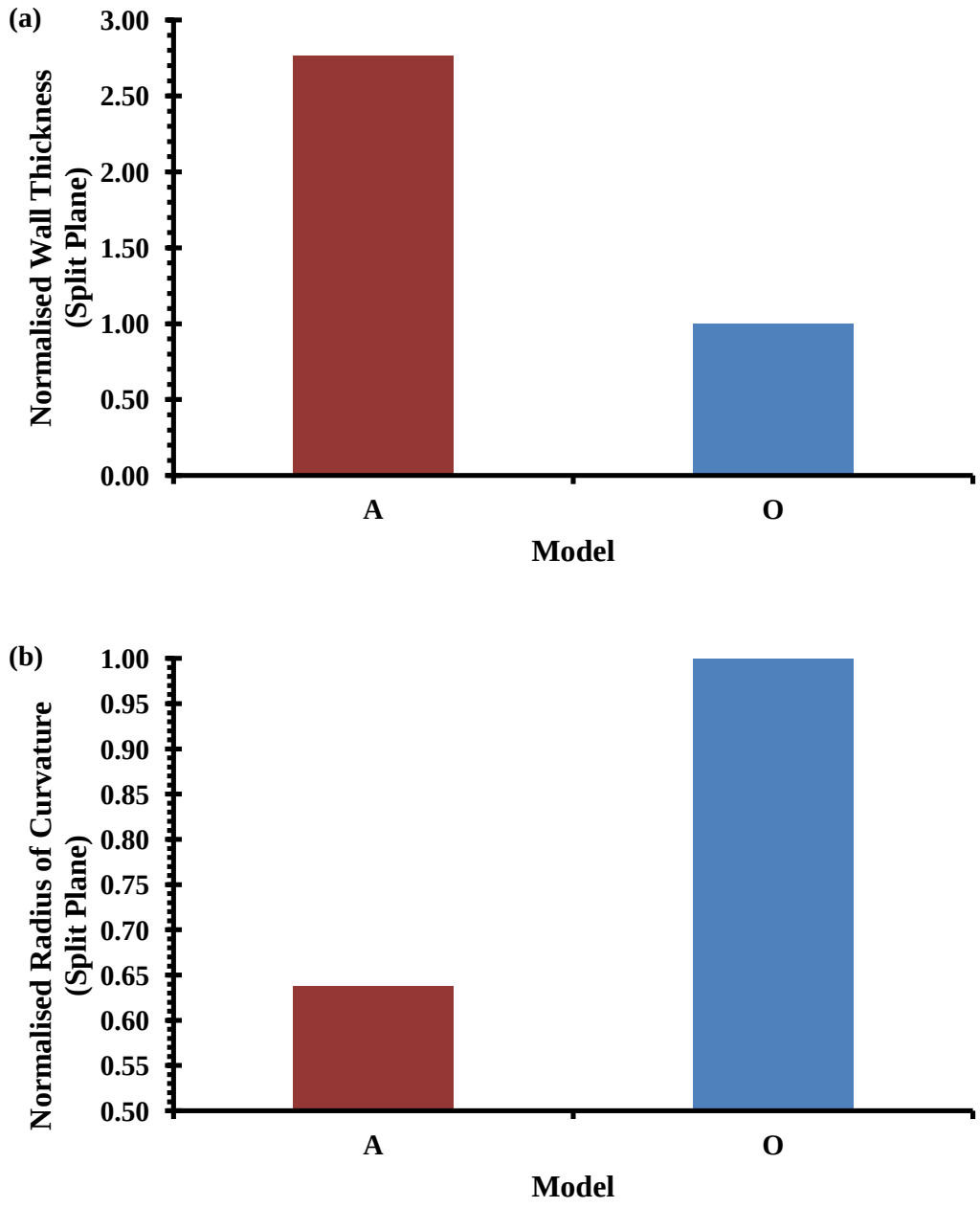

Figure 5-36 : Graphical comparison of normalised (a) wall thickness; (b) radius of curvature; measured along the cross-section of the split plane for model A and model O.

Considering Figure 5-32, the porosity of the original Schwarz P unit cell i.e. model O is higher compared to that of the reconstructed unit cell i.e. model A. The same also applies in terms of the dimensional volume as implied from Figure 5-33. Based on results for normalised wall thickness shown in Figure 5-34(a) through Figure 5-36(a), it can be implied that the wall thickness of model A measured at different cross-sectional planes is consistently thicker compared to model O. However, the radius of curvature of model O measured at different cross-sectional planes is consistently higher compared to model A as implied by results for normalised radius of curvature shown in Figure 5-34(b) through Figure 5-36(b). The parameters mentioned theoretically influences the resulting effective modulus of the unit cell. In the context of comparison between the different unit cell models, these parameters can also compensate with one another to influence the resulting effective modulus.

5.7 Discussion

Initial investigations in the INNOVABONE project have observed geometrical transformations in terms of different dimensional parameters for the fabricated Schwarz P unit cell based tissue scaffolds [122]. Schwarz P unit cells consist of height, width and lengths which are equivalent to subsequently give an aspect ratio equivalent to 1. However, investigations found changes in terms of the aspect ratio and thus imply the said geometrical transformations. This has been investigated further by way of SEM micrographs. Based on measurement analyses of averaged unit cell SEM micrographs, geometrical transformation from the intended Schwarz P unit cell design to the unit cells comprising the fabricated tissue scaffolds implied by changes in aspect ratio indicated the occurrence of shrinkage. Due to confidentiality of the INNOVABONE project, it is to the author's knowledge that the two-photon polymerisation (2PP) fabrication parameters used to fabricate the tissue scaffolds have only been brief. However, one could speculate that the fabrication process including its parameters is the general main source of discrepancy.

Polymerisation is known to be accompanied by a reduction in the total volume of the material. This phenomenon is known as volumetric or polymerisation shrinkage [209]. Shrinkage does play an important role in the fabrication of tiny structure with high resolution features. However, it does become an obstacle in the fabrication of complex structures [166]. There is a balance that lies with the functionalities of fabricated tissue scaffolds from a mechanical and biological aspect. Depending on the extent of shrinkage, tissue scaffolds which comprise of porous structures undergoing shrinkage would potentially lead to smaller pores for the entry of cells and further cellular migration. This

would then lead to inefficient cell growth and cellular activity when cells are seeded within the tissue scaffold construct.

Differences between the high mass density of the solid phase compared to the liquid phase during polymerisation results in the occurrence of shrinkage. This has been demonstrated with the 2PP fabrication of photonic crystals [167]. Shrinkage observed in the fabricated tissue scaffold can also be speculated to be a result of post-processing procedures. Post-processing potentially involves rinsing out the unpolymerised residue to obtain the freestanding scaffold structure. Final evaporative drying gives way to capillary force which results in further subsequent shrinkage in a phenomenon known as “stiction” or the “stiction problem” [177,210,211].

Shrinkage was reported to be a side effect of working the sub-diffraction regime when the polymerised volume is minimized due to the reduction of the monomer-to-polymer conversion rate [166]. This would thus imply the influence of the degree of polymerisation on shrinkage rate. The degree of polymerisation is influenced by both laser power and writing speed. A study investigating the shrinkage of Zr-based hybrid photosensitive materials produced by 2PP found that at laser powers below a certain threshold results in shrinkage of the overall dimensions of fabricated structures. The study observed a structural shrinkage of up to 18% with line width shrinkage of up to 35% of the original values [172]. This would complement another previous study by Weissman which suggests that the ultimate shrinkage and shrinkage rate is dependent on the amount of energy required to polymerise the polymers [212]. The amount of energy required to polymerise the polymers i.e polymerised threshold fluence must exceed the threshold dose of the photoresist and is mathematically related to the two-photon absorption (TPA) coefficient and the peak intensity of the laser [164]. The laser power

should also be selected appropriately so that 2PP occurs without laser damage of the photoresists above the damage threshold. Laser damage would subsequently result in weakening of the microstructures [171]. It can be speculated that the above partially contributes to the discrepancy between the computational and experimental modulus values although this has not been previously confirmed through investigations made by INNOVABONE. No method of evaluating the above has also been made to confirm the above due to limited samples in this study. With the damage threshold and the polymerised threshold fluence being mathematically related, careful selection must be made to parameters making up the variable for polymerised threshold fluence in conjunction to the peak intensity of the incident laser power to ensure polymerisation without the occurrence of laser damage to the photoresists. Adding to the complexity above, the damage threshold is also dependent on the proximity features of the structure being fabricated [171].

The influence of writing speed is implied through the time between pulse of femtosecond laser i.e. exposure time during TPP in which increased writing speed would correspond to lower exposure times [173]. In par with the polymerised threshold fluence, voxelation occurs after a particular threshold exposure time. The growth of the voxel described in terms of diameter and height can be mathematically expressed as a function power and time [175]. Line writing experiments evaluating the expansion of voxels in terms of width with respect to the writing speed has generally shown that higher writing speeds give way to thinner polymerised line widths. This complements investigations done under the INNOVABONE project [178]. Therefore, it can be speculated that the writing speed has some contribution to shrinkage. It is possible that writing speeds higher than ideal

subsequently resulted in thin polymerised line widths and eventually smaller than intended gross build-up of voxels making up the fabricated structure.

The geometrical transformations between the original Schwarz P unit cell and the unit cells comprising the tissue scaffolds fabricated via two-photon polymerisation (2PP) have been taken into account. SEM micrographs of unit cells have been averaged to give a single micrograph for each view perspective from which the scans were made. Measurement analyses were made to the averaged SEM micrograph before reconstructing the Schwarz P unit cell CAD model to accommodate the measurements. This gives a unit cell that was reconstructed to approximately represent an average of the unit cells comprising the fabricated tissue scaffold. The CAD model of the reconstructed unit cell was then re-implemented into revised derivations for micromechanical analysis.

The effective modulus obtained from the analysis falls within the experimental modulus range values obtained from compression experiments of fabricated tissue scaffolds presented and discussed in Chapter 4. To emphasise this further, the reconstructed unit cell model only differs by an over-estimated 6.94% from the experimental mean. This is a significant contrast to the effective modulus obtained from micromechanical analysis of the original Schwarz P unit cell which differs by 86.05% from the experimental mean. Different dimensional parameters influence the resulting effective modulus of the unit cell and subsequently the tissue scaffold as a whole. The predominant surface curvatures inherent in the Schwarz P architecture provide bending resistance for the structure under compression which subsequently affects the resulting effective modulus. The relevance between the wall thicknesses and radius of curvature in regards to the surface curvatures mentioned were observed at cross-sectional planes in Figure 5-28 at line segments shown in Figure 5-29.

For surface curvatures connecting two adjacent pores such as those lying along the cross-sectional plane of YZ and YX, the bending resistance can be described in terms of Castigliano's theorem for curved thin beams [213]. Consider a curved beam which is loaded as shown in Figure 5-37, the deflection equates to the mathematical expression shown in Equation (16). Full mathematical derivations are appended in Appendix B.4.2.

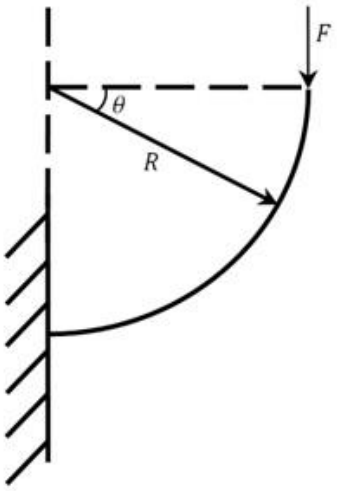

Figure 5-37 : Curved beam with a pinned end. The beam has a curvature defined by the radius, R and an applied force F.

$$\delta = \frac{FR^3}{EI}\left[\frac{3\pi}{4} - 2\right] \quad \textbf{(16)} \ [213]$$

for which F, E and $\left[\left({}^{3\pi}/_{4}\right) - 2\right]$ are constants. The resulting deflection is highly dependent on both the radius of curvature, R and the moment of inertia, I. From here it can be implied that a particular value of δ can be obtained by compensations between R and I in which I is particularly related to the wall thickness. A high radius of curvature at constant I gives higher amount of deflections and lower bending resistance. Thicker walls give higher values of I which compensates to give lower deflections and therefore contributes to increasing bending resistance. The contribution for the normalised wall

thickness and normalised radius of curvature to the effective modulus can be assessed through the evaluation of the ratio between R^3 and I as shown in Equation (16). This evaluation can be implied through the ratio between the cube of the normalised radius of curvature and the normalised wall thickness.

For surface curvatures connecting two opposite pores such as those lying along the split plane, the bending resistance can be described in terms of Euler's buckling theorem for initially curved beams [213,214]. Consider a column with an initial lateral deflection of δ_i and an additional lateral deflection, γ_i after load application, F as shown in Figure 5-38.

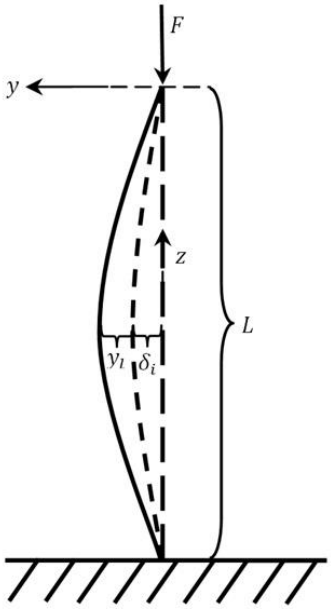

Figure 5-38 : Column with a pinned end where y and z represents the directional axes. The column has a length, L and an initial deflection defined by δ_i. With the application of force, F in the direction shown, the column undergoes an additional lateral deflection defined by γ_i.

The deflection of the column can be generally expressed with the equation in Equation (17).

$$y = \delta_i \left[\frac{1 - \cos\left(L\sqrt{\frac{F}{EI}}\right)}{\sin\left(L\sqrt{\frac{F}{EI}}\right)} \right] \sin\left(z\sqrt{\frac{F}{EI}}\right) + \delta_i \cos\left(z\sqrt{\frac{F}{EI}}\right) - \delta_i \quad (17)$$

The maximum lateral deflection of the column, y_{max} occurs at $z = {}^{L}/_{2}$. With this,

$$y_{max} = \delta_i \left[\sec\left(\frac{L}{2}\sqrt{\frac{F}{EI}}\right) - 1 \right] \quad (18)$$

Assume that the initial lateral deflection, δ_i follows a radial curvature as shown in Figure 5-39, the initial deflection takes the expression shown in Equation (19).

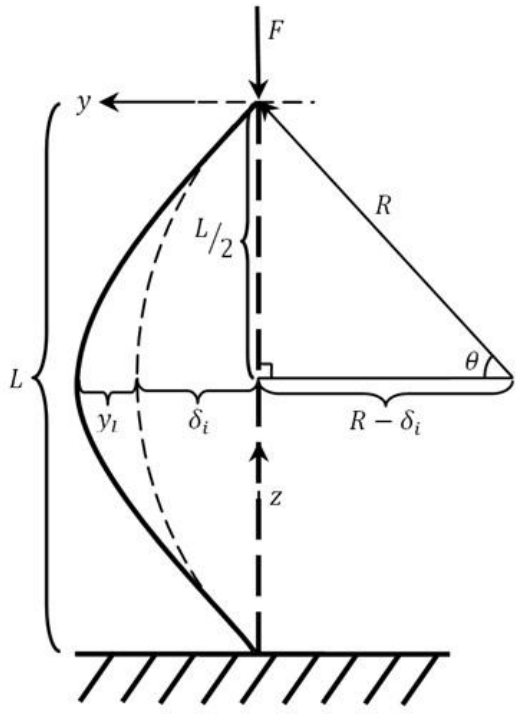

Figure 5-39 : Column with an initial deflection that follows a radial curvature. The representation is similar to that of Figure 5-38 with the difference being in terms of the initial deflection.

$$\delta_i = \left[R - {}^{L}/_{2}\cot(\theta)\right] \quad (19)$$

The maximum deflection is then determined to be the expression as shown in Equation (20). Full and complete derivations are appended in Appendix B.4.3.

$$y_{max} = \left[R - \frac{L}{2}\cot(\theta)\right]\left[\sec\left(\frac{L}{2}\sqrt{\frac{F}{EI}}\right) - 1\right] \quad (20)$$

Consider the term $\left\{\sec\left[\left({}^{L}/_{2}\right)\left(\sqrt{{}^{F}/_{EI}}\right)\right]\right\}$ in the expression shown in Equation (20). As the term approaches infinity, the evaluation of $\left\{\sec\left[\left({}^{L}/_{2}\right)\left(\sqrt{{}^{F}/_{EI}}\right)\right]\right\}$ approaches ${}^{\pi}/_{2}$. As θ in the term $\left[R - {}^{L}/_{2}\cot\theta\right]$ approaches infinity, $\cot\theta$ approaches 0 and subsequently, the initial deflection approaches the value of the radius of curvature. The radius of curvature thus acts as a scaling factor to the resulting maximum lateral deflection. With this, the main contribution along the split plane is mainly made by R as shown in Equation (20). Hence, a higher radius of curvature will result in higher maximum deflection and thus imply lower bending resistance.

To oversee the contributions to the normalised wall thickness and/or the normalised radius of curvature to the resulting effective modulus with respect to the different cross-sectional planes, a ranking system is established. This will show how one model succeeds another in terms of the effective modulus with respect to the parameters mentioned above. The reconstructed unit cell and the original Schwarz P unit cell model is ranked between 1 and 2, with the ranking numbers indicating the expectancy for higher values of deflections i.e. low modulus values. Hence, a ranking of 2 would imply low deflections and thus imply higher modulus values.

Table 5-23 : Evaluation of ratios between cube of normalised radius of curvature and the normalised wall thickness along the plane YZ and YX; and the normalised radius of curvature along the split plane for the reconstructed unit cell model and the original Schwarz P unit cell. Rank numberings indicate the expectancy for high values of deflections i.e. low modulus values and is numbered in brackets. Specifications for the calculations for the ratio and the normalised radius of curvature can be referred to the tabulated version of the results in Appendix B.4.1.

Model	Ratio between cube of normalised radius of curvature and the normalised wall thickness		Normalised radius of curvature
	Plane YZ	Plane YX	Split plane
O	1 (1)	1 (1)	1 (1)
A	0.3940 (2)	0.3493 (2)	0.638 (2)

Based on the rankings in Table 5-23, it can be observed that the normalised wall thickness and/or normalised radius of curvature of the original unit cell model consistently succeeds the reconstructed unit cell for high deflections at different cross-sectional planes. Hence, it can be deduced that the original Schwarz P unit cell is expected to have a lower effective modulus than the reconstructed unit cell.

To further add to the above, consider the porosity and normalised dimensional volume of the two models. Assuming porosity is constant between the two models, a smaller dimensional volume would imply smaller amount of void space within the confines of the unit cell available for compression. With constant application of load across the different models consisting of the same material, the unit cell with the smaller dimensional volume would give higher modulus values. The original Schwarz P unit cell design has a larger dimensional volume and porosity that is 25.96% higher compared to that of the

reconstructed unit cell. Here, it can also be deduced that the original Schwarz P unit cell is expected to have a lower effective modulus than the reconstructed unit cell. This adds into effect with the expectation that the original design should have a lower effective modulus due to its attribution in terms of the wall thickness and radius of curvature. With the above, it can be confirmed that the theoretical background for column buckling and beam bending applies to the findings in this study and is proven by consideration of the results shown in Figure 5-31 through Figure 5-36.

Consideration of the above and taking into account that the effective modulus results of the reconstructed unit cell shows only a 6.94% difference from the experimental mean modulus implies the effectiveness of reconstructing the Schwarz P unit cell CAD model to resemble an average of unit cells comprising the fabricated tissue scaffold. Initially, measurement analyses involved independently measuring the dimensional parameters on a unit cell per unit cell basis from the SEM micrographs of fabricated tissue scaffolds. Sample sets of height, width, length and wall thickness measurements were taken for reconstruction of 5 unit cells. With subsequent micromechanical analysis, it was found that the results gave discrepancies between the different unit cells despite 3 of the 5 unit cells falling within the experimental modulus range. The SEM averaging method was constructed to improve upon the initial measurement analyses methodology. The methodology and results obtained from the initial approach described above are appended in Appendix 0.

With only a small margin of error between the average effective modulus and the mean experimental modulus, the suitability of micromechanical analysis as a suitable approach to characterising the mechanical properties of Schwarz P unit cell-based tissue scaffolds can be implied. Furthermore, micromechanical analysis was able to accommodate the

geometrical transformations as a result of two-photon polymerisation. With this, the implementation of micromechanical analyses to the reconstructed unit cell model can be investigated in a more complex context of non-linear analyses. This is presented in the following sub-chapter.

Sub-Chapter 5B : Non-linear Analysis

5.8 Case III

5.8.1 Background

SEM micrographs have confirmed geometrical transformations particularly in the form of shrinkage have occurred between the intended Schwarz P unit cell design and the resulting unit cells comprising the fabricated tissue scaffolds. Measurement analyses were performed on averaged unit cell SEM micrographs to obtain measurements of different dimensional parameters. Based on the measurements, the Schwarz P unit cell CAD model was reconstructed to approximately represent an average of unit cells comprising the scaffold and thus take into account geometrical transformations before its subsequent re-implementation in revised linear analyses as discussed in Case II. The revised linear analyses gave effective modulus results with a small margin of error compared to the experimental modulus.

Following success of the linear analyses, this sub-chapter investigates micromechanical analyses of the reconstructed unit cell model in the complex context of non-linear analysis. Revised derivations for displacement boundary conditions in regards to micromechanical analysis (similar to that in Case II) is implemented to the reconstructed unit cell and oversee mechanical characterisation defined in terms of the average stress-strain response. The stress-strain curves obtained will then be compared to the experimental stress-strain curves obtained from compression experiments of fabricated Schwarz P unit cell-based tissue scaffolds.

5.8.2 Discretisation of the Reconstructed Unit Cell

The non-linear analyses investigated here considers the implementation of the reconstructed unit cell model used in Case II. Hence, the surface geometry CAD model of the reconstructed unit cell model previously implemented in the revised linear analyses is implemented here. The reconstructed unit cell CAD model was discretised into tetrahedral, hybrid C3D10H elements using the methodology described in Sub-section 5.2.3 of Section 5.2. A hyperelastic material model was assigned to the discretised unit cell model and thus required material input data in the form of nominal stress-strain data and a selection of a form of strain energy potential as discussed in Chapter 4. The nominal stress-strain data for the lower limit (based on specimen 5), the average and the upper limit (based on specimen 3) obtained from compression of bulk LCM3 cylinders are assigned to the discretised reconstructed unit cell model. A reduced polynomial with a strain energy potential order of 4 is applied as the selection for strain energy potential. The revised derivations of displacement boundary conditions for micromechanical analysis as discussed in Section 5.5 were implemented on the reconstructed unit cell model. Macroscopic load was applied at increasing values along with the displacement boundary conditions to determine respective average strain values. Information in regards to the discretised reconstructed unit cell model, the material model, the revised derivations of displacement boundary conditions and macroscopic load were compiled into an input file according to the methodology discussed in Sub-section 5.2.5 of Section 5.2. One input file was made for each macroscopic load value for each material model. Each input file was processed in ABAQUS/Standard in a dynamic, non-linear implicit analysis. With subsequent processing, the results obtained are discussed in the following sub-section.

5.8.3 Results

Average strains and average shear strain results were obtained after subsequent micromechanical analysis of the reconstructed unit cell model. Since the revised displacement boundary conditions for micromechanical analysis has already been validated in Case II, no discussion in regards to validation will be made here. However, it can be confirmed that the average strain and average shear strain results comply with the validation methods for correct implementation of displacement boundary conditions in regards to revised micromechanical analysis as discussed in Sub-section 5.5.3 of Section 5.5. A representative example for average strain and average shear strain result in regards to the compliance above is appended in Appendix B.5.1. The average stress (determined from the macroscopic load value) is plotted against the respective average strain obtained from micromechanical analysis in Figure 5-40 for each material model of LCM3. A tabulated version of the average stress-strain data is tabulated in Appendix B.5.2. The lower limit, averaged and upper limit experimental stress-strain curves obtained from compression experiments of fabricated Schwarz P unit cell-based tissue scaffolds are also plotted in the same figure. Since the fabricated scaffolds were compressed height-wise (along the y-axis), only the average stress-strain curve in the 2^{nd} degree of freedom in regards to micromechanical analyses is presented. This would allow comparisons between the experimental and computational models.

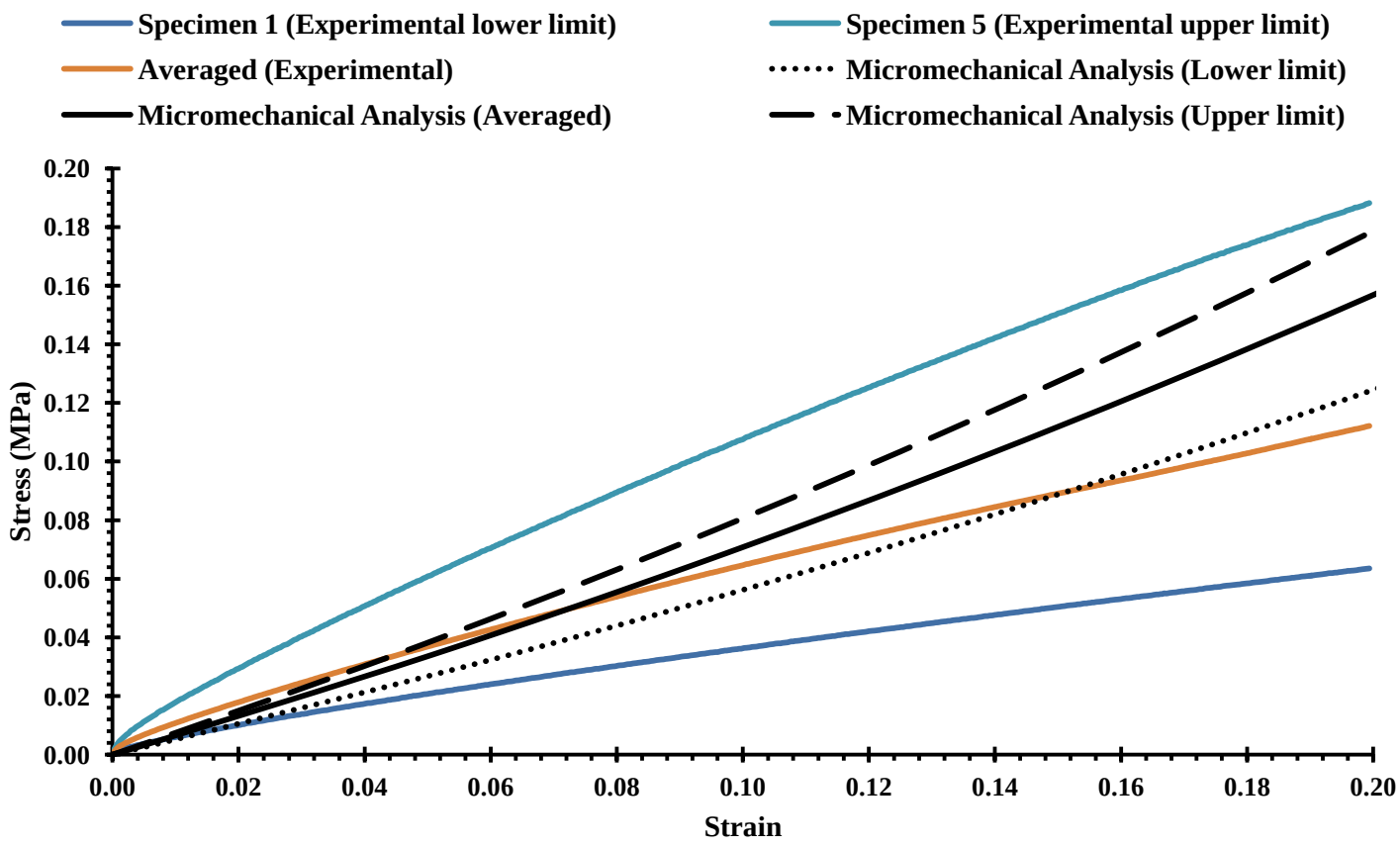

Figure 5-40 : Graphical plot of stress against strain for the lower limit, averaged and upper limit curves obtained non-linear micromechanical analyses of the reconstructed unit cell model. The lower limit, averaged and upper limit stress-strain curves obtained from experimental compression tests of physical fabricated tissue scaffolds are also presented. Specimen 1 represents the lower limit experimental stress-strain curve while specimen 5 represents the upper limit experimental stress strain curve. The region bounded by the stress-strain curves from micromechanical analysis mostly overlaps the averaged experimental stress-strain curve.

Considering Figure 5-40, it can be observed that the stress-strain curves obtained from micromechanical analysis and experimental compression tests generally show an increasing trend. However, differences in terms of this increasing trend lie in terms of their concavity. The stress-strain curve obtained from micromechanical analysis exhibits a slight upward concavity implying an increase in stiffness with increasing strains. On the other hand, the experimental stress-strain curve exhibits a downward concavity thus implying decreasing stiffness with increasing strains. This will be discussed further in the following sub-section.

5.9 Discussion

Comparisons between stress-strain curves obtained from micromechanical analyses and experimental stress-strain curves generally show an increasing trend with main differences being in terms of whether the stiffness increases or decreases with increasing strains. Early investigations considering the compression of physical fabricated Schwarz P unit cell-based tissue scaffolds have involved unconfined and confined compression experiments. Unconfined compression revolves around a similar methodology to that in Chapter 4 while confined compression involves the confinement of all four sides of a tissue scaffold positioned height-wise while undergoing compression (detailed in Appendix B.5.3). Both types of compression showed differences in terms of experimental stress-strain curves which actually correspond to those presented in Figure 5-40. The stress-strain curves for unconfined and confined compression of Schwarz P unit cell-based tissue scaffolds are graphically presented in Figure 5-41. It can be observed that the experimental stress-strain curve obtained from unconfined compression shown in Figure 5-41(a) corresponds to the experimental stress-strain curve in Figure 5-40. The experimental stress-strain curve obtained from confined compression shown in Figure 5-41(b) on the other hand corresponds to stress-strain curves obtained from micromechanical analyses.

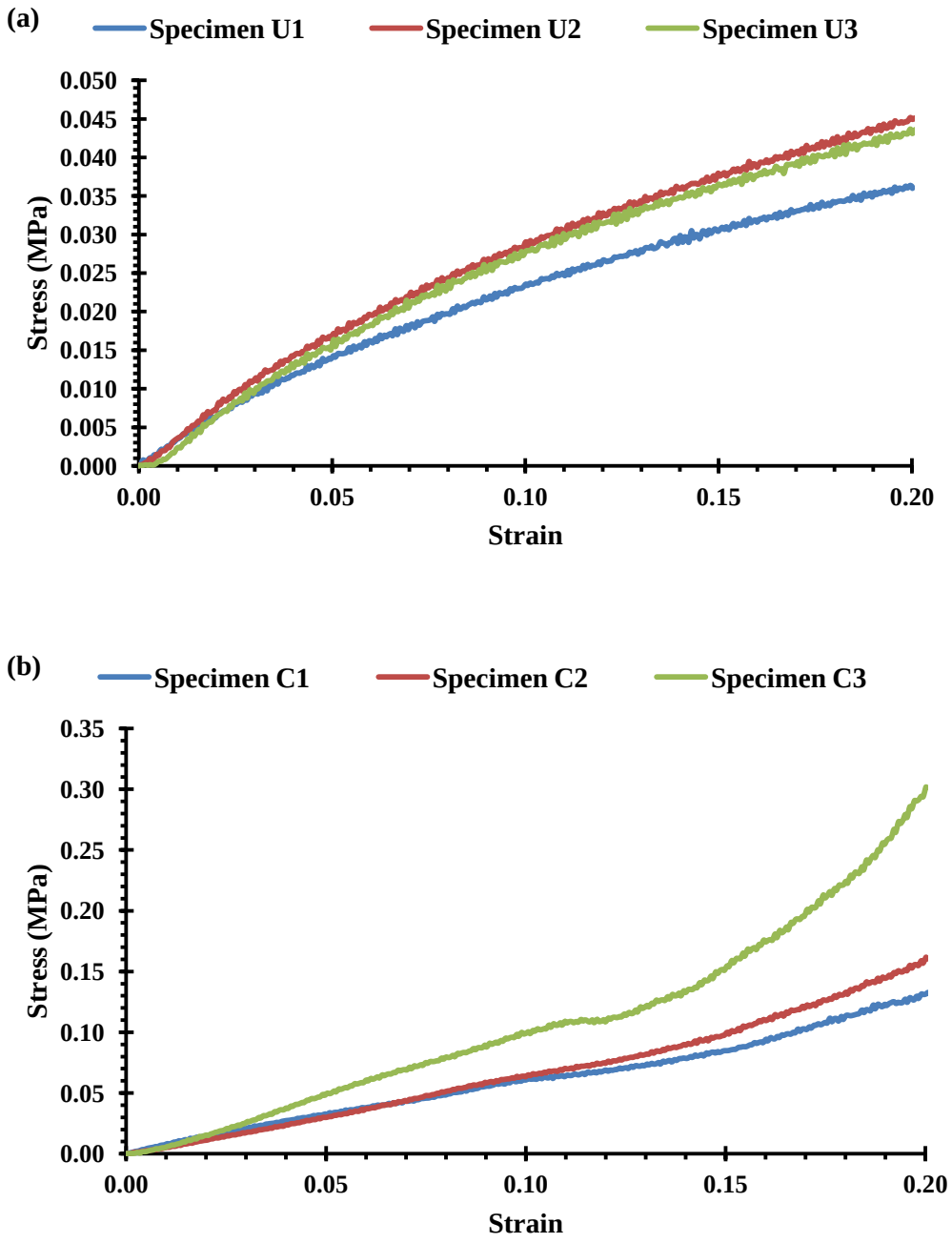

Figure 5-41 : Experimental stress-strain curves obtained from (a) unconfined and; (b) confined compression of fabricated Schwarz P unit cell-based LCM3 tissue scaffolds. The stress-strain curves in (a) correspond to that of the experimental stress-strain curves in Figure 5-40. The stress-strain curves in (b) correspond to the stress-strain curve obtained from micromechanical analysis. The methodology

in performing unconfined and confined compression of the tissue scaffolds are detailed in Appendix B.5.3.

Stress-strain curves of elastomeric cellular foams such as the Schwarz P unit cell-based tissue scaffolds considered in this study can be typically characterised by an 'S' shaped curve consisting of three different regimes i.e. cell wall bending, plateau and the densification regime. This is graphically presented in Figure 5-42 [215].

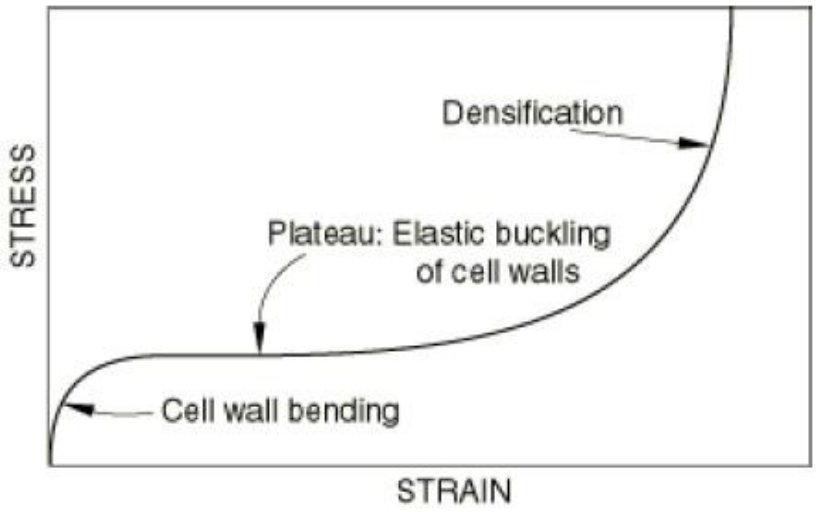

Figure 5-42 : Typical stress-strain curve of elastomeric cellular foams. The curve can be characterised by the cell wall bending regime, the plateau and the densification regime [208].

Unconfined compression of Schwarz P unit cell-based tissue scaffolds would initially undergo small deformations resulting in an approximately linear stress-strain response. With further compression, strains percolate through the structure. The persistence of high strains has been observed to be acting in a direction perpendicular to the application of load [216]. With this, the walls of the unit cells start to buckle resulting in lateral expansion of the tissue scaffold as graphically presented in Figure 5-43. At this stage, the lateral expansion serves as a damping effect resulting in reduction of longitudinal

stiffness [217]. The above would describe the experimental stress-strain curves obtained in Figure 5-40 and how it is complemented by the experimental stress-strain curve obtained from unconfined compression in Figure 5-41.

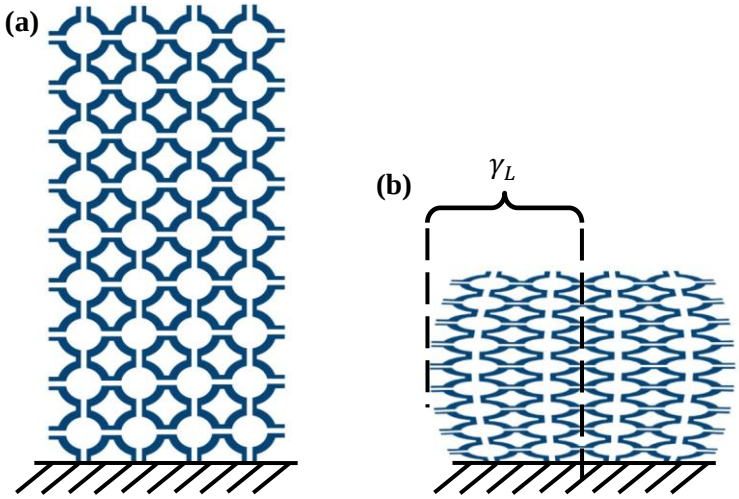

Figure 5-43 : Graphical presentation of unconfined compression of Schwarz P unit cell-based tissue scaffolds. (a) Graphical representation of Schwarz P unit cell-based tissue scaffolds before compression; (b) Graphical representation of unconfined compression which results in lateral expansion, γ_L. The pore spaces within the unit cells couple with the lateral expansion acts as a damping effect resulting in reduction of longitudinal stiffness.

During confined compression, physical tissue scaffolds initially undergo small deformations to give a linear stress-strain response similar to as in unconfined compression. At a critical compressive strain, the walls of Schwarz P unit cells buckle without the occurrence of lateral expansion since the sides of the scaffold are confined as graphically presented in Figure 5-44. With further compression, internal contact between the walls of unit cells increasingly occurs resulting in densification. This is indicated by the slight upward concavity observed from the stress-strain curves obtained from non-linear micromechanical analysis shown in Figure 5-40. The stiffness of the scaffold

increases to a point where the response reaches that of a homogenous solid phase [217]. With this, the above would describe the stress-strain curve obtained from non-linear micromechanical analysis shown in Figure 5-40 as well as how it is complemented by the experimental stress-strain curve obtained from confined compression in Figure 5-41.

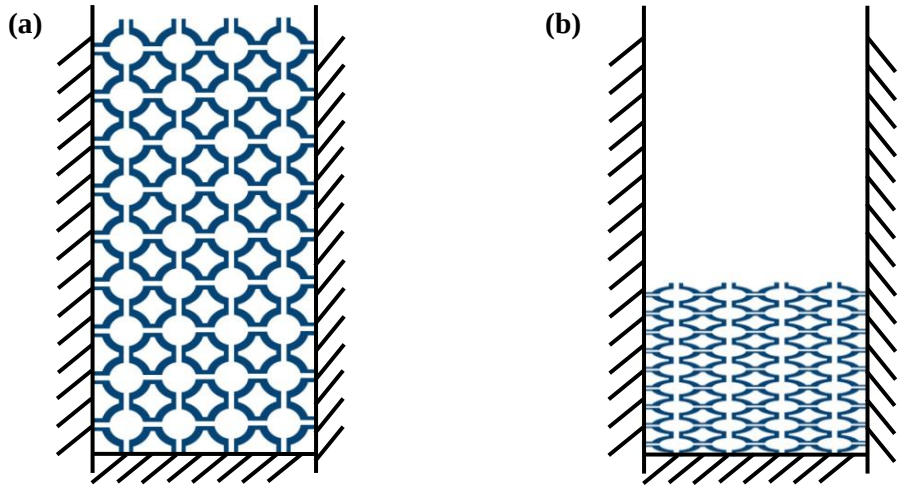

Figure 5-44 : Graphical presentation of confined compression of Schwarz P unit cell-based tissue scaffolds. (a) Graphical representation of Schwarz P unit cell-based tissue scaffolds before compression; (b) Graphical representation of confined compression. No lateral expansion occurs since the sides of the scaffolds are confined. With increasing compression, internal contact between unit cell walls increasingly occurs. This results in an increase in stiffness and is indicated by an upward concavity in terms of stress-strain curves.

From an experimental perspective, the discussions presented above have shown that non-linear micromechanical analysis considers mechanical characterisation for stress-strain response under confined compression. This also holds true from a computational perspective based on derivations of displacement boundary conditions for micromechanical analysis. The derived displacement boundary conditions are applied to two opposite faces lying along a common directional axes. Emphasising this further,

these two opposite faces consist of identical tessellations which are “tied” with a particular boundary condition. This thus gives the impression of a confined compression.

With this, the implementation of micromechanical analysis in a non-linear context can at first hand be construed to be disadvantageous. However, *in vivo* implantation of scaffolds in a defect potentially involves some form of confinement to the scaffolds and would thus simulate confined compression under load [218–220]. Therefore, micromechanical analysis in a non-linear context can potentially be implemented to oversee *in* vivo stress-strain response. Micromechanical analysis in a non-linear context would be limited in mechanical characterisation for stress-strain response of scaffolds *in vitro*. However, this can be simply mitigated by implementing micromechanical analysis in a linear context to determine the effective properties of scaffolds in an initial study instead. The effectiveness of this has been demonstrated and justified in Case II.

With micromechanical analysis having been established in the context of linear and non-linear analysis, it would prove beneficial to construct a predictive model for the design of Schwarz P unit cell architectures. Mechanical characterisation in terms of effective modulus would give good initial indications to the suitability of a design from a mechanical aspect. Coupled with design considerations in terms of the different dimensional parameters making up the Schwarz P unit cell architecture, biological aspects can also be considered. This is presented in the following sub-chapter.

Sub-Chapter 5C : Predictive Modeling

5.10 Predictive Modeling of Schwarz P Unit Cell Designs

5.10.1 Background

Micromechanical analysis has proved itself to be a suitable approach in characterising the mechanical properties of the Schwarz P unit cell-based tissue scaffolds considered in this study. Linear analyses that was performed and rectified to take into account geometrical transformations gave computational results that are in excellent agreement with the experimental results in a small margin of error. Non-linear analyses that were performed has demonstrated and placed the computational mechanical characterisation of the tissue scaffold in a more realistic context considering *in vivo* implantation. With the above in mind, the generalisation of the inter-relationships between different dimensional parameters of the unit cell to the mechanical properties of the Schwarz P unit cell structure defined in terms of the modulus can be performed by implementing micromechanical analysis in linear analyses to construct a predictive model. Throughout this sub-chapter, the term ‘height’ will be used interchangeably to refer to the width and length since height is equivalent to the two latter dimensional parameters.

This sub-chapter discusses the different dimensional parametric configurations in modeling Schwarz P unit cells for linear analyses. Schwarz P minimal surfaces can be configured according to two different modeling constraints i.e. Schwarz P structures with thickness variations at constant surface radius and Schwarz P structures with radius variations at constant thickness. Schwarz P unit cells considered in this part of the study are based on Schwarz P structures with thickness variations at constant surface radius. The material data assignment for discretised models of the unit cells along with the

implementation of displacement boundary conditions for micromechanical analysis is also discussed. Subsequently, the relationship between different configurative dimensional parameters to the effective modulus will be determined. From there, mathematical expressions describing the relationships will also be determined.

5.10.2 Configurations for Schwarz P Unit Cells

The original Schwarz P unit cell CAD model was used as a foundation to create unit cells with different configurations. The original height of the unit cell was scaled accordingly using the 'Scaling' reconstruction technique discussed in Sub-section 5.4.5 of Section 5.4. At each scaled height, the wall thickness was also scaled accordingly using the 'Offset' reconstruction technique discussed in the same sub-section. The configurations for all the Schwarz P unit cells that have been modeled are tabulated in Table 5-24. The internal pore throat size, pore size and porosity were determined after subsequent scaling of the original Schwarz P unit cell CAD model with respect to each configuration set of height and wall thickness.

Table 5-24 : Dimensional parameters of Schwarz P unit cells used to scale the height and wall thickness of the unit cells. The internal pore throat size, pore size and porosity were measured after subsequent scaling of the original Schwarz P unit cell model.

Height (= Width = Length) (mm)	Wall thickness (mm)	Internal pore throat size (mm)	Pore size (mm)	Porosity (%)
0.48	0.01278	0.2272	0.4029	88.2
	0.02558	0.2144	0.3901	77.8
0.50	0.01331	0.2367	0.4197	88.2
	0.02665	0.2233	0.4063	77.8
	0.03999	0.2100	0.3930	68.6

	0.05332	0.1967	0.3797	60.4
	0.06665	0.1834	0.3665	52.9
0.52	0.01385	0.2462	0.4365	88.2
	0.02772	0.2323	0.4226	77.8
	0.04158	0.2184	0.4087	68.6
	0.05545	0.2046	0.3950	60.4
	0.06932	0.1907	0.3817	52.9
0.54	0.01438	0.2556	0.4533	88.2
	0.02878	0.2412	0.4389	77.8
	0.04318	0.2268	0.4245	68.6
	0.05758	0.2124	0.4100	60.4
	0.07199	0.1980	0.3955	52.9
0.56	0.01491	0.2651	0.4700	88.2
	0.02985	0.2502	0.4551	77.9
	0.04478	0.2352	0.4402	68.6
	0.05972	0.2203	0.4252	60.4
	0.07465	0.2054	0.4102	52.9
0.58	0.01544	0.2746	0.4868	88.2
	0.03091	0.2591	0.4714	77.9
	0.04638	0.2436	0.4559	68.6
	0.06185	0.2282	0.4404	60.4
	0.07732	0.2127	0.4250	52.9
0.60	0.01598	0.2840	0.5036	88.2
	0.03198	0.2680	0.4876	77.9
	0.04798	0.2520	0.4718	68.6
	0.06398	0.2360	0.4556	60.3
	0.07998	0.2200	0.4396	52.9

5.10.3 Schwarz P Unit Cell Discretisation

Each unit cell model tabulated in Table 5-24 was discretised with second-order tetrahedral C3D10 elements using the mesh discretisation methodology described in Sub-section 5.2.4 of Section 5.2. Linear analyses require the input of bulk material Young's modulus and Poisson's ratio, both discussed in Chapter 4. Similar to all three previous cases, the lower, averaged and upper limit material data of bulk LCM3 was used. Hence, the Young's modulus for the lower limit (based on specimen 5), the average and the upper limit (based on specimen 3) were assigned to each discretised unit cell model for 3 main separate analyses. The value of Poisson's ratio is taken to be 0.3. With equivalency between height, width and length, the displacement boundary conditions derived for a simple cubic packing system (discussed in Sub-section 5.2.3 of Section 5.2) was implemented for micromechanical analyses. Information in regards to the discretised unit cell models, the material model considered and the displacement boundary conditions for micromechanical analysis along with the application of load were compiled. The input file for each configuration was processed in a static, linear perturbation analysis through ABAQUS/Standard. The results obtained were post-process and are presented in the following sub-sections.

5.10.4 Results

The average strains and average shear strains have been obtained from micromechanical analysis of each unit cell model configured with the dimensional parameters tabulated in Table 5-24 in due respect to the different material models of LCM3. Since the implementation of displacement boundary conditions for micromechanical analysis based on a simple cubic packing system have been previously validated in Sub-section 5.2.7 of Section 5.2 and in Case I, no further discussion for validation will be made here. Based

on the results for average strains, the effective modulus was subsequently determined. Tabulated forms for these results with respect to each material of LCM3 are presented in Appendix B.6.1.

Several relationships between different dimensional parameters and the effective modulus values determined previously will be considered. They are as follows, (a) Height vs. internal pore throat size vs. pore size; (b) Height vs. pore size vs. wall thickness; (c) Height vs. pore size vs. volume; (d) Height vs. pore size vs. porosity; (e) Height vs. pore size vs. average effective modulus. A custom MATLAB algorithm was implemented to produce a 3-dimensional surface plot to oversee the relationships mentioned above. This algorithm cycles through different types of fits and evaluates the root-mean-square error (RMSE). The best fit type is selected based on the lowest value of RMSE before producing a 3D surface plot of the relationship being considered with respect to the selection. Mathematical expressions based on the surface plot were determined that would describe the relationships. Each relationship considered is divided into different subsub-sections and are presented in the following.

5.10.4.1 Height vs. Internal Pore Throat Size vs. Pore Size

The surface plot for the relationship between height, the internal pore throat size and pore size is shown in Figure 5-45. The relationship can be expressed through the mathematical expression in Equation (21).

$$P_S(H, D_T^{Int}) = \begin{matrix} 0.001825 + 0.4560H + 0.7906D_T^{Int} - 0.8258(H \times D_T^{Int}) - \\ 1.8129(D_T^{Int})^2 + 1.8776[H \times (D_T^{Int})^2] - 4.0502(D_T^{Int})^3 \end{matrix} \quad (21)$$

for which,

P_S : Pore size (mm)

H : Height of the unit cell (mm)

D_T^{Int} : Internal pore throat size (mm)

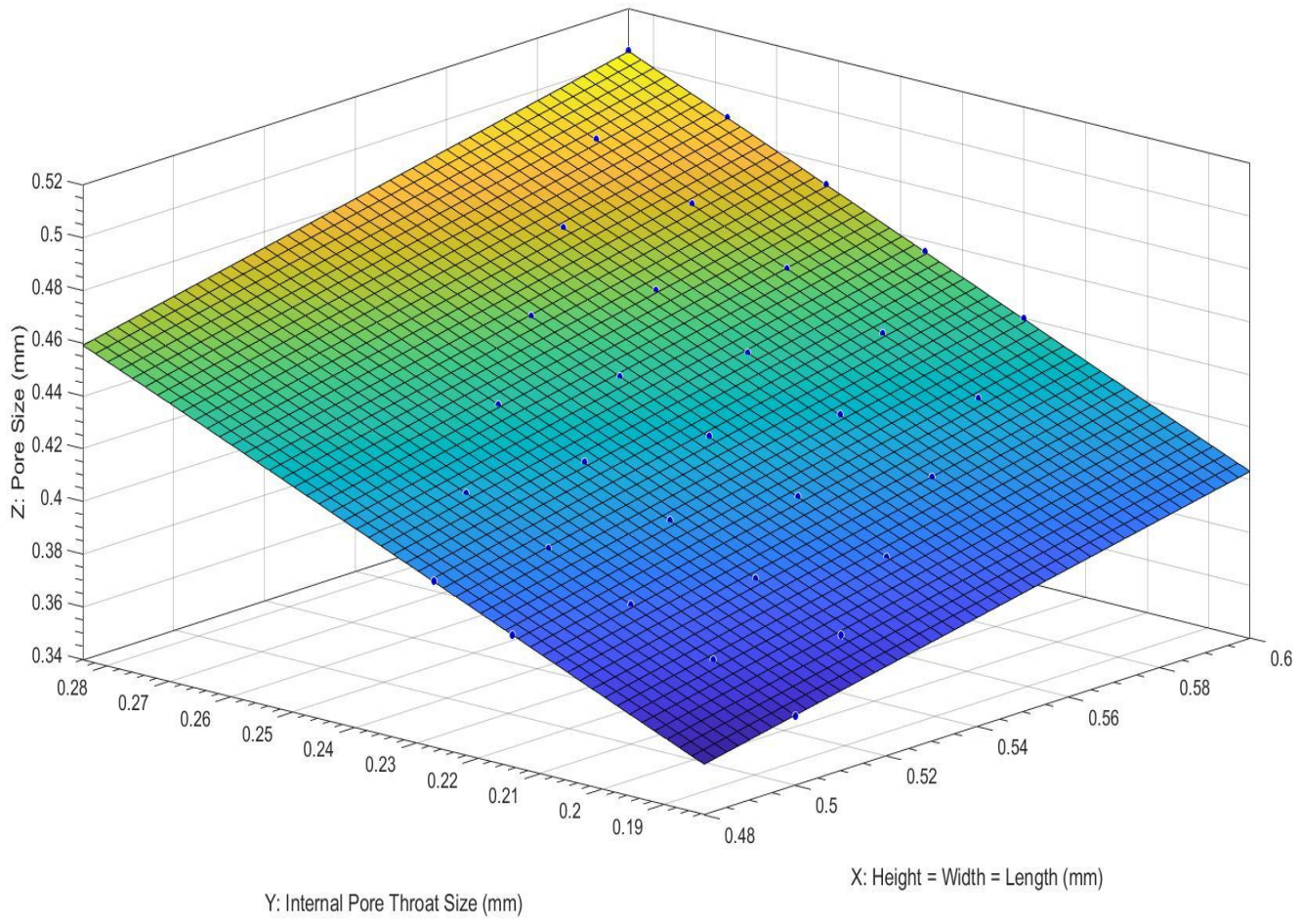

Figure 5-45 : 3D surface plot relating the height, internal pore throat size and pore size of Schwarz P unit cells with configurations tabulated in Table 5-24. A linear relationship in 3-dimensional space can be observed from the surface plot relating the height, pore size and internal pore throat size.

5.10.4.2 Height vs. Pore Size vs. Wall Thickness

The surface plot for the relationship between height, pore size and wall thickness is shown in Figure 5-46. The relationship between the height, pore size and wall thickness can be expressed through the mathematical expression in Equation (22).

$$T(H, P_S) = \begin{matrix} -0.05608 + 1.3398H - 1.1930P_S - 2.2042(H \times P_S) + \\ 1.8090(P_S)^2 + 2.5570[H \times (P_S)^2] - 2.4498(P_S)^3 \end{matrix} \quad (22)$$

for which,

T : Wall thickness (mm)

H : Height of unit cell (mm) ; The height is equivalent to the width and length

P_S : Pore size (mm)

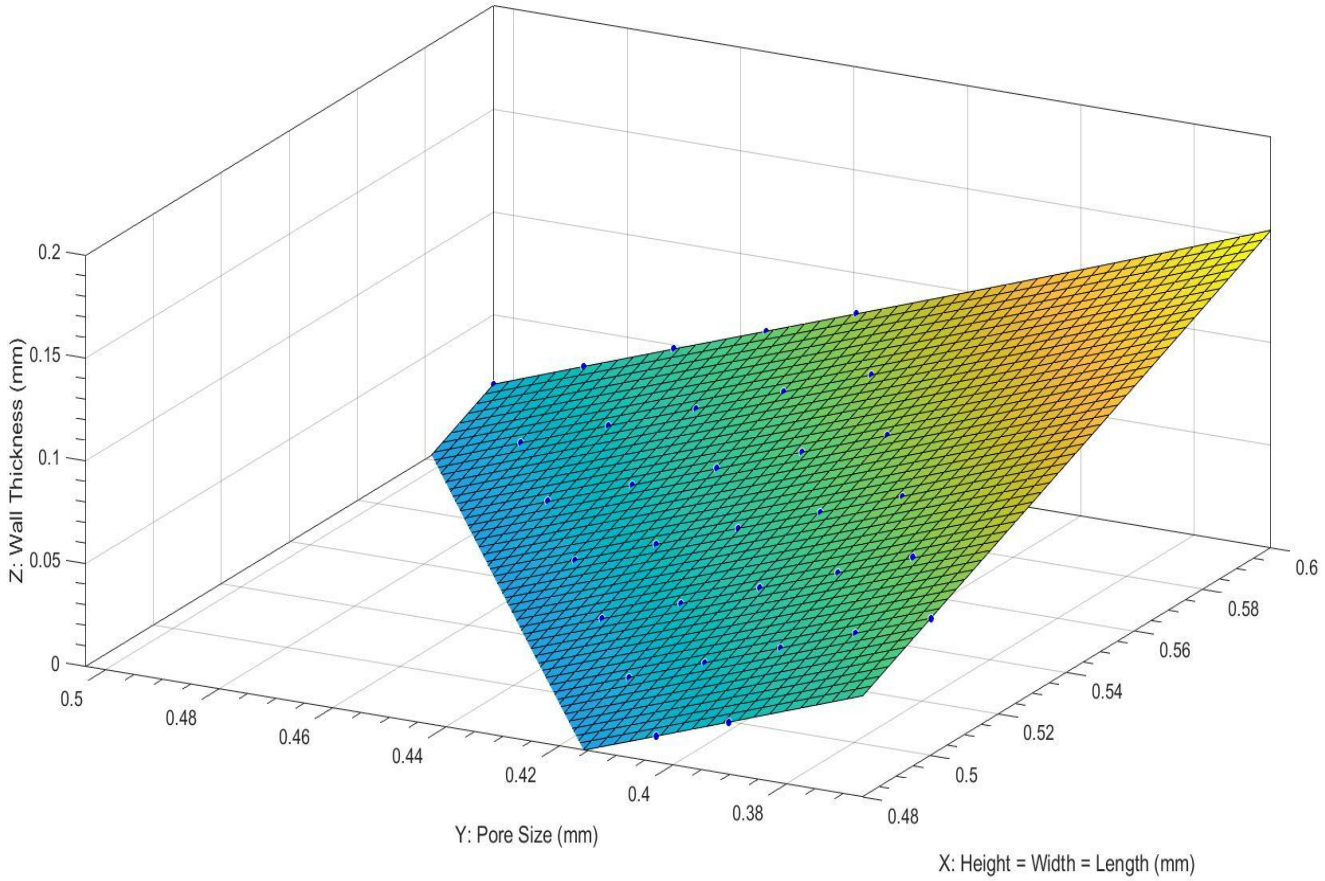

Figure 5-46 : 3D surface plot relating the height, pore size and wall thickness of Schwarz P unit cells with configurations tabulated in Table 5-24. The relationship between the height, pore size and wall thickness can be characterised by a linear surface in a 3-dimensional space. Results in the negative region (for $Z \leq 0$) were removed.

5.10.4.3 Height vs. Pore Size vs. Volume

The surface plot the relationship between height, pore size and volume is shown in Figure 5-47. The relationship for the parameters above can be mathematically expressed as shown in Equation (23).

$$V(H, P_S) = \begin{matrix} -0.03068 + 0.3028H - 0.1595P_S - 0.06786H^2 - \\ 1.2645(H \times P_S) + 1.1653(P_S)^2 + 1.0245(H)^3 + \\ 1.2321[(H)^2 \times P_S] - 2.5684[H \times (P_S)^2] \end{matrix} \quad (23)$$

for which,

V : Volume (mm^3)

H : Height of unit cell (mm) ; The height is equivalent to the width and length.

P_S : Pore size (mm)

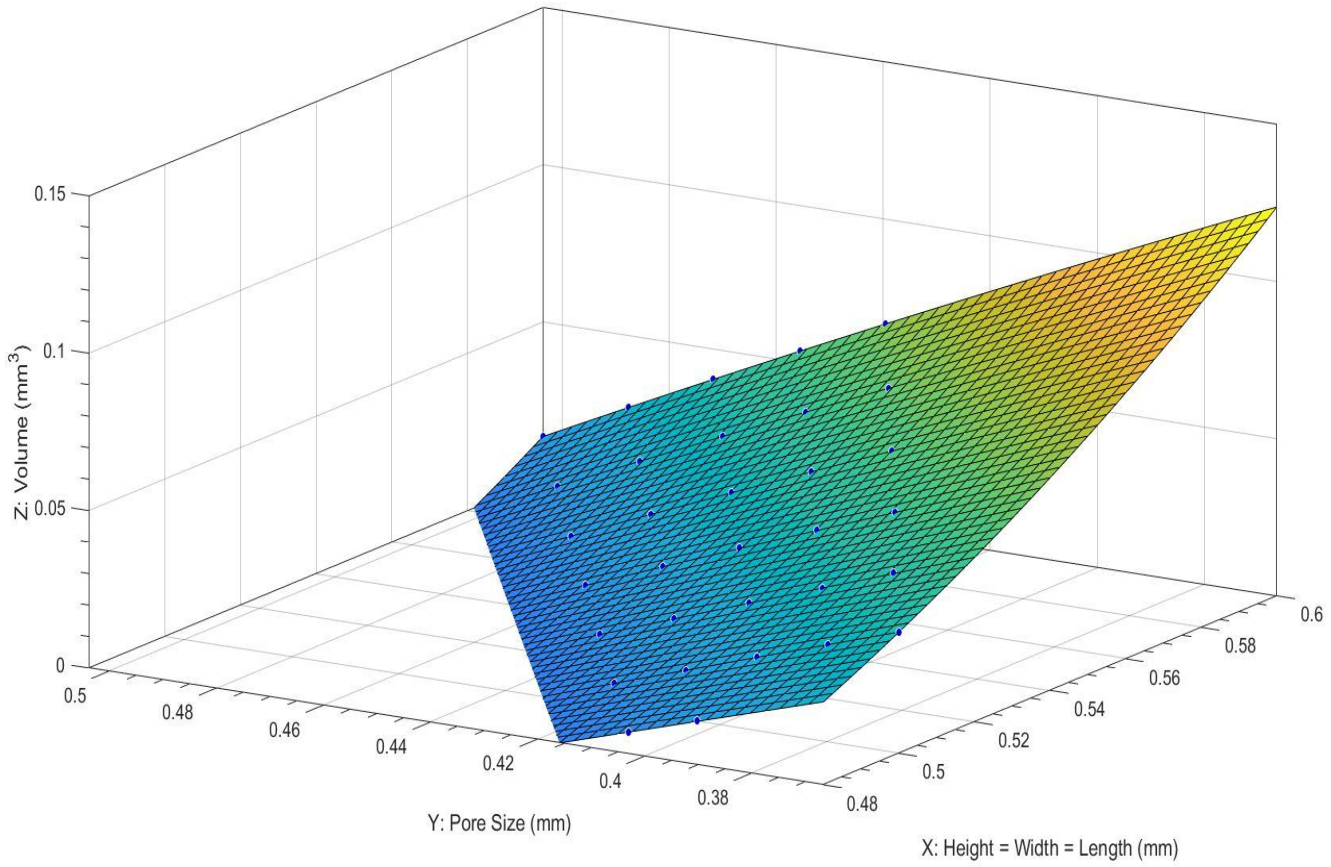

Figure 5-47 : 3D surface plot relating the height, pore size and volume of Schwarz P unit cells with configurations tabulated in Table 5-24. The relationship can be characterised by a linear surface in a 3-dimensional space. The results for negative values ($Z \leq 0$) of volume are omitted from the graphical plot.

5.10.4.4 Height vs. Pore Size vs. Porosity

The relationship between height, pore size and porosity can be characterised through a surface plot as shown in Figure 5-48 and is mathematically expressed in Equation (24).

$$\phi(H, P_S) = \begin{matrix} 1.3359 - 20.6149H + 21.5883P_S + 80.9399H^2 - \\ 143.0543(H \times P_S) + 61.9970(P_S)^2 - 123.7658(H)^3 + \\ 339.0583[(H)^2 \times P_S] - 321.7975[H \times (P_S)^2] + 106.7835(P_S)^3 \end{matrix} \quad (24)$$

for which,

ϕ : Porosity (in fractions)

H : Height of the unit cell (mm)

P_S : Pore size (mm)

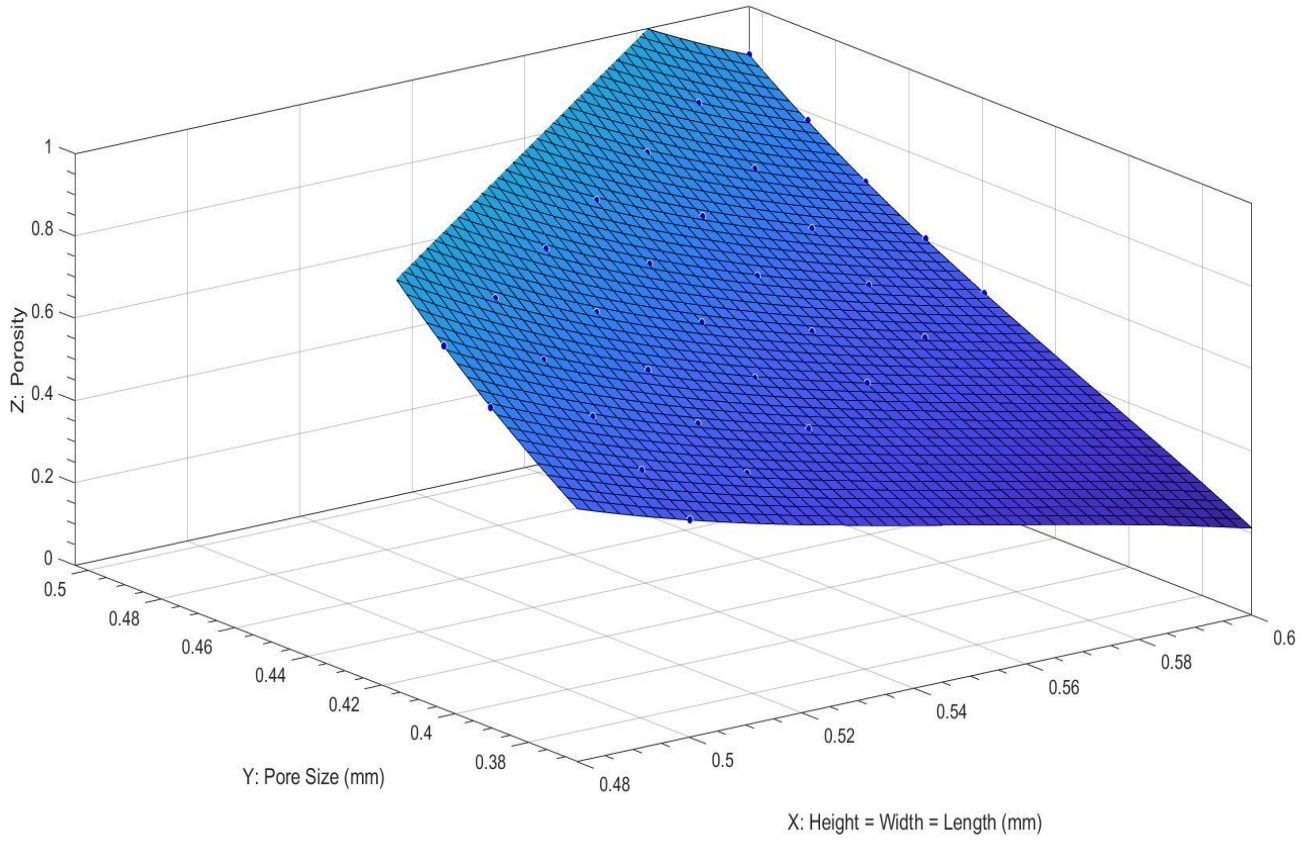

Figure 5-48 : 3D surface plot relating the height, pore size and porosity of Schwarz P unit cells with configurations tabulated in Table 5-24. The porosity values in the mentioned table are taken in fractions rather than percentages in plotting the 3D surface above. The graphical plot relating the height, pore size and porosity obtained is characterised by a slight curvature. The maximum porosity in any one structure is 100% (also equivalent to 1). Hence, plots for porosity being more than 1 ($Z \geq 1$) were removed.

5.10.4.5 Height vs. Pore Size vs. Averaged Effective Modulus

As discussed previously, the Schwarz P unit cell configurations tabulated in Table 5-24 were implemented with three different material models based on LCM3 i.e. the lower limit (based on specimen 5), the average and the upper limit (based on specimen 3). Hence, three different 3D surface plots were obtainable respective of the material model considered. The 3D surface plots relating the height, pore size and average effective modulus for unit cells assigned the lower limit, average and upper limit material model are shown in Figure 5-49, Figure 5-50 and Figure 5-51 respectively.

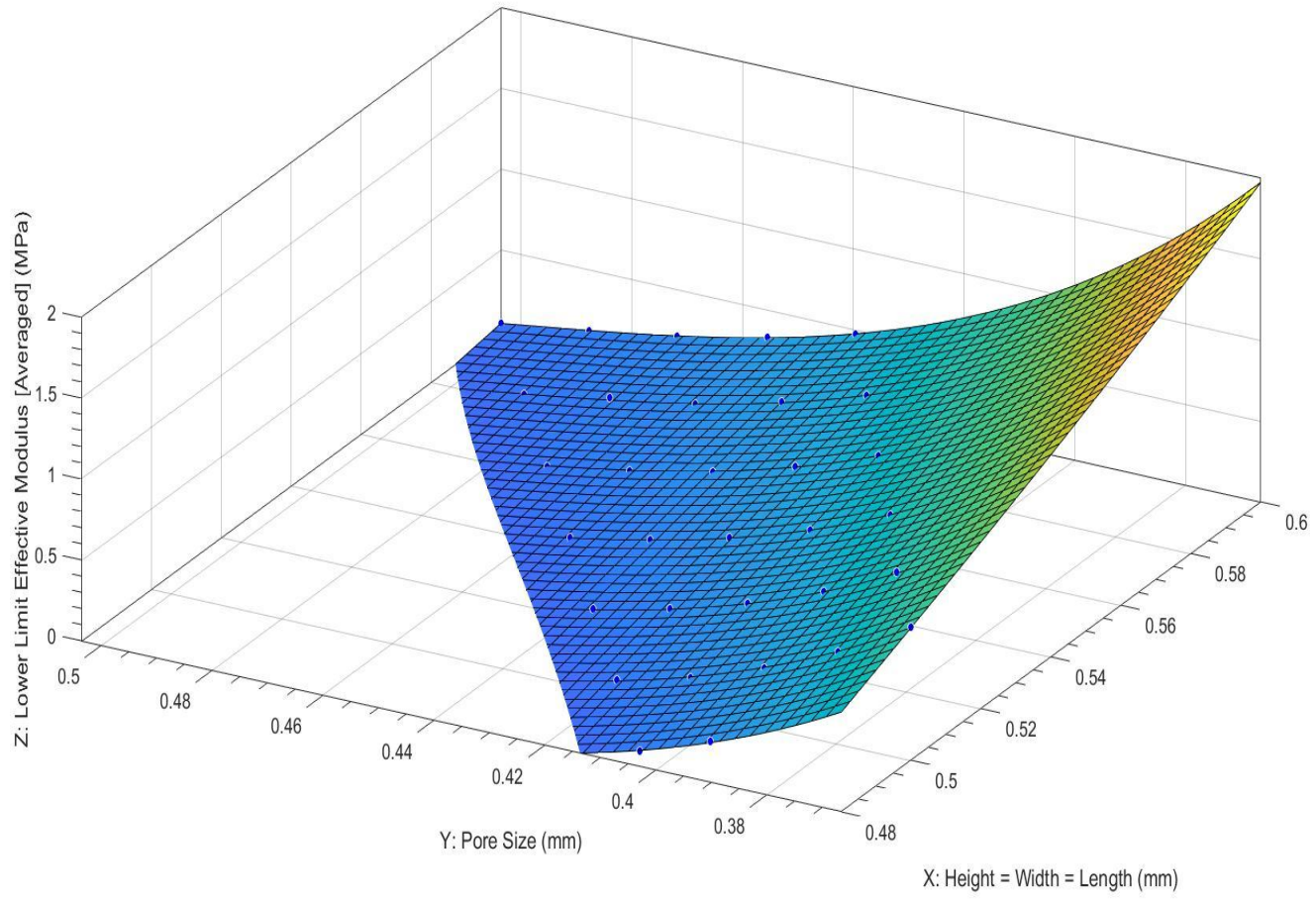

Figure 5-49 : 3D surface plot showing the relationship between height, pore size and the averaged effective modulus for Schwarz P unit cells assigned the lower limit material data of LCM3. The lower limit material data is based on specimen 5 of LCM3. For the surface plot above, negative effective modulus are removed ($Z \leq 0$).

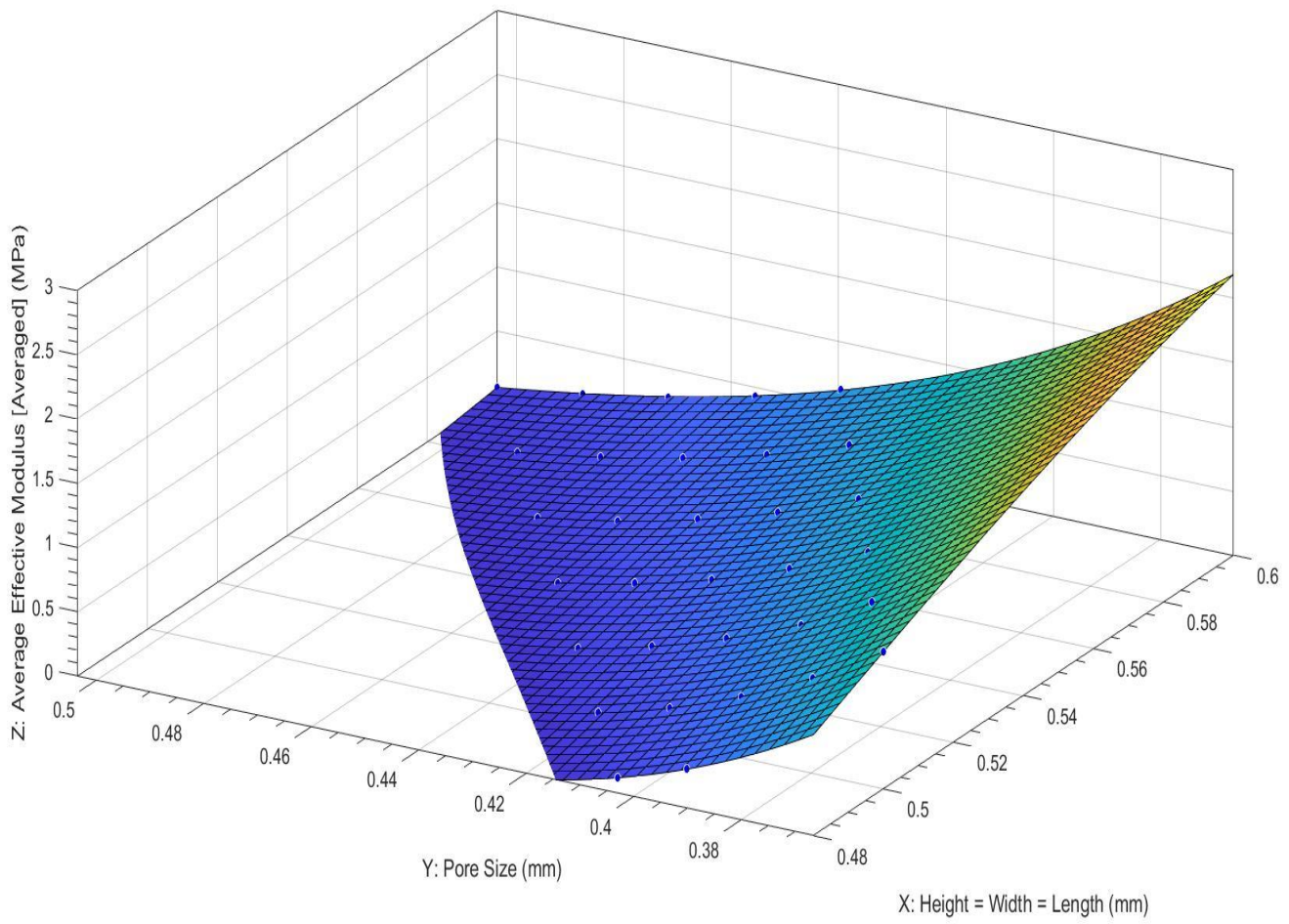

Figure 5-50 : 3D surface plot showing the relationship between height, pore size and the average effective modulus for Schwarz P unit cells assigned the averaged material data of LCM3. The negative effective modulus ($Z \leq 0$) are removed from the presentation.

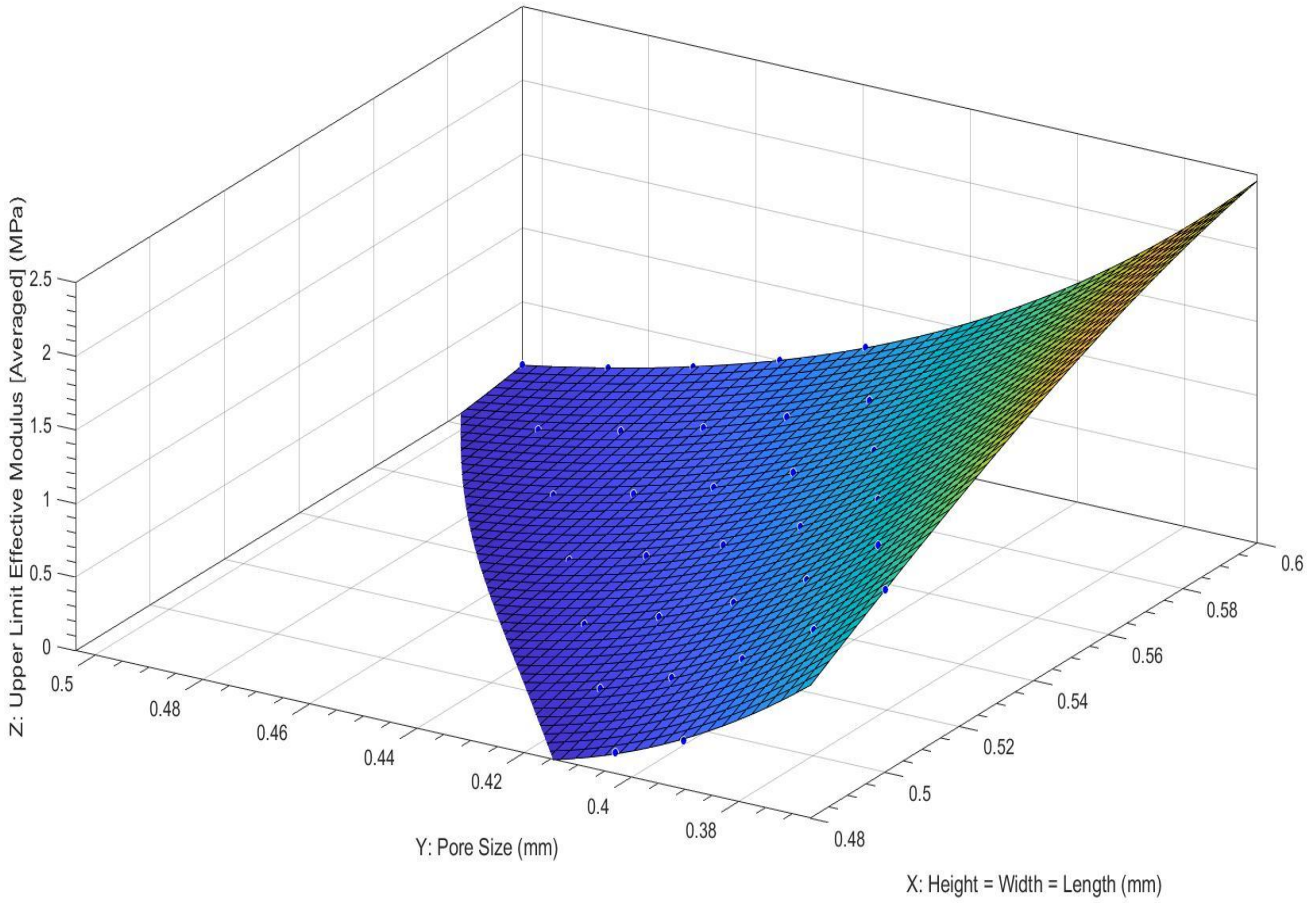

Figure 5-51 : 3D surface plot showing the relationship between height, pore size and the average effective modulus for Schwarz P unit cells assigned the upper limit material data of LCM3. The upper limit material data is based on specimen 3 of LCM3. Similar to as in Figure 5-49 and Figure 5-50, the negative effective modulus ($Z \leq 0$) are removed from presentation of the surface plot.

The relationship between the height, pore size and effective modulus with respect to different material models can be expressed through the mathematical expressions in Equations (25), (26) and (27).

$$\bar{E}_L(H, P_S) = 12.1226 + 70.7383H - 162.9120P_S - 248.2683(H \times P_S) + 467.1744(P_S)^2 + 226.1802[H \times (P_S)^2] - 394.3009(P_S)^3 \quad (25)$$

$$\bar{E}_A(H, P_S) = 5.2316 + 136.6879H - 195.7460P_S - 25.1083H^2 - 464.6575(H \times P_S) + 660.3726(P_S)^2 - 126.0483(H)^3 + 545.9054[(H)^2 \times P_S] - 245.5728[H \times (P_S)^2] - 321.1958(P_S)^3 \quad (26)$$

$$\bar{E}_U(H, P_S) = 1.2388 + 182.6031H - 224.2892P_S - 51.6708H^2 - 592.6229(H \times P_S) + 793.9714(P_S)^2 - 181.7815H^3 + 822.6547[(H)^2 \times P_S] - 466.0832[H \times (P_S)^2] - 316.5523(P_S)^3 \quad (27)$$

for which,

$\bar{E}_L$: Average effective modulus in linear analyses with lower limit material model (MPa)

$\bar{E}_A$: Average effective modulus in linear analyses with the averaged material model (MPa)

$\bar{E}_U$: Average effective modulus in linear analyses with the upper limit material model (MPa)

H : Height of unit cells (mm)

P_S : Pore size of unit cells (mm)

5.11 Discussion

The design for a Schwarz P unit cell and its subsequent array into a tissue scaffold can be done in consideration of mechanical and biological aspects. In this study, the mechanical aspect would consider the mechanical properties defined in terms of the modulus; the biological aspect would consider cell infiltration into the unit cells and hence their migration throughout the rest of the tissue scaffold. The pore size dictates cell adhesion, migration, tissue formation as well as the exchange of nutrients and oxygen as well as the removal of waste [221].

Schwarz P unit cells have been modeled at variations of thickness at constant surface radius. Unit cells were configured at different scaled heights and scaled wall thickness with each respective height. The internal pore throat size, the pore size and the porosity was determined after reconstruction for each configuration. Following discretisation and subsequent implementation of micromechanical analysis, the effective modulus was determined. In post-processing the entirety of the results, 3D surface plots were created to give a graphical presentation of the relationships relating different parameters. Mathematical expressions describing these relationships were also determined.

In implementing the mathematical expressions for design, a particular set of height and pore size can be initially selected before using the respective values to subsequently determine the wall thickness, pore throat size, volume, porosity and effective modulus. However, since the pore throat size does dictate cell infiltration and cell migration through a tissue scaffold, it is essential to initially select a set of height and pore throat size instead. This will decidedly be more efficient in the design process since the pore throat size is always smaller compared to the pore size for a Schwarz P architecture as graphically presented in Figure 5-45. The pore size can subsequently be determined using

Equation (21). In cases where a set of height and pore size is initially chosen, the graphical surface plot and the mathematical expression relating height and pore size to the resultant pore throat size is appended in Appendix B.6.2. Once a suitable pore size has been determined, the wall thickness, volume and porosity can be determined using the equations derived in Equations (22), (23) and (24) respectively.

Since the relationships between different dimensional parameters are structure-dependent, the equations derived in Equations (21) through (24) can be implemented regardless of the material model in the context of Schwarz P structures with thickness variations at constant surface radius. Despite this, the relationships between different dimensional parameters are interdependent of each other and therefore the implementation of any of the equations should not be used in isolation. This also applies for the equations for effective modulus. The effective modulus is a material dependent property. Three different material data for LCM3 i.e. lower, averaged and upper limit were assigned as material models in performing linear analyses via micromechanical analysis. With the Young's modulus values for each material data, the effective modulus equations obtained can generally be normalised as shown in Equation (28).

$$\bar{E}^{*}_{lim} = \frac{\bar{E}_{lim}}{E_{lim}} \quad (28)$$

for which,

$\bar{E}^{*}_{lim}$: Normalised effective modulus for a particular limit [lim : L (lower limit) ; lim : A (average) or lim : U (upper limit)] (MPa)

$\bar{E}_{lim}$: Effective modulus for material model based on the limit, lim

E_{lim} : Young's modulus of LCM3 sample material model based on the limit, lim

With the above, the equations (29), (30) and (31) for normalised effective modulus can be obtained.

$$\bar{E}_L^*(H, P_S) = 2.7604 + 16.1073H - 37.0955P_S - 56.5314(H \times P_S) + 106.3769(P_S)^2 + 51.5019[H \times (P_S)^2] - 89.7834(P_S)^3 \quad (29)$$

$$\bar{E}_A^*(H, P_S) = 0.9114 + 23.8135H - 34.1024P_S - 4.3743H^2 - 80.9516(H \times P_S) + 115.0486(P_S)^2 - 21.9598(H)^3 + 95.1064[(H)^2 \times P_S] - 42.7831[H \times (P_S)^2] - 55.9580(P_S)^3 \quad (30)$$

$$\bar{E}_U^*(H, P_S) = 0.1864 + 27.4722H - 33.7437P_S - 7.7737H^2 - 89.1585(H \times P_S) + 119.4509(P_S)^2 - 27.3485H^3 + 123.7662[(H)^2 \times P_S] - 70.1210[H \times (P_S)^2] - 47.6245(P_S)^3 \quad (31)$$

No ranges of values were established for valid implementation of each of the equation obtained. Since the equations relating different dimensional parameters are interdependent of each other, a maximum range can be established based on the height, internal pore throat size and pore size of the original Schwarz P unit cell i.e. height = 0.52mm, internal pore throat size = 0.246mm and pore size = 0.436mm. This maximum range is scalable and hence the scaled internal pore throat size and pore size would serve as the maximum range at a particular scaled height.

A custom MATLAB algorithm was constructed taking into account the above to determine sets of height in the range of 0.1mm – 1.0mm and internal pore throat size in the range of 0.1mm – 0.9mm (i.e. 100μm – 900μm) while also fulfilling the following conditions :

- 0 < Porosity (in fractions) < 1 i.e. 0% < Porosity (in percentage) < 100%
- Wall thickness > 0
- Volume > 0

Initial construction of the algorithm showed that some normalised effective modulus values and subsequent effective modulus values; at a particular height and internal pore throat size were of negative values. Since a range of effective modulus values is obtainable at any one particular height and internal pore throat size (as a result of obtained lower, averaged and upper limit equations for normalised effective modulus), extra conditions shown in the following must be fulfilled in regards to the algorithm :

- Lower limit effective modulus < Averaged limit effective modulus
- Averaged limit effective modulus < Upper limit effective modulus
- Upper limit effective modulus > 0

The upper limit effective modulus value obtained must always be of positive value. In cases where the lower and/or averaged limit effective modulus value is of negative value, only the upper limit value should then be considered. Based on the algorithm (appended in Appendix B.6.3), 8,727 potential designs fulfill the conditions mentioned above. The range of values for dimensional parameters to be used in respective equations cannot be generalised since a particular height considered for a Schwarz P unit cell has its own range of valid internal pore throat size and pore size that would fulfill the conditions above.

Theoretically, the obtained mathematical expressions including those for normalised effective modulus serve as predictive tools in determining a suitable Schwarz P unit cell design. Hence it is only appropriate to implement the mathematical models obtained in an attempt to design a Schwarz P unit cell for applications outside of this current study in conjunction to available literature. In designing a tissue engineering scaffold, the structure must be able to maintain sufficient mechanical properties in order to ensure its

integrity once implanted. In regards to bone tissue engineering applications, the mechanical properties of the scaffold should be within range or similar to that of bone [30,222,223]. In cases where scaffolds are implemented for bone tissue regeneration purposes, another design factor to consider is the pore size and porosity which inevitability affects both the mechanical properties of the scaffold as well as its viability to provide an environment for bone tissue growth [55]. For a Schwarz P unit cell, the internal pore throat size is smaller than the pore size. Hence, a minimum internal pore size throat size of 300μm should be entailed with the design instead of the pore size. In regards to porosity, a minimum porosity of 55% should be considered along with the two previous two targets mentioned above for Schwarz P unit cell design. The justifications for the above were made based on literature review presented in Chapter 2. It shall be noted here that the pore size and porosity considered is subject to change and will be restated if required depending on the application being considered.

The following sub-section firstly discusses the implementation of the mathematical models to determine the suitability of LCM3 as a material model for Schwarz P unit cell-based tissue scaffolds in conjunction to established targets for mechanical properties, pore size and porosity mentioned previously. Various dimensional parameters for Schwarz P unit cells can be considered based on the constructed algorithm to oversee its implementation as scaffolds purposed for bone regeneration.

5.11.1 LCM3 & Optimum Schwarz P Unit Cell Design

Considering the LCM3 material model and taking into account the target values in regards to mechanical properties, pore size and porosity previously discussed into an extension of the custom algorithm, 1,192 Schwarz P unit cell configurations were obtainable; all with predicted effective modulus values which fall outside modulus values

of cortical and trabecular bone. All the designs are graphically presented in a 3-dimensional plot based on respective configurations of height, internal pore throat size and determined porosity in Figure 5-52. The minimum Schwarz P unit cell that allows the internal pore throat size and porosity target to be achieved is 0.64mm.

The configurations that gave the highest predicted effective modulus range at each one particular height among the potential designs are graphically presented in Figure 5-53 and Figure 5-54; and are also tabulated in Appendix B.6.4. Among these, the maximum range of predicted effective modulus is valued at an upper limit of 1.53MPa; obtainable from a Schwarz P unit cell configured with a height of 0.89mm, an internal pore throat size of 0.363mm and a porosity of 55%. On the other hand, a Schwarz P unit cell configured at a height of 0.78mm, an internal pore throat size of 0.363mm and a porosity of 81.9% gives the minimum range of predicted effective modulus with an upper limit of 0.11×10^{-2}MPa.

Disregarding the consideration for target pore size and porosity, the maximum attainable predicted effective modulus is valued at an upper limit of 5.59MPa. This is obtainable through a Schwarz P unit cell configured at a height of 1.0mm, an internal pore throat size of 0.375mm and a porosity of 0.13%. With the above, no Schwarz P unit cell design configurations are able to achieve the desired target for mechanical properties and subsequently no configurations are able to simultaneously achieve the desired targets for mechanical properties, pore size and porosity. This is attributed to the low mechanical stiffness of LCM3 as a material model for Schwarz P unit cell designs. This would suggest that the use of LCM3 is unsuitable for load bearing applications unless the scaffold is implanted in small sized defects or where a fixation method is implemented

along with the implantation. Hence, the Schwarz P unit cell configurations with a LCM3 material model is not completely ruled out from being implemented as a design.

Alternative material models can be considered for the design of Schwarz P unit cells. From compression experiments, the Young's modulus of bulk LCM3 was determined to be at a lower limit of 4.39MPa, an average of 5.74MPa and an upper limit of 6.65MPa. Therefore, it is suggested that the alternative material model should have modulus values higher than that mentioned. Two such material models considered here are calcium phosphates (CaP) and titanium. These are discussed in the sub-sections that follow.

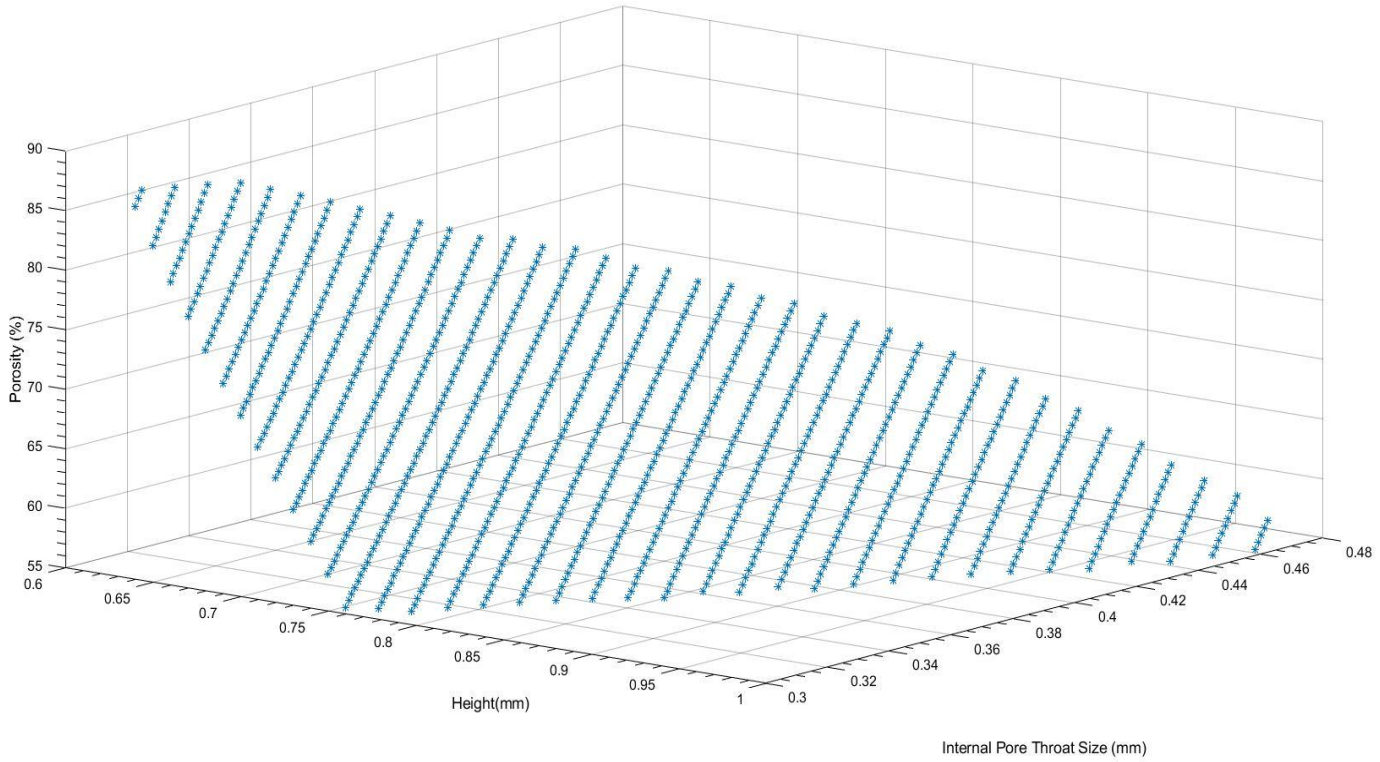

Figure 5-52 : 3-dimensional plot of all potential Schwarz P unit cell designs with an LCM3 material model that comprise of internal pore throat sizes greater than 300μm and porosity above 55%. Each '*' indicates one Schwarz P unit cell design represented by height, internal pore throat size and respective porosity. The porosity was determined using the obtained mathematical expression in Equation (24) into a custom MATLAB algorithm. Based on the height and internal pore throat values presented above, the pore size, wall thickness, volume and average effective modulus (lower limit, averaged and upper limit) can be determined through respective mathematical expressions obtained in Sub-section 5.10.4. Despite achieving the target for internal pore throat size and porosity, all the potential designs gave respective effective modulus which fall outside the modulus values for cortical and trabecular bone.

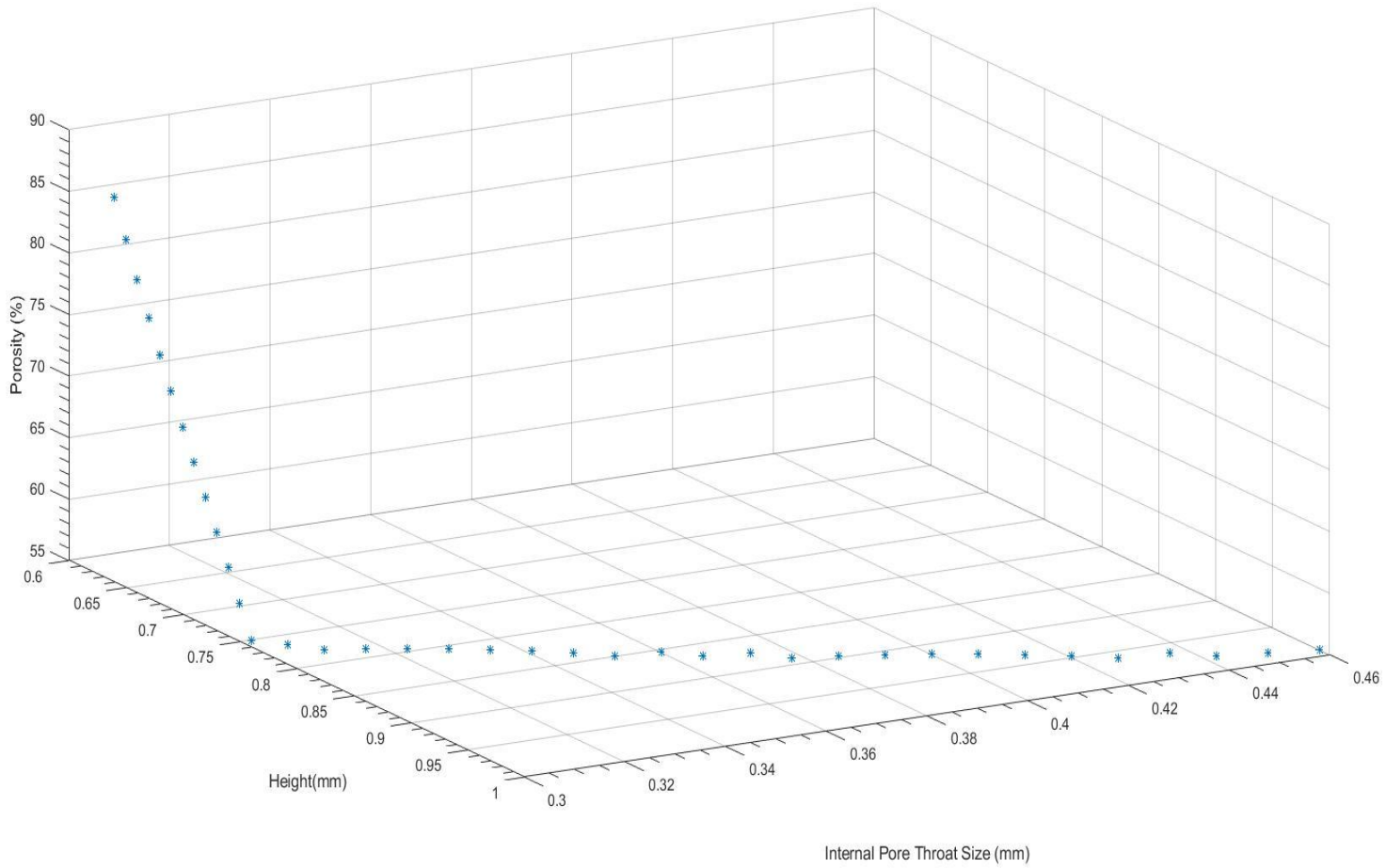

Figure 5-53 : 3-dimensional plot of Schwarz P unit cell configurations with a LCM3 material model that gives the highest range of predicted effective modulus values (between the lower and upper limit) each one particular height configuration. Each * indicates one Schwarz P unit cell design represented by height, internal pore throat size and porosity.

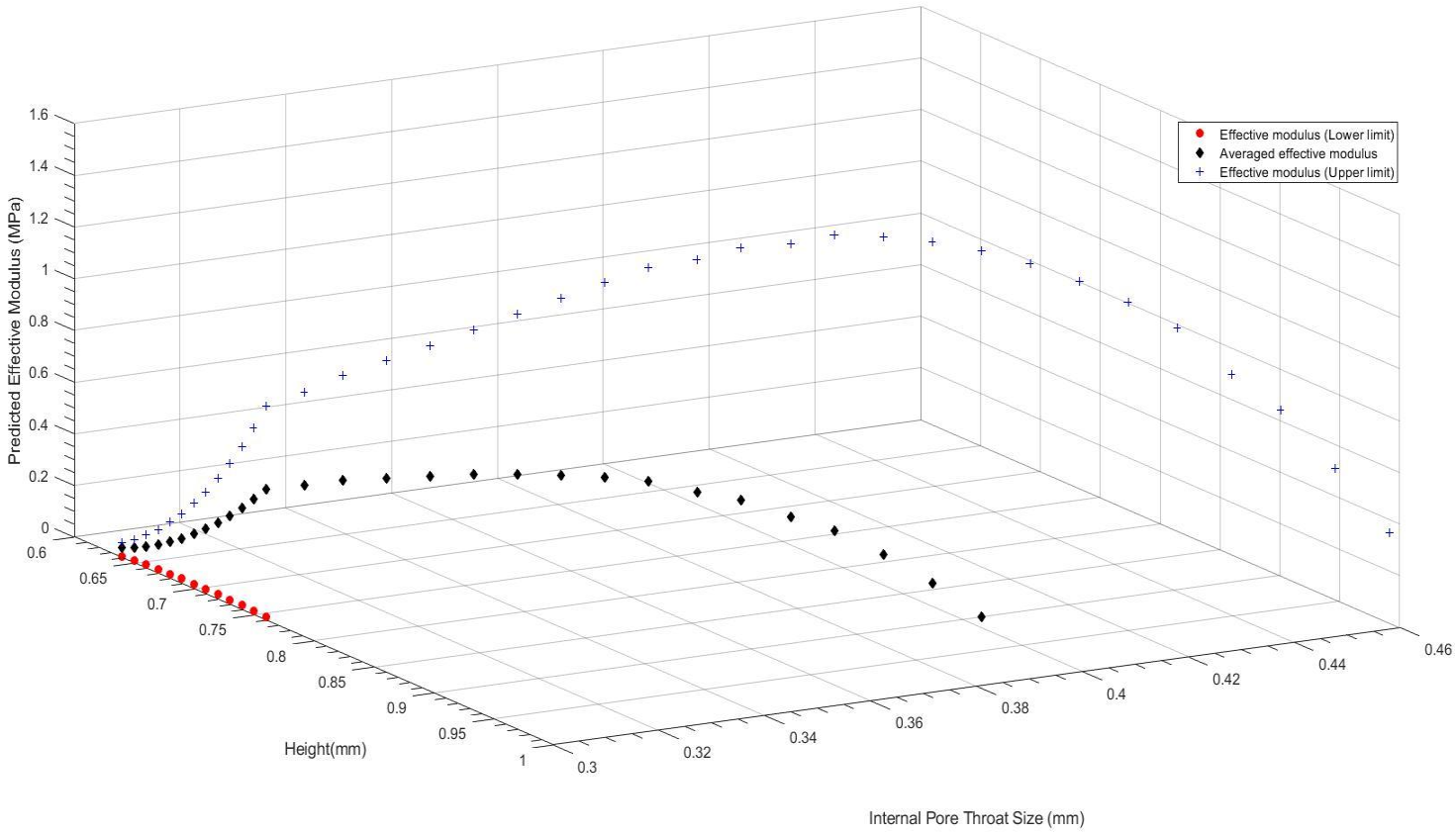

Figure 5-54 : Predicted effective modulus values (lower, averaged and upper) for Schwarz P unit cell designs based on height, internal pore throat size and porosity shown in Figure 5-53. The predicted effective modulus values shown are within the highest range for each particular height. It can be observed that the predicted effective modulus decreases as the height of a unit cell increases. In selecting designs to consist of porosity above 55%, the minimum internal pore throat size increases which result in the increase of bulk space within the confines of a unit cell. This would thus result in the decreasing effective modulus. Some effective modulus values were predicted to be of negative values and were omitted from presentation.

5.11.2 Calcium Phosphates (CaP) & Schwarz P Unit Cell Design

Calcium phosphate (CaP) makes up one of the components of bone matrix. These bioactive molecules are involved in protein adsorption, attachment of bone cells and deposition of apatite [224,225]. One common calcium phosphate used in bone tissue engineering is hydroxyapatite (HA). HA is an osteoconductive material that is chemically similar to the inorganic component of bone matrix [75]. HA is also attributed to an affinity towards various adhesive proteins and is involved in bone cell differentiation and mineralisation [226]. Despite this, HA comes at a disadvantage in terms of mechanical properties due to its high brittleness and low fatigue strength [227,228]. In mediating this, hydroxyapatite (HA) can be integrated into polymer composites such as polycaprolactone (PCL) to improve its mechanical properties while also enhancing bioactivity and bone regeneration capabilities *in vivo* [158,229,230].

A previous study investigated the implementation of polycaprolactone/hydroxyapatite, PCL/HA scaffolds consisting of 20wt% HA nanorods for use in bone tissue engineering applications. The study determined that cylinders of PCL/HA with 20wt% HA measured a modulus value of 241.6 ± 12MPa. Scaffolds consisting of the material model with measured pore sizes in the range of 10μm - 200μm and porosity greater than 90% gave a modulus of 1.99 ± 0.076MPa. In addition, the scaffolds also showed cell viability and proliferation through MIT assays in human osteosarcoma cell lines [231]. A separate study investigated the osteoconductivity and mechanical properties of porous calcium phosphate cement (CPC) scaffolds in a rabbit model. Findings from the study suggested that among CPC consisting of pore sizes in the range of 200μm - 600μm, scaffolds with pore sizes ranging between 200μm - 300μm and a porosity of 70.7 ± 6.3% gave the highest mechanical properties in terms of compressive strength and modulus after 12

weeks of implantation with the occurrence of bone ingrowth. However, the compressive strength and modulus among scaffolds with different pore size groupings were not significantly different after 24 weeks of implantation. This would thus suggest that scaffolds with pore sizes ranging between 200μm - 300μm had the best osteoconductive effects as implied by the amount of bone ingrowth measured after 12 weeks and the measured mechanical properties [232].

Consider Schwarz P unit cells consisting of a PCL/HA with 20wt% HA material model with a lower limit modulus of 229.12MPa, an average of 241.6MPa and an upper limit modulus of 253.66MPa. Taking into account desired targets for pore sizes greater than 10μm and porosity values above 55%, 2,488 potential designs are obtainable. These potential designs are graphically presented in Figure 5-55 and is represented by their configurations in terms of height, internal pore throat size and porosity. Representative sample configurations among the potential designs are graphically presented in terms of their height, internal pore throat size and porosity in Figure 5-56. Their respective predicted effective modulus is graphically presented in Figure 5-57. A tabulated form of the results for the representative sample configurations is appended in Appendix B.6.5.

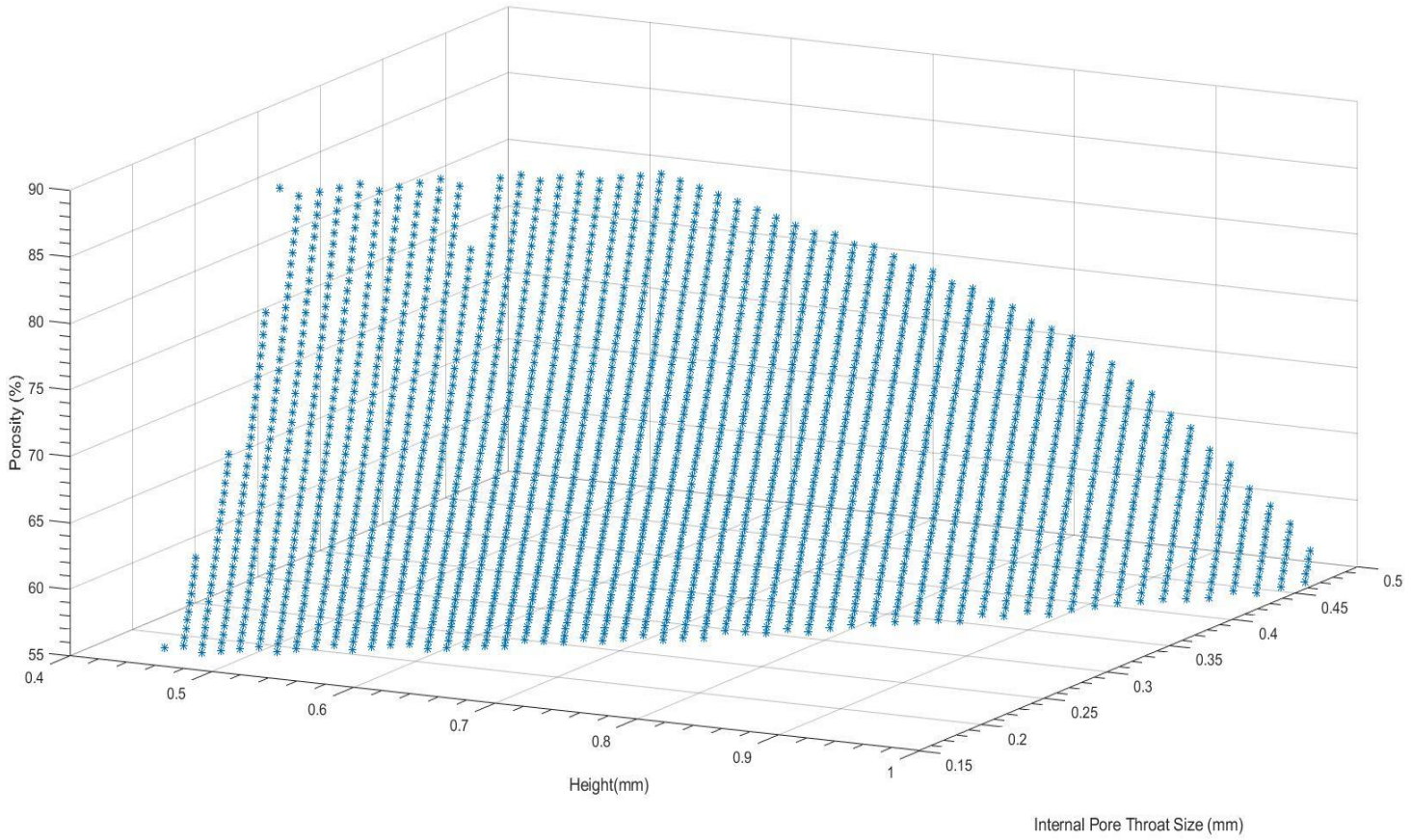

Figure 5-55 : 3-dimensional plot of all potential Schwarz P unit cell designs with a PCL/HA (20wt% HA) material model that comprise of internal pore throat sizes greater than 10μm and porosity values above 55%. Each '*' indicates one Schwarz P unit cell design represented by height, internal pore throat size and respective porosity. Based on the height and internal pore throat values presented above, the pore size, wall thickness, volume and average effective modulus (lower limit, averaged and upper limit) can be determined through respective mathematical expressions obtained in Sub-section 5.10.4.

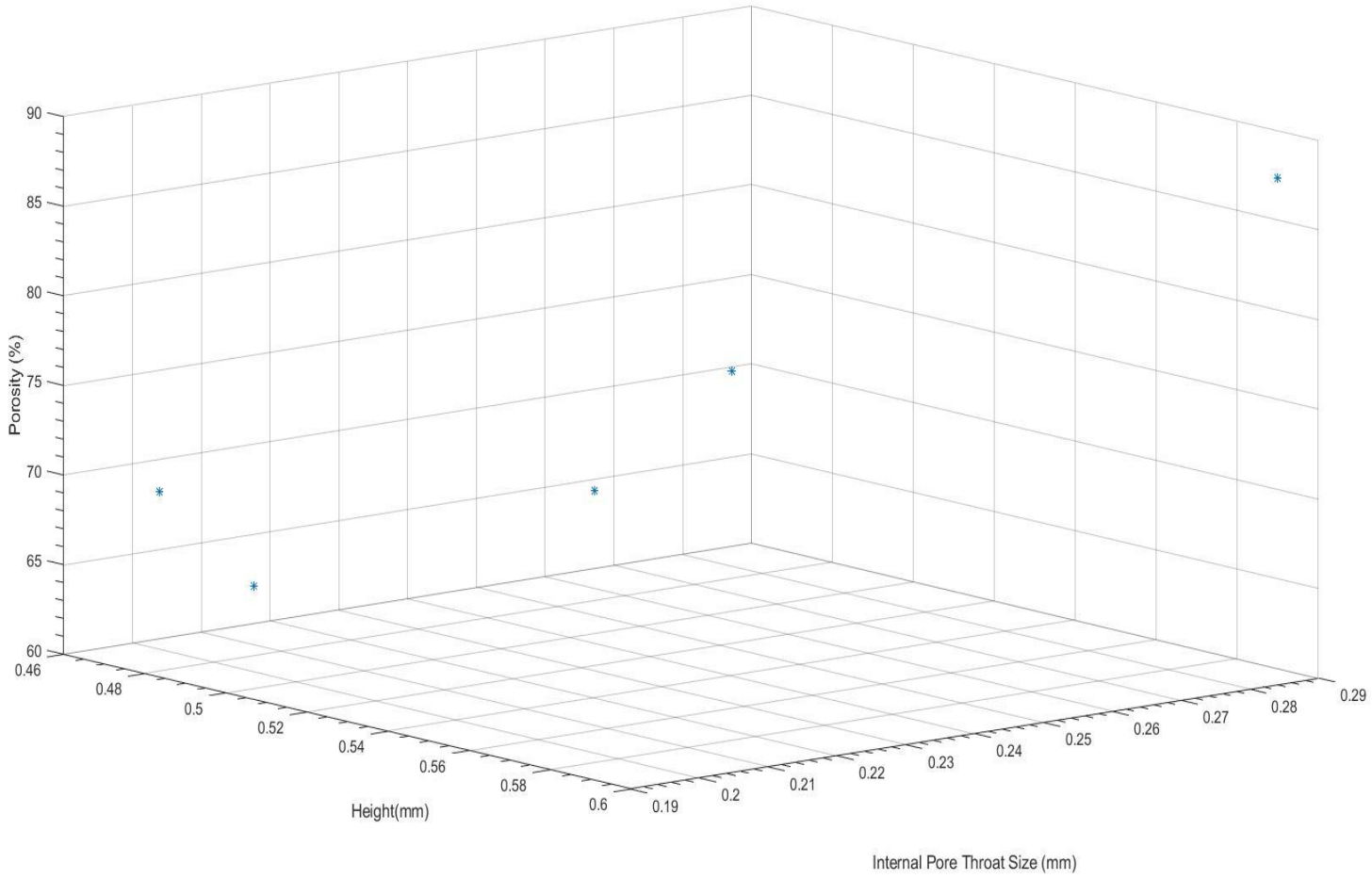

Figure 5-56 : Representative sample configurations among the potential designs of Schwarz P unit cells with PCL/HA (20wt% HA) with an internal pore throat size greater than 10μm and porosity values above 55%. Each '*' indicates one configuration and is represented in terms of their height, internal pore throat size and porosity. The respective predicted effective modulus for each sample configuration is graphically presented in the following figure.

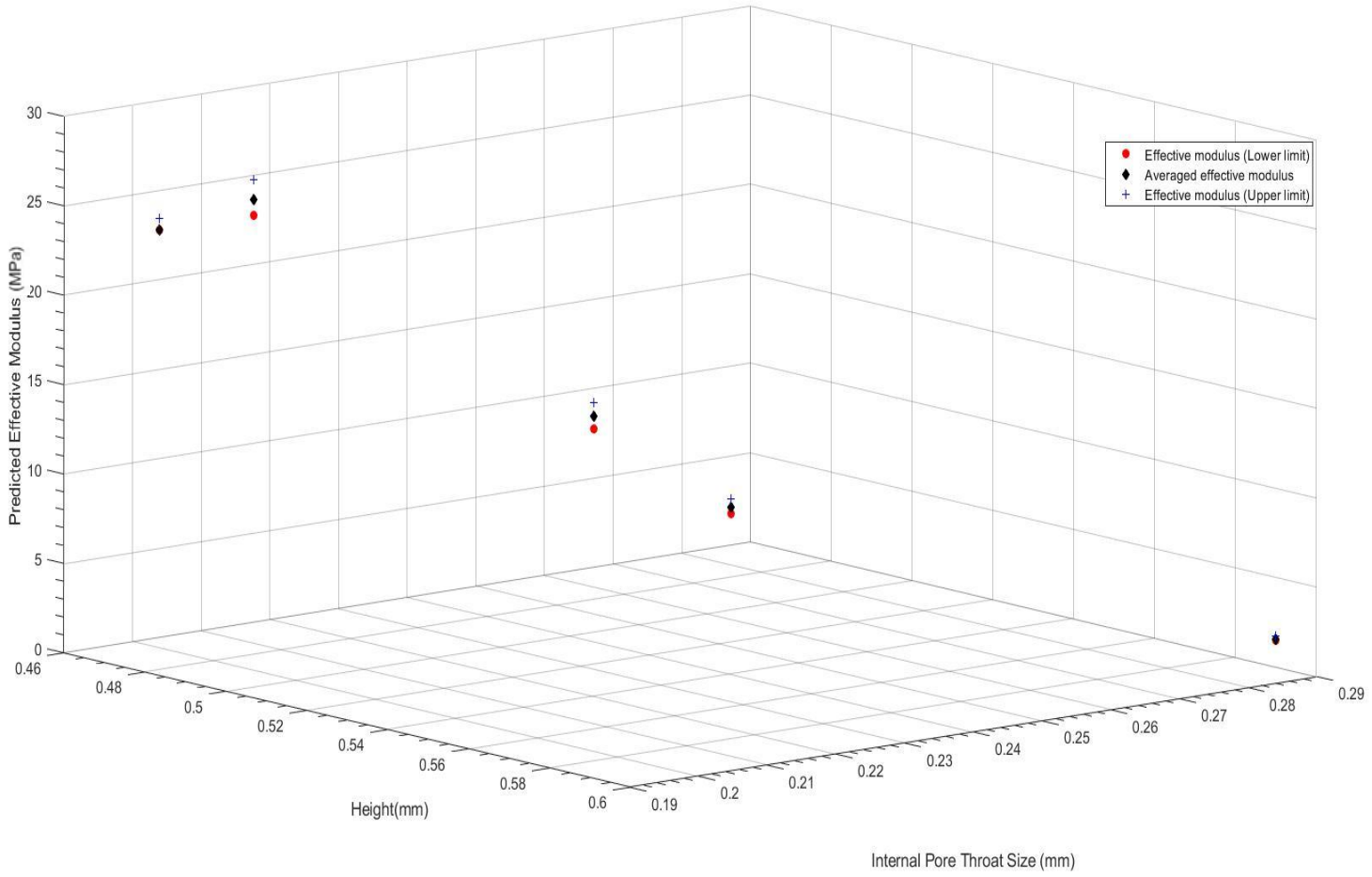

Figure 5-57 : Predicted effective modulus values (lower, averaged and upper) for Schwarz P unit cell sample configurations based on height, internal pore throat size and porosity shown in Figure 5-56. The Schwarz P unit cells comprised of a material model based on PCL/HA (20wt% HA). Various range of predicted effective modulus values can be obtained based on different levels of internal pore throat size and porosity.

Considering designs with an internal pore throat size ranging between 10μm - 200μm, the maximum attainable porosity is valued at 69.1%; obtainable from a Schwarz P unit cell configured at a height of 0.47mm and an internal pore throat size of 0.198mm. This is a 20.9% difference compared to the porosity of scaffolds investigated by Moeini et al. (2017) [231]. Among all 2,488 potential designs (including those between 10μm - 200μm), the maximum attainable porosity is valued at 88.3%; obtainable from a Schwarz P unit cell configured with a height of 0.60mm and an internal pore throat size of 0.284mm. This configuration gives a predicted effective modulus of 2.48MPa with a predicted lower and upper limit effective modulus at 2.37MPa and 2.60MPa respectively. Despite the 1.7% difference compared to the porosity of scaffolds investigated by Moeini et al. (2017) [231], a Schwarz P unit cell configuration still has potential to be implemented for cell viability and proliferation while being able to maintain sufficient mechanical properties since the predicted effective modulus is higher compared to those found in the literature (1.99 $\pm$ 0.076MPa). Emphasising this further, the said configurations has an internal pore throat size which is within range of the 200μm - 300μm pore size of CaP scaffolds implemented by Y. Zhao et al (2017) [232] while also having a higher porosity.

Considering designs with an internal pore throat size ranging between 200μm - 300μm and porosity values between 64.4% - 77.0%, 483 potential designs can be obtained as graphically presented in Figure 5-58.

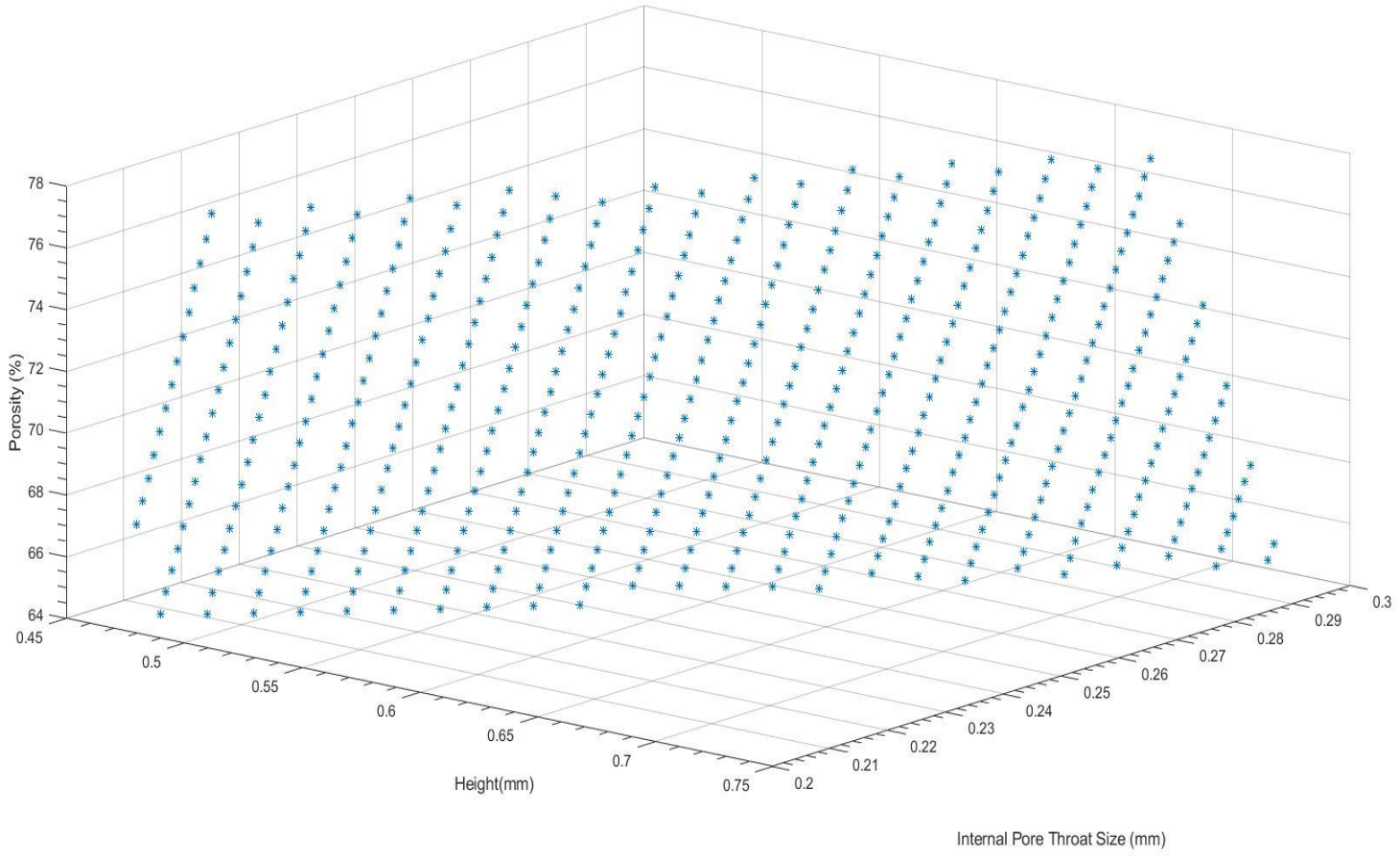

Figure 5-58 : 3-dimensional plot of Schwarz P unit cell designs with a PCL/HA (20wt% HA) material model that comprise of internal pore throat size in the range of 200μm - 300μm and porosity values in the range of 64.4% - 77.0%. Each '*' indicates one Schwarz P unit cell design represented by its configuration in terms of height, internal pore throat size and respective porosity.

The maximum attainable predicted effective modulus averages at 26.3MPa with a predicted lower and upper limit effective modulus of 25.4MPa and 27.4MPa respectively. This is obtained with a Schwarz P unit cell design configured at a height of 0.49mm and an internal pore throat size of 0.20mm. The porosity for the configuration is determined to be 64.8% (in the low range of 64.4% - 77.0%). A Schwarz P unit cell design configured at a height of 0.54mm and an internal pore throat size of 0.24mm gives the highest porosity among all 483 designs at a value of 76.9%. The predicted effective modulus for this configuration is averaged at 9.34MPa with a predicted lower and upper limit effective modulus of 8.97MPa and 9.80MPa respectively.

Consider the desired target values for internal pore throat size and porosity set for the LCM3 material model in 5.11.1 i.e. internal pore throat size greater than 300μm and a porosity value above 55%. Based on the LCM3 material model, a Schwarz P unit cell design configured at a height of 0.89mm, an internal pore throat size of 0.378mm and a porosity of 55% gave the highest range of predicted effective modulus with an upper limit value of 1.53MPa. At the same configuration, the upper limit effective modulus is predicted to be valued at 58.4MPa with a PCL/HA (20wt% HA). Considering designs configured for an internal pore throat size ranging between 200μm - 300μm and a porosity between 64.4% - 77.0% for the LCM3 material model, a Schwarz P unit cell configured at a height of 0.49mm, an internal pore throat size of 0.20mm and a porosity of 64.8% gives the maximum predicted effective modulus averaged at 0.48MPa with a predicted lower and upper limit effective modulus of 0.11MPa and 0.63MPa respectively. This is significantly lower when compared to the predicted effective modulus obtained from a unit cell with a PCL/HA (20wt% HA) material model at the same configuration.

With the discussions, it can be implied that PCL/HA (20wt% HA) is more advantageous in terms of mechanical properties compared to LCM3 when implemented as a material model for Schwarz P unit cells and subsequently its array into tissue scaffolds. Despite being a suitable alternative to LCM3 in terms of mechanical properties, the predicted effective modulus for all potential configurations still fall outside the range of modulus values of cortical and trabecular bone. This would thus suggest that Schwarz P unit cell-based tissue scaffolds with PCL/HA (20wt% HA) is more suitable for non-load bearing applications. Similar to tissue scaffolds with LCM3 as a material model, the tissue scaffolds would be suitable for implantation in small sized defects or where a fixation method is implemented along with the implantation.

5.11.3 Titanium & Schwarz P Unit Cell Design

Titanium has been implemented for use in biomedical applications such as hip stems, joints and osteosynthesis materials which include screws, plates and nails [47]. The biocompatibility of titanium and its alloys has been cited to be superior compared to other metallic biomaterials used in biomedical applications such as stainless steel and cobalt-chrome (Co-Cr-Mo) alloys [233,234]. A previous study investigated the effect of pore size and porosity on the mechanical properties and biological response of porous titanium scaffolds. Findings from the study concluded that titanium scaffolds with pore sizes ranging from 45μm - 500μm gave modulus values ranging between 15.46GPa – 18.12GPa which fall in range of the elastic modulus for cortical bone. Biological responses in terms of cell proliferation of seeded osteosarcoma osteoblasts 143B was most prominent at pore ranges greater than 300μm while scaffolds with pore sizes ranging between 212μm – 300μm gave the poorest conditions for cell proliferation. Lower porosities in the range of 27% - 37% with pore sizes above 300μm indicated low

levels of cell proliferation. Low levels of cell proliferations were also observed at higher porosities within the range of 38% - 56% at pore sizes ranging between 212μm - 300μm, suggested to be due to difficulty of cell spanning. This was also suggested to be due to the influence of microarchitecture on cell proliferation [31]. Titanium alloy β-type Ti-29Nb-13Ta-4.6Zr (TNTZ) was reported to have good mechanical properties, corrosion resistance, biocompatibility and a low Young's modulus (~60GPa) comparable to that of bone. The obtainable Young's modulus of TNTZ is reported to be between 55GPa – 100GPa [234].

Consider Schwarz P unit cell models consisting of a TNTZ material model with a lower limit modulus of 55GPa, an average modulus of 77.5GPa and an upper limit modulus of 100GPa. Taking into account target values of internal pore throat sizes greater than 300μm and porosity values above 27%, 2,152 potential designs are obtainable. This is graphically presented in Figure 5-59.

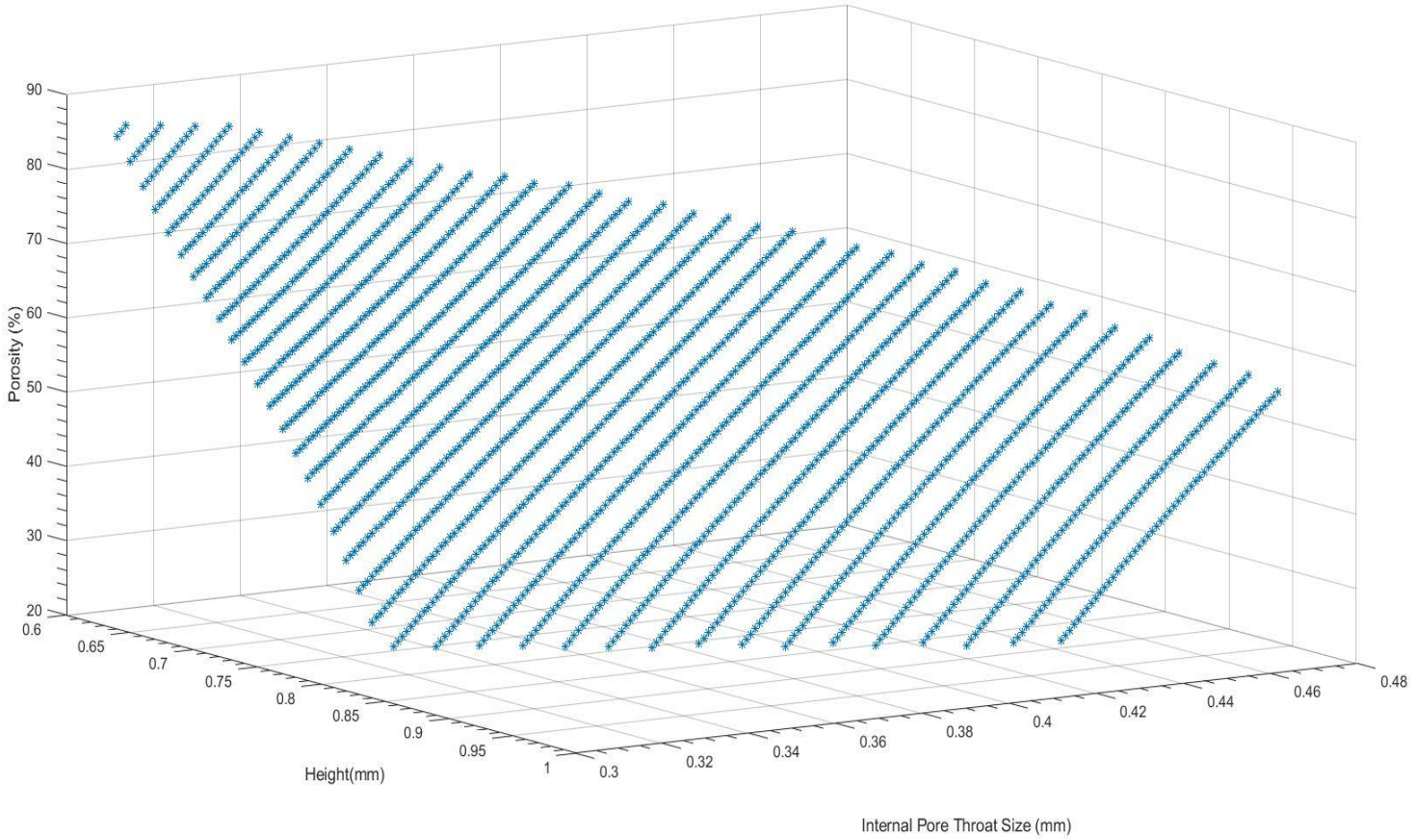

Figure 5-59 : 3-dimensional plot of all potential Schwarz P unit cell designs with a TNTZ material model that comprise of internal pore throat sizes greater than 300μm and a porosity value above 27%. Each '*' indicates one Schwarz P unit cell design and is represented by its respective configuration in terms of height, internal pore throat size and porosity. Based on the configurations, a range of predicted effective modulus values which fall within the modulus values of cortical and trabecular bone are attainable.

Consider Schwarz P unit cell designs with a porosity ranging between 27% - 37% among the determined potential configurations in Figure 5-59. A Schwarz P unit cell configured at a height of 0.92mm, an internal pore throat size of 0.367mm gives a porosity valued at 36.9% i.e. in the higher porosity range between 27% - 37%. Since it has been reported that higher porosities within the range of 27% - 37% and pore sizes above 300μm indicated higher levels of cell proliferation, the configuration mentioned exhibits potential for encouragement of cell proliferation. The predicted effective modulus was determined to be valued at an average of 16.3GPa and a predicted upper limit effective modulus of 41.8GPa. This falls within the 15.46GPa – 18.12GPa range of modulus values determined for titanium scaffolds and therefore also falls in range of the elastic modulus of cortical bone [31].

A range of predicted effective modulus values which fall within modulus value of both cortical and trabecular bone are attainable. Representative sample configurations of Schwarz P unit cell designs that give predicted effective modulus values within range of cortical bone are graphically presented in Figure 5-60 and Figure 5-61. On the other hand, representative sample configurations of Schwarz P unit cells that give predicted effective modulus values within range of trabecular bone are graphically presented in Figure 5-62 and Figure 5-63. A tabulated form of the results is appended in Appendix B.6.6.

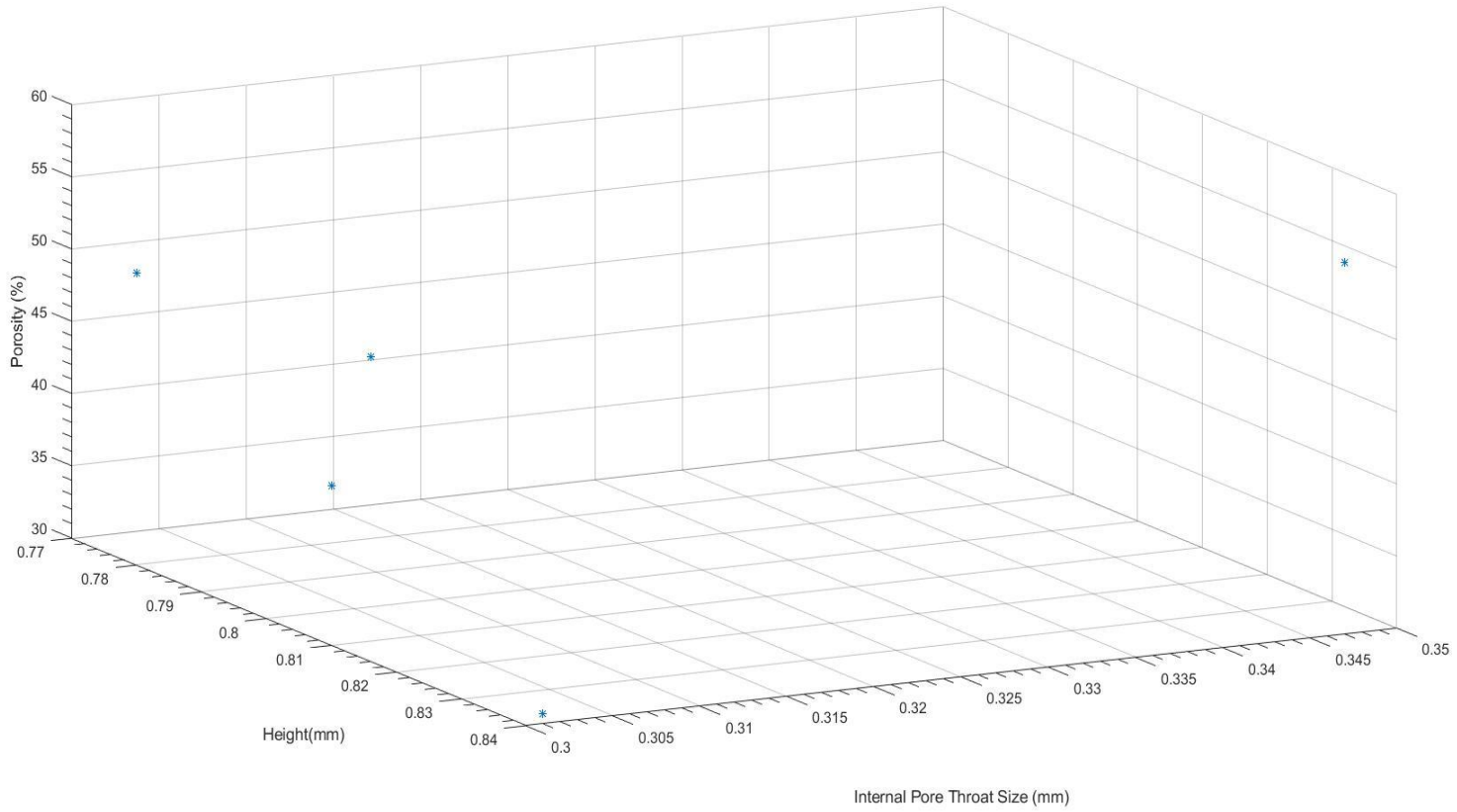

Figure 5-60 : Representative Schwarz P unit cell sample configurations with titanium TNTZ material model that give predicted effective modulus values that fall in the typical range of modulus values of cortical bone (15GPa – 19GPa). These sample configurations were taken from the 2,152 potential Schwarz P unit cell design configurations which are attributed to internal pore throat sizes greater than 300μm and porosity values higher than 27%. Each '*' indicates a single configuration and is represented by its height, internal pore throat size and porosity. The respective predicted effective modulus for each representative sample is graphically presented in the following figure.

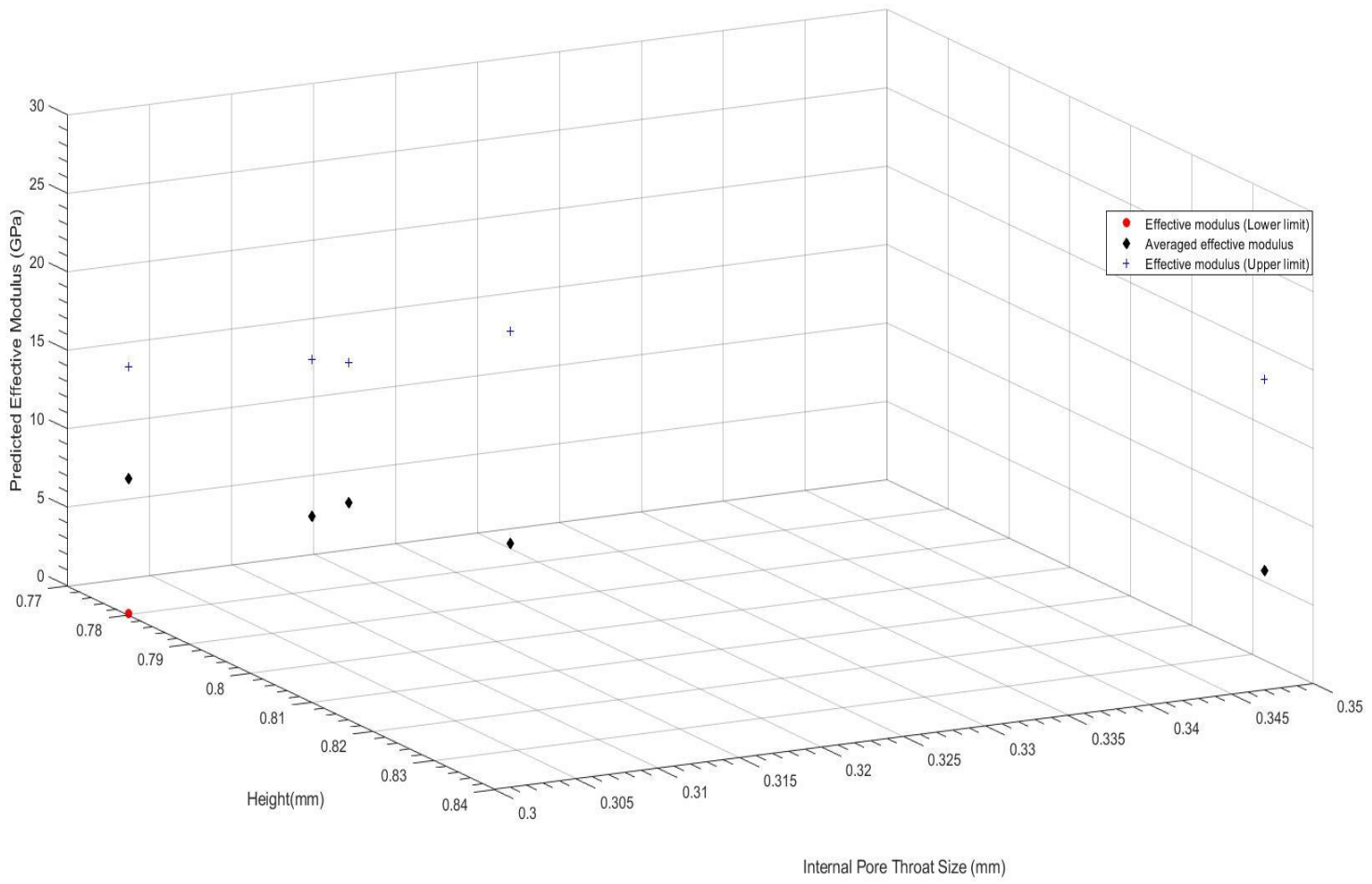

Figure 5-61 : Predicted effective modulus values (lower, averaged and upper) of representative Schwarz P unit cell samples configurations with titanium TNTZ graphically presented in Figure 5-60. The predicted effective modulus values shown fall within the typical range of modulus values of cortical bone (15GPa – 19GPa). Some data for lower limit effective modulus are not shown due to their values being negative.

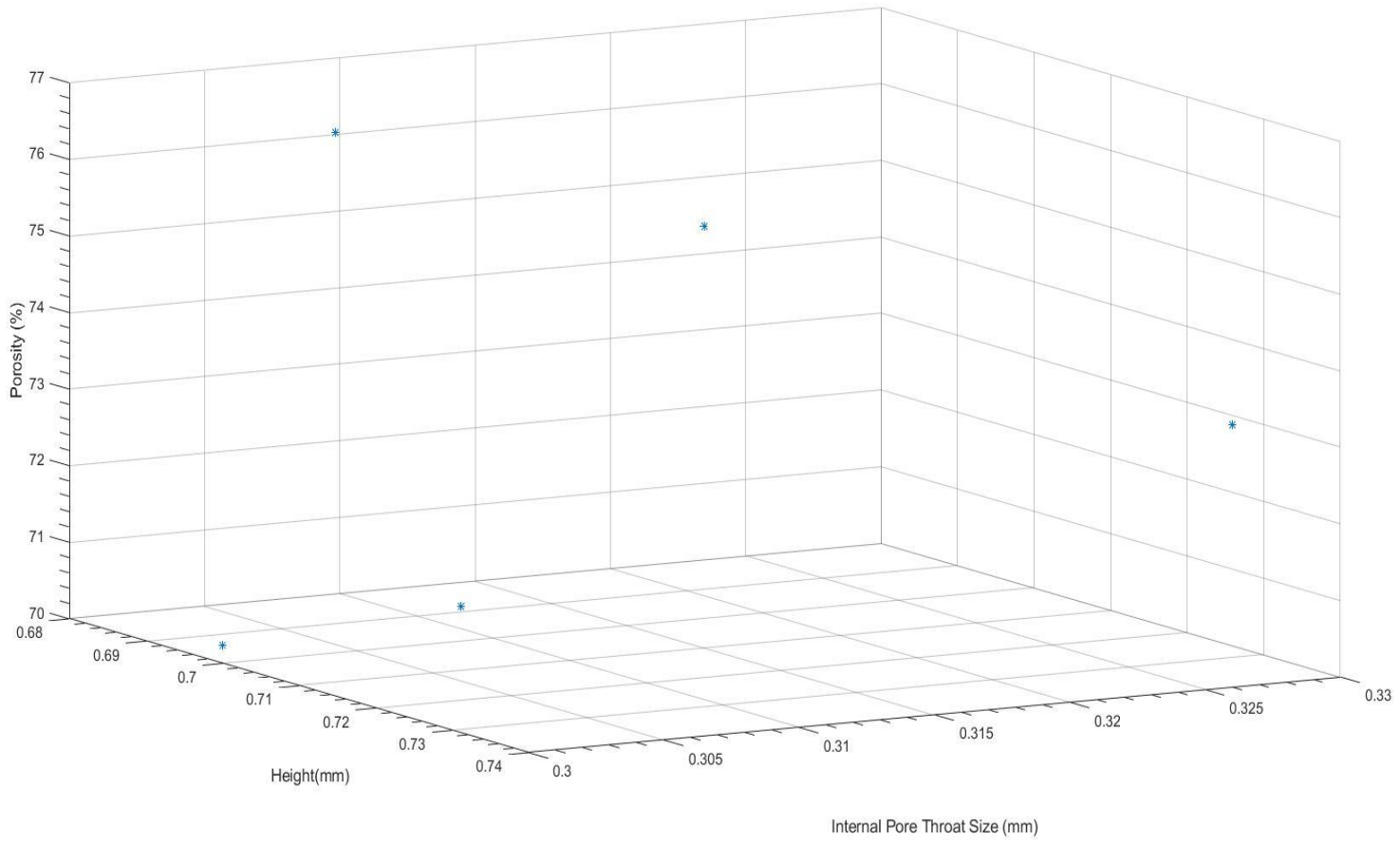

Figure 5-62 : Representative Schwarz P unit cell unit cell configurations with titanium TNTZ material model that give predicted effective modulus values that fall in the typical range of modulus values of trabecular bone (2GPa – 5GPa). Each '*' indicates a single configuration and is represented by its height, internal pore throat size and porosity. The respective predicted effective modulus value (lower, averaged and upper) for each representative sample is graphically presented in the following figure.

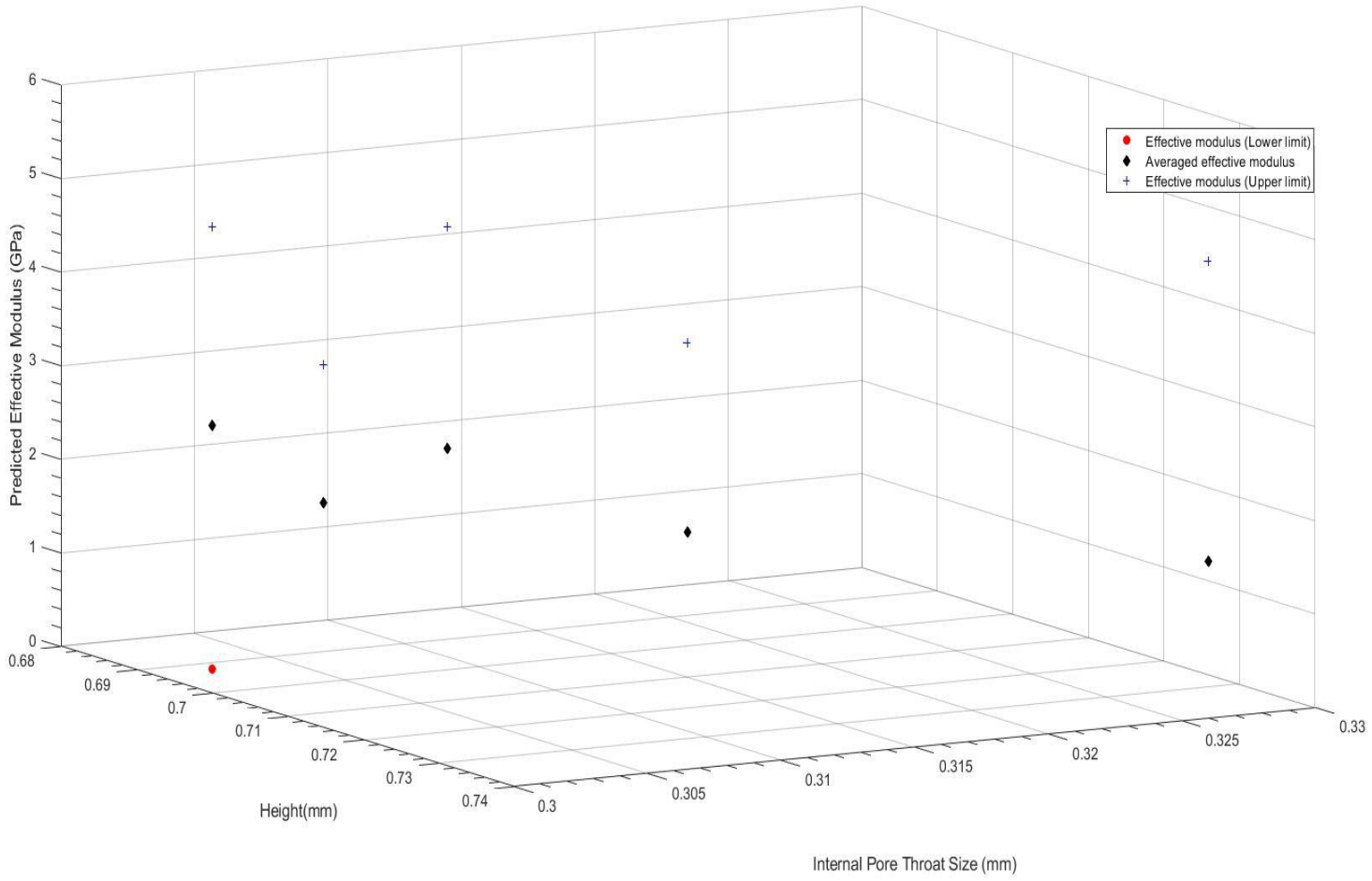

Figure 5-63 : Lower, averaged and upper values of predicted effective values for each representative Schwarz P unit cell sample configuration with titanium TNTZ graphically presented in Figure 5-62. The predicted effective modulus values fall within the typical range of modulus values of trabecular bone. Negative lower limit predicted effective modulus values were omitted from the graphical presentation.

Despite potential designs being compatible with cortical bone from the aspect of modulus matching, the porosity for a particular unit cell design is much higher compared to that of cortical bone. The minimum porosity that would give an effective modulus at the low end of the modulus for cortical bone i.e. 7GPa is in the range of 53.4% - 54.4%. This is a significant difference compared to reported porosity of cortical bone which is in the range of 5% - 10% [39,235,236]. Mediating this significant different would require the use of a material that would enable modulus match at low porosity values.

The porosity of trabecular bone has been reported to be in the range of 75% and 90% [39,235,236]. Considering the above, potential designs were able to have a predicted effective modulus falling within range of that of trabecular bone while also simultaneously being within range of the porosity. Hence, it can be suggested that Schwarz P unit cell-based tissue scaffolds comprising of TNTZ is more suitable for bone defects in trabecular bone regions.

With all of the above, the predictive models for the design of Schwarz P unit cells in conjunction to their respective predicted effective modulus has been tried and tested. The LCM3 material model was generally found to be weak and hence, alternate material models i.e. polycaprolactone/hydroxyapatite, PCL with 20wt% HA and titanium TNTZ was suggested. Despite being advantageous in terms of mechanical properties over the LCM3 material model, PCL with 20wt% HA was not able to simultaneously have the predicted effective modulus values within range of cortical or trabecular bone at target pore sizes and porosity. Titanium TNTZ was able to simultaneously achieve the target mechanical properties, pore size and porosity in consideration of trabecular bone. However, the minimum porosity of a Schwarz P unit cell design configuration that would give an effective modulus at the low end of typical modulus range for cortical bone is

significantly higher compared to the porosity of that particular bone tissue. More material models can be considered as alternatives in further investigations depending on availability of bulk material data.

Chapter 6

Conclusion

6.1 Thesis Summary

The main aim of this study was to characterise the mechanical properties of Schwarz P unit cell-based tissue scaffolds via a computational approach. The scaffolds mentioned have been fabricated via two-photon polymerisation (2PP) as part of the European Union Research and Innovation 7th Framework Programme (FP7) under grant agreement no. 2633 63 (INNOVABONE) with TETRA – Society for Sensoric, Robotics and Automation GmbH (Ilmenau, Germany). These scaffolds were fabricated using copolymer materials based on methacrylated poly(D,L-lactide-co- ε -caprolactone) (PLCL).

Different inputs were required to implement a computational approach in regards to mechanical characterisation. One such input is a usable computer aided design (CAD) model of the Schwarz P unit cell. This CAD model makes an essential part of computational work as boundary conditions are generally applied to its' discretised form. Hence, a CAD model must be discretised to give nodal and element information before proceeding further with computational analyses. A stereolithography (.STL) file containing the Schwarz P unit cell model was limited in its ability to be used. This is due to the nature of the stereolithography files that store information about a particular model as a collection of triangles without any information pertaining to the connectivity between the vertices of triangles. With this, practical use of the .STL file in the context of

implementing it as an input for computational work becomes limited. Chapter 3 discusses the ‘reverse engineering’ performed to convert the .STL containing the Schwarz P unit cell into a surface geometry model that is usable and manipulable for use in computational work. Based on the methodology performed, a surface geometry CAD model of a Schwarz P unit cell was obtained. This would indicate that the objective set out in (b) in Section 1.3 of Chapter 1 has been achieved.

Another input required to implement a computational approach comes in terms of material data. Methacrylated poly(D,L-lactide-co-ε-caprolactone) (PLCL) was used to fabricate the scaffolds at different lactide (L) to caprolactone (C) compositions. This study focused on PLCL with a lactide to caprolactone ratio of 16:4 i.e. LCM3. Bulk cylinders of LCM3 by the scaffold provider, TETRA were implemented in compression experiments to obtain stress-strain data. The stress-strain data was analysed further according to the input requirements of the computational model that is to be done. Due to discrepancies in terms of stress-strain data/curve for each respective sample, it was unfeasible to use each data for further analysis to establish material data input for computational models. A lower limit, average and upper limit material data was implemented to obtain results that are within a range instead. With the lower and upper limit material data already attainable from the obtained stress-strain data, only the averaged data needed to be determined. This was done through the use of a custom MATLAB algorithm. Subsequently, the lower limit, average and upper limit stress-strain data were analysed further to establish material data required for input in computational models. In regards to computational models, this study examines the mechanical characterisation through micromechanical analysis in linear and non-linear analyses.

Linear analysis requires material data input in the form of Young's modulus and Poisson's ratio. The Poisson's ratio for LCM3 was taken to be 0.3. Hence, only determination of the Young's modulus was required. This was obtained from the gradient of the linear region of the stress-strain curves of the bulk LCM3 cylinders according to standards set out in British Standard BS EN ISO 604:1997. With this, the input required for linear analysis has been established. Non-linear analysis with a hyperelastic material model requires material input data in the form of nominal stress-strain curves and a selection of a form of strain energy potential. Since the nominal stress-strain curve is already at hand through the stress-strain data obtained, only a form of strain energy potential was required to be determined. For this, a built-in 'Evaluate' option in ABAQUS was used to assess the different forms of strain energy potential for each respective stress-strain data with respect to the lower, average and upper limit material data. Stress-strain data output from the evaluation was implemented in a custom MATLAB algorithm which determines the root-mean-square error (RMSE) between the evaluated stress-strain data of a particular form of strain energy potential and the respective experimental stress-strain data used in 'Evaluate'. The form of strain energy potential with the least RMSE is then selected. A form of strain energy potential selected was intended to be similar across the lower, average and upper limit material data based on the lowest RMSE however, this was not the case. The form of strain energy potential with the least RMSE was similar between the average and upper limit material data but not with the lower limit. Hence, the selection was based around the lower limit material data. With this, the input required for non-linear analysis has been established. In due regards to the above, the material data input required for computational analysis is ultimately established in Chapter 4 thus fulfilling objective (c) in Section 1.3 of Chapter 1.

In order to validate the computational approach considered for this study, mechanical characterisation for the fabricated Schwarz P unit cell-based tissue scaffold was required in an experimental context. Compression experiments performed on fabricated tissue scaffold samples gave stress-strain data which were evaluated further to determine the respective stiffness i.e. modulus. A range of values of modulus was obtained and therefore an average was determined with a standard deviation. These values serves as a basis of comparison with modulus results obtained from the computational approach of mechanical characterisation. Chapter 4 discusses the mechanical characterisation of the fabricated tissue scaffolds in an experimental context. The results obtained have also been discussed in the same chapter. This thus fulfills objective (d) set out for this study.

The foundational work for micromechanical analysis used in this study was established by Li et al. [189]. In the context of this study, this approach seeks to reduce the macrostructure of the whole tissue scaffold to the analysis of a single representative unit cell through its idealisation as a crystal packing system and subsequent derivation of boundary conditions. Different crystal packing systems have been established in the aforementioned literature [189]. Through the two-photon polymerisation (2PP) fabrication process performed under INNOVABONE, Schwarz P unit cells were simply translated in the x, y and z directions in an array to form the tissue scaffold structure. This is further evidenced through scanning electron microscope (SEM) micrographs of fabricated tissue scaffold sample. Based on the above and noting that the Schwarz P unit cells consist of equal height, width and length, cubic translational symmetries are inherent between the unit cells and the whole tissue scaffold structure. Therefore, the fabricated tissue scaffold is most suitably idealised as a simple cubic packing system with the Schwarz P unit cell itself as the representative unit cell i.e. Voronoi cell. Subsequently, the necessary boundary conditions were then derived as shown in Section

5.2 Chapter 5. This would fulfill the objective set out in (e) to derive the necessary boundary conditions for implementation of the computational approach to mechanical characterisation i.e. micromechanical analysis. These boundary conditions can then be imposed as required to discretised Schwarz P unit cell models. Discretisation of the Schwarz P unit cell surface geometry CAD model required some specificity in terms of their meshing in order to apply the derived boundary conditions. Here, the meshing between two opposite faces of a unit cell lying along a common directional axes (either in the x, y or z axis) must be identical. Particular emphasis on this requirement needed to be taken into account for discretisation before further compilation into a processing file which is used for simulation processing with respect to micromechanical analysis. This has primarily been discussed in Sub-section 5.2.4.

With the above, the material data required for input has been established; the discretisation information of the Schwarz P unit cell model has also been established; and the necessary boundary conditions for implementation of micromechanical analysis have been derived. An input file containing complete model information to perform micromechanical analysis can then be compiled.

An input file is first compiled for the simple case of a linear analysis to justify a computational approach for mechanical characterisation. This is done in comparison between homogenisation via finite element and micromechanical analysis. Micromechanical analysis gave stable effective modulus values as the number of elements used to discretise the Schwarz P unit cell increases. On the contrary, homogenisation via finite element gave step increases in terms of effective modulus values across the range of number of elements used for discretisation. Successive increase in the level of mesh refinement (defined by the increase in number of elements

used for discretisation) subsequently increases the number of discretised layers throughout cross-sectional thickness of the unit cell. This would subsequently lead to increasing stiffness and therefore increasing effective modulus. The number of layers throughout cross-sectional thickness has been tabulated. Despite this, micromechanical analysis managed to maintain stability in the order of (1×10^{-4})MPa. Furthermore, based on tabulated average strain and average shear strain results and graphical presentations of stress distribution obtained from micromechanical analysis, it has been confirmed that the results comply with the validation methods to ensure correct implementation of boundary conditions on a Schwarz P unit cell as discussed in Sub-section 5.2.6. This thus fulfills objective (h). With an approach that reduces the computational analysis of a periodic microstructure i.e. tissue scaffold to the analysis of a single representative unit cell coupled with the capability to obtain stable effective modulus results across a wide range of mesh refinements, it stands to prove that micromechanical analysis is an efficient and justifiable approach to computationally characterise the mechanical properties of Schwarz P unit cell-based tissue scaffolds. With this, the objective set out in (a) is fulfilled.

With an approach to computationally characterise the mechanical properties of Schwarz P unit cell-based tissue scaffolds i.e. micromechanical analysis appropriately justified, linear analyses can be performed in context of comparisons with experimental mechanical characterisation results. Necessary material data required for linear analysis, discretisation information of the Schwarz P unit cell model along with the derived boundary conditions were compiled into an input file before subsequent processing in ABAQUS/Standard for a static, linear perturbation micromechanical analysis. Based on the lower, average and upper limit material data, three main separate analyses were performed in conjunction to analysis at each respective degree of freedom. The average

effective modulus results obtained from analyses shows a significant discrepancy of 86.05% compared to the mean modulus obtained from experimental mechanical characterisation of Schwarz P unit cell-based tissue scaffolds. Previous investigations performed under the INNOVABONE project has found geometrical transformations between the intended original Schwarz P unit cell design and unit cells comprising the physical tissue scaffolds fabricated via 2PP [122]. SEM micrographs were implemented into an approach that would average the unit cell micrographs comprising the fabricated tissue scaffolds as discussed in Section 5.4 of Chapter 5. Measurement analyses on the averaged unit cell SEM micrograph confirmed that geometrical transformations have occurred as cited in the aforementioned literature. More specifically, the geometrical transformations have occurred in the form of shrinkage. This would lead to the significant discrepancy between the experimental modulus and the modulus obtained computationally. Thus, discrepancy found does not at all reflect the limitation in the application of micromechanical analysis.

To mediate the geometrical transformations, the measurements for the different dimensional parameters which include height, width, length and wall thickness made from the averaged unit cell SEM micrographs were used to reconstruct the Schwarz P unit cell surface geometry CAD model through CAD modeling techniques. The reconstructed unit cell would thus give an approximate representation of the average of unit cell comprising the fabricated tissue scaffolds. To allow for re-implementation of the model into micromechanical analysis, the unit cell was reconstructed to exhibit quarter symmetry. The reconstructed unit cell model was then discretised according to the methodologies discussed and presented in Sub-section 5.2.4. Compared to the original Schwarz P unit cell design, the measurement analyses of the averaged unit cell comprising the fabricated tissue scaffold consist of non-uniform height, width and length

measurements. This required the derivations for boundary conditions with respect to micromechanical analysis to be revised. Originally the Schwarz P unit cell design was represented as a cube in a simple cubic packing system. The non-uniformity of height, width and length of the averaged unit cell should then be represented as a cuboid in a simple cuboidal packing system while having the reconstructed unit cell itself as the representative unit cell. The alterations made to the derivations for boundary conditions has been discussed in Section 5.5 of Chapter 5 before subsequent re-implementation in a revised linear analysis with the reconstructed unit cell model. Similar to the initial linear case (Case I), the necessary lower limit, averaged and upper limit material data; the discretisation information of the reconstructed unit cell model; and the revised boundary conditions for a cuboidal packing system along with the application of load was compiled into an input file before further processing in ABAQUS/Standard for a static, linear perturbation micromechanical analysis. Results obtained from micromechanical analyses of the reconstructed unit cell model gave an average effective modulus which only differs by 6.94% from the mean modulus results obtained from experimental mechanical characterisation of Schwarz P unit cell-based tissue scaffolds. Tabulated average strain and average shear strain results complied with the validation methods for correct implementation of displacement boundary conditions for revised micromechanical analysis. With only a small margin of error, the effectiveness of reconstructing the unit cell model to approximately represent an average of unit cells comprising the fabricated tissue scaffold to mediate the geometrical transformations that occurred has been demonstrated. Furthermore, the application of micromechanical analysis in the context of linear analysis to computationally characterise the mechanical properties of Schwarz P unit cell-based tissue scaffolds made from PLCL with a lactide (L) to caprolactone (C) ratio of 16:4 i.e. LCM3 has also been demonstrated and justified. The results obtained

along with possible causes for geometrical transformations have been discussed. The mechanism behind how different dimensional parameters affect the resulting effective modulus has also been discussed through beam bending and column buckling theories.

With the implementation of micromechanical analysis in the context of linear analyses having been established, the study was succeeded with its implementation in the complex context of non-linear analyses. Here, the derived displacement boundary conditions for a simple cuboidal packing system (similar to the revised linear case in Case II) were applied on the reconstructed unit cell which is assigned the required material input data for non-linear analyses. The necessary lower limit, averaged and upper limit material data; the discretisation information of the reconstructed unit cell model; and the revised boundary conditions for a cuboidal packing system was compiled into an input file before further processing through ABAQUS/Standard for a dynamic, implicit micromechanical analysis. Macroscopic load was applied along with the displacement boundary conditions at varying increasing values. Based on the average strain results obtained from micromechanical analyses, an average stress-strain curve can be constructed. Comparisons of the obtained average stress-strain curve and the experimental stress-strain curve obtained from compression experiments of Schwarz P unit cell-based tissue scaffolds showed differences in terms of trend. The trend of the experimental stress-strain curve was found to have similarities with observed stress-strain curves from unconfined compression of Schwarz P unit cell-based tissue scaffolds. The trend of the average stress-strain curves obtained from micromechanical analyses on the other hand was found to have similarities with obtained stress-strain curves from confined compression Schwarz P unit cell-based tissue scaffolds. This was found to be due to the nature of derivations for micromechanical analysis that requires two opposite faces lying along a common directional axis of the representative unit cell to be identical in terms of its

discretisation. The displacement boundary conditions are then applied to nodes (formed by the discretisation) that lie along a common directional axis for each pair of faces. This could be seen as a limitation to micromechanical analysis depending on the perspective taken. The implantation of tissue scaffolds *in vivo* would resemble confined compression under loading making micromechanical analysis potentially applicable to oversee the stress-strain response. In the context of *in vitro* testing, micromechanical analysis can be performed with a linear analysis rather than a non-linear analysis for mechanical characterisation of respective effective properties. Based on summarisation in regards to linear and non-linear analyses, objectives (e) through (h) have been successfully achieved.

Validation of micromechanical analysis has been made in terms of the results obtained against itself with respect to discussed validation methods in different cases; and in terms of comparison with experimental results of mechanical characterisation following a small margin of error. The relationships between different dimensional parameters to the resulting mechanical properties (defined in terms of their modulus) of a Schwarz P unit cell-based tissue scaffold have then been investigated in linear analyses. Approaching the investigation from the perspective of linear analyses allows mathematical expressions describing the relationships to be determined while also allowing the expressions to be generalised to accommodate other materials. The generalised mathematical expressions would thus serve as a predictive tool to determine a suitable set of dimensional parameters in designing a Schwarz P unit cell in tandem to their mechanical properties. This allows initial studies to be done in a simple context before delving further into more complex contexts for a considered material. Linear analysis in this study considers Schwarz P unit cells with thickness variations at constant surface radius. The original Schwarz P unit cell CAD model was used to create unit cells with different configurations where the height of the unit cell was scaled accordingly; and at each

scaled height, the wall thickness was also scaled accordingly. The models were discretised in a similar manner to previous cases according to methodologies discussed in Sub-section 5.2.4. Since the Schwarz P unit cells configured all have equivalent measurements of height, width and length, the boundary conditions derived for a simple cubic packing system was implemented. An input file was then compiled containing material data required for linear analysis according to the lower, average and upper limits; the discretisation information of a particular Schwarz P unit cell model among the configurations made and the necessary boundary conditions. The results obtained from micromechanical analyses were assessed to investigate the relationships as follows;

- Height, internal pore throat size and pore size
- Height, pore size and wall thickness
- Height, pore size and volume
- Height, pore size and porosity
- Height, pore size and average effective modulus

Each relationship were graphically presented as 3-dimensional surface plots before subsequently determining the relationship in terms of mathematical expressions. The relationships in terms of the above were discussed. The implications in regards to the obtained derived mathematical expressions were also discussed through their application to design Schwarz P unit cell-based tissue scaffolds comprised of other materials besides LCM3. This was done in due regards to previous literature. With this, the objective set in (i) has been fully accomplished.

6.2 Conclusions

Micromechanical analysis was used as a computational approach to characterise the mechanical properties of Schwarz P unit cell-based tissue scaffolds using a material model based on methacrylated poly(D,L-lactide-co-ε-caprolactone) (PLCL) with a lactide (L) to caprolactone (C) ratio of 16:4 i.e. LCM3. This approach which reduces the tissue scaffolds structure to the analysis of a single representative unit cell has been consistently validated thus proving its correct implementation.

In the context of linear analysis, micromechanical analysis has demonstrated excellent agreement to experimental mechanical characterisation with only a small margin of error at 6.94% in terms of modulus values despite the geometrical transformations that have occurred. In the context of non-linear analysis, micromechanical analysis was implemented to oversee mechanical characterisation of the scaffolds considered in terms of their stress-strain response. The stress-strain curves obtained from micromechanical analyses were found to have parallels with experimental stress-strain curves obtained from confined compression of the tissue scaffolds. This was further justified through the mathematical expressions defining the boundary conditions derived for micromechanical analysis. With this, non-linear micromechanical analysis is applicable to mechanically characterise the stress-strain response of the tissue scaffold under realistic *in vivo* loading conditions.

The use of the approach has been constantly validated and has been able to position itself within experimental contexts. With various different packing systems which can be used to idealise structures consisting of a periodic arrangement of microstructures, micromechanical analysis can be applied to other regular tissue scaffold architecture. Furthermore, micromechanical analysis can also be used to computationally characterise

structures outside of the field of bone tissue engineering under the condition that they can be idealised as a crystal packing system. With this in mind and the nature of micromechanical analysis which reduces a structure with periodic microstructure to the analysis of a single representative unit cell, efficiency in terms of time and computational resources is maintained.

The relationships between different dimensional parameters to the resulting effective modulus of Schwarz P unit cells configured with thickness variations at constant surface radius have successfully been assessed. Mathematical expressions describing the relationships have been obtained specific for the Schwarz P architecture made of LCM3. From there, the appropriate expressions were normalised to allow the equations to be used as a predictive tool while also allowing the accommodation of other possible material models. With respect to a considered material model, a suitable set of dimensional parameters can then be selected with due regards to the determined effective modulus before delving into more complex analysis whether it be computationally or experimentally.

With all the above, the aims and objectives set out for this study have been fully and successfully achieved.

6.3 Further Improvements

The following sub-sections highlight further improvements that can be performed in regards to this study.

6.3.1 Extended Averaging of Unit Cell SEM Micrographs

In mediating geometrical transformations, SEM micrographs of tissue scaffolds were split into individual observable unit cells before performing the averaging in accordance to the methodology that has been discussed. The Schwarz P unit cell CAD model was reconstructed to take measurements from the averaged SEM while idealising it with 3-dimensional quarter symmetry. An alternative method to averaging a whole collection of unit cell SEM micrograph is to further split each unit cell micrograph into four different SEM micrographs. Consider an example of a unit cell SEM micrograph as shown in Figure 6-1.

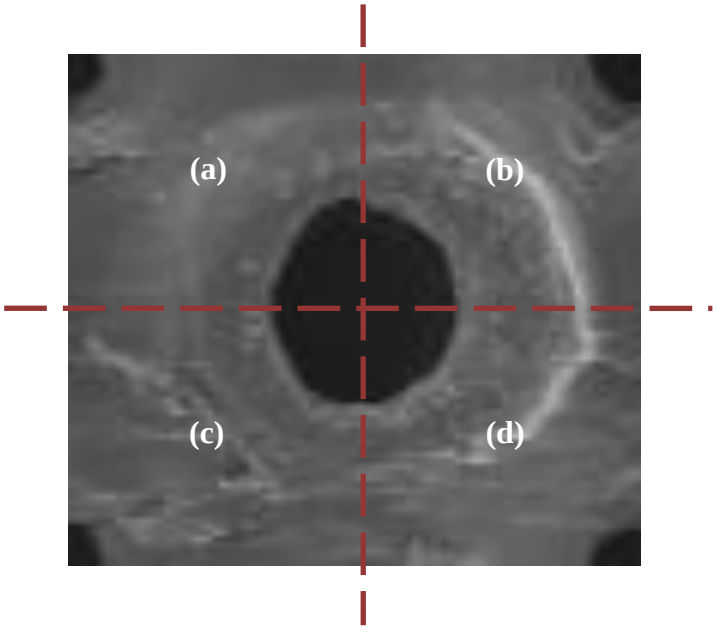

Figure 6-1 : Graphical presentation of an individual unit cell SEM micrograph being split into four with the center of the internal pore diameter as a reference point. The micrograph is split along the horizontal and vertical axes at the center point.

Splitting of the unit cell SEM micrograph would create 4 individual SEM counterparts namely; (a), (b), (c) and (d). The individual counterparts for (b) can be reflected along the vertical axis so that it 'stacks' above (a). Individual counterpart (c) can be reflected along the horizontal axis so that it 'stacks' above (a) and (b). Individual counterpart (d) can be reflected along the horizontal axis and subsequently the vertical axis or vice versa so that it 'stacks' above individual SEM counterparts (a), (b) and (c). Hence, for a single unit cell SEM micrograph the counterparts (b), (c) and (d) will be stacked above (a) with the same orientation. The averaging can then be proceeded as usual before subsequent measurement analyses. A computational algorithm can be constructed based off of this concept rather than manually splitting each unit cell micrograph. The measurements made can then be used to reconstruct the Schwarz P unit cell and thus mediate the geometrical transformations.

6.3.2 Imaging Modality Based Model

A Schwarz P unit cell-based tissue scaffold sample can be scanned through an imaging modality such as micro-CT scanning. The image data of the scaffold can then be imported into reverse engineering software such as Simpleware (Synopsys, Inc., California, US) or Materialise MIMICS (Materialise, Belgium) before subsequently performing segmentation to obtain a 3D model of the scanned tissue scaffold sample. Based on the concept above, a methodology can be constructed to average every unit cell comprising the scaffold sample. This is an advantage over using SEM micrographs which only averages the observable unit cells on the external sides of samples.

6.4 Future Work

The following sub-sections highlight potential future work from which this study can be extended to.

6.4.1 Schwarz P Configuration : Surface Radius Variations at Constant Thickness

Linear analysis was performed for Schwarz P configurations with thickness variations at constant surface radius with the implementation of micromechanical analysis. A similar approach as performed in this study can be performed for Schwarz P configurations with surface radius variations at constant thickness. The boundary conditions required for micromechanical analysis to be implemented is similar since there are no changes in terms of the equivalency between height, width and length. Relationships between different dimensional parameters and the resulting effective modulus can be assessed. The relationships can then be further expressed in terms of mathematical equations.

Analysis for the above would imply completion in assessing the relationship between different dimensional parameters and the respective effective modulus for the two modeling constraints for Schwarz P architecture i.e. thickness variations at constant surface radius and surface radius variations at constant thickness.

6.4.2 Computational Biological Characterisation

Previous studies have been performed in regards to simulating tissue growth. Various custom algorithms can be constructed based on different concepts. Random walk models have been proposed to differentiate tissue differentiation. The proposed model has compiled cell proliferation, cell migration, and mechanoregulation model into a mechanobiological model to simulate the tissue differentiation [237]. The mechanoregulation model builds upon foundational work investigating the relationship between biophysical stimuli in terms of octahedral shear strain and relative fluid/solid velocity to regulate tissue differentiation [12]. Computational simulations for bone regeneration have also been performed [185]. The above can be further combined with concepts such as nutrient oxygen supply and cell apoptosis to simulate cell growth within the confines of a scaffold in a more realistic sense [238,239]. Completion of the above covers two crucial aspects in tissue scaffold design i.e. mechanical and biological aspect. With the mechanical characterisation and the relationships already established in terms of mathematical equations, computational biological characterisation can be built upon to oversee the efficiency of the implementation of Schwarz P unit cell-based scaffold design. This will reduce experimental trial and error work to make the design process more reproducible.

Some attempts have been performed in plans to simulate tissue differentiation through the incorporation of strains/stresses from micromechanical analysis together with a random walk model and a mechanobiological model. Cells were assumed to be seeded within the confines of a Schwarz P unit cell and were modeled as spheres. In the attempt, the pore space surface geometry CAD model of a Schwarz P unit cell was obtained based on the Schwarz P unit cell surface geometry CAD model itself as shown in Figure 6-2

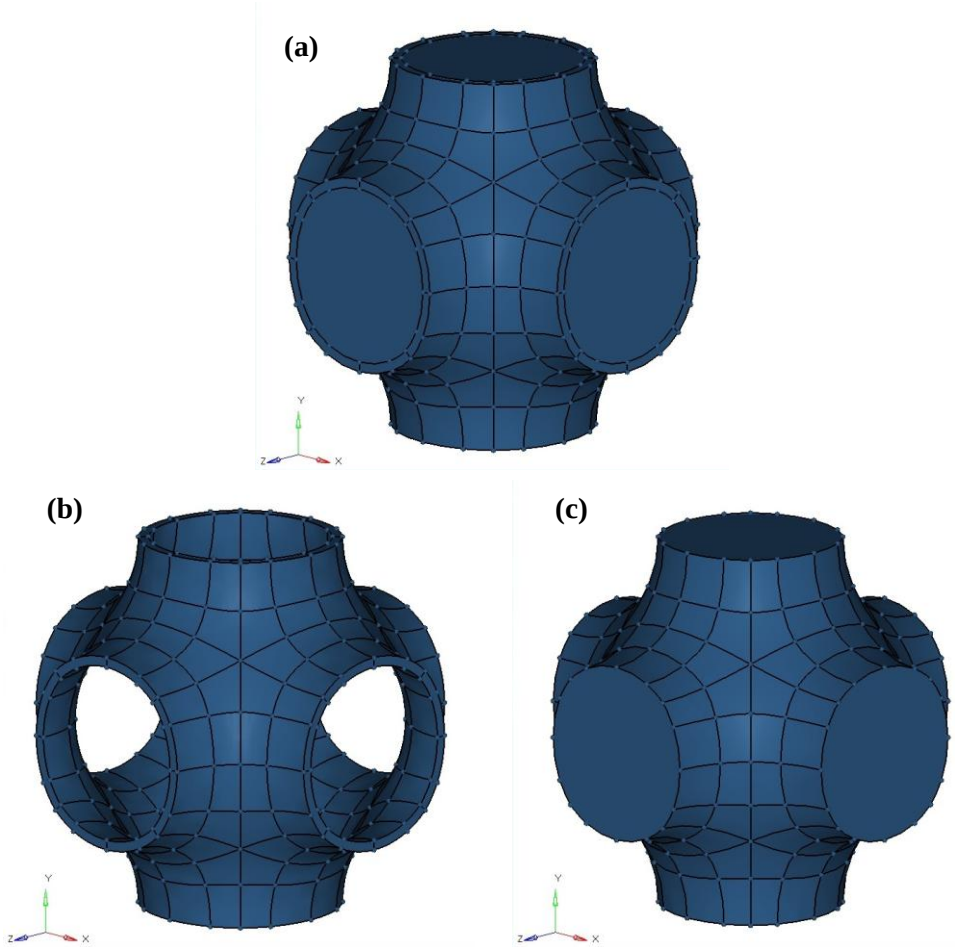

Figure 6-2 : Creation of a Schwarz P unit cell pore space surface geometry CAD model. (a) Schwarz P unit cell with enclosed pore space; (b) Isolation of the unit cell surface geometry model from (a); (c) Isolation of the pore space surface geometry model from (a). The pore space of the Schwarz P unit cell was enclosed through the creation of a surface around the internal diameter of the pore throat. The pore space surface geometry model was obtained by performing a Boolean operation from which the model in (b) is subtracted from the model in (a) i.e. (a-c).

The pore space was then subsequently discretised into tetrahedrals (as shown in Figure 6-3) after which the nodal coordinates were used in a custom MATLAB algorithm.

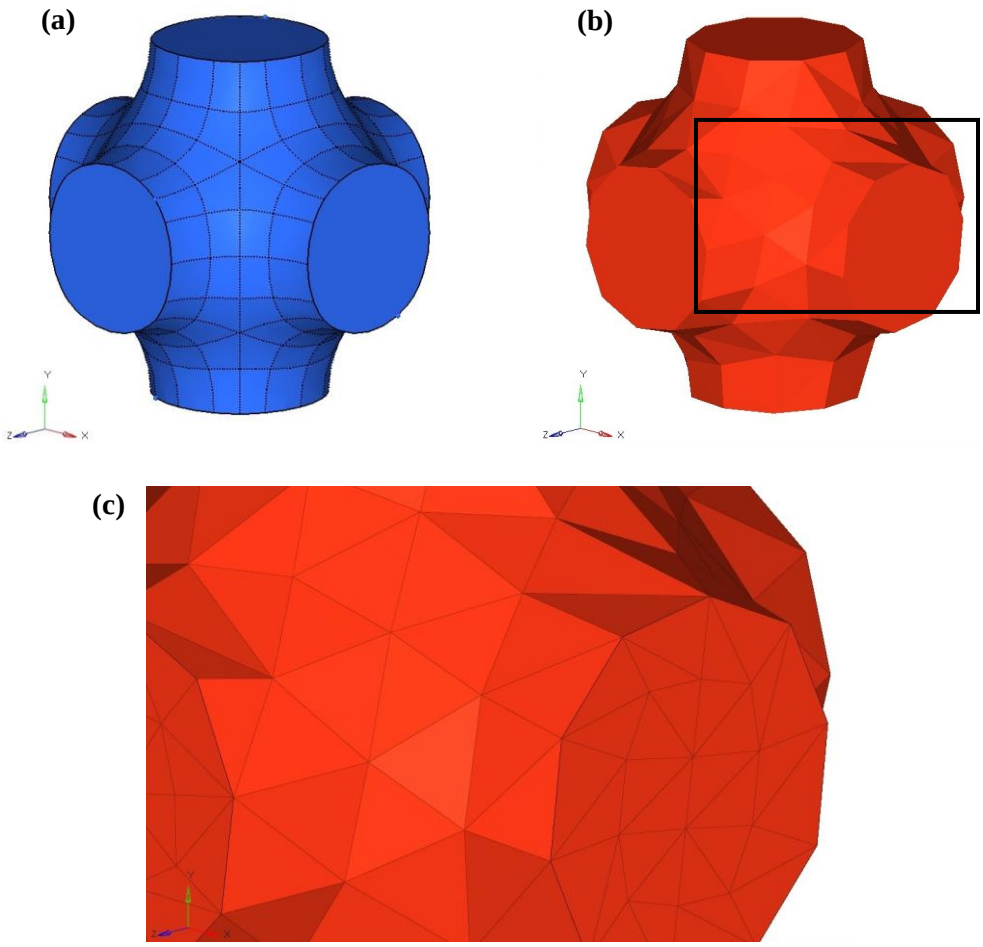

Figure 6-3 : Discretisation of the pore space surface geometry CAD model. (a) The pore space surface geometry model in Figure 6-2(c) was scaled down slightly in size to prevent future complications between the discretisation of the Schwarz P unit cell model and subsequent discretisation of spheres (used to model cells) during compilation; (b) Discretisation of the Schwarz P pore space surface geoemetry CAD model; (c) Zoomed view of the region within the bounded box in (b).

The algorithm takes the nodal coordinates for the formation of each tetrahedral i.e. nodal coordinates of the vertices; to determine the maximum allowable diameter of a sphere. The center point for each sphere that gives the maximum diameter was also determined. The process above was repeated until a suitable average diameter of a desired value was

obtained. For trial purposes, the above attempts were repeated to obtain diameters of approximately 25μm to represent the average diameter of a eukaryotic cell.

With the maximum diameter and the center point established for each tetrahedral, the information was used in a custom TCL script (specific for Altair Hyperworks). The TCL script generates spheres consisting of maximum diameters at center points for each respective tetrahedral within the confines of the Schwarz P unit cell surface geometry CAD model. A graphical presentation of the generation of spheres based on the discretised tetrahedrals is shown in Figure 6-4.

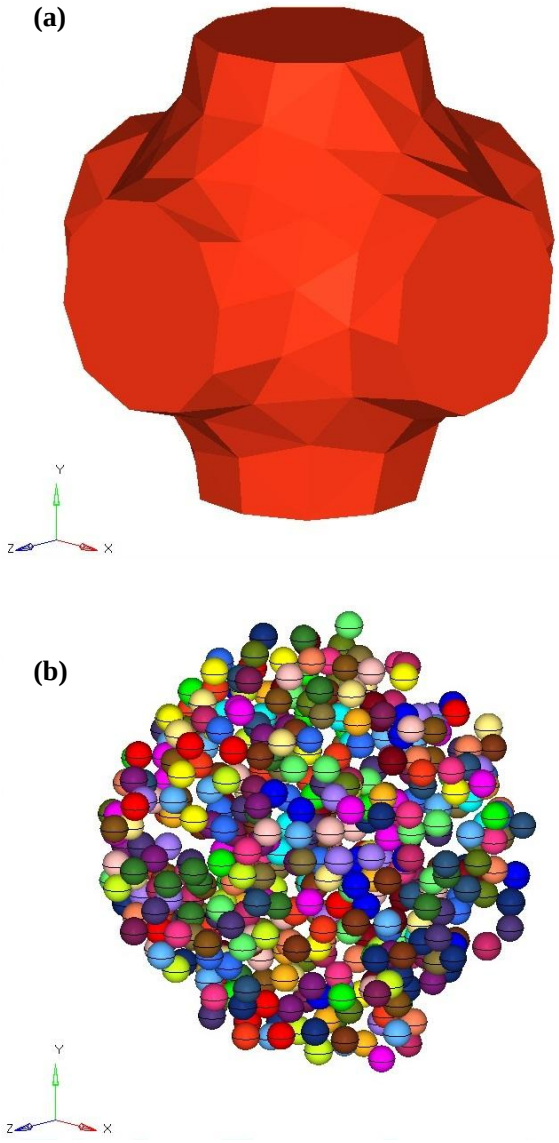

Figure 6-4 : Creation of spheres representing possible locations for cell growth and cell migration. (a) Discretisation of the pore space surface geometry CAD model; (b) Collection of spheres with the maximum allowable diameter within each discretised tetrahedral in (a). A custom MATLAB algorithm was constructed to process each discretised tetrahedral and determine the maximum allowable sphere diameter that is able to be accommodated. The center point for the maximum allowable sphere diameter was also determined. Based on the sphere diameter size and the center points, a TCL script was used to generate spheres within Altair Hyperworks.

well as the spheres. Alongside performing the simulation, a custom MATLAB algorithm has also been constructed to track the random movement of cells. Based on these movements, the required extensions to the algorithm were due to be constructed for a random walk model and a mechanobiological model depending on the success of initial simulations discussed previously. However, progress in regards to above was halted due to processing difficulties in running the simple simulation.

With the above, progress in regards to biological characterisation has only been able to be committed with success from a CAD modeling perspective as well as the construction of a MATLAB algorithm for the foundation of a random walk model and potentially a mechanobiological model.

6.4.3 Characterisation of Scaffold Transport Pathways

A previous study has investigated different methodologies in parameterising scaffold transport pathways through the use of micro-computed tomography (μCT) scans of scaffolds as a foundation. Such methodologies include 'Flood Fill', '3D Shrink-Wrap', 'Directional Shrink Wrap' and 'Percolation'. The 'Percolation' method follows percolation theory to determine the diameter of the largest sphere that can travel through a scaffold with a specified direction [240].

Segmentation can be performed on microCT scans of scaffolds to subsequently obtain a respective 3D model through the use of reverse engineering software. Alongside the scaffold structure, a 3D model of the transport pathways within the scaffold can also be obtained before its subsequent discretisation into tetrahedrals. A custom MATLAB algorithm can be constructed to take nodal information from the discretised tetrahedrals to determine the maximum allowable diameter of a sphere in each tetrahedral. In addition, the algorithm can be extended to take the context behind tracking the movement of cells discussed in the previous sub-section. By combining the two contexts, the maximum diameter of a size that is able to "move" throughout the scaffold transport pathways can be determined.

6.4.4 Two-Photon Polymerisation (2PP) & Schwarz P Fabrication Modeling

The literature review has discussed different 2PP configurative parameters involved in producing a structure. In the context of Schwarz P unit cell-based tissue scaffolds in this study, it has been determined that geometrical transformations in terms of shrinkage have occurred. By setting different 2PP configurative parameters before proceeding with fabrication, the resulting output structure can be scanned via imaging modalities and imported into a reverse engineering software to produce a 3D model of the scaffold fabricated. An average of the unit cells comprising the fabricated tissue scaffold can then be obtained. By performing the above by setting different configurative parameters as control, measurement analyses can be performed on the averaged unit cell. With this, relationships between different parameters and the resulting output structure in terms of their measurements can be determined. Subsequently, an optimum configuration can be selected for fabrication.

Appendices

A Chapter 4 : Experimental Model

A.1 Bulk LCM3 Averaging Algorithm

The following custom algorithm was constructed using a combination of MATLAB and a proprietary package, SLM. The algorithm determines an average stress-strain data based on stress-strain data of different samples involved. Stress-strain data are compiled into a single excel file with each sample being specified a sheet. This excel file was titled 'LCM3 – Best Fit Line (Hyperelastic Fitting)'.

```
LCM3_datafile = 'LCM3 - Best Fit Line (Hyperelastic Fitting)';
LCM3_file_name_xlsx = strcat(LCM3_datafile, '.xlsx');
[~, LCM3_specimen_sheets_name] = xlsfinfo(LCM3_file_name_xlsx);
LCM3_specimen_sheets_N = numel(LCM3_specimen_sheets_name);

specimen_strain_eval = linspace(0, 0.60, 3000);
specimen_stress_coll = [];
for sheet = 1:LCM3_specimen_sheets_N
    LCM3_stress_strain_read = xlsread(LCM3_file_name_xlsx,
sheet);
    strain_coll = LCM3_stress_strain_read(:,1);
    stress_coll = LCM3_stress_strain_read(:,2);

    [slm, xp, yp] = slmengine(strain_coll, ...
        stress_coll, ...
        'plot', 'off', ...
        'knots', 20, ...
        'extrapolation', 'cubic', ...
        'leftminvalue', 0);

    stress_eval = slmeval(specimen_strain_eval, slm, 0);
    specimen_stress_coll(:, end+1) = stress_eval;
end

stress_avg_coll = [];
[stress_data_N, spec_N] = size(specimen_stress_coll);
for d = 1:stress_data_N
    stress_avg = (sum(specimen_stress_coll(d,:))) / spec_N;
    stress_avg_coll(d,1) = stress_avg;
end
```

```
plot(specimen_strain_eval, specimen_stress_coll(:,1), 'magenta');
hold on
plot(specimen_strain_eval, specimen_stress_coll(:,2), 'cyan');
hold on
plot(specimen_strain_eval, specimen_stress_coll(:,3), 'red');
hold on
plot(specimen_strain_eval, specimen_stress_coll(:,4), 'green');
hold on
plot(specimen_strain_eval, specimen_stress_coll(:,5), 'blue');
hold on
plot(specimen_strain_eval, stress_avg_coll, 'black'); hold on
xlabel('Strain'); ylabel('Stress (MPa)')

specimen_avg_coll = [specimen_strain_eval', stress_avg_coll];
file_name_txt = strcat(LCM3_datafile, '_AvgFit.txt');
specimen_avg_stress_strain_write = fopen(file_name_txt, 'w');
fprintf(specimen_avg_stress_strain_write, file_name_txt);
fprintf(specimen_avg_stress_strain_write, '\n\n');
fprintf(specimen_avg_stress_strain_write, ...
    '%.20f , %.20f\n', specimen_avg_coll');
fclose(specimen_avg_stress_strain_write);
```

B Chapter 5 : Computational Model

B.1 Tabulated Results for Effective Modulus with Respect to Micromechanical Analysis and Homogenisation via Finite Element

Table B.1-1 : Reaction force and calculated effective modulus obtained from homogenisation via finite element; and the calculated effective modulus obtained from micromechanical analysis approach in characterising the mechanical properties of Schwarz P unit cell at different levels of mesh refinement.

No. of elements	**Homogenisation via finite element**			**Micromechanical analysis**
	Reaction force ($\times 10^{-6}$ kN)	**Surface area (mm^2)**	**Effective modulus, E_H (MPa)**	**Effective modulus, E_M (MPa)**
53053	3.1621	0.01143	0.2766	0.10979
82558	3.1621		0.2766	0.10975
110613	3.2069		0.2805	0.10971
137535	3.2097		0.2807	0.10970
159981	3.2091		0.2807	0.10970
178154	3.2094		0.2807	0.10969
225276	3.2102		0.2808	0.10969
265403	3.2121		0.2809	0.10969
359853	3.2176		0.2814	0.10968
473631	3.2204		0.2817	0.10968
605997	3.2209		0.2817	0.10968
814883	3.2226		0.2819	0.10968
1121026	3.3484		0.2929	0.10968

B.2 Case I

B.2.1 Average Strain & Average Shear Strain Results

Table B.2-1 : Average strain values obtained from static, linear perturbation micromechanical analysis of discretised Schwarz P unit cell models assigned with 3 different LCM3 material models i.e. specimen 5 (for the lower limit), the calculated average and specimen 3 (for an upper limit). For each material model, the average strain results are symmetric along the diagonal with equivalent values within the diagonal. This thus validates correct implementation of displacement boundary conditions derived from the simple cubic packing system for micromechanical analysis.

Material model	**Degree of freedom of macroscopic load application**	**Average strain**		
		x	y	z
Specimen 5 (Lower limit)	ε_x^0	0.541	0.226	0.227
	ε_y^0	0.226	0.541	0.227
	ε_z^0	0.226	0.226	0.541
Average	ε_x^0	0.429	0.180	0.180
	ε_y^0	0.180	0.429	0.180
	ε_z^0	0.180	0.180	0.429
Specimen 3 (Upper limit)	ε_x^0	0.377	0.158	0.158
	ε_y^0	0.158	0.377	0.158
	ε_z^0	0.158	0.158	0.377

Table B.2-2 : Average shear strain values obtained from static, linear perturbation micromechanical analysis of discretised Schwarz P unit cell models assigned with 3 different LCM3 models i.e. specimen 5 (for the lower limit), the calculated average and specimen 3 (for an upper limit). For each material model, the average shear strain results are symmetric along the diagonal with equivalent values within the diagonal. This thus validates correct implementation of displacement boundary conditions derived from the simple cubic packing system for micromechanical analysis.

Material model	**Degree of freedom of macroscopic load application**	**Average shear strain**		
		x	y	z
Specimen 5 (Lower limit)	γ^0_{yz}	0.506	1.867E-06 (≈ 0)	1.981E-06 (≈ 0)
	γ^0_{xz}	1.867E-06 (≈ 0)	0.506	6.357E-06 (≈ 0)
	γ^0_{xy}	1.981E-06 (≈ 0)	6.357E-06 (≈ 0)	0.506
Average	γ^0_{yz}	0.402	1.482E-06 (≈ 0)	1.572E-06 (≈ 0)
	γ^0_{xz}	1.482E-06 (≈ 0)	0.402	5.044E-06 (≈ 0)
	γ^0_{xy}	1.572E-06 (≈ 0)	5.044E-06 (≈ 0)	0.402
Specimen 3 (Upper limit)	γ^0_{yz}	0.353	1.301E-06 (≈ 0)	1.381E-06 (≈ 0)
	γ^0_{xz}	1.301E-06 (≈ 0)	0.353	4.431E-06 (≈ 0)
	γ^0_{xy}	1.381E-06 (≈ 0)	4.431E-06 (≈ 0)	0.353

B.3 Schwarz P Unit Cell CAD Model Reconstruction

B.3.1 Python Algorithm : Unit Cell SEM Micrograph Center Point Transposition

The following Python algorithm transposes the center point (defined by the center point of the internal pore diameter) of a unit cell SEM micrograph on a blank black canvas.

```
from PIL import Image
import pandas as pd

UC_view = 'II_'
UC_center_points_coll = pd.read_excel(UC_view + 'UC_CenterPoints.xlsx', sheetname = 'Sheet1')
UC_center_X_coll = UC_center_points_coll['round(X)']
UC_center_Y_coll = UC_center_points_coll['round(Y)']
UC_img_N = len(UC_center_X_coll)

def main():
    for img_n in range(0, UC_img_N):
            img_Background = Image.open('Background_Canvas.jpg')
            Background_width = img_Background.size[0]
            Background_height = img_Background.size[1]
            Background_center_X = Background_width / 2
            Background_center_Y = Background_height / 2

            img_ToPaste_name = UC_view + str(img_n + 1) + '.jpg'
            img_ToPaste_savename = UC_view + str(img_n + 1) + '_Centered.jpg'
            img_ToPaste = Image.open(img_ToPaste_name)

            UC_center_X = UC_center_X_coll[img_n]
            UC_center_Y = UC_center_Y_coll[img_n]

            img_shift_X = int(Background_center_X - UC_center_X)
            img_shift_Y = int(Background_center_Y - UC_center_Y)

            try:
                img_Background.paste(img_ToPaste, (img_shift_X, img_shift_Y))
                img_Background.save(img_ToPaste_savename)

            except IOError:
                pass


if __name__ == "__main__":
    main()
```

B.3.2 Python Algorithm : Unit Cell SEM Micrograph Averaging

The following algorithm was used to average the collection of unit cell SEM micrographs with the black background. The averaged unit cell SEM micrograph and the scale cropped from the tissue scaffold SEM micrograph was then transposed on a separate black canvas.

```
from PIL import Image
import pandas as pd
import numpy as np

UC_view = 'II_'
UC_center_points_coll = pd.read_excel(UC_view + 'UC_CenterPoints.xlsx', sheetname = 'Sheet1')
UC_center_X_coll = UC_center_points_coll['round(X)']
UC_center_Y_coll = UC_center_points_coll['round(Y)']
UC_img_N = len(UC_center_X_coll)

file_nameList = []
for img_n in range(0, UC_img_N):
    file_name = UC_view + str(img_n + 1) + '_Centered.jpg'
    file_nameList.append(file_name)

img_data = np.array([np.array(Image.open(image_name)) for image_name in file_nameList])
img_data_array = np.array(np.mean(img_data, axis = (0)), dtype = np.uint8)
average_img = Image.fromarray(img_data_array)
average_img.save(UC_view + 'Average.jpg')

img_CompleteBackground = Image.open('Complete_Canvas.jpg')
CompleteBackground_width = img_CompleteBackground.size[0]
CompleteBackground_height = img_CompleteBackground.size[1]
CompleteBackground_center_X = CompleteBackground_width / 2
CompleteBackground_center_Y = CompleteBackground_height / 2

average_img = Image.open(UC_view + 'Average.jpg')
average_img_center_X = int(UC_center_points_coll['round(avg(X))'][0])
img_UCAvg_Paste_shift_X = int(CompleteBackground_center_X - average_img_center_X)

img_scale = Image.open(UC_view + 'Scale.jpg')
img_UCScale_Paste_shift_X = int(CompleteBackground_center_X - img_scale.size[0])
img_UCScale_Paste_shift_Y = int(CompleteBackground_center_Y - img_scale.size[1])

try:
```

```
36.     img_CompleteBackground.paste(average_img, (img_UCAvg_Paste_shift_X,0
    ))
37.     img_CompleteBackground.paste(img_scale, (0, int(CompleteBackground_h
    eight - img_scale.size[1])))
38. 
39. except IOError:
40.     pass
41. 
42. img_CompleteBackground.save(UC_view + 'AverageWithScale.jpg')
```

B.4 Case II

B.4.1 Tabulated Results for Different Dimensional Parameters and Respective Effective Modulus for the Reconstructed Unit Cell Model and the Original Schwarz P Unit Cell

Table B.4-1 : Calculated normalised dimensional volume, normalised wall thickness, normalised radius of curvature and porosity for the original Schwarz P unit cell ('O') and reconstructed unit cell model ('A') along with their respective effective modulus.

Model	Normalised dimensional volume	Normalised wall thickness			Normalised radius of curvature			Porosity (%)	Effective modulus, E_y (MPa)
		Plane YZ	Plane YX	Split plane	Plane YZ	Plane YX	Split plane		
O	1.000	1.000	1.000	1.000	1.000	1.000	1.000	88.2	0.0968
A	0.461	2.031	2.121	2.761	0.928	0.905	0.638	65.3	0.742

B.4.2 Application & Derivations of Castigliano's Theorem for Curved Thin Beams

For surface curvatures lying along the cross-sectional planes of YZ and YX, the bending resistance can be described in terms of Castigliano's theorem for curved thin beams where the strain energy due to moment can be approximated as shown in Equation (B.1).

$$U = \int \frac{M^2}{2EI} R \, d\theta \quad \text{(B.1)}$$

for which,

M : Moment due to bending

E : Young's modulus

I : Second moment of area

R : Radius of curvature

Consider a curved beam which is loaded as shown in Figure B.4-1.

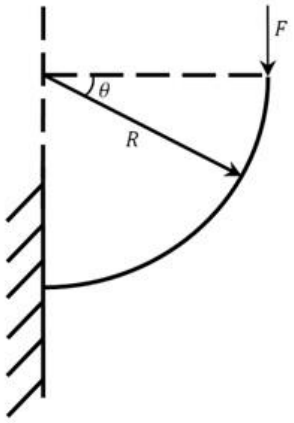

Figure B.4-1 : Curved beam with a pinned end. The beam has a curvature defined by the radius, R and an applied force F.

The moment due to bending can be defined as follows,

$$M = F[R - (R\cos\theta)]$$

$$= FR(1 - \cos\theta)$$

The equivalent strain energy,

$$U = \int_0^{\pi/2} \frac{[FR(1-\cos\theta)]^2}{2EI} R\, d\theta$$

The deflection,

$$\delta = \frac{\delta U}{\delta F}$$

Substituting for U in the equation for deflection, δ, Equation (B.2) is obtained.

$$\delta = \frac{FR^3}{EI}\left[\frac{3\pi}{4} - 2\right] \quad \text{(B.2)}$$

B.4.3 Application & Derivation of Euler Buckling Theorem for Initially Curved Beams

In the case for surface curvatures lying along the split plane, the bending resistance can be described in terms of Euler buckling theorem for initially curved columns. Consider a column with an initial lateral deflection of δ_i and an additional lateral deflection, γ_i after load application, F as shown in Figure B.4-2.

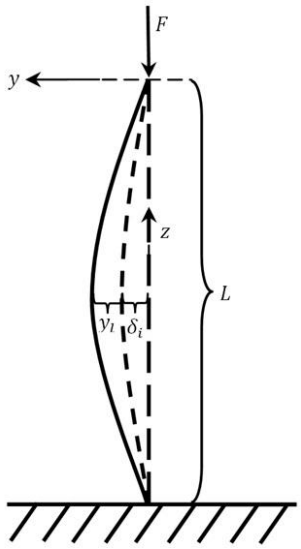

Figure B.4-2 : Column with a pinned end where y and z represents the directional axes. The column has a length, L and an initial deflection defined by $\boldsymbol{\delta_i}$. With the application of force, F in the direction shown, the column undergoes an additional lateral deflection defined by $\boldsymbol{\gamma_i}$.

The bending moment developed in the column,

$$M = -F(y_l + \delta_i)$$

Using bending relations where,

$$\frac{d^2y}{dz^2} = \frac{M}{EI}$$

for M is the developed bending moment, E is the Young's Modulus of the column and I is the second moment of area, the following is obtained,

$$\frac{d^2y}{dz^2} = -\frac{F}{EI}(y_l + \delta_i)$$

$$\frac{d^2y}{dz^2} + \frac{F}{EI}y_l = -\frac{F}{EI}\delta_i$$

Taking $k^2 = {}^{F}/_{EI}$, gives a second order, non-homogenous differential equation,

$$\frac{d^2y}{dz^2} + ky = -k\delta_i$$

The general solution for the equation above is,

$$y = A\sin(kz) + B\cos(kz) - \delta_i$$

Imposing boundary conditions where $y = 0$ at $z = 0$ and $z = L$:

$$B - \delta_i = 0$$

$$B = \delta_i$$

and,

$$y = A\sin(kz) + \delta_i\cos(kz) - \delta_i$$

Also,

$$A\sin(kL) + \delta_i[\cos(kL) - 1] = 0$$

$$A\sin(kL) = \delta_i[1 - \cos(kL)]$$

$$A = \delta_i\left[\frac{1 - \cos(kL)}{\sin(kL)}\right]$$

$$y = \delta_i\left[\frac{1 - \cos(kL)}{\sin(kL)}\right]\sin(kz) + \delta_i\cos(kz) - \delta_i$$

$$\therefore y = \delta_i\left[\frac{1 - \cos\left(L\sqrt{\frac{F}{EI}}\right)}{\sin\left(L\sqrt{\frac{F}{EI}}\right)}\right]\sin\left(z\sqrt{\frac{F}{EI}}\right) + \delta_i\cos\left(z\sqrt{\frac{F}{EI}}\right) - \delta_i$$

Maximum lateral deflection of the column, y_{max} occurs at $z = {}^{L}/_{2}$. With this,

$$y_{max} = \delta_i\left\{\left[\frac{1 - \cos(kL)}{\sin(kL)}\right]\sin\left(\frac{kL}{2}\right) + \left[\cos\left(\frac{kL}{2}\right) - 1\right]\right\}$$

$$= \delta_i\left\{\left[\frac{1 - \cos(kL)}{\sin(kL)}\right]\left[\frac{\sin(kL)}{2\cos\left(\frac{kL}{2}\right)}\right]\right\}$$

$$= \delta_i\left\{\left[2\left(\sin\frac{kL}{2}\right)^2\right]\left[\frac{1}{2\cos\left(\frac{kL}{2}\right)}\right] + 2\left[\cos\left(\frac{kL}{2}\right)\right]^2 - 2\cos\left(\frac{kL}{2}\right)\right\}$$

$$= \delta_i\left[\frac{1}{\cos\left(\frac{kL}{2}\right)} - 1\right]$$

$$= \delta_i\left[\sec\left({}^{kL}/_{2}\right) - 1\right]$$

$$\therefore y_{max} = \delta_i\left[\sec\left(\frac{L}{2}\sqrt{\frac{F}{EI}}\right) - 1\right]$$

Assume that the initial lateral deflection, δ_i follows a radial curvature as shown in Figure B.4-3, the initial deflection takes the expression shown in Equation (B.3).

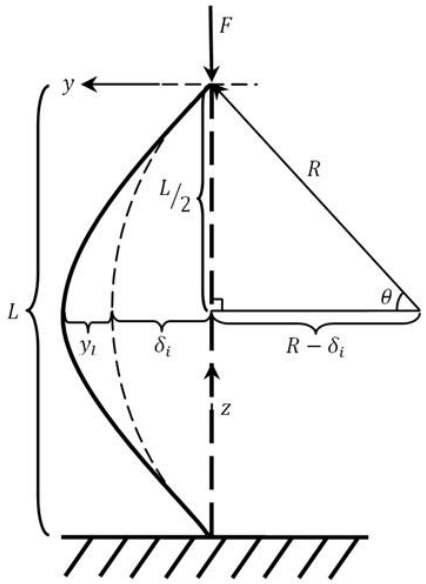

Figure B.4-3 : Column with an initial deflection that follows a radial curvature. The representation is similar to that of Figure B.4-2 with the difference being in terms of the initial deflection.

$$\delta_i = \left[R - {}^{L}/_{2}\cot(\theta)\right] \quad \textbf{(B.3)}$$

The maximum deflection is then determined to be the expression as shown in Equation (B.4).

$$y_{max} = \left[R - \frac{L}{2}\cot(\theta)\right]\left[\sec\left(\frac{L}{2}\sqrt{\frac{F}{EI}}\right) - 1\right] \quad \textbf{(B.4)}$$

B.4.4 Initial Method for Schwarz P Unit Cell-Based Tissue Scaffold SEM Measurement Analysis – Direct Measurement Approach

The ‘Direct Measurement’ approach performs measurement analysis on each unit cell comprising the fabricated tissue scaffold directly from SEM micrographs. Through this approach, , the dimensions of a unit cell i.e. height, width, length and wall thicknesses were measured directly using available measurement tools within ImageJ.

A comparison of the height, width and length measurements made found through the ‘Direct Measurement’ approach and that of the original Schwarz P unit cell design is tabulated in Table B.4-2. A comparison of the wall thickness between measurements made through the same approach and the original Schwarz P unit cell design is tabulated in Table B.4-3. For brevity, averaged values of wall thickness are tabulated.

Table B.4-2 : Comparison of height, width and length measurements of unit cells comprising the physical tissue scaffolds obtained from the 'Direct Measurement' approach and the intended Schwarz P unit cell design.

Parameter	**Measurement (Mean ± Standard deviation) (mm)**	
	Unit cells comprising fabricated scaffolds	**Intended Schwarz P unit cell design**
Height	0.406 ± 0.012	0.520
Width	0.420 ± 0.012	
Length	0.421 ± 0.007	

Table B.4-3 : Comparison of wall thickness measurements of unit cell comprising the physical tissue scaffold made through the 'Direct Measurement' approach and the original intended Schwarz P unit cell design.

Plane	**Wall Thickness Measurement (Mean ± Standard deviation) (mm)**	
	Unit cells comprising fabricated scaffolds	**Intended Schwarz P unit cell design**
YX	0.054 ± 0.012	0.014
YZ	0.054 ± 0.012	
XZ	0.053 ± 0.014	

The 'Direct Measurement' approach involved independently measuring dimensional parameters on a unit cell per unit cell basis. Hence, sample sets of height, width, length and wall thickness measurements were taken. Five unit cell models were reconstructed with respect to sample sets taken from the 'Direct Measurement' approach. These sample sets were taken from measurements tabulated in Table B.4-2 for the height, width and length; and Table B.4-3 for the wall thickness. The configurations for the height, width, length and wall thickness for each of the 6 reconstructed unit cell models are tabulated in Table B.4-4. The dimensional volume (product of height, width and length) and the measured radius of curvature are also tabulated in the same table. In regards to the wall thickness, the average lengths of the two ends of enclosed line segments for each cross-sectional plane are tabulated.

Table B.4-4 : Configurations for reconstructed unit cell models based on dimensional parameters obtained through the 'Direct Measurement' approach and the resulting dimensional volume and radius of curvature.

Model	Height (mm)	Width (mm)	Length (mm)	Dimensional volume (mm^3)	Average wall thickness (mm)			Radius of curvature (mm)		
					Plane YZ	Plane YX	Split Plane	Plane YZ	Plane YX	Split Plane
1-A	0.404	0.422	0.419	0.0715	0.0432	0.0454	0.0276	0.0957	0.1013	0.8589
2-A	0.406	0.427	0.424	0.0736	0.0700	0.0700	0.0704	0.1017	0.0982	0.7498
3-A	0.408	0.422	0.419	0.0722	0.0433	0.0456	0.0292	0.0958	0.1020	0.6923
4-A	0.404	0.415	0.419	0.0703	0.0369	0.0369	0.0369	0.1021	0.1015	0.7384
5-A	0.406	0.420	0.424	0.0724	0.0593	0.0592	0.0593	0.1031	0.1025	1.3007
O	0.520	0.520	0.520	0.1406	0.0139	0.0139	0.0139	0.1209	0.1209	0.1933

Each unit cell model was discretised using C3D10H elements and assigned material models based on the average, upper and lower limit material data for LCM3 in 3 separate analyses. With 5 reconstructed models, there are 15 main analyses in total i.e. each model is assigned the average, upper and lower limit material data of LCM3. Implementing the revised derivations of displacement boundary conditions for micromechanical analyses on each model, the results are discussed in the following.

Consider the results of average strains and average shear strains obtained for model 1-A (graphically presented in Figure B.4-4) as a representative example for the purpose of validating correct implementation of the revised displacement boundary conditions. The obtained average strains and average shear strains from micromechanical analysis of model 1-A is tabulated in Table B.4-5 and Table B.4-6 respectively.

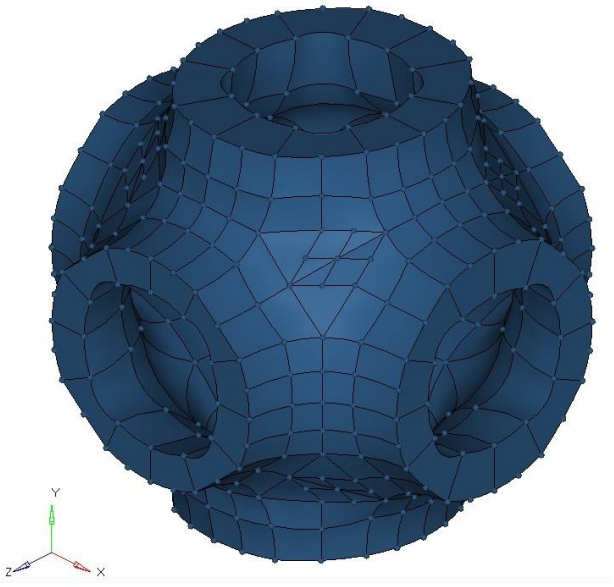

Figure B.4-4 : Graphical representation of model 1-A.

Table B.4-5 : Average strain values obtained from micromechanical analysis of reconstructed unit cell model 1-A assigned with 3 different LCM3 material models.

Material model	**Degree of freedom of load/displacement application**	**Average strain (4 s.f.)**		
		x	y	z
Specimen 3 (Upper limit)	ε_x^0	0.06879	0.02788	0.02551
	ε_y^0	0.02788	0.07448	0.02772
	ε_z^0	0.02551	0.02772	0.07270
Average	ε_x^0	0.07832	0.03174	0.02904
	ε_y^0	0.03174	0.08480	0.03156
	ε_z^0	0.02904	0.03156	0.08277
Specimen 5 (Lower limit)	ε_x^0	0.09871	0.04000	0.03660
	ε_y^0	0.04000	0.1069	0.03977
	ε_z^0	0.03660	0.03977	0.1043

Table B.4-6 : Average shear strain values obtained from micromechanical analysis of reconstructed unit cell model 1-A assigned with 3 different LCM3 material models.

Material model	**Degree of freedom of load/displacement application**	**Average shear strain (4 s.f.)**		
		x	y	z
Specimen 3 (Upper limit)	γ_{yz}^0	0.09350	9.736E-08 (≈ 0)	6.362E-08 (≈ 0)
	γ_{xz}^0	9.736E-08 (≈ 0)	0.09351	2.290E-08 (≈ 0)
	γ_{xy}^0	6.362E-08 (≈ 0)	2.290E-08 (≈ 0)	0.08793
Average	γ_{yz}^0	0.1064	1.109E-07 (≈ 0)	7.244E-08 (≈ 0)
	γ_{xz}^0	1.109E-07 (≈ 0)	0.1065	2.607E-08 (≈ 0)
	γ_{xy}^0	7.244E-08 (≈ 0)	2.607E-08 (≈ 0)	0.1001
Specimen 5	γ_{yz}^0	0.1342	1.397E-07 (≈ 0)	9.129E-08 (≈ 0)

(Lower limit)	γ_{xz}^{0}	1.397E-07 (≈ 0)	0.1342	3.286E-08 (≈ 0)
	γ_{xy}^{0}	9.129E-08 (≈ 0)	3.286E-08 (≈ 0)	0.1262

As observed from Table B.4-5 and Table B.4-6 respectively, the values of average strain and average shear strain is symmetric along the diagonal with differing values in the diagonal for each material model. This complies with the validation methods discussed the revised displacement boundary conditions derived for a simple cuboidal packing system. With this, the calculated effective modulus and shear modulus with respect to the x, y and z directions for model 1-A are tabulated in Table B.4-7.

Table B.4-7 : Effective modulus and effective shear modulus in accordance to directional axes obtained from micromechanical analyses of discretised reconstructed unit cell model 1-A with 3 different LCM3 material models.

Material model	**Direction**	**Effective modulus (MPa)**	**Effective shear modulus (MPa)**
Specimen 3 (Upper limit)	$\boldsymbol{x}$	1.017	0.7484
	$\boldsymbol{y}$	0.940	0.7483
	$\boldsymbol{z}$	0.963	0.7958
Average	$\boldsymbol{x}$	0.893	0.6574
	$\boldsymbol{y}$	0.825	0.6573
	$\boldsymbol{z}$	0.845	0.6990
Specimen 5 (Lower limit)	$\boldsymbol{x}$	0.709	0.5216
	$\boldsymbol{y}$	0.655	0.5215
	$\boldsymbol{z}$	0.671	0.5546

The effective modulus results are tabulated for each respective reconstructed unit cell model as shown in Table B.4-8. Since physical tissue scaffolds were compressed height-

wise (y-axis) before determining the experimental stress-strain curve and subsequent Young's modulus, only the effective modulus with respect to the y-axis will be considered. Graphical presentations of the results are also presented in Figure B.4-5 through Figure B.4-10.

Table B.4-8 : Calculated normalised dimensional volume, normalised wall thickness, normalised radius of curvature and porosity for the original Schwarz P unit cell ('O') and reconstructed unit cell models (1-A through 5-A) along with their respective effective modulus.

Model	**Normalised dimensional volume**	**Normalised wall thickness**			**Normalised radius of curvature**			**Porosity (%)**	**Effective modulus, E_y (MPa)**
		Plane YZ	**Plane YX**	**Split plane**	**Plane YZ**	**Plane YX**	**Split plane**		
O	1.000	1.000	1.000	1.000	1.000	1.000	1.000	88.2	0.0828
1-A	0.508	3.117	3.277	1.990	0.792	0.838	0.859	63.5	0.825
2-A	0.523	5.053	5.056	5.075	0.842	0.812	0.750	44.7	2.157
3-A	0.514	3.130	3.295	2.106	0.792	0.844	0.693	63.4	0.833
4-A	0.500	2.665	2.661	2.660	0.845	0.840	0.738	64.0	0.799
5-A	0.515	4.282	4.279	4.275	0.853	0.848	1.300	49.1	1.666

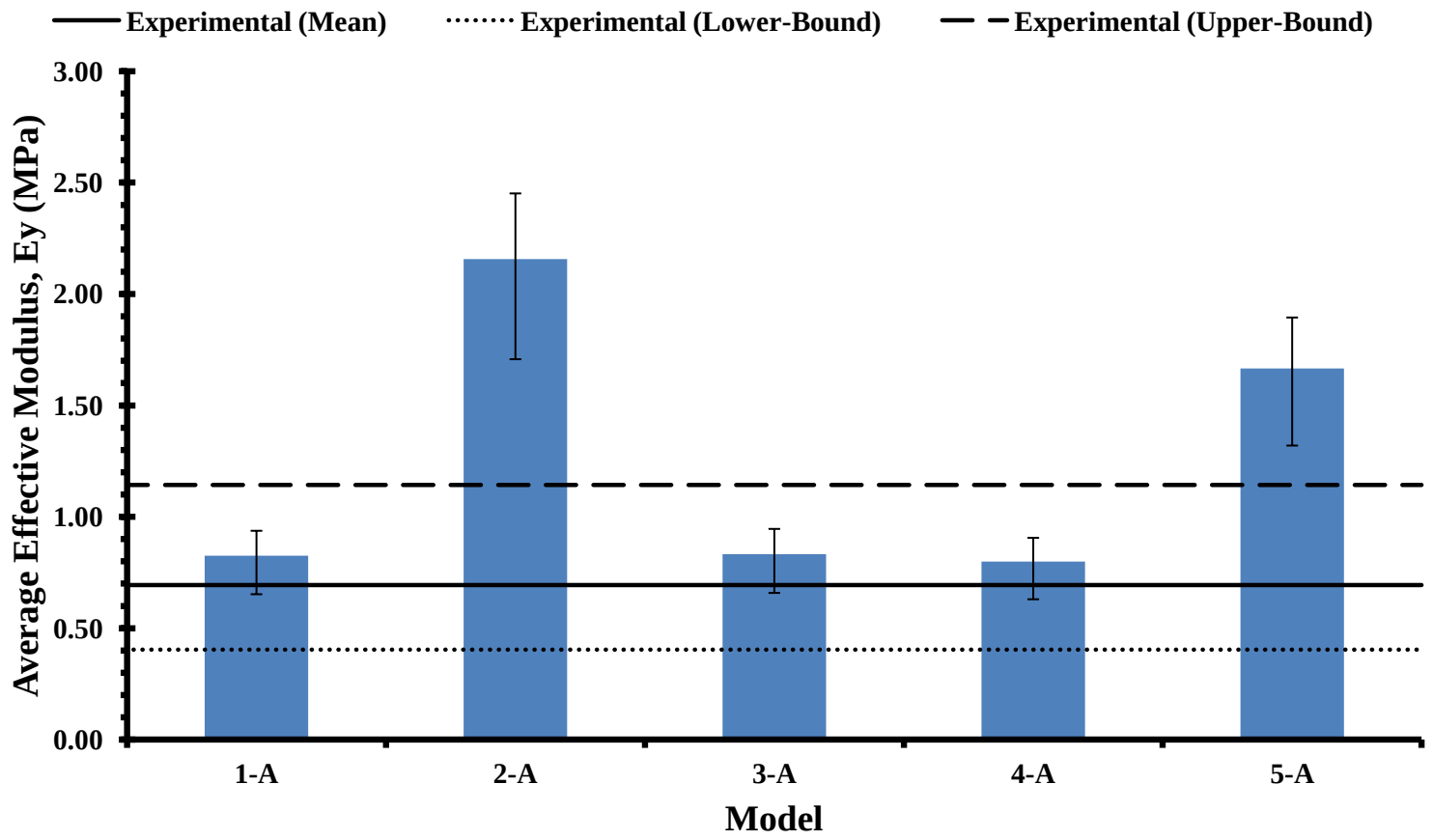

Figure B.4-5 : Average effective modulus across 5 different reconstructed unit cell models. The experimental results are represented as horizontal lines according to the lower limit, average and upper limit of modulus values obtained from compression experiments of fabricated tissue scaffolds.

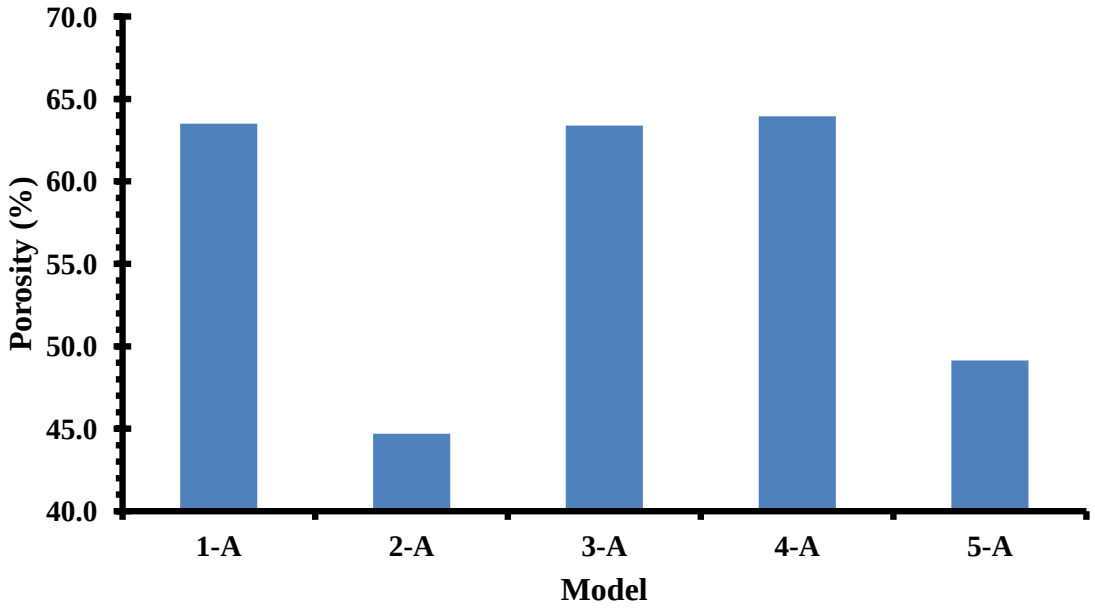

Figure B.4-6 : Graphical comparison of porosity across 5 different reconstructed unit cell models.

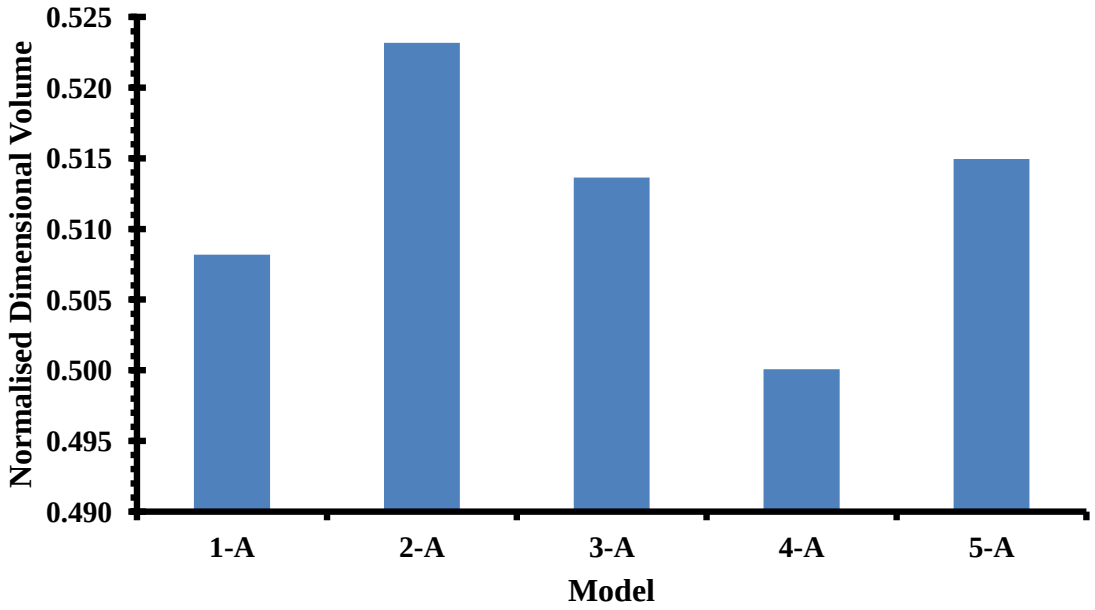

Figure B.4-7 : Graphical comparison of normalised dimensional volume across 5 different reconstructed unit cell models.

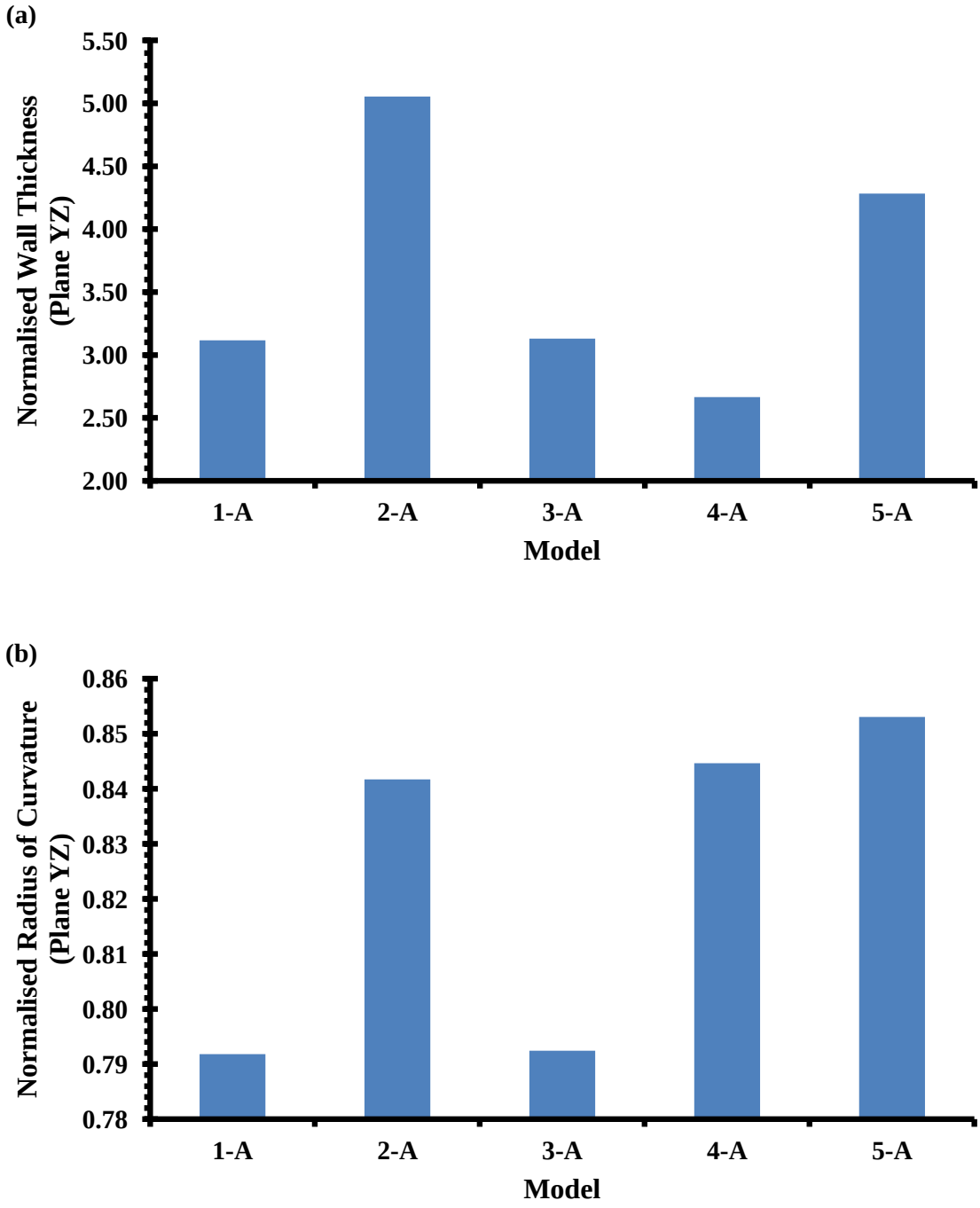

Figure B.4-8 : Graphical comparison of normalised (a) wall thickness; (b) radius of curvature; measured along the plane YZ for all 5 different reconstructed unit cell models.

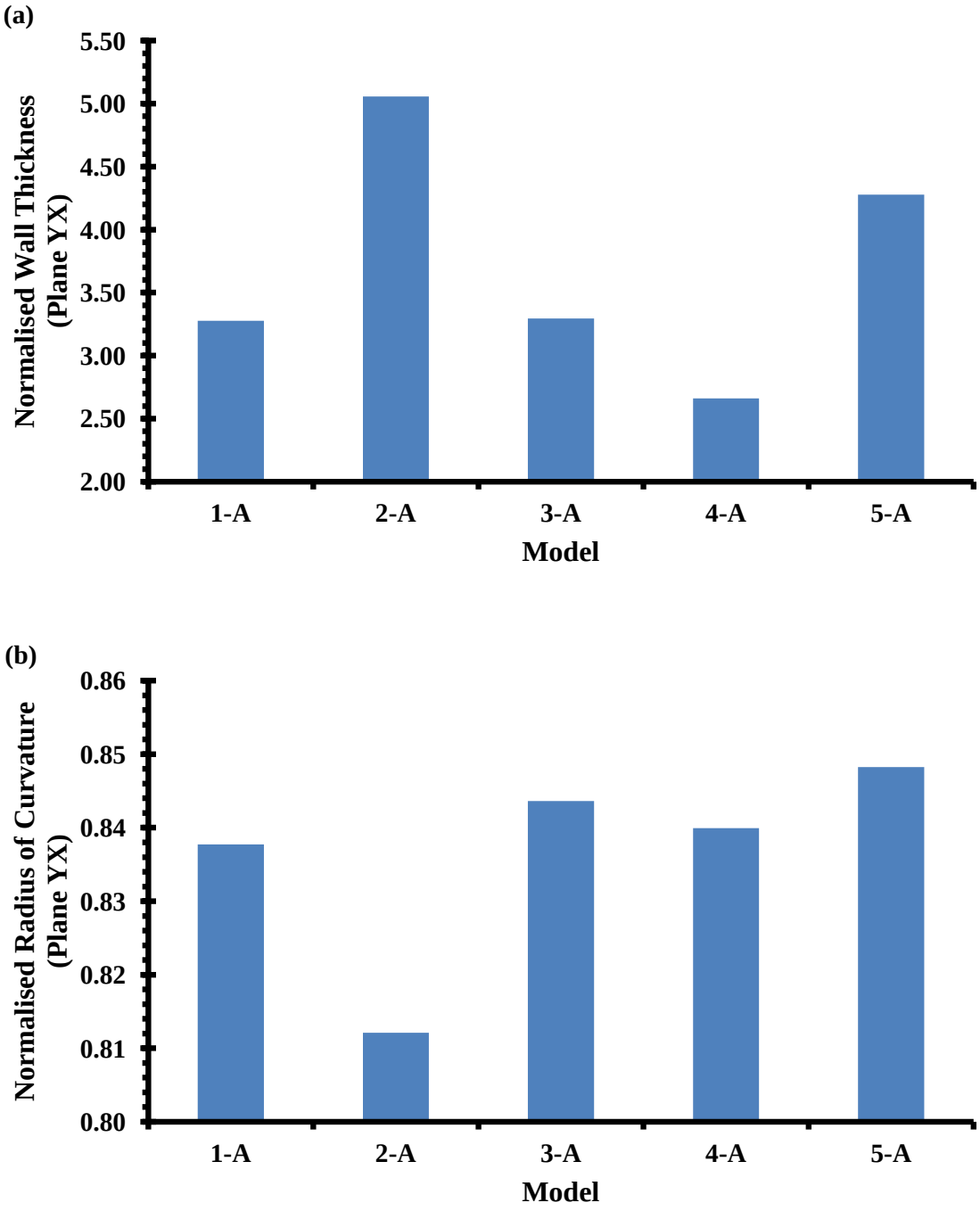

Figure B.4-9 : Graphical comparison of normalised (a) wall thickness; (b) radius of curvature; measured along the plane YX for all 5 different reconstructed unit cell models.

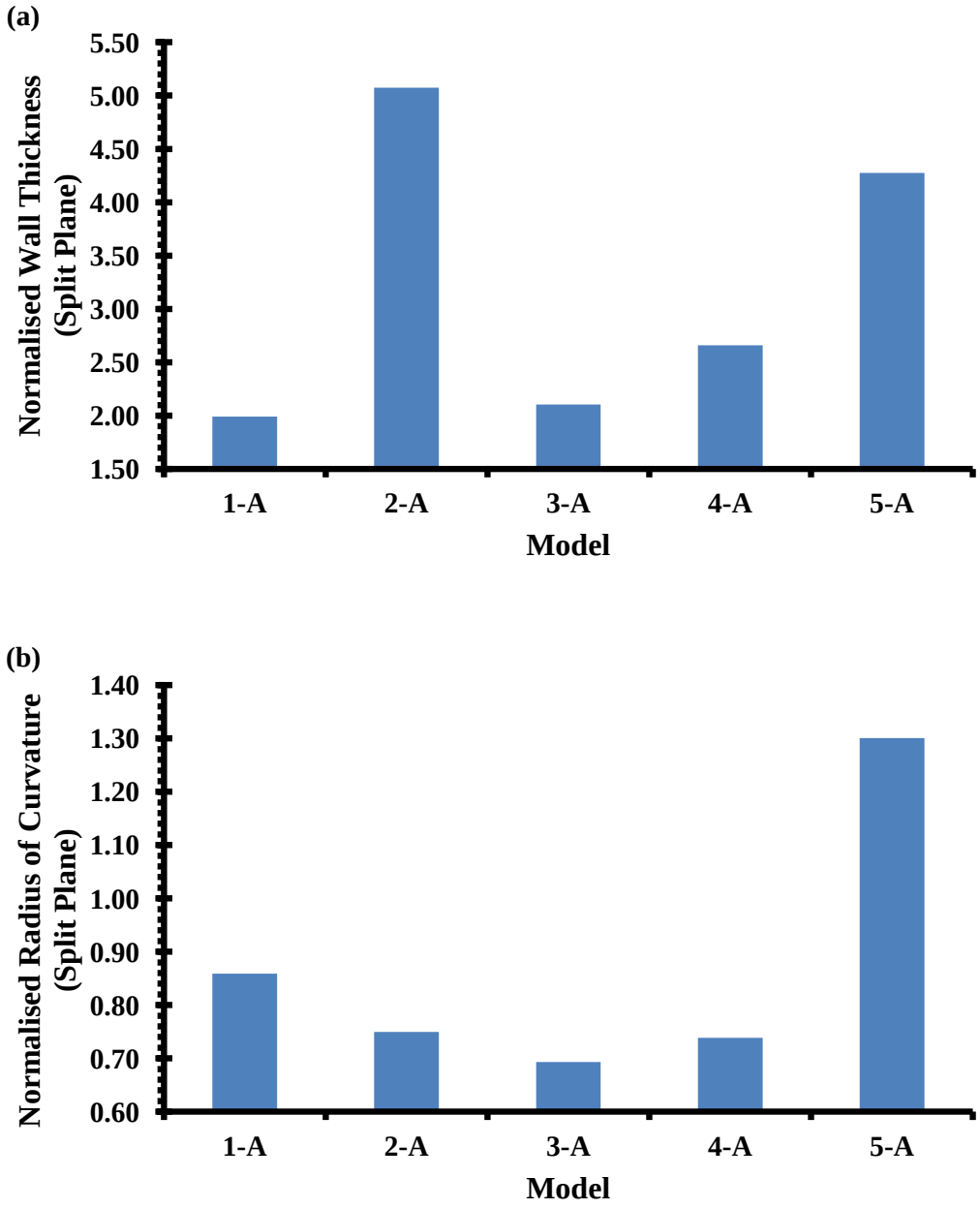

Figure B.4-10 : Graphical comparison of normalised (a) wall thickness; (b) radius of curvature; measured along the split plane for all 5 different reconstructed unit cell models.

Considering the 5 unit cell models reconstructed based on the 'Direct Measurement' approach, model 4-A is the closest to the experimental mean with a difference of 15.13%.

B.5 Case III

B.5.1 Average Strain & Average Shear Strain Results

Table B.5-1 : Representative example of average strain results obtained from dynamic, implicit, non-linear micromechanical analysis of the reconstructed unit cell model (assigned the averaged LCM3 material model) at an applied macroscopic load of 0.002N. The average strain results are symmetric along the diagonal with differing values within the diagonal. Therefore, the average strain results comply with the validation methods for correct implementation of displacement boundary conditions derived based on the simple cuboidal packing system for micromechanical analysis.

Material model	**Degree of freedom of macroscopic load application**	**Average strain**		
		x	***y***	***z***
Average	$\boldsymbol{\varepsilon_x^0}$	0.00365	0.00212	0.000429
	$\boldsymbol{\varepsilon_y^0}$	0.00212	0.00483	0.00189
	$\boldsymbol{\varepsilon_z^0}$	0.000429	0.00189	0.00320

Table B.5-2 : Average shear strain results obtained from dynamic, implicit, non-linear micromechanical analysis of the reconstructed unit cell model (assigned the averaged LCM3 material model) at an applied macroscopic load of 0.002N. The results shown were found to be non-symmetric along the diagonal. This is due to the dynamic, implicit analysis used for micromechanical analysis which is an iterative approach. Hence, the values tabulated are obtained after subsequent convergence of average force.

Material model	**Degree of freedom of macroscopic load application**	**Average shear strain**		
		x	***y***	***z***
Average	$\boldsymbol{\gamma_{yz}^0}$	0.00436	6.496E-9 (≈ 0)	1.389E-8 (≈ 0)
	$\boldsymbol{\gamma_{xz}^0}$	6.857E-9(≈ 0)	0.00628	1.047E-8(≈ 0)
	$\boldsymbol{\gamma_{xy}^0}$	1.351E-8 (≈ 0)	1.024E-8 (≈ 0)	0.00444

B.5.2 Tabulated Results of Average Stress-Strain Data Obtained From Micromechanical Analysis of the Reconstructed Unit Cell

Table B.5-3 : Tabulated representation of average stress-strain data obtained from dynamic, implicit non-linear micromechanical analyses of the reconstructed unit cell model in the 2nd degree of freedom. '*' indicates the occurence of excessive distortion during computational analysis and no result was able to be obtained.

Dimensional volume, V_D (mm^3)	**Load, F_y (N)**	**Average stress $= \left[\frac{F_y}{V_D}\right]$ (MPa)**	**Average strain, ε_y^0**		
			Lower limit (Specimen 5)	**Average**	**Upper limit (Specimen 3)**
0.0648	0.000	0.0000	0.0000	0.0000	0.0000
	0.0002	0.0031	0.0061	0.0048	0.0042
	0.0022	0.0340	0.0629	0.0506	0.0447
	0.0042	0.0648	0.1138	0.0923	0.0820
	0.0062	0.0957	0.1601	0.1309	0.1166
	0.0082	0.1265	0.2029	0.1668	0.1491
	0.0102	0.1574	0.2428	0.2006	0.1798
	0.0122	0.1883	0.2803	0.2326	0.2089
	0.0142	0.2191	*	0.2631	0.2366
	0.0162	0.2500	*	0.2921	0.2632

B.5.3 Confined Compression

A custom device was machined to confine the sides of a particular tissue scaffold specimen. The schematic for the custom device is presented in Figure B.5-11 through Figure B.5-14. The final product is shown in Figure B.5-15 and Figure B.5-16.

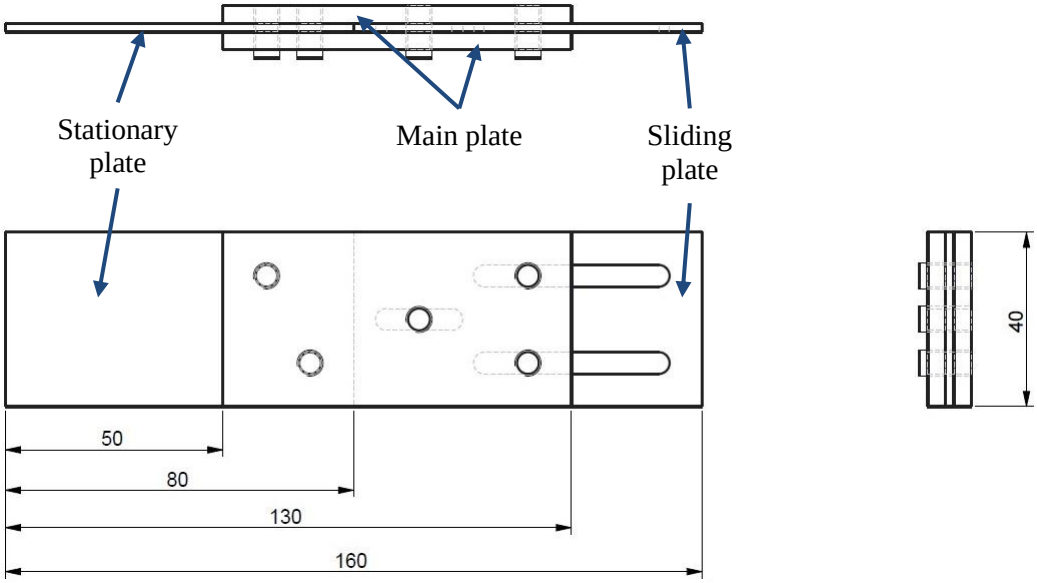

Figure B.5-11 : Schematic 2D drawing of the overall assembly for the device used to experiment confined compression. The device consists of a stationary plate and sliding plate sandwiched between two main plates bounded by a setup nuts and bolts. Nuts and bolts holding the sliding plate can be loosened to allow lateral movement of the sliding plate while those holding the stationary plate are always remained tightened. As a tissue scaffold is placed between the stationary and sliding plates, the sliding plate is slid in place and the nuts and bolts are tightened to confine the tissue scaffold. All the measurements shown are in the units of millimeters.

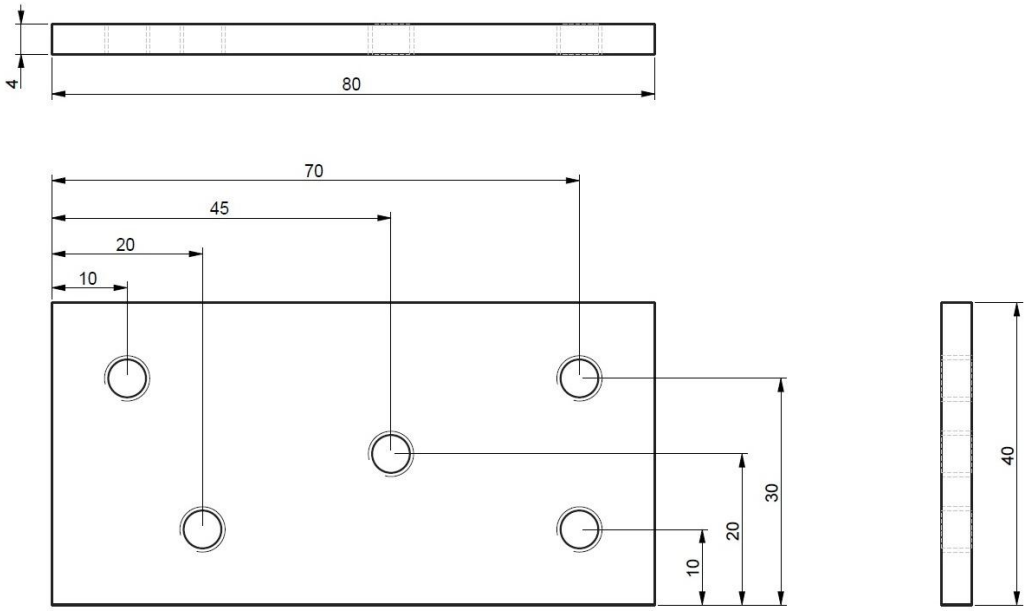

Figure B.5-12 : Schematic 2D drawing of the main plates used to sandwich the stationary and sliding plates. All the measurements shown are in millimeters.

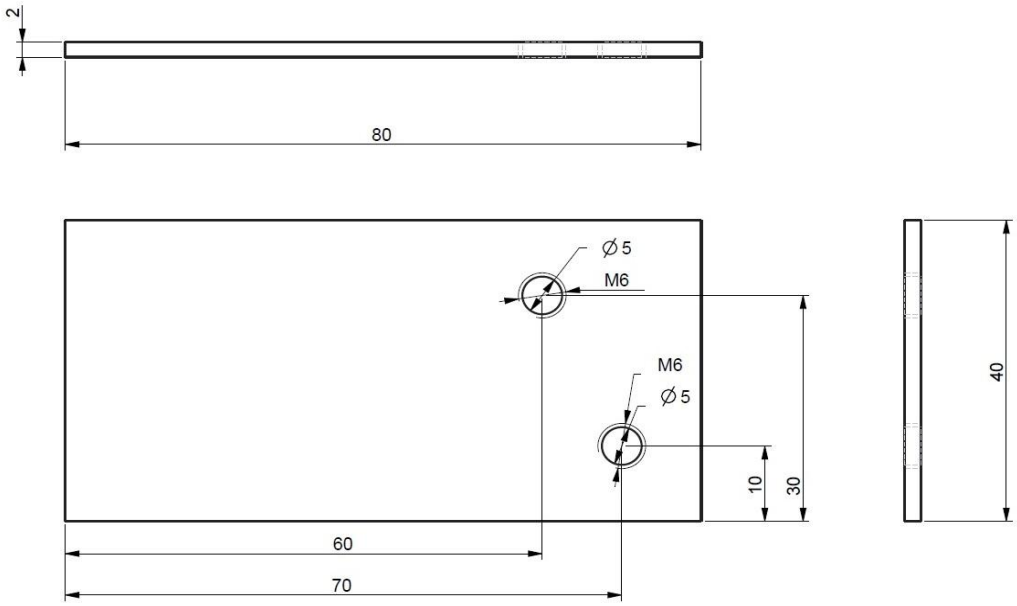

Figure B.5-13 : Schematic 2D drawing of the stationary plate. The stationary plate is sandwiched between the main plates and held into place by a setup of two nuts and bolts. All the measurements shown are in millimeters.

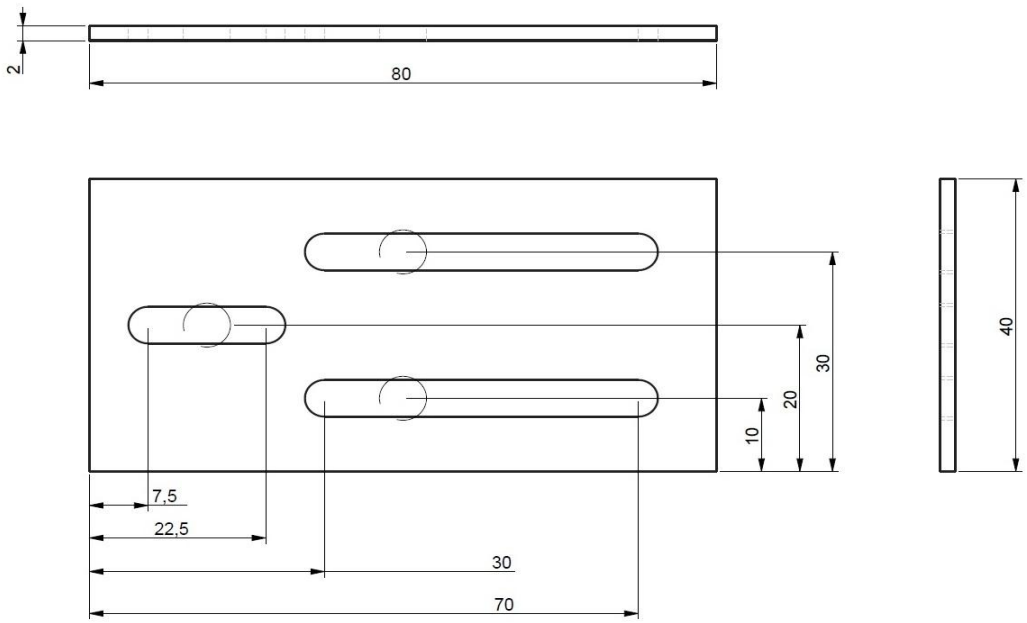

Figure B.5-14 : Schematic 2D drawing of the sliding plate. The sliding plate is also sandwiched between the main plates and held into place by a setup of 3 nuts and bolts. The nuts and bolts can be loosed to allow lateral movement of the plate. After placing a tissue scaffold sample between the stationary and sliding plate, the sliding plate is slid to confine the walls of the sample.

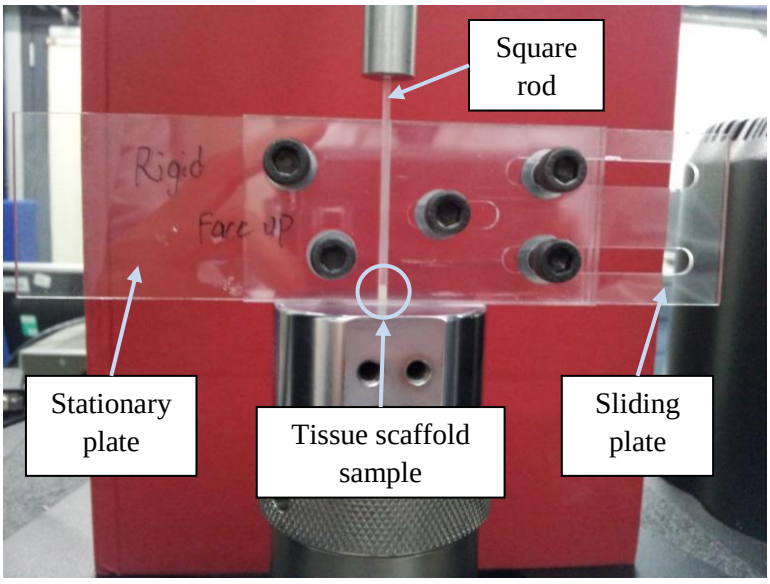

Figure B.5-15 : Machined device used to experiment confined compression of Schwarz P unit cell-based tissue scaffold samples.

Figure B.5-16 : Close up view of the tissue scaffold sample placed into the slot formed by the walls of the two main plates, the stationary plate and the sliding plate. Strain is transmitted from the compressor through the square rod which has its flat square bottom touching the top surface of the scaffold.

In performing experimental compression for confined tissue scaffolds, a tissue scaffold sample was placed in the slot before a square rod was inserted such that the flat bottom of the rod is touching the top surface of the tissue scaffold. Similar to the methodology for unconfined compression of fabricated Schwarz P unit cell-based tissue scaffolds detailed in Chapter 4, a Hounsfield testing machine was used to compress the confined tissue scaffold sample to 20% strain at a crosshead speed of 0.5mm min^{-1} with a 5N load cell. However, the strain was transmitted from the compressor of the machine through the square rod and subsequently the fabricated tissue scaffold.

B.6 Predictive Modeling & Schwarz P Unit Cell Design

B.6.1 Tabulated Effective Modulus Results for Linear Analyses

Table B.6-1 : Effective modulus obtained from application of macroscopic load in the X, Y and Z directions for Schwarz P unit cells assigned a bulk LCM3 specimen 5 material model. The effective modulus was determined from average strain obtained from static, linear perturbation micromechanical analyses.

Material Model : LCM3 Specimen 5 – Lower limit material data				
Height (= Width = Length) (mm)	**Wall thickness (mm)**	**Effective modulus (MPa)**		
		X	**Y**	**Z**
0.48	0.01278	0.0942	0.0942	0.0942
	0.02558	0.231	0.302	0.231
0.50	0.01331	0.0833	0.0833	0.0833
	0.02665	0.205	0.205	0.205
	0.03999	0.363	0.363	0.363
	0.05332	0.566	0.567	0.566
	0.06665	0.821	0.821	0.821
0.52	0.01385	0.0740	0.0741	0.0741
	0.02772	0.182	0.182	0.182
	0.04158	0.323	0.323	0.323
	0.05545	0.503	0.503	0.502
	0.06932	0.728	0.729	0.728
0.54	0.01438	0.0661	0.0661	0.0661
	0.02878	0.162	0.162	0.162
	0.04318	0.288	0.288	0.288
	0.05758	0.449	0.451	0.450
	0.07199	0.651	0.650	0.651
0.56	0.01491	0.0593	0.0593	0.0593

	0.02985	0.146	0.146	0.146
	0.04478	0.258	0.257	0.256
	0.05972	0.403	0.405	0.405
	0.07465	0.584	0.584	0.584
0.58	0.01544	0.0534	0.0534	0.0534
	0.03091	0.198	0.131	0.131
	0.04638	0.233	0.233	0.233
	0.06185	0.362	0.364	0.364
	0.07732	0.525	0.525	0.525
0.60	0.01598	0.04820	0.04820	0.04820
	0.03198	0.118	0.118	0.118
	0.04798	0.210	0.209	0.208
	0.06398	0.329	0.329	0.329
	0.07998	0.476	0.476	0.475

Table B.6-2 : Effective modulus obtained from application of macroscopic load in the X, Y and Z directions for Schwarz P unit cells assigned a bulk LCM3 averaged material model. The effective modulus was determined from average strain obtained from static, linear perturbation micromechanical analyses.

Material Model : LCM3 averaged material data				
Height (= Width = Length) (mm)	**Wall thickness (mm)**	**Effective modulus (MPa)**		
		X	**Y**	**Z**
0.48	0.01278	0.123	0.123	0.123
	0.02558	0.302	0.302	0.302
0.50	0.01331	0.109	0.109	0.109
	0.02665	0.267	0.267	0.267
	0.03999	0.475	0.475	0.475

	0.05332	0.740	0.741	0.740
	0.06665	1.073	1.073	1.073
0.52	0.01385	0.0968	0.0968	0.0968
	0.02772	0.238	0.238	0.238
	0.04158	0.422	0.422	0.422
	0.05545	0.657	0.657	0.657
	0.06932	0.952	0.952	0.952
0.54	0.01438	0.0864	0.0864	0.0864
	0.02878	0.212	0.212	0.212
	0.04318	0.377	0.377	0.377
	0.05758	0.587	0.589	0.588
	0.07199	0.850	0.850	0.851
0.56	0.01491	0.0775	0.0775	0.0775
	0.02985	0.190	0.190	0.1903
	0.04478	0.337	0.336	0.335
	0.05972	0.527	0.529	0.529
	0.07465	0.763	0.763	0.763
0.58	0.01544	0.0697	0.0697	0.0697
	0.03091	0.171	0.171	0.171
	0.04638	0.304	0.304	0.304
	0.06185	0.473	0.476	0.475
	0.07732	0.687	0.686	0.686
0.60	0.01598	0.0630	0.0630	0.0630
	0.03198	0.155	0.155	0.155
	0.04798	0.275	0.273	0.272
	0.06398	0.430	0.430	0.430
	0.07998	0.622	0.622	0.620

Table B.6-3 : Effective modulus obtained from application of macroscopic load in the X, Y and Z directions for Schwarz P unit cells assigned a bulk LCM3 upper material model. The effective modulus was determined from average strain obtained from static, linear perturbation micromechanical analyses.

Material Model : LCM3 Specimen 3 – Upper limit material data				
Height (= Width = Length) (mm)	**Wall thickness (mm)**	**Effective modulus (MPa)**		
		X	**Y**	**Z**
0.48	0.01278	0.143	0.143	0.143
	0.02558	0.350	0.350	0.350
0.50	0.01331	0.126	0.126	0.126
	0.02665	0.310	0.310	0.310
	0.03999	0.550	0.550	0.550
	0.05332	0.857	0.858	0.857
	0.06665	1.242	1.242	1.243
0.52	0.01385	0.112	0.112	0.112
	0.02772	0.275	0.275	0.275
	0.04158	0.488	0.488	0.489
	0.05545	0.761	0.761	0.761
	0.06932	1.102	1.103	1.102
0.54	0.01438	0.1000	0.1000	0.1001
	0.02878	0.246	0.246	0.246
	0.04318	0.436	0.436	0.436
	0.05758	0.680	0.682	0.681
	0.07199	0.985	0.984	0.986
0.56	0.01491	0.0897	0.0897	0.0897
	0.02985	0.220	0.220	0.220
	0.04478	0.390	0.390	0.390
	0.05972	0.610	0.613	0.613

	0.07465	0.883	0.884	0.883
0.58	0.01544	0.0808	0.0808	0.0808
	0.03091	0.198	0.198	0.198
	0.04638	0.352	0.352	0.352
	0.06185	0.548	0.551	0.550
	0.07732	0.795	0.795	0.794
0.60	0.01598	0.0730	0.0730	0.0730
	0.03198	0.179	0.179	0.179
	0.04798	0.318	0.317	0.315
	0.06398	0.497	0.498	0.498
	0.07998	0.720	0.721	0.718

B.6.2 Height vs. Pore Size vs. Internal Pore Throat Size

The surface plot characterising the relationship between height, pore size and internal pore throat size is shown in Figure B.6-17. The relationship can be expressed through the mathematical expression in Equation (B.5).

$$D_T^{Int}(H, P_S) = \begin{array}{l} 0.05658 - 0.8427H + 1.1927P_S + 2.2220(H \times P_S) - \\ 1.8211(P_S)^2 - 2.5811[H \times (P_S)^2] + 2.471(P_S)^3 \end{array} \quad \text{(B.5)}$$

for which,

D_T^{Int} : Internal pore throat size (mm)

H : Height of the unit cell (mm)

P_S : Pore size (mm)

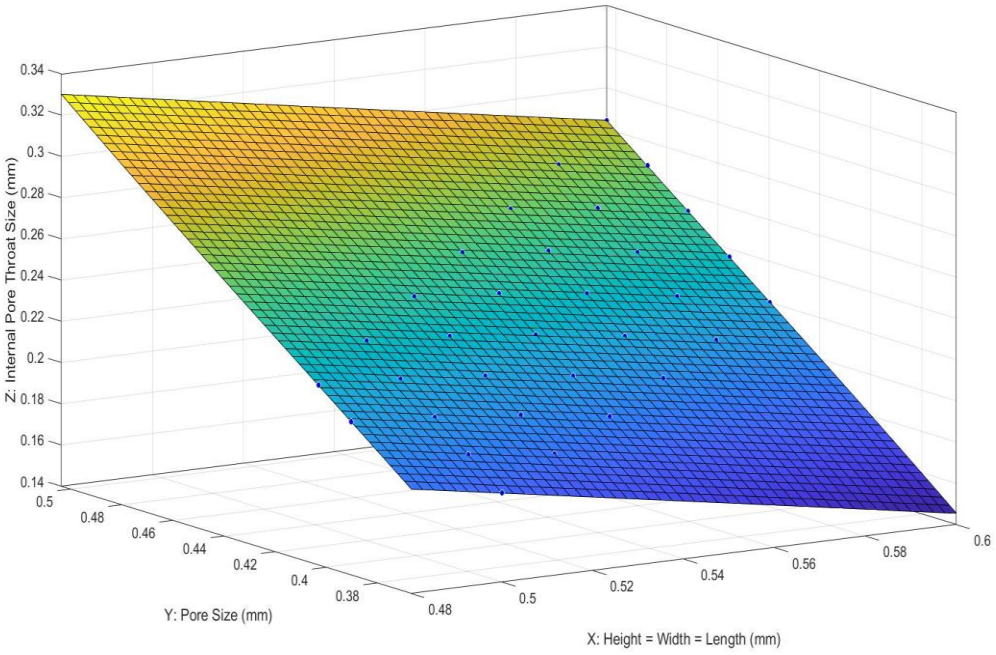

Figure B.6-17 : 3D surface plot relating the height, pore size and internal pore throat size of Schwarz P unit cells.

B.6.3 MATLAB Algorithms for Predictive Modeling

The following MATLAB script is the main algorithm used for predictive modeling and consists of 2 parts and an extension. The first part defines the original Schwarz P unit cell architecture in terms of height, internal pore throat size and pore size. The second part establishes configurations based on ranges of height and internal pore throat sizes as input for prediction. The 'for loop' goes through different functions which calculate the pore size, wall thickness, volume and porosity. The lower limit, averaged and upper limit normalised effective modulus and predicted effective modulus values are also determined. 'If' statements were added that filters every configuration based on the discussions made. The extension to the algorithm goes through all potential configurations and filters them based on target requirements for internal pore throat size and porosity.

Part 1:

```
orig_H = 0.52;
orig_internalporethroatsize = 0.246153;
orig_poresize = 0.436467;
%%%%%%%%%%%%%%%%%%%%%%%%%%%%%%%%%%%%%%%%%%%%%%%%%%%%%%%%%%%%%%%%%%%%%%%%%%%%%%%
```

Part 2:

```
height_coll = [0.1:0.01:1.0]; porethroatsize_coll = [0.1:0.001:0.9];

mat_YoungsMod_low = 4.39168976979119;   % In MPa
mat_YoungsMod_avg = 5.73994347345265;   % In MPa
mat_YoungsMod_upper = 6.64684409133563; % In MPa

full_design_coll = []; potential_design_coll = [];
for input_H = height_coll
    for input_porethroatsize = porethroatsize_coll
        scaling_H = input_H / orig_H;
        lim_internalporethroatsize = scaling_H*orig_internalporethroatsize;
        lim_poresize = scaling_H*orig_poresize;

        pore_size = Height_IntPoreThroatSize_PoreSize(input_H,
input_porethroatsize);
```

```
        wall_thickness = Height_PoreSize_WallThickness(input_H, pore_size);

        volume = Height_PoreSize_Volume(input_H, pore_size);

        porosity = Height_PoreSize_Porosity(input_H, pore_size);
        porosity_percentage = (porosity)*100;

        NORM_effect_mod_low = Height_PoreSize_NORMEffectModLow(input_H,
pore_size);
        YoungsMod_low = (mat_YoungsMod_low)*(NORM_effect_mod_low);

        NORM_effect_mod_avg = Height_PoreSize_NORMEffectModAvg(input_H,
pore_size);
        YoungsMod_avg = (mat_YoungsMod_avg)*(NORM_effect_mod_avg);

        NORM_effect_mod_upper = Height_PoreSize_NORMEffectModUpper(input_H,
pore_size);
        YoungsMod_upper = (mat_YoungsMod_upper)*(NORM_effect_mod_upper);

        %%%%%%%%%%%%%%%% Complete listing of designs %%%%%%%%%%%%%%%%%%%%
        full_design_coll(end+1,:) = [input_H, ...
            input_porethroatsize, ...
            pore_size, ...
            wall_thickness, ...
            volume, ...
            porosity_percentage, ...
            NORM_effect_mod_low, NORM_effect_mod_avg, NORM_effect_mod_upper, ...
            YoungsMod_low, YoungsMod_avg, YoungsMod_upper];
        %%%%%%%%%%%%%%%%%%%%%%%%%%%%%%%%%%%%%%%%%%%%%%%%%%%%%%%%%%%%%%%%%%%

        %%%%%%%%%%%%%%%% Potential designs %%%%%%%%%%%%%%%%%%%%%%%%%%%%%%
        if ((porosity < 1) && (porosity > 0)) && ...
                (input_H > input_porethroatsize) && ...
                (input_porethroatsize < lim_internalporethroatsize) && ...
                ((pore_size > 0) && (pore_size < lim_poresize)) && ...
                (wall_thickness > 0) && ...
                (volume > 0) && ...
                ((NORM_effect_mod_low > 0) || (NORM_effect_mod_avg > 0) ||
(NORM_effect_mod_upper > 0)) && ...
                ((YoungsMod_avg > YoungsMod_low) && (YoungsMod_upper >
YoungsMod_avg))

            potential_design_coll(end+1,:) = [input_H, ...
                input_porethroatsize, ...
                pore_size, ...
                wall_thickness, ...
                volume, ...
                porosity_percentage, ...
                NORM_effect_mod_low, NORM_effect_mod_avg,
NORM_effect_mod_upper, ...
                YoungsMod_low, YoungsMod_avg, YoungsMod_upper];
        end
```

```
        %%%%%%%%%%%%%%%%%%%%%%%%%%%%%%%%%%%%%%%%%%%%%%%%%%%%%%%%%%%%%%%%%%%%%%%
    end
end
```

Extension :

```
max_internalporethroatsize_lim = max(porethroatsize_coll);
max_porosity_lim = 100;

design_lim_coll = DesignLimitSelector(0.3, ...
    max_internalporethroatsize_lim, ...
    55.0, ...
    max_porosity_lim, ...
    potential_design_coll);
```

The functions used in the main script contain the mathematical expressions for the different relationships.

- Height vs. Internal pore throat size vs. Pore size

```
function [pore_size] = Height_IntPoreThroatSize_PoreSize(height,
internal_pore_throat_size)

C0 = 0.00182469634318102;
C1 = 0.456044169797153; C2 = 0.790593336233567; C3 = -0.825816065166204;
C4 = 1.81291549647643; C5 = 1.87761232558125; C6 = -4.05022498874102;

% p00 + p10*x + p01*y + p11*x*y + p02*y^2 + p12*x*y^2 + p03*y^3
pore_size = C0 + ...
    C1*(height) + ...
    C2*(internal_pore_throat_size) + ...
    C3*(height)*(internal_pore_throat_size) + ...
    C4*((internal_pore_throat_size)^2) + ...
    C5*(height)*((internal_pore_throat_size)^2) + ...
    C6*((internal_pore_throat_size)^3);
end
```

- Height vs. Internal pore throat size vs. Wall thickness

```
function [wall_thickness] = Height_PoreSize_WallThickness(height, pore_size)

C0 = -0.056075504394958;
C1 = 1.33978577198189; C2 = -1.19299230502787;
C3 = -2.20419223906699; C4 = 1.80902381444448;
C5 = 2.55701680528767; C6 = -2.44979519654334;

% p00 + p10*x + p01*y + p11*x*y + p02*y^2 + p12*x*y^2 + p03*y^3
wall_thickness = C0 + ...
    C1*(height) + ...
    C2*(pore_size) + ...
    C3*(height)*(pore_size) + ...
    C4*((pore_size)^2) + ...
    C5*(height)*((pore_size)^2) + ...
    C6*((pore_size)^3);
end
```

- Height vs. Internal pore throat size vs. Volume

```
function [volume] = Height_PoreSize_Volume(height, pore_size);

C0 = -0.0306844862576278;
C1 = 0.302770739075247; C2 = -0.159520155170833;
C3 = -0.0678564678840614; C4 = -1.26453811537437;
C5 = 1.16529684253626; C6 = 1.02454855780095;
C7 = 1.23212131086692; C8 = -2.56839663671292;

% p00 + p10*x + p01*y + p20*x^2 + p11*x*y + p02*y^2 + p30*x^3 + p21*x^2*y +
p12*x*y^2
volume = C0 + ...
    C1*(height) + ...
    C2*(pore_size) + ...
    C3*((height)^2) + ...
    C4*(height)*(pore_size) + ...
    C5*((pore_size)^2) + ...
    C6*((height)^3) + ...
    C7*((height)^2)*(pore_size) + ...
    C8*(height)*((pore_size)^2);
end
```

- Height vs. Internal pore throat size vs. Porosity

```
function [porosity] = Height_PoreSize_Porosity(height, pore_size);

C0 = 1.33585222158246;
C1 = -20.614874838717; C2 = 21.5882985727196;
C3 = 80.9399238197703; C4 = -143.054337884311;
C5 = 61.9970278871132; C6 = -123.765772237958;
C7 = 339.058295641095; C8 = -321.79752217621;
C9 = 106.783503020858;

% p00 + p10*x + p01*y + p20*x^2 + p11*x*y + p02*y^2 + p30*x^3 + p21*x^2*y +
p12*x*y^2 + p03*y^3
porosity = C0 + ...
    C1*(height) + ...
    C2*(pore_size) + ...
    C3*((height)^2) + ...
    C4*(height)*(pore_size) + ...
    C5*((pore_size)^2) + ...
    C6*((height)^3) + ...
    C7*((height)^2)*(pore_size) + ...
    C8*(height)*((pore_size)^2) + ...
    C9*((pore_size)^3);
end
```

- Height vs. Internal pore throat size vs. Lower limit normalised effective modulus

```
function [NORM_effect_mod_low] = Height_PoreSize_NORMEffectModLow(height,
pore_size)

C0 = 2.76035165711757;
C1 = 16.1073036006891; C2 = -37.0955102000939;
C3 = -56.5313842277314; C4 = 106.376907311163;
C5 = 51.5018680572226; C6 = -89.7834029850632;

% p00 + p10*x + p01*y + p11*x*y + p02*y^2 + p12*x*y^2 + p03*y^3
NORM_effect_mod_low = C0 + ...
    C1*(height) + ...
    C2*(pore_size) + ...
    C3*(height)*(pore_size) + ...
    C4*((pore_size)^2) + ...
    C5*(height)*((pore_size)^2) + ...
    C6*((pore_size)^3);
end
```

- Height vs. Internal pore throat size vs. Average normalised effective modulus

```
function [NORM_effect_mod_avg] = Height_PoreSize_NORMEffectModAvg(height,
pore_size)

C0 = 0.911445208803997;
C1 = 23.8134526021596; C2 = -34.102418817443;
C3 = -4.37430295956592; C4 = -80.9515805289468;
C5 = 115.048631154819; C6 = -21.9598481515736;
C7 = 95.1064010076289; C8 = -42.7831423575635;
C9 = -55.9580148916839;

% p00 + p10*x + p01*y + p20*x^2 + p11*x*y + p02*y^2 + p30*x^3 + p21*x^2*y +
p12*x*y^2 + p03*y^3
NORM_effect_mod_avg = C0 + ...
    C1*(height) + ...
    C2*(pore_size) + ...
    C3*((height)^2) + ...
    C4*(height)*(pore_size) + ...
    C5*((pore_size)^2) + ...
    C6*((height)^3) + ...
    C7*((height)^2)*(pore_size) + ...
    C8*(height)*((pore_size)^2) + ...
    C9*((pore_size)^3);
end
```

- Height vs. Internal pore throat size vs. Upper limit normalised effective modulus

```
function [NORM_effect_mod_upper] = Height_PoreSize_NORMEffectModUpper(height,
pore_size)

C0 = 0.186369306488605;
C1 = 27.4721548156633; C2 = -33.7437133544444;
C3 = -7.77373494901471; C4 = -89.1585321838277;
C5 = 119.450877815623; C6 = -27.3485483281896;
C7 = 123.766208960233; C8 = -70.1209765444099;
C9 = -47.6244531950931;

% p00 + p10*x + p01*y + p20*x^2 + p11*x*y + p02*y^2 + p30*x^3 + p21*x^2*y +
p12*x*y^2 + p03*y^3
NORM_effect_mod_upper = C0 + ...
    C1*(height) + ...
    C2*(pore_size) + ...
    C3*((height)^2) + ...
```

```
    C4*(height)*(pore_size) + ...
    C5*((pore_size)^2) + ...
    C6*((height)^3) + ...
    C7*((height)^2)*(pore_size) + ...
    C8*(height)*((pore_size)^2) + ...
    C9*((pore_size)^3);
end
```

- Function for extension

```
function [design_lim_selector] =
DesignLimitSelector(min_internalporethroatsize_lim, ...
    max_internalporethroatsize_lim, ...
    min_porosity_lim, ...
    max_porosity_lim, ...
    potential_design_listing)

[potential_design_N,~] = size(potential_design_listing);

design_lim_selector = [];
for design_n = 1:potential_design_N
    design_consd = potential_design_listing(design_n,:);
    internalporethroatsize_consd = design_consd(:,2);
    porosity_consd = design_consd(:,6);

    if ((internalporethroatsize_consd >= min_internalporethroatsize_lim) && ...
            (internalporethroatsize_consd <= max_internalporethroatsize_lim))
&& ...
            ((porosity_consd >= min_porosity_lim) && ...
            (porosity_consd <= max_porosity_lim))
        design_lim_selector(end+1,:) = design_consd;
    end
end
end
```

B.6.4 LCM3 & Schwarz P Unit Cell Design

Table B.6-4 : Configurations for Schwarz P unit cell designs with internal pore throat sizes greater than 300microns and porosity above 55%. The values for pore size, wall thickness volume of the unit cell, porosity and effective modulus values were determined based on the implementation of obtained respective equations into a custom MATLAB algorithm. Negative effective modulus values are indicated with '*'.

Height (mm)	Internal pore throat size (mm)	Pore size (mm)	Wall thickness (mm)	Volume of unit cell (mm^3)	Porosity (%)	Effective modulus (MPa)		
						Lower limit	Averaged	Upper limit
0.64	0.300	0.534	0.020	0.019	86.26	0.004	0.040	0.059
0.65	0.300	0.538	0.025	0.025	83.30	0.009	0.061	0.092
0.66	0.300	0.542	0.030	0.031	80.48	0.013	0.086	0.129
0.67	0.300	0.546	0.036	0.037	77.79	0.016	0.113	0.171
0.68	0.300	0.549	0.041	0.044	75.19	0.019	0.143	0.219
0.69	0.300	0.553	0.046	0.050	72.68	0.020	0.176	0.272
0.70	0.300	0.557	0.051	0.058	70.23	0.021	0.212	0.331
0.71	0.300	0.561	0.056	0.065	67.82	0.021	0.252	0.396
0.72	0.300	0.564	0.062	0.073	65.42	0.020	0.295	0.468
0.73	0.300	0.568	0.067	0.082	63.02	0.019	0.343	0.547
0.74	0.300	0.572	0.072	0.090	60.59	0.017	0.394	0.633
0.75	0.300	0.576	0.078	0.099	58.12	0.015	0.449	0.726
0.76	0.300	0.580	0.083	0.109	55.57	0.013	0.508	0.826

0.77	0.305	0.588	0.084	0.112	55.33	*	0.530	0.889
0.78	0.310	0.597	0.084	0.115	55.04	*	0.553	0.957
0.79	0.316	0.607	0.084	0.116	55.18	*	0.565	1.018
0.80	0.322	0.617	0.084	0.118	55.27	*	0.576	1.081
0.81	0.328	0.627	0.083	0.120	55.32	*	0.584	1.145
0.82	0.334	0.637	0.083	0.121	55.32	*	0.588	1.209
0.83	0.340	0.647	0.083	0.123	55.27	*	0.588	1.273
0.84	0.346	0.657	0.083	0.124	55.17	*	0.583	1.336
0.85	0.352	0.666	0.083	0.125	55.02	*	0.571	1.396
0.86	0.359	0.677	0.082	0.125	55.35	*	0.529	1.426
0.87	0.365	0.687	0.082	0.126	55.11	*	0.501	1.478
0.88	0.372	0.698	0.081	0.126	55.35	*	0.435	1.491
0.89	0.378	0.708	0.081	0.127	55.01	*	0.386	1.531
0.90	0.385	0.719	0.080	0.127	55.16	*	0.293	1.523
0.91	0.392	0.729	0.080	0.126	55.26	*	0.182	1.503
0.92	0.399	0.740	0.079	0.125	55.32	*	0.054	1.468
0.93	0.406	0.751	0.079	0.124	55.33	*	*	1.418
0.94	0.413	0.761	0.078	0.123	55.28	*	*	1.353
0.95	0.420	0.772	0.078	0.122	55.19	*	*	1.271
0.96	0.427	0.783	0.078	0.121	55.04	*	*	1.173

0.97	0.435	0.794	0.077	0.118	55.39	*	*	0.989
0.98	0.442	0.804	0.077	0.117	55.12	*	*	0.853
0.99	0.450	0.816	0.076	0.114	55.34	*	*	0.624
1.00	0.458	0.827	0.075	0.111	55.49	*	*	0.370

B.6.5 Calcium Phosphates (CaP) & Schwarz P Unit Cell Design

Table B.6-5 : Representative sample configurations of Schwarz P unit cell designs with internal pore throat sizes greater than 10μm and porosity values above 55%. The Schwarz P unit cells are assigned with PCL/HA (20wt% HA) material model.

Height (mm)	Internal pore throat size (mm)	Pore size (mm)	Wall thickness (mm)	Volume of unit cell (mm^3)	Porosity (%)	Effective modulus (MPa)		
						Lower limit	Averaged	Upper limit
0.47	0.198	0.370	0.037	0.019	69.10	23.68	23.70	24.34
0.60	0.284	0.504	0.016	0.014	88.25	2.37	2.48	2.60
0.49	0.200	0.379	0.045	0.025	64.79	25.45	26.34	27.44
0.53	0.226	0.420	0.039	0.026	70.66	14.06	14.77	15.50
0.54	0.240	0.438	0.030	0.020	76.97	8.97	9.34	9.80

B.6.6 Titanium & Schwarz P Unit Cell Design

Table B.6-6 : Sample configurations of Schwarz P unit cell designs with titanium alloy TNTZ material model. The configurations are classified according to their predicted effective modulus values being within range of the modulus values of either cortical or trabecular bone.

Height (mm)	Internal pore throat size (mm)	Pore size (mm)	Wall thickness (mm)	Volume of unit cell (mm^3)	Porosity (%)	Effective modulus (GPa)			Bone tissue compatibility
						Lower limit	Averaged	Upper limit	
0.78	0.300	0.587	0.094	0.129	50.18	0.09	8.65	15.82	Cortical
0.80	0.306	0.601	0.100	0.142	47.30	-0.71	10.06	18.99	
0.81	0.300	0.598	0.111	0.162	41.04	-0.03	11.83	21.86	
0.84	0.301	0.611	0.128	0.198	30.70	-0.27	15.56	29.08	
0.84	0.347	0.658	0.082	0.122	55.68	-8.39	7.60	19.76	
0.69	0.307	0.560	0.039	0.043	76.42	-0.35	1.58	3.06	Trabecular
0.70	0.300	0.557	0.051	0.058	70.23	0.26	2.87	4.98	
0.71	0.306	0.567	0.050	0.058	70.83	-0.29	2.70	5.06	
0.71	0.315	0.576	0.041	0.048	75.51	-1.18	1.55	3.57	
0.74	0.326	0.598	0.046	0.057	73.42	-2.72	1.68	4.87	

References

[1] R. Langer, J.P. Vacanti, Tissue engineering, Science (80-.). 260 (1993) 920. doi:10.1126/science.8493529.

[2] R.S. Langer, J.P. Vacanti, Tissue engineering: the challenges ahead., Sci. Am. 280 (1999) 86–89.

[3] D.J. Mooney, A.G. Mikos, Growing new organs., Sci. Am. 280 (1999) 60–65.

[4] C.A. Vacanti, J.P. Vacanti, THE SCIENCE OF TISSUE ENGINEERING, Orthop. Clin. North Am. 31 (2000) 351–355. doi:10.1016/S0030-5898(05)70155-3.

[5] E. Sachlos, J.T. Czernuszka, Making tissue engineering scaffolds work. Review: the application of solid freeform fabrication technology to the production of tissue engineering scaffolds., Eur. Cell. Mater. 5 (2003) 29–40.

[6] M.B. Fisher, R.L. Mauck, Tissue engineering and regenerative medicine: recent innovations and the transition to translation., Tissue Eng. Part B. Rev. 19 (2013) 1–13. doi:10.1089/ten.TEB.2012.0723.

[7] J.R. Porter, T.T. Ruckh, K.C. Popat, Bone tissue engineering: a review in bone biomimetics and drug delivery strategies., Biotechnol. Prog. 25 (2009) 1539–1560. doi:10.1002/btpr.246.

[8] C.R.M. Black, V. Goriainov, D. Gibbs, J. Kanczler, R.S. Tare, R.O.C. Oreffo, Bone Tissue Engineering, Curr. Mol. Biol. Reports. 1 (2015) 132–140. doi:10.1007/s40610-015-0022-2.

[9] R.J. Zdrahala, I.J. Zdrahala, In vivo tissue engineering: Part I. Concept genesis and guidelines for its realization., J. Biomater. Appl. 14 (1999) 192–209. doi:10.1177/088532829901400205.

[10] B. Thavornyutikarn, N. Chantarapanich, K. Sitthiseripratip, G.A. Thouas, Q. Chen, Bone tissue engineering scaffolding: computer-aided scaffolding techniques, Prog. Biomater. 3 (2014) 61–102. doi:10.1007/s40204-014-0026-7.

[11] R.G.M. Breuls, T.U. Jiya, T.H. Smit, Scaffold Stiffness Influences Cell Behavior: Opportunities for Skeletal Tissue Engineering, Open Orthop. J. 2 (2008) 103–109. doi:10.2174/1874325000802010103.

[12] P.J. Prendergast, R. Huiskes, K. Søballe, Biophysical stimuli on cells during tissue differentiation at implant interfaces, J. Biomech. 30 (1997) 539–548. doi:10.1016/S0021-9290(96)00140-6.

[13] M. Hart, J. Lauer, M. Selig, M. Hanak, B. Walters, B. Rolauffs, Shaping the Cell and the Future: Recent Advancements in Biophysical Aspects Relevant to Regenerative Medicine, J. Funct. Morphol. Kinesiol. 3 (2017) 2. doi:10.3390/jfmk3010002.

[14] B. Dhandayuthapani, Y. Yoshida, T. Maekawa, D.S. Kumar, Polymeric Scaffolds in Tissue Engineering Application: A Review, Int. J. Polym. Sci. 2011 (2011). http://dx.doi.org/10.1155/2011/290602.

[15] I.L.S. Chua, H.W. Kim, J.H. Lee, Signaling of extracellular matrices for tissue regeneration and therapeutics, Tissue Eng. Regen. Med. 13 (2016) 1–12. doi:10.1007/s13770-016-9075-0.

[16] F. Guilak, D. Cohen, B. Estes, Control of stem cell fate by physical interactions with the extracellular matrix, Cell Stem Cell. 5 (2009) 17–26. doi:10.1016/j.stem.2009.06.016.Control.

[17] X.D. Chen, Extracellular matrix provides an optimal niche for the maintenance and propagation of mesenchymal stem cells, Birth Defects Res. Part C - Embryo Today Rev. 90 (2010) 45–54. doi:10.1002/bdrc.20171.

[18] A.J. Engler, S. Sen, H.L. Sweeney, D.E. Discher, Matrix Elasticity Directs Stem Cell Lineage Specification, Cell. 126 (2006) 677–689. doi:10.1016/j.cell.2006.06.044.

[19] F.G. Giancotti, E. Ruoslahti, Integrin signaling., Science. 285 (1999) 1028–32. doi:10.1126/science.285.5430.1028.

[20] B.P. Chan, K.W. Leong, Scaffolding in tissue engineering: general approaches and tissue-specific considerations, Eur. Spine J. 17 (2008) 467–479. doi:10.1007/s00586-008-0745-3.

[21] D. Lacroix, J.A. Planell, P.J. Prendergast, Computer-aided design and finite-element modelling of biomaterial scaffolds for bone tissue engineering, Philos. Trans. R. Soc. A Math. Phys. Eng. Sci. 367 (2009) 1993–2009. doi:10.1098/rsta.2009.0024.

[22] W. Sun, B. Starly, J. Nam, A. Darling, Bio-CAD modeling and its applications in computer-aided tissue engineering, Bio-CAD. 37 (2005) 1097–1114. doi:10.1016/j.cad.2005.02.002.

[23] M. Liebschner, M.A. Wettergreen, Optimization of bone scaffold engineering for load bearing applications, 2003.

[24] C.J. Little, N.K. Bawolin, X. Chen, Mechanical properties of natural cartilage and tissue-engineered constructs., Tissue Eng. Part B. Rev. 17 (2011) 213–227. doi:10.1089/ten.TEB.2010.0572.

[25] A. Kumar, K. Biswas, B. Basu, On the toughness enhancement in hydroxyapatite-based composites, Acta Mater. 61 (2013) 5198–5215. doi:10.1016/j.actamat.2013.05.013.

[26] A.K. Dubey, A. Ea, K. Balani, B. Basu, Multifunctional properties of multistage spark plasma sintered HA-BaTiO3-based piezobiocomposites for bone replacement applications, J. Am. Ceram. Soc. 96 (2013) 3753–3759. doi:10.1111/jace.12566.

[27] Y. Chandorkar, G. Madras, B. Basu, Structure, tensile properties and cytotoxicity assessment of sebacic acid based biodegradable polyesters with ricinoleic acid, J. Mater. Chem. B. 1 (2013) 865–875. doi:10.1039/c2tb00304j.

[28] S.L. Zhu, X.J. Yang, M.F. Chen, C.Y. Li, Z.D. Cui, Effect of porous NiTi alloy on bone formation: A comparative investigation with bulk NiTi alloy for 15 weeks in vivo, Mater. Sci. Eng. C. 28 (2008) 1271–1275. doi:10.1016/j.msec.2007.11.010.

[29] N.K. Bawolin, W.J. Zhang, X.B. Chen, A Brief Review of the Modelling of the Time Dependent Mechanical Properties of Tissue Engineering Scaffolds, J. Biomim. Biomater. Tissue Eng. 6 (2010) 19–33. doi:10.4028/www.scientific.net/JBBTE.6.19.

[30] I. Sabree, J.E. Gough, B. Derby, Mechanical properties of porous ceramic scaffolds: Influence of internal dimensions, Ceram. Int. 41 (2015) 8425–8432. doi:10.1016/j.ceramint.2015.03.044.

[31] C. Torres-Sanchez, F.R.A. Al Mushref, M. Norrito, K. Yendall, Y. Liu, P.P. Conway, The effect of pore size and porosity on mechanical properties and biological response of porous titanium scaffolds, Mater. Sci. Eng. C. 77 (2017) 219–228. doi:10.1016/j.msec.2017.03.249.

[32] D.C. Wirtz, N. Schiffers, R. Forst, T. Pandorf, D. Weichert, K. Radermacher, Critical evaluation of known bone material properties to realize anisotropic FE-simulation of the proximal femur, J. Biomech. 33 (2000) 1325–1330. doi:10.1016/S0021-9290(00)00069-5.

[33] R.P. Dickenson, W.C. Hutton, J.R. Stott, The mechanical properties of bone in osteoporosis., J. Bone Joint Surg. Br. 63–B (1981) 233–238.

[34] A.H. Burstein, D.T. Reilly, M. Martens, Aging of bone tissue: mechanical properties., J. Bone Joint Surg. Am. 58 (1976) 82–86.

[35] S. Bandyopadyay-Ghosh, Bone as a collagen-hydroxyapatite composite and its repair, Trends Biomater. Artif. Organs. 22 (2008) 112–120.

[36] E.F. Morgan, T.M. Keaveny, Dependence of yield strain of human trabecular bone on anatomic site, J. Biomech. 34 (2001) 569–577. doi:10.1016/S0021-9290(01)00011-2.

[37] P.K. Zysset, X. Edward Guo, C. Edward Hoffler, K.E. Moore, S.A. Goldstein, Elastic modulus and hardness of cortical and trabecular bone lamellae measured by nanoindentation in the human femur, J. Biomech. 32 (1999) 1005–1012. doi:10.1016/S0021-9290(99)00111-6.

[38] E.F. Morgan, H.H. Bayraktar, T.M. Keaveny, Trabecular bone modulus-density relationships depend on anatomic site, J. Biomech. 36 (2003) 897–904. doi:10.1016/S0021-9290(03)00071-X.

[39] K. Choi, J.L. Kuhn, M.J. Ciarelli, S.A. Goldstein, The elastic moduli of human subchondral, trabecular, and cortical bone tissue and the size-dependency of

cortical bone modulus, J. Biomech. 23 (1990) 1103–1113. doi:10.1016/0021-9290(90)90003-L.

[40] S. Hofmann, M. Hilbe, R.J. Fajardo, H. Hagenmüller, K. Nuss, M. Arras, R. Müller, B. Von Rechenberg, D.L. Kaplan, H.P. Merkle, L. Meinel, Remodeling of tissue-engineered bone structures in vivo, Eur. J. Pharm. Biopharm. 85 (2013) 119–129. doi:10.1016/j.ejpb.2013.02.011.

[41] S. Sturm, S. Zhou, Y.-W. Mai, Q. Li, On stiffness of scaffolds for bone tissue engineering-a numerical study., J. Biomech. 43 (2010) 1738–1744. doi:10.1016/j.jbiomech.2010.02.020.

[42] M.W. Naing, C.K. Chua, K.F. Leong, Y. Wang, Fabrication of customised scaffolds using computer-aided design and rapid prototyping techniques, Rapid Prototyp. J. 11 (2005) 249–259. doi:10.1108/13552540510612938.

[43] M.A. Woodruff, C. Lange, J. Reichert, A. Berner, F. Chen, P. Fratzl, J.-T. Schantz, D.W. Hutmacher, Bone tissue engineering: from bench to bedside, Mater. Today. 15 (2012) 430–435. doi:10.1016/S1369-7021(12)70194-3.

[44] V.I. Sikavitsas, J.S. Temenoff, A.G. Mikos, Biomaterials and bone mechanotransduction., Biomaterials. 22 (2001) 2581–2593.

[45] K. Whang, K.E. Healy, D.R. Elenz, E.K. Nam, D.C. Tsai, C.H. Thomas, G.W. Nuber, F.H. Glorieux, R. Travers, S.M. Sprague, Engineering bone regeneration with bioabsorbable scaffolds with novel microarchitecture., Tissue Eng. 5 (1999) 35–51. doi:10.1089/ten.1999.5.35.

[46] Z. Esen, Ş. Bor, Processing of titanium foams using magnesium spacer particles, Scr. Mater. 56 (2007) 341–344. doi:10.1016/j.scriptamat.2006.11.010.

[47] M. Bram, H. Schiefer, D. Bogdanski, M. Köller, H.P. Buchkremer, D. Stöver, Implant surgery: How bone bonds to PM titanium, Met. Powder Rep. 61 (2006) 26–31. doi:10.1016/S0026-0657(06)70603-8.

[48] Q.L. Loh, C. Choong, Three-dimensional scaffolds for tissue engineering applications: role of porosity and pore size., Tissue Eng. Part B. Rev. 19 (2013) 485–502. doi:10.1089/ten.TEB.2012.0437.

[49] A.C. Jones, C.H. Arns, D.W. Hutmacher, B.K. Milthorpe, A.P. Sheppard, M.A. Knackstedt, The correlation of pore morphology, interconnectivity and physical properties of 3D ceramic scaffolds with bone ingrowth, Biomaterials. 30 (2009) 1440–1451. doi:10.1016/j.biomaterials.2008.10.056.

[50] B. Dabrowski, W. Swieszkowski, D. Godlinski, K.J. Kurzydlowski, Highly porous titanium scaffolds for orthopaedic applications., J. Biomed. Mater. Res. B. Appl. Biomater. 95 (2010) 53–61. doi:10.1002/jbm.b.31682.

[51] F.J. O'Brien, B.A. Harley, I. V Yannas, L.J. Gibson, The effect of pore size on cell adhesion in collagen-GAG scaffolds., Biomaterials. 26 (2005) 433–441. doi:10.1016/j.biomaterials.2004.02.052.

[52] D. Tadic, F. Beckmann, T. Donath, M. Epple, Comparison of different methods for the preparation of porous bone substitution materials and structural investigations by synchrotron µ-computer tomography, Materwiss. Werksttech. 35 (2004) 240–244. doi:10.1002/mawe.200400730.

[53] S.M.M. Roosa, J.M. Kemppainen, E.N. Moffitt, P.H. Krebsbach, S.J. Hollister, The pore size of polycaprolactone scaffolds has limited influence on bone regeneration in an in vivo model., J. Biomed. Mater. Res. A. 92 (2010) 359–368. doi:10.1002/jbm.a.32381.

[54] S.F. Hulbert, F.A. Young, R.S. Mathews, J.J. Klawitter, C.D. Talbert, F.H. Stelling, Potential of ceramic materials as permanently implantable skeletal prostheses., J. Biomed. Mater. Res. 4 (1970) 433–456. doi:10.1002/jbm.820040309.

[55] V. Karageorgiou, D. Kaplan, Porosity of 3D biomaterial scaffolds and osteogenesis, Biomaterials. 26 (2005) 5474–5491. doi:10.1016/j.biomaterials.2005.02.002.

[56] S.H. Oh, I.K. Park, J.M. Kim, J.H. Lee, In vitro and in vivo characteristics of PCL scaffolds with pore size gradient fabricated by a centrifugation method, Biomaterials. 28 (2007) 1664–1671. doi:10.1016/j.biomaterials.2006.11.024.

[57] D.L. Guy, Definitions in biomaterials, D. F. Williams, Ed., Elsevier, Amsterdam, 1987, 72 pp., J. Polym. Sci. Part C Polym. Lett. 26 (1988) 414. doi:10.1002/pol.1988.140260910.

[58] D.W. Grainger, The Williams dictionary of biomaterials, Mater. Today. 2 (1999) 29. doi:10.1016/S1369-7021(99)80066-2.

[59] F.J. O'Brien, Biomaterials & scaffolds for tissue engineering, Mater. Today. 14 (2011) 88–95. doi:10.1016/S1369-7021(11)70058-X.

[60] W. Elshahawy, Biocompatibility, Adv. Ceram. - Electr. Magn. Ceram. Bioceram. Ceram. Environ. (2011). doi:10.5772/18475.

[61] M.A. Velasco, C.A. Narvaez-Tovar, D.A. Garzon-Alvarado, Design, materials, and mechanobiology of biodegradable scaffolds for bone tissue engineering., Biomed Res. Int. 2015 (2015) 729076. doi:10.1155/2015/729076.

[62] Z. Sheikh, S. Najeeb, Z. Khurshid, V. Verma, H. Rashid, M. Glogauer, Biodegradable materials for bone repair and tissue engineering applications, Materials (Basel). 8 (2015) 5744–5794. doi:10.3390/ma8095273.

[63] S.J. Hollister, C.Y. Lin, E. Saito, C.Y. Lin, R.D. Schek, J.M. Taboas, J.M. Williams, B. Partee, C.L. Flanagan, A. Diggs, E.N. Wilke, G.H. Van Lenthe, R. Muller, T. Wirtz, S. Das, S.E. Feinberg, P.H. Krebsbach, Engineering craniofacial scaffolds., Orthod. Craniofac. Res. 8 (2005) 162–173. doi:10.1111/j.1601-6343.2005.00329.x.

[64] Y. Wen, S. Xun, M. Haoye, S. Baichuan, C. Peng, L. Xuejian, Z. Kaihong, Y.

Xuan, P. Jiang, L. Shibi, 3D printed porous ceramic scaffolds for bone tissue engineering: A review, Biomater. Sci. 5 (2017) 1690–1698. doi:10.1039/c7bm00315c.

[65] M. Ebrahimi, M.G. Botelho, S. V Dorozhkin, Biphasic calcium phosphates bioceramics (HA/TCP): Concept, physicochemical properties and the impact of standardization of study protocols in biomaterials research, Mater. Sci. Eng. C. 71 (2017) 1293–1312. doi:10.1016/j.msec.2016.11.039.

[66] C.R. T., W.E. W., W.J. N., R. Della M., Tissue ingrowth of replamineform implants, J. Biomed. Mater. Res. 9 (1975) 29–45. doi:10.1002/jbm.820090407.

[67] W.E. W., W.J. N., R. Della M., O.E. L., C.R. T., W.R. A., Replamineform porous biomaterials for hard tissue implant applications, J. Biomed. Mater. Res. 9 (1975) 23–27. doi:10.1002/jbm.820090406.

[68] L.L. Hench, Bioceramics, Stress Int. J. Biol. Stress. 28 (1998) 1705–1728. doi:10.1111/j.1151-2916.1998.tb02540.x.

[69] F. Alaribe, S. Manoto, S. Motaung, Scaffolds from biomaterials: Advantages and limitations in bone and tissue engineering, 2016.

[70] F. Baino, C. Vitale-Brovarone, Three-dimensional glass-derived scaffolds for bone tissue engineering: current trends and forecasts for the future., J. Biomed. Mater. Res. A. 97 (2011) 514–535. doi:10.1002/jbm.a.33072.

[71] Q. Fu, E. Saiz, M.N. Rahaman, A.P. Tomsia, Bioactive glass scaffolds for bone tissue engineering: state of the art and future perspectives, Mater. Sci. Eng. C. 31 (2011) 1245–1256. doi:10.1016/j.msec.2011.04.022.

[72] Q. Fu, E. Saiz, A.P. Tomsia, Bioinspired Strong and Highly Porous Glass Scaffolds., Adv. Funct. Mater. 21 (2011) 1058–1063. doi:10.1002/adfm.201002030.

[73] S.M. Best, A.E. Porter, E.S. Thian, J. Huang, Bioceramics: Past, present and for the future, Dev. Ceram. Sci. Eng. Last 50 Years. A Meet. Celebr. Profr. Sir Richard Brook's 70th Birthd. 28 (2008) 1319–1327. doi:10.1016/j.jeurceramsoc.2007.12.001.

[74] M. Vallet-Regí, Revisiting ceramics for medical applications, Dalt. Trans. (2006) 5211–5220. doi:10.1039/b610219k.

[75] L.L. Hench, D.L. Wheeler, D.C. Greenspan, Molecular Control of Bioactivity in Sol-Gel Glasses, J. Sol-Gel Sci. Technol. 9 (1998) 245–250. doi:10.1023/a:1008643303888.

[76] K.J.L. Burg, S. Porter, J.F. Kellam, Biomaterial developments for bone tissue engineering, Orthop. Polym. Biomater. Basic Asp. Biodegrad. 21 (2000) 2347–2359. doi:10.1016/S0142-9612(00)00102-2.

[77] M. Jarcho, C.H. Bolen, M.B. Thomas, J. Bobick, J.F. Kay, R.H. Doremus,

Hydroxylapatite synthesis and characterization in dense polycrystalline form, J. Mater. Sci. 11 (1976) 2027–2035. doi:10.1007/PL00020328.

[78] L.L. Hench, The story of Bioglass®, J. Mater. Sci. Mater. Med. 17 (2006) 967–978. doi:10.1007/s10856-006-0432-z.

[79] J.R. Jones, Review of bioactive glass: From Hench to hybrids, Acta Biomater. 9 (2013) 4457–4486. doi:10.1016/j.actbio.2012.08.023.

[80] W. Cao, L.L. Hench, Bioactive materials, Ceram. Int. 22 (1996) 493–507. doi:10.1016/0272-8842(95)00126-3.

[81] C. Gao, Y. Deng, P. Feng, Z. Mao, P. Li, B. Yang, J. Deng, Y. Cao, C. Shuai, S. Peng, Current progress in bioactive ceramic scaffolds for bone repair and regeneration., Int. J. Mol. Sci. 15 (2014) 4714–4732. doi:10.3390/ijms15034714.

[82] S.-S. Kim, M. Sun Park, O. Jeon, C. Yong Choi, B.-S. Kim, Poly(lactide-co-glycolide)/hydroxyapatite composite scaffolds for bone tissue engineering, Biomaterials. 27 (2006) 1399–1409. doi:10.1016/j.biomaterials.2005.08.016.

[83] S. Stratton, N.B. Shelke, K. Hoshino, S. Rudraiah, S.G. Kumbar, Bioactive polymeric scaffolds for tissue engineering, Bioact. Mater. 1 (2016) 93–108. doi:10.1016/j.bioactmat.2016.11.001.

[84] X. Liu, P.X. Ma, Polymeric scaffolds for bone tissue engineering., Ann. Biomed. Eng. 32 (2004) 477–486.

[85] M. Jafari, Z. Paknejad, M.R. Rad, S.R. Motamedian, M.J. Eghbal, N. Nadjmi, A. Khojasteh, Polymeric scaffolds in tissue engineering: a literature review, J. Biomed. Mater. Res. - Part B Appl. Biomater. 105 (2017) 431–459. doi:10.1002/jbm.b.33547.

[86] T.S. Girton, V.H. Barocas, R.T. Tranquillo, Confined Compression of a Tissue-Equivalent: Collagen Fibril and Cell Alignment in Response to Anisotropic Strain, J. Biomech. Eng. 124 (2002) 568–575. doi:10.1115/1.1504099.

[87] K.E. Kadler, D.F. Holmes, J.A. Trotter, J.A. Chapman, Collagen fibril formation., Biochem. J. 316 (Pt 1 (1996) 1–11.

[88] S. Heike, A. Jörn, H. Ingo, R. Günter, Control of pore structure and size in freeze-dried collagen sponges, J. Biomed. Mater. Res. 58 (2002) 352–357. doi:10.1002/jbm.1028.

[89] X. Wang, X. Li, R.A. Bank, C.M. Agrawal, Effects of collagen unwinding and cleavage on the mechanical integrity of the collagen network in bone, Calcif. Tissue Int. 71 (2002) 186–192. doi:10.1007/s00223-001-1082-2.

[90] S.M. Oliveira, R.A. Ringshia, R.Z. Legeros, E. Clark, M.J. Yost, L. Terracio, C.C. Teixeira, An improved collagen scaffold for skeletal regeneration, J. Biomed. Mater. Res. - Part A. 94 (2010) 371–379. doi:10.1002/jbm.a.32694.

[91] Y. Pang, H.P. Greisler, Using a type I collagen based system to understand cell-scaffold interactions and to deliver chimeric collagen binding growth factors for vascular tissue engineering, J. Investig. Med. 58 (2010) 845–848. doi:10.231/JIM.0b013e3181ee81f7.Using.

[92] S.M. Vickers, L.S. Squitieri, M. Spector, Effects of cross-linking type II collagen-GAG scaffolds on chondrogenesis in vitro: dynamic pore reduction promotes cartilage formation., Tissue Eng. 12 (2006) 1345–1355. doi:10.1089/ten.2006.12.1345.

[93] C.P. Barnes, C.W. Pemble, D.D. Brand, D.G. Simpson, G.L. Bowlin, Cross-linking electrospun type II collagen tissue engineering scaffolds with carbodiimide in ethanol., Tissue Eng. 13 (2007) 1593–1605. doi:10.1089/ten.2006.0292.

[94] D. Ceballos, X. Navarro, N. Dubey, G. Wendelschafer-Crabb, W.R. Kennedy, R.T. Tranquillo, Magnetically Aligned Collagen Gel Filling a Collagen Nerve Guide Improves Peripheral Nerve Regeneration, Exp. Neurol. 158 (1999) 290–300. doi:10.1006/exnr.1999.7111.

[95] A. Aravamudhan, D.M. Ramos, J. Nip, M.D. Harmon, R. James, M. Deng, C.T. Laurencin, X. Yu, S.G. Kumbar, Cellulose and collagen derived micro-nano structured scaffolds for bone tissue engineering., J. Biomed. Nanotechnol. 9 (2013) 719–731.

[96] R. Parenteau-Bareil, R. Gauvin, F. Berthod, Collagen-Based Biomaterials for Tissue Engineering Applications, Materials (Basel). 3 (2010). doi:10.3390/ma3031863.

[97] M. Mizuno, M. Shindo, D. Kobayashi, E. Tsuruga, A. Amemiya, Y. Kuboki, Osteogenesis by bone marrow stromal cells maintained on type I collagen matrix gels in vivo, Bone. 20 (1997) 101–107. doi:10.1016/S8756-3282(96)00349-3.

[98] M.M. Stevens, Biomaterials for bone tissue engineering, Mater. Today. 11 (2008) 18–25. doi:10.1016/S1369-7021(08)70086-5.

[99] L. Lu, S.J. Peter, M. D. Lyman, H.-L. Lai, S.M. Leite, J.A. Tamada, S. Uyama, J.P. Vacanti, R. Langer, A.G. Mikos, In vitro and in vivo degradation of porous poly(dl-lactic-co-glycolic acid) foams, Biomaterials. 21 (2000) 1837–1845. doi:10.1016/S0142-9612(00)00047-8.

[100] S.H. Oh, S.G. Kang, E.S. Kim, S.H. Cho, J.H. Lee, Fabrication and characterization of hydrophilic poly(lactic-co-glycolic acid)/poly(vinyl alcohol) blend cell scaffolds by melt-molding particulate-leaching method, Biomaterials. 24 (2003) 4011–4021. doi:10.1016/S0142-9612(03)00284-9.

[101] A.S. Rowlands, S.A. Lim, D. Martin, J.J. Cooper-White, Polyurethane/poly(lactic-co-glycolic) acid composite scaffolds fabricated by thermally induced phase separation, Biomaterials. 28 (2007) 2109–2121. doi:10.1016/j.biomaterials.2006.12.032.

[102] J.M. Karp, P.D. Dalton, M.S. Shoichet, Scaffolds for Tissue Engineering, MRS Bull. 28 (2003) 301–306. doi:10.1557/mrs2003.85.

[103] E.S. Place, J.H. George, C.K. Williams, M.M. Stevens, Synthetic polymer scaffolds for tissue engineering, Chem. Soc. Rev. 38 (2009) 1139–1151. doi:10.1039/b811392k.

[104] P.A. Gunatillake, R. Adhikari, Biodegradable synthetic polymers for tissue engineering., Eur. Cell. Mater. 5 (2003) 1–16; discussion 16.

[105] H. Liu, E.B. Slamovich, T.J. Webster, Less harmful acidic degradation of poly(lactic-co-glycolic acid) bone tissue engineering scaffolds through titania nanoparticle addition, Int. J. Nanomedicine. 1 (2006) 541–545. http://www.ncbi.nlm.nih.gov/pmc/articles/PMC2676635/.

[106] M. Erol-Taygun, K. Zheng, A.R. Boccaccini, Nanoscale Bioactive Glasses in Medical Applications, Int. J. Appl. Glas. Sci. 4 (2013) 136–148. doi:10.1111/ijag.12029.

[107] E. Ramin, R.A. Harris, Advanced computer-aided design for bone tissue-engineering scaffolds, Proc. Inst. Mech. Eng. Part H J. Eng. Med. 223 (2009) 289–301. doi:10.1243/09544119JEIM452.

[108] D.-J. Yoo, Recent trends and challenges in computer-aided design of additive manufacturing-based biomimetic scaffolds and bioartificial organs, Int. J. Precis. Eng. Manuf. 15 (2014) 2205–2217. doi:10.1007/s12541-014-0583-7.

[109] S.M. Giannitelli, D. Accoto, M. Trombetta, A. Rainer, Current trends in the design of scaffolds for computer-aided tissue engineering, Acta Biomater. 10 (2014) 580–594. doi:10.1016/j.actbio.2013.10.024.

[110] A.H. Schoen, Infinite periodic minimal surfaces without self-intersections, NASA Tech. Note D-5541. (1997).

[111] S. Torquato, A. Donev, Minimal surfaces and multifunctionality, Proc. R. Soc. London A Math. Phys. Eng. Sci. 460 (2004) 1849–1856. doi:10.1098/rspa.2003.1269.

[112] D.W. Abueidda, A.S. Dalaq, R.K. Abu Al-Rub, H.A. Younes, Finite element predictions of effective multifunctional properties of interpenetrating phase composites with novel triply periodic solid shell architectured reinforcements, Int. J. Mech. Sci. 92 (2015) 80–89. doi:10.1016/j.ijmecsci.2014.12.004.

[113] T. Femmer, A.J.C. Kuehne, M. Wessling, Estimation of the structure dependent performance of 3-D rapid prototyped membranes, Chem. Eng. J. 273 (2015) 438–445. doi:10.1016/j.cej.2015.03.029.

[114] B. Sahab, V. Nicolas, W. Pai, F.N. X., B. Katia, Harnessing Deformation to Switch On and Off the Propagation of Sound, Adv. Mater. 28 (2015) 1631–1635. doi:10.1002/adma.201504469.

[115] N. Sreedhar, N. Thomas, O. Al-Ketan, R. Rowshan, H.H. Hernandez, R.K. Abu Al-Rub, H.A. Arafat, Mass transfer analysis of ultrafiltration using spacers based on triply periodic minimal surfaces: Effects of spacer design, directionality and voidage, J. Memb. Sci. 561 (2018) 89–98. doi:10.1016/j.memsci.2018.05.028.

[116] O. Al-Ketan, M. Adel Assad, R.K. Abu Al-Rub, Mechanical properties of periodic interpenetrating phase composites with novel architected microstructures, Compos. Struct. 176 (2017) 9–19. doi:10.1016/j.compstruct.2017.05.026.

[117] S. Rajagopalan, R.A. Robb, Schwarz meets Schwann: design and fabrication of biomorphic and durataxic tissue engineering scaffolds., Med. Image Anal. 10 (2006) 693–712. doi:10.1016/j.media.2006.06.001.

[118] F.P.W. Melchels, K. Bertoldi, R. Gabbrielli, A.H. Velders, J. Feijen, D.W. Grijpma, Mathematically defined tissue engineering scaffold architectures prepared by stereolithography., Biomaterials. 31 (2010) 6909–6916. doi:10.1016/j.biomaterials.2010.05.068.

[119] S.C. Kapfer, S.T. Hyde, K. Mecke, C.H. Arns, G.E. Schröder-Turk, Minimal surface scaffold designs for tissue engineering, Biomaterials. 32 (2011) 6875–6882. doi:10.1016/j.biomaterials.2011.06.012.

[120] A. Ronca, L. Ambrosio, D.W. Grijpma, Preparation of designed poly(d,l-lactide)/nanosized hydroxyapatite composite structures by stereolithography, Acta Biomater. 9 (2013) 5989–5996. doi:10.1016/j.actbio.2012.12.004.

[121] J. Shin, S. Kim, D. Jeong, H.G. Lee, D. Lee, J.Y. Lim, J. Kim, Finite Element Analysis of Schwarz P Surface Pore Geometries for Tissue-Engineered Scaffolds, Math. Probl. Eng. 2012 (2012) 13. http://dx.doi.org/10.1155/2012/694194.

[122] R.M. Felfel, L. Poocza, M. Gimeno-Fabra, T. Milde, G. Hildebrand, I. Ahmed, C. Scotchford, V. Sottile, D.M. Grant, K. Liefeith, In vitro degradation and mechanical properties of PLA-PCL copolymer unit cell scaffolds generated by two-photon polymerization., Biomed. Mater. 11 (2016) 15011. doi:10.1088/1748-6041/11/1/015011.

[123] H.A. Almeida, P.J. Bártolo, Tensile and Shear Stress Evaluation of Schwartz Surfaces for Scaffold Design, 4th Int. Conf. Tissue Eng. ICTE2015, An ECCOMAS Themat. Conf. 110 (2015) 167–174. doi:10.1016/j.proeng.2015.07.025.

[124] Y. Jung, S. Torquato, Fluid permeabilities of triply periodic minimal surfaces, Phys. Rev. E. 72 (2005) 56319. doi:10.1103/PhysRevE.72.056319.

[125] R. Zhang, P.X. Ma, Synthetic nano-fibrillar extracellular matrices with predesigned macroporous architectures., J. Biomed. Mater. Res. 52 (2000) 430–438.

[126] P.X. Ma, Scaffolds for tissue fabrication, Mater. Today. 7 (2004) 30–40. doi:10.1016/S1369-7021(04)00233-0.

[127] E. Chevalier, D. Chulia, C. Pouget, M. Viana, Fabrication of porous substrates: a review of processes using pore forming agents in the biomaterial field., J. Pharm. Sci. 97 (2008) 1135–1154. doi:10.1002/jps.21059.

[128] P.K.D. V Yarlagadda, M. Chandrasekharan, J.Y.M. Shyan, Recent advances and current developments in tissue scaffolding., Biomed. Mater. Eng. 15 (2005) 159–177.

[129] A.G. Mikos, J.S. Temenoff, Formation of highly porous biodegradable scaffolds for tissue engineering, Electron. J. Biotechnol. Vol 3, No 2. (2000). http://www.ejbiotechnology.info/index.php/ejbiotechnology/article/view/427.

[130] B. Subia, J. Kundu, S. C., Biomaterial Scaffold Fabrication Techniques for Potential Tissue Engineering Applications, Tissue Eng. (2010) 141–159. doi:10.5772/8581.

[131] A.G. Mikos, G. Sarakinos, S.M. Leite, J.P. Vacant, R. Langer, Laminated three-dimensional biodegradable foams for use in tissue engineering, Biomaterials. 14 (1993) 323–330. doi:10.1016/0142-9612(93)90049-8.

[132] A.G. Mikos, A.J. Thorsen, L.A. Czerwonka, Y. Bao, R. Langer, D.N. Winslow, J.P. Vacanti, Preparation and characterization of poly(l-lactic acid) foams, Polymer (Guildf). 35 (1994) 1068–1077. doi:10.1016/0032-3861(94)90953-9.

[133] P. Plikk, S. Malberg, A.-C. Albertsson, Design of resorbable porous tubular copolyester scaffolds for use in nerve regeneration., Biomacromolecules. 10 (2009) 1259–1264. doi:10.1021/bm900093r.

[134] T. Johnson, R. Bahrampourian, A. Patel, K. Mequanint, Fabrication of highly porous tissue-engineering scaffolds using selective spherical porogens., Biomed. Mater. Eng. 20 (2010) 107–118. doi:10.3233/BME-2010-0621.

[135] D.J. Mooney, D.F. Baldwin, N.P. Suh, J.P. Vacanti, R. Langer, Novel approach to fabricate porous sponges of poly(d,l-lactic-co-glycolic acid) without the use of organic solvents, Biomaterials. 17 (1996) 1417–1422. doi:10.1016/0142-9612(96)87284-X.

[136] Q.L. Loh, C. Choong, Three-Dimensional Scaffolds for Tissue Engineering Applications: Role of Porosity and Pore Size, Tissue Eng. Part B Rev. 19 (2013) 485–502. doi:10.1089/ten.teb.2012.0437.

[137] V. Keskar, N.W. Marion, J.J. Mao, R.A. Gemeinhart, *In Vitro* Evaluation of Macroporous Hydrogels to Facilitate Stem Cell Infiltration, Growth, and Mineralization, Tissue Eng. Part A. 15 (2009) 1695–1707. doi:10.1089/ten.tea.2008.0238.

[138] C. Wachiralarpphaithoon, Y. Iwasaki, K. Akiyoshi, Enzyme-degradable phosphorylcholine porous hydrogels cross-linked with polyphosphoesters for cell matrices, Biomaterials. 28 (2007) 984–993. doi:10.1016/j.biomaterials.2006.10.024.

[139] Y.S. Nam, T.G. Park, Biodegradable polymeric microcellular foams by modified thermally induced phase separation method., Biomaterials. 20 (1999) 1783–1790. doi:10.1016/S0142-9612(99)00073-3.

[140] J. Shao, C. Chen, Y. Wang, X. Chen, C. Du, Early stage structural evolution of PLLA porous scaffolds in thermally induced phase separation process and the corresponding biodegradability and biological property, Polym. Degrad. Stab. 97 (2012) 955–963. doi:10.1016/j.polymdegradstab.2012.03.014.

[141] T. Lu, Y. Li, T. Chen, Techniques for fabrication and construction of three-dimensional scaffolds for tissue engineering., Int. J. Nanomedicine. 8 (2013) 337–350. doi:10.2147/IJN.S38635.

[142] V.J. Chen, L.A. Smith, P.X. Ma, Bone regeneration on computer-designed nano-fibrous scaffolds, Biomaterials. 27 (2006) 3973–3979. doi:10.1016/j.biomaterials.2006.02.043.

[143] K. Whang, C.H. Thomas, K.E. Healy, G. Nuber, A novel method to fabricate bioabsorbable scaffolds, Polymer (Guildf). 36 (1995) 837–842. doi:10.1016/0032-3861(95)93115-3.

[144] F.J. O'Brien, B.A. Harley, I. V. Yannas, L. Gibson, Influence of freezing rate on pore structure in freeze-dried collagen-GAG scaffolds, Biomaterials. 25 (2004) 1077–1086. doi:10.1016/S0142-9612(03)00630-6.

[145] W.-Y. Yeong, C.-K. Chua, K.-F. Leong, M. Chandrasekaran, Rapid prototyping in tissue engineering: challenges and potential, Trends Biotechnol. 22 (2004) 643–652. doi:10.1016/j.tibtech.2004.10.004.

[146] F. Shen, C. YL, Y. LF, Y. KD, D. XH, J. WY, S. HD, A study on the fabrication of porous chitosan/gelatin network scaffold for tissue engineering, Polym. Int. 49 (2000) 1596–1599. doi:10.1002/1097-0126(200012)49:12<1596::AID-PI553>3.0.CO;2-S.

[147] A.J. Salgado, O.P. Coutinho, R.L. Reis, Bone tissue engineering: state of the art and future trends., Macromol. Biosci. 4 (2004) 743–765. doi:10.1002/mabi.200400026.

[148] M. Lee, J.C.Y. Dunn, B.M. Wu, Scaffold fabrication by indirect three-dimensional printing, Biomaterials. 26 (2005) 4281–4289. doi:10.1016/j.biomaterials.2004.10.040.

[149] O.A. Abdelaal, S.M. Darwish, Fabrication of Tissue Engineering Scaffolds Using Rapid Prototyping Techniques, World Acad. Sci. Eng. Technol. Int. Sci. Index. 59 (2011) 1325–1333. doi:10.1007/978-3-642-31470-4_3.

[150] D.W. Hutmacher, Scaffolds in tissue engineering bone and cartilage, Biomaterials. 21 (2000) 2529–2543. doi:10.1016/S0142-9612(00)00121-6.

[151] H.N. Chia, B.M. Wu, Recent advances in 3D printing of biomaterials., J. Biol. Eng. 9 (2015) 4. doi:10.1186/s13036-015-0001-4.

[152] S.S. Kim, H. Utsunomiya, J.A. Koski, B.M. Wu, M.J. Cima, J. Sohn, K. Mukai, L.G. Griffith, J.P. Vacanti, Survival and function of hepatocytes on a novel three-dimensional synthetic biodegradable polymer scaffold with an intrinsic network of channels., Ann. Surg. 228 (1998) 8–13.

[153] K.F. Leong, C.M. Cheah, C.K. Chua, Solid freeform fabrication of three-dimensional scaffolds for engineering replacement tissues and organs, Focus Biomater. Sci. Asia. 24 (2003) 2363–2378. doi:10.1016/S0142-9612(03)00030-9.

[154] R.A. Giordano, B.M. Wu, S.W. Borland, L.G. Cima, E.M. Sachs, M.J. Cima, Mechanical properties of dense polylactic acid structures fabricated by three dimensional printing., J. Biomater. Sci. Polym. Ed. 8 (1996) 63–75.

[155] B. Yuan, S.-Y. Zhou, X.-S. Chen, Rapid prototyping technology and its application in bone tissue engineering., J. Zhejiang Univ. Sci. B. 18 (2017) 303–315. doi:10.1631/jzus.B1600118.

[156] G.-H. Wu, S. Hsu, Review: Polymeric-Based 3D Printing for Tissue Engineering, J. Med. Biol. Eng. 35 (2015) 285–292. doi:10.1007/s40846-015-0038-3.

[157] Y. Xia, P. Zhou, X. Cheng, Y. Xie, C. Liang, C. Li, S. Xu, Selective laser sintering fabrication of nano-hydroxyapatite/poly-ε-caprolactone scaffolds for bone tissue engineering applications, Int. J. Nanomedicine. 8 (2013) 4197–4213. doi:10.2147/IJN.S50685.

[158] J.M. Williams, A. Adewunmi, R.M. Schek, C.L. Flanagan, P.H. Krebsbach, S.E. Feinberg, S.J. Hollister, S. Das, Bone tissue engineering using polycaprolactone scaffolds fabricated via selective laser sintering, Biomaterials. 26 (2005) 4817–4827. doi:10.1016/j.biomaterials.2004.11.057.

[159] K.F. Leong, K.K. Phua, C.K. Chua, Z.H. Du, K.O. Teo, Fabrication of porous polymeric matrix drug delivery devices using the selective laser sintering technique., Proc. Inst. Mech. Eng. H. 215 (2001) 191–201. doi:10.1243/0954411011533751.

[160] A.-V. Do, B. Khorsand, S.M. Geary, A.K. Salem, 3D Printing of Scaffolds for Tissue Regeneration Applications, Adv. Healthc. Mater. 4 (2015) 1742–1762. doi:10.1002/adhm.201500168.

[161] K. Kim, A. Yeatts, D. Dean, J.P. Fisher, Stereolithographic bone scaffold design parameters: osteogenic differentiation and signal expression., Tissue Eng. Part B. Rev. 16 (2010) 523–539. doi:10.1089/ten.TEB.2010.0171.

[162] J.W. Lee, J.Y. Kim, D.-W. Cho, Solid Free-form Fabrication Technology and Its Application to Bone Tissue Engineering, Int. J. Stem Cells. 3 (2010) 85–95. http://www.ncbi.nlm.nih.gov/pmc/articles/PMC4021802/.

[163] F. Burmeister, S. Steenhusen, R. Houbertz, U.D. Zeitner, S. Nolte, A. Tünnermann, Materials and technologies for fabrication of three-dimensional microstructures with sub-100 nm feature sizes by two-photon polymerization, J. Laser Appl. 24 (2012) 42014. doi:10.2351/1.4730807.

[164] B. Tan, K. Venkatakrishnan, A. Makaronets, Effects of pulsewidth on two-photon polymerization, Des. Monomers Polym. 16 (2013) 145–150. doi:10.1080/15685551.2012.705502.

[165] K. Sugioka, Y. Cheng, Femtosecond laser three-dimensional micro-and nanofabrication, Appl. Phys. Rev. 1 (2014). doi:10.1063/1.4904320.

[166] M. Malinauskas, V. Purlys, M. Rutkauskas, R. Gadonas, Two-photon polymerization for fabrication of three-dimensional micro- and nanostructures over a large area, 2009.

[167] X. Zhou, Y. Hou, J. Lin, A review on the processing accuracy of two-photon polymerization, AIP Adv. 5 (2015). doi:10.1063/1.4916886.

[168] R.J. Narayan, A. Doraiswamy, D.B. Chrisey, B.N. Chichkov, Medical prototyping using two photon polymerization, Mater. Today. 13 (2010) 42–48. doi:10.1016/S1369-7021(10)70223-6.

[169] M.T. Raimondi, S.M. Eaton, M.M. Nava, M. Lagana, G. Cerullo, R. Osellame, Two-photon laser polymerization: from fundamentals to biomedical application in tissue engineering and regenerative medicine., J. Appl. Biomater. Funct. Mater. 10 (2012) 55–65. doi:10.5301/JABFM.2012.9278.

[170] K. Sugioka, Y. Cheng, Femtosecond laser three-dimensional micro- and nanofabrication, Appl. Phys. Rev. 1 (2014) 41303. doi:10.1063/1.4904320.

[171] S.K. Saha, C. Divin, J.A. Cuadra, R.M. Panas, Part Damage due to Proximity Effects During Sub-Micron Additive Manufacturing via Two-Photon Lithography, (2016) V001T02A084. doi:10.1115/MSEC2016-8793.

[172] A. Ovsianikov, X. Shizhou, M. Farsari, M. Vamvakaki, C. Fotakis, B.N. Chichkov, Shrinkage of microstructures produced by two-photon polymerization of Zr-based hybrid photosensitive materials., Opt. Express. 17 (2009) 2143–2148.

[173] T. Baldacchini, S. Snider, R. Zadoyan, Two-photon polymerization with variable repetition rate bursts of femtosecond laser pulses., Opt. Express. 20 (2012) 29890–29899.

[174] H.B. Sun, K. Takada, M.S. Kim, K.S. Lee, S. Kawata, Scaling laws of voxels in two-photon photopolymerization nanofabrication, Appl. Phys. Lett. 83 (2003) 1104–1106. doi:10.1063/1.1599968.

[175] D.-Y. Yang, S.H. Park, T.W. Lim, H.-J. Kong, S.W. Yi, H.K. Yang, K.-S. Lee, Ultraprecise microreproduction of a three-dimensional artistic sculpture by multipath scanning method in two-photon photopolymerization, Appl. Phys. Lett. 90 (2007) 13113. doi:10.1063/1.2425022.

[176] H.-B. Sun, M. Maeda, K. Takada, J.W.M. Chon, M. Gu, S. Kawata, Experimental investigation of single voxels for laser nanofabrication via two-photon photopolymerization, Appl. Phys. Lett. 83 (2003) 819–821. doi:10.1063/1.1598293.

[177] Y. Li, F. Qi, H. Yang, Q. Gong, X. Dong, X. Duan, Nonuniform shrinkage and stretching of polymerized nanostructures fabricated by two-photon photopolymerization., Nanotechnology. 19 (2008) 55303. doi:10.1088/0957-4484/19/05/055303.

[178] L. Poocza, M. Gottschaldt, E. Markweg, N. Hauptmann, G. Hildebrand, D. Pretzel, M. Hartlieb, C. Reichardt, J. Kübel, U.S. Schubert, O. Mollenhauer, B. Dietzek, K. Liefeith, Optimized Photoinitiator for Fast Two-Photon Absorption Polymerization of Polyester-Macromers for Tissue Engineering, Adv. Eng. Mater. 19 (2017) 1600686–n/a. doi:10.1002/adem.201600686.

[179] L. Macarie, G. Ilia, The influence of temperature and photoinitiator concentration on photoinitiated polymerization of diacrylate monomer, Cent. Eur. J. Chem. 3 (2005) 721–730. doi:10.2478/BF02475199.

[180] L. Xu, N. Sheybani, W.A. Yeudall, H. Yang, The effect of photoinitiators on intracellular AKT signaling pathway in tissue engineering application, Biomater. Sci. 3 (2015) 250–255. doi:10.1039/C4BM00245H.

[181] J.D. Sipe, Tissue engineering and reparative medicine., Ann. N. Y. Acad. Sci. 961 (2002) 1–9.

[182] F. ALOUGES, Introduction to Periodic Homogenization, Interdiscip. Inf. Sci. 22 (2016) 147–186. doi:10.4036/iis.2016.A.01.

[183] Z. Fang, C. Yan, W. Sun, A. Shokoufandeh, W. Regli, Homogenization of Heterogeneous Tissue Scaffold: A Comparison of Mechanics, Asymptotic Homogenization, and Finite Element Approach, Appl. Bionics Biomech. 2 (2005). http://dx.doi.org/10.1533/abbi.2004.0002.

[184] Z. Fang, B. Starly, W. Sun, Computer-aided characterization for effective mechanical properties of porous tissue scaffolds, Comput. Des. 37 (2005) 65–72. doi:10.1016/j.cad.2004.04.002.

[185] T. Adachi, Y. Osako, M. Tanaka, M. Hojo, S.J. Hollister, Framework for optimal design of porous scaffold microstructure by computational simulation of bone regeneration., Biomaterials. 27 (2006) 3964–3972. doi:10.1016/j.biomaterials.2006.02.039.

[186] D.P. Byrne, D. Lacroix, J.A. Planell, D.J. Kelly, P.J. Prendergast, Simulation of tissue differentiation in a scaffold as a function of porosity, Young's modulus and dissolution rate: Application of mechanobiological models in tissue engineering, Biomaterials. 28 (2007) 5544–5554. doi:10.1016/j.biomaterials.2007.09.003.

[187] S. Truscello, G. Kerckhofs, S. Van Bael, G. Pyka, J. Schrooten, H. Van Oosterwyck, Prediction of permeability of regular scaffolds for skeletal tissue engineering: A combined computational and experimental study, Acta Biomater. 8 (2012) 1648–1658. doi:10.1016/j.actbio.2011.12.021.

[188] S. Li, Boundary conditions for unit cells from periodic microstructures and their implications, Compos. Sci. Technol. 68 (2008) 1962–1974.

doi:10.1016/j.compscitech.2007.03.035.

[189] S. Li, A. Wongsto, Unit cells for micromechanical analyses of particle-reinforced composites, Mech. Mater. 36 (2004) 543–572. doi:10.1016/S0167-6636(03)00062-0.

[190] S. Li, On the unit cell for micromechanical analysis of fibre-reinforced composites, Proc. R. Soc. London A Math. Phys. Eng. Sci. 455 (1999) 815–838. http://rspa.royalsocietypublishing.org/content/455/1983/815.abstract.

[191] S. Li, General unit cells for micromechanical analyses of unidirectional composites, Compos. Part A Appl. Sci. Manuf. 32 (2001) 815–826. doi:https://doi.org/10.1016/S1359-835X(00)00182-2.

[192] A. Ghali, A. Neville, T. G. Brown, Structural Analysis: A Unified Classical and Matrix Approach, 6th Editio, CRC Press, London, 2009.

[193] H.P. Gavin, The Principle of Virtual Work, 2012. doi:10.1142/9789812815637_0002.

[194] H.P. Gavin, Introduction to The Principles of Virtual Work, 2014.

[195] H.P. Gavin, Strain Energy in Linear Elastic Solids, 2015.

[196] T. Brugarolas, D.S. Gianola, L. Zhang, G.M. Campbell, J.L. Bassani, G. Feng, D. Lee, Tailoring and understanding the mechanical properties of nanoparticle-shelled bubbles, ACS Appl. Mater. Interfaces. 6 (2014) 11558–11572. doi:10.1021/am502290h.

[197] X. LIU, F. CHEN, A review of void formation and its effects on the mechanical performance of carbon fiber reinforced plastic, Eng. Trans. 64 (2016) 33–51. http://et.ippt.gov.pl/index.php/et/article/view/280.

[198] A. Zhang, H. Lu, D. Zhang, Research on the mechanical properties prediction of carbon/epoxy composite laminates with different void contents, Polym. Compos. 37 (n.d.) 14–20. doi:10.1002/pc.23149.

[199] J.C.S.F.M.A. Guemes, Void content in carbon fibre/epoxy resin composites and its effects on compressive properties, Def. Tech. Infromation Cent. OAI-PMH Repos. (1996).

[200] S. Hernández Rueda, Curing , Defects and Mechanical Performance of Fiber-Reinforced Composites, (2013) 198.

[201] P.O. Hagstrand, F. Bonjour, J.A.E. Månson, The influence of void content on the structural flexural performance of unidirectional glass fibre reinforced polypropylene composites, Compos. Part A Appl. Sci. Manuf. 36 (2005) 705–714. doi:10.1016/j.compositesa.2004.03.007.

[202] W. Jiang, Z. Huang, Y. Wang, B. Zheng, H. Zhou, Voids formation and their effects on mechanical properties in thermoformed carbon fiber fabric-reinforced

composites, Polym. Compos. (2018) 19–21. doi:10.1002/pc.24876.

[203] L. Maragoni, P.A. Carraro, M. Quaresimin, Effect of voids on the crack formation in a [45/−45/0]slaminate under cyclic axial tension, Compos. Part A Appl. Sci. Manuf. 91 (2016) 493–500. doi:10.1016/j.compositesa.2016.02.018.

[204] H.Y. Kim, H.N. Kim, S.J. Lee, J.E. Song, S.Y. Kwon, J.W. Chung, D. Lee, G. Khang, Effect of pore sizes of PLGA scaffolds on mechanical properties and cell behaviour for nucleus pulposus regeneration in vivo, J. Tissue Eng. Regen. Med. 11 (2017) 44–57. doi:10.1002/term.1856.

[205] M.S. Aly, Effect of pore size on the tensile behavior of open-cell Ti foams: Experimental results, Mater. Lett. 64 (2010) 935–937. doi:10.1016/j.matlet.2010.01.064.

[206] Y.T. Jian, Y. Yang, T. Tian, C. Stanford, X.P. Zhang, K. Zhao, Effect of pore size and porosity on the biomechanical properties and cytocompatibility of porous NiTi alloys, PLoS One. 10 (2015) 1–10. doi:10.1371/journal.pone.0128138.

[207] H. Yu, H.W. Matthew, P.H. Wooley, S.Y. Yang, Effect of porosity and pore size on microstructures and mechanical properties of poly-epsilon-caprolactone-hydroxyapatite composites, J. Biomed. Mater. Res. - Part B Appl. Biomater. 86 (2008) 541–547. doi:10.1002/jbm.b.31054.

[208] Abaqus 6.13 Documentation, Abaqus Analysis User's Guide, Elements, 28 Continuum Elements, 28.1 General-purpose continuum elements, 28.1.1 Solid (continuum) elements, Choosing an appropiate element, Choosing between bricks/quadrilaterals and tetrahedra/tri, (2013).

[209] L. Musanje, J.L. Ferracane, R.L. Sakaguchi, Determination of the optimal photoinitiator concentration in dental composites based on essential material properties, Dent. Mater. 25 (2009) 994–1000. doi:10.1016/j.dental.2009.02.010.

[210] D. Wu, N. Fang, C. Sun, X. Zhang, Adhesion force of polymeric three-dimensional microstructures fabricated by microstereolithography, Appl. Phys. Lett. 81 (2002) 3963–3965. doi:10.1063/1.1522825.

[211] D. Wu, N. Fang, C. Sun, X. Zhang, Stiction problems in releasing of 3D microstructures and its solution, Sensors Actuators A Phys. 128 (2006) 109–115. doi:10.1016/j.sna.2005.12.041.

[212] D. Karalekas, D. Rapti, E.E. Gdoutos, A. Aggelopoulos, Investigation of shrinkage-induced stresses in stereolithography photo-curable resins, Exp. Mech. 42 (2002) 439–444. doi:10.1007/BF02412150.

[213] J. Case, C. T.F. Ross, 18 Buckling of columns and beams 18.1, in: Strength Mater. Struct., 4th Editio, Butterworth-Heinemann, 1999: pp. 424–457.

[214] N.J. Sniadecki, Eccentric loading (lecture 33), Univ. Washingt. (2008).

[215] 22.5.2 Hyperelastic behavior in elastomeric foams Products: Abaqus/Standard

Abaqus/Explicit Abaqus/CAE, (2018) 1–11. https://www.sharcnet.ca/Software/Abaqus/6.14.2/v6.14/books/usb/default.htm?startat=pt05ch22s05.html.

[216] R. Lakes, P. Rosakis, A. Ruina, Microbuckling instability in elastomeric cellular solids, J. Mater. Sci. 28 (1993) 4667–4672. doi:10.1007/BF00414256.

[217] P. Hård af Segerstad, S. Toll, Open-cell cellular solids: A constitutive equation for hyperelasticity with deformation induced anisotropy, Int. J. Solids Struct. 45 (2008) 1978–1992. doi:10.1016/j.ijsolstr.2007.11.003.

[218] D. Périé, D. Korda, J.C. Iatridis, Confined compression experiments on bovine nucleus pulposus and annulus fibrosus: Sensitivity of the experiment in the determination of compressive modulus and hydraulic permeability, J. Biomech. 38 (2005) 2164–2171. doi:10.1016/j.jbiomech.2004.10.002.

[219] M.A. Soltz, G.A. Ateshian, Experimental verification and theoretical prediction of cartilage interstitial fluid pressurization at an impermeable contact interface in confined compression, J. Biomech. 31 (1998) 927–934. doi:10.1016/S0021-9290(98)00105-5.

[220] J. Tong, Y.-H. Hsu, K. Madi, A. Cossey, A. Au, Characterisation of Hydrogel Scaffolds Under Compression BT - Biomaterials for Implants and Scaffolds, in: Q. Li, Y.-W. Mai (Eds.), Springer Berlin Heidelberg, Berlin, Heidelberg, 2017: pp. 319–347. doi:10.1007/978-3-662-53574-5_11.

[221] S.M. Lien, L.Y. Ko, T.J. Huang, Effect of pore size on ECM secretion and cell growth in gelatin scaffold for articular cartilage tissue engineering, Acta Biomater. 5 (2009) 670–679. doi:10.1016/j.actbio.2008.09.020.

[222] L. Polo-Corrales, M. Latorre-Esteves, J.E. Ramirez-Vick, Scaffold Design for Bone Regeneration, J. Nanosci. Nanotechnol. 14 (2014) 15–56. http://www.ncbi.nlm.nih.gov/pmc/articles/PMC3997175/.

[223] S. Prasadh, R.C.W. Wong, Unraveling the mechanical strength of biomaterials used as a bone scaffold in oral and maxillofacial defects, Oral Sci. Int. 15 (2018) 48–55. doi:10.1016/S1348-8643(18)30005-3.

[224] S. Eshraghi, S. Das, Micromechanical finite-element modeling and experimental characterization of the compressive mechanical properties of polycaprolactone-hydroxyapatite composite scaffolds prepared by selective laser sintering for bone tissue engineering, Acta Biomater. 8 (2012) 3138–3143. doi:10.1016/j.actbio.2012.04.022.

[225] L.L. Hench, J.M. Polak, Third-generation biomedical materials., Science. 295 (2002) 1014–7. doi:10.1126/science.1067404.

[226] Y. Liu, G. Wang, Y. Cai, H. Ji, G. Zhou, X. Zhao, R. Tang, M. Zhang, In vitro effects of nanophase hydroxyapatite particles on proliferation and osteogenic differentiation of bone marrow-derived mesenchymal stem cells., J. Biomed. Mater. Res. A. 90 (2009) 1083–1091. doi:10.1002/jbm.a.32192.

[227] Y. Liu, M. Wang, Fabrication and characteristics of hydroxyapatite reinforced polypropylene as a bone analogue biomaterial, J. Appl. Polym. Sci. 106 (2007) 2780–2790. doi:10.1002/app.26917.

[228] H.L. Nichols, N. Zhang, J. Zhang, D. Shi, S. Bhaduri, X. Wen, Coating nanothickness degradable films on nanocrystalline hydroxyapatite particles to improve the bonding strength between nanohydroxyapatite and degradable polymer matrix., J. Biomed. Mater. Res. A. 82 (2007) 373–382. doi:10.1002/jbm.a.31066.

[229] S.A. Park, S.H. Lee, W.D. Kim, Fabrication of porous polycaprolactone/hydroxyapatite (PCL/HA) blend scaffolds using a 3D plotting system for bone tissue engineering, Bioprocess Biosyst. Eng. 34 (2011) 505–513. doi:10.1007/s00449-010-0499-2.

[230] Y.H. Koh, I.K. Jun, H.E. Kim, Fabrication of poly(ε-caprolactone)/hydroxyapatite scaffold using rapid direct deposition, Mater. Lett. 60 (2006) 1184–1187. doi:10.1016/j.matlet.2005.10.103.

[231] S. Moeini, M.R. Mohammadi, A. Simchi, In-situ solvothermal processing of polycaprolactone/hydroxyapatite nanocomposites with enhanced mechanical and biological performance for bone tissue engineering, Bioact. Mater. 2 (2017) 146–155. doi:10.1016/j.bioactmat.2017.04.004.

[232] Y.-N. Zhao, J.-J. Fan, Z.-Q. Li, Y.-W. Liu, Y.-P. Wu, J. Liu, Effects of Pore Size on the Osteoconductivity and Mechanical Properties of Calcium Phosphate Cement in a Rabbit Model, Artif. Organs. 41 (2017) 199–204. doi:10.1111/aor.12742.

[233] A. Nouri, P. D., C. We, Biomimetic Porous Titanium Scaffolds for Orthopedic and Dental Applications, Biomimetics Learn. from Nat. (2010) 415–450. doi:10.5772/8787.

[234] M. Niinomi, Y. Liu, M. Nakai, H. Liu, H. Li, Biomedical titanium alloys with Young's moduli close to that of cortical bone, Regen. Biomater. 3 (2016) 173–185. doi:10.1093/rb/rbw016.

[235] D.B. Burr, R.B. Martin, Errors in bone remodeling: toward a unified theory of metabolic bone disease., Am. J. Anat. 186 (1989) 186–216. doi:10.1002/aja.1001860208.

[236] J.-Y. Rho, L. Kuhn-Spearing, P. Zioupos, Mechanical properties and the hierarchical structure of bone, Med. Eng. Phys. 20 (1998) 92–102. doi:https://doi.org/10.1016/S1350-4533(98)00007-1.

[237] M.A. Pérez, P.J. Prendergast, Random-walk models of cell dispersal included in mechanobiological simulations of tissue differentiation, J. Biomech. 40 (2007) 2244–2253. doi:10.1016/j.jbiomech.2006.10.020.

[238] A. Mohyeldin, T. Garzon-Muvdi, A. Quinones-Hinojosa, Oxygen in stem cell biology: a critical component of the stem cell niche., Cell Stem Cell. 7 (2010)

150–161. doi:10.1016/j.stem.2010.07.007.

[239] P. Massari, A Mathematical Model For Dynamic Simulation of Apoptosis Pathways, (2014). http://tesi.cab.unipd.it/45682/.

[240] J.C. Ashworth, M. Mehr, P.G. Buxton, S.M. Best, R.E. Cameron, Parameterizing the Transport Pathways for Cell Invasion in Complex Scaffold Architectures, Tissue Eng. Part C Methods. 22 (2016) 409–417. doi:10.1089/ten.tec.2015.0483.